UNIVERSITY OF CALIFORNIA

Los Angeles

Expanding the $^{171}Yb^{+}$ toolbox: the $^{2}F^{o}_{7/2}$ state as resource for quantum information science

A dissertation submitted in partial satisfaction
of the requirements for the degree
Doctor of Philosophy in Physics

by

Conrad Harrison Roman

2021

ABSTRACT OF THE DISSERTATION

Expanding the $^{171}Yb^{+}$ toolbox:
the $^{2}F^{o}_{7/2}$ state as resource for quantum information science

by

Conrad Harrison Roman
Doctor of Philosophy in Physics
University of California, Los Angeles, 2021
Professor Wesley C. Campbell, Chair

The $^{171}Yb^{+}$ ion has seen wide scale adoption as a trapped ion qubit across the globe for use in quantum information experiments. It has emerged as a mature and highly efficient platform for large scale quantum simulation and as the workhorse for pushing trapped ion quantum computation into the realm where the so called "quantum advantage" may be realized.

In this thesis we investigate and develop methods of performing state preparation and measurement of the $^{171}Yb^{+}$ ground state qubit that takes advantage of the often overlooked long lived $^{2}F^{o}_{7/2}$ state. By performing narrow-band optical pumping of qubit population to the $^{2}F^{o}_{7/2}$ state, we show that high fidelity state preparation and measurement in $^{171}Yb^{+}$ is possible without the need to enhance photon detection efficiency. We achieve a state preparation and measurement fidelity of $\mathcal{F} = 0.99984^{+4}_{-4}$, the best to date demonstrated in any qubit platform we are aware of, limited by our single qubit gates. We use multiple microwave pulses to show that a state preparation and measurement fidelity of 0.99993^{+2}_{-3} is achievable with better single qubit gates.

We then utilize the optically separated qubit populations to perform high fidelity background free state detection of the ground state qubit with mode locked lasers, achieving a state preparation and measurement fidelity of $\mathcal{F} = 0.9993^{+3}_{-6}$ in the presence of large amounts

of background scatter. This method increased the signal to background ratio by a factor of 150, and provides a pathway to faithful qubit readout in environments where rejection of excitation laser scatter is difficult.

We begin development of a new trapped ion quantum information paradigm, utilizing additional qubits hosted in metastable electronic states to improve the flexibility of quantum information processors. The metastable qubit we develop in $^{171}Yb^{+}$ is a zero-field clock state qubit in the $^{2}F^{o}_{7/2}$ state. We identify the qubit transition frequency and develop a method for heralding state preparation of both computational basis states. The ability to herald state preparation allows us to demonstrate high fidelity state preparation and measurement of the metastable qubit, achieving a fidelity of $\mathcal{F} = 0.9995^{+2}_{-3}$. In this proposed architecture, dissipative operations in the ground state manifold can be implemented in the presence of metastable qubit for sympathetic cooling, and we quantify the effects these lasers may have on the metastable qubit.

The dissertation of Conrad Harrison Roman is approved.

Eric R. Hudson

Paul Hamilton

Justin Ryan Caram

Wesley C. Campbell, Committee Chair

University of California, Los Angeles

2021

To my partner in all things I do, Jenna.

"..you've....you've been talking about laser diodes for the last three nights, and...and I just don't know how to make it stop."

$\sim$ *Jenna*

TABLE OF CONTENTS

LIST OF FIGURES

LIST OF TABLES

ACKNOWLEDGMENTS

First of all I would like to thank my advisor, Wes Campbell, without whom I would not have had such a great experiment to work on. Wes always encourages us to explore new ideas and pursue whatever we think is interesting, which gives us the flexibility to fail and succeed on our own. In both cases, we learned a lot. He taught me how to think like a atomic physicist, both on paper and in the lab, a mindset I will carry with me throughout my career.

I have immensely enjoyed my time in the AMO community at UCLA over the past five years. This is owed entirely to the close group of researchers we have always had, the open collaboration between the various experiments, and the friendliness of all those involved. Each person has contributed to making my time with UCLA AMO a great delight.

In particular, I spent a lot of time with Anthony Ransford, Justin Christensen, and Dave Hucul. Dave taught me a lot about operating the $^{171}Yb^{+}$ qubit when we first started working with it. Justin was always around for conversations regarding high fidelity data, and would always be down to take a walk around the block for a break. Tony was possibly the best lab partner I could have asked for, and I owe a lot of my ion trapping knowledge, for better or worse, to him.

Special thanks go to Matthew Boguslawski, without whom this thesis would have far more errors and make much less sense.

The future of our experiment is in good hands with the new graduate students, Thomas Dellaert and Patrick McMillan. Thank you both for all of your help over the last couple years. Hopefully you can find more elegant solutions for the vast amounts of duct tape I have left all over the experiment (but sometimes duct tape is all you need).

Thanks to my family, whose constant support and encouragement kept me going through my time at UCLA. My mom and dad were always there if I needed someone to call to get a break from the lab for a few minutes. It has often been hard to see my parents and brothers throughout graduate school, and I miss them all very much.

Lastly I have to thank my wife, Jenna, for everything. Her support throughout the years was unbroken, always warm, and frequently necessary. She kept me from working myself to exhaustion, and balanced me out when I needed to put physics aside for a day or two. I am not sure how she dealt with my often random bouts of stress and anxiety, especially over the past year, but I am eternally grateful that she stuck around.

VITA

2011–2015	B.A. (Physics), Physics Department, Boston University
2015-2017	M.S (Physics), Physics and Astronomy Department, University of California, Los Angeles

PUBLICATIONS

Roman, Conrad, Anthony Ransford, Michael Ip, and Wesley C. Campbell. 2020. "Coherent Control for Qubit State Readout," New J. Phys. 22 073038

Di Xiao, Jiguang Li, Wesley C. Campbell, Thomas Dellaert, Patrick McMillin, Anthony Ransford, Conrad Roman, and Andrei Derevianko. 2020. "Hyperfine structure of $^{173}Yb^{+}$: Toward resolving the ^{173}Yb nuclear-octupole-moment puzzle". Phys. Rev. A 102, 022810

Ip, Michael, Anthony Ransford, Andrew M. Jayich, Xueping Long, Conrad Roman, and Wesley C. Campbell. 2018. "Phonon Lasing from Optical Frequency Comb Illumination of Trapped Ions." Phys. Rev. Lett. 121 (4).

CHAPTER 1

Introduction

It has been long realized that there may be power in scaling down the fundamental bits used for computation, to the point where the bits can no longer be modeled classically [Fey82]. The scaling down of modern transistor technology, which aims to continuously increase the transistor density within processors by decreasing the size of the individual transistors, is already in the realm where quantum effects need to be accounted for. Suppression of electron tunneling within transistors at the < 10 nm scale is an active area of research. If instead of suppressing the quantum nature of these devices, we construct our bits as purely quantum mechanical objects, a new range of applications arises.

Collections of quantum bits ("qubits") can be brought together and made to interact in well engineered ways to perform quantum computations. The advantage here becomes clearer when we consider the size of the computational space of an N-bit computer. Classically, an N-bit computer can encode N-bits of information, with the information represented by a bit in the states 0 or 1. Quantum mechanically, an N-qubit quantum computer can encode 2^N bits of information with careful engineered entanglement between the qubits. As a simple example, consider a 2 qubit quantum computer. The state of a single qubit $|q_i\rangle$ can be written as:

$$|q_i\rangle = \alpha\,|0\rangle + \beta\,|1\rangle \tag{1.1}$$

where the constants α and β are the *amplitudes* of each qubit state. If we now have two qubits, the combined state of the two qubit system can be written

$$|\psi\rangle = |q_1\rangle \otimes |q_2\rangle = \alpha\,|00\rangle + \beta\,|11\rangle + \eta\,|01\rangle + \rho\,|10\rangle \tag{1.2}$$

The two qubits now contain information encoded in the amplitudes across four different quantum states. It is the careful and creative manipulation of these amplitudes that leads to powerful quantum information algorithms. The common example given is that if we had a fully controlled 500 qubit quantum computer, we would have a computational space of $2^{500} \approx 10^{150}$ amplitudes, more than there are particles in the known universe (and hence more information than could be ever stored in a classical computer the size of the known universe).

But, with great information, comes the necessity for great control. Algorithms are often designed such that the amplitudes of all the individual states, at the end of an algorithm, coherently interfere in such a way as to provide an answer of interest. This interference is delicate, and can be completely washed out by perturbations from the environment, poor implementation of quantum gates, or simply by limitations of our qubit. It was the discovery of fault tolerant quantum error correction that gave the quantum information community hope that a real processor large enough to perform computationally interesting tasks may one day be feasible [Sho96].

Although there is great promise in the future for producing fault tolerant error corrected quantum computers, current systems lack the necessary gate fidelities and qubit register sizes to make use of these codes. These current machines have been dubbed noisy intermediate scale quantum devices (NISQ devices)[Pre18], and still may have many uses both academically and practically.

1.1 Trapped ion quantum information

The quantum information platform discussed in this thesis is composed of multiple atomic ions levitated in high quality vacuum as to isolate the ions from background gasses. The qubit is defined by choosing two appropriate quantum states of the ion that should be able to satisfy the Divencenzo criteria [DiV00]:

1. The system must be scalable with well defined qubits

2. The qubits must all be able to be initialized to a well known initial state

3. The qubit coherence times must significantly exceed the gate times

4. The system must have access to a gate set that comprises a universal gate set for quantum computation

5. There must be a way to measure and distinguish the qubit states

Items (2-5) have all been demonstrated in various ion species with various qubit encodings [HAB14, NSD86, CHC19, WLQ21]. The qubits are certainly well defined and understood (1), but proving that the system is scalable is hard to prove theoretically. The essential requirement agreed upon for scalability is that the addition of more qubits does not cause an exponential increase in the necessary resources.

With the primitives for creating a quantum computer established, the choice of ion species and qubit type becomes the next step. Each species and isotope thereof has its own advantage and disadvantage. In general, there are three types of qubits widely used in trapped ion quantum information experiments: hyperfine qubits ($\sim$ GHz), Zeeman qubits ($\sim$ MHz), and optical qubits ($\sim$ THz). For a great review on the different types of qubits and best attained fidelities for each gate primitive in each type see [BCM19]. We choose to work with the nuclear spin 1/2 isotope of Yb^+ that hosts a zero field clock state hyperfine qubit that has demonstrated extreme coherence times in excess of 1 hour [WLQ21], high fidelity microwave and laser driven single qubit gates [EHH20, PDF20], and two qubit gates comparable to the best demonstrated in any ion species [PDF20, BBF21].

With current devices still limited in size and gate depth, we are still in the era of NISQ devices. While not always true, measurement of the trapped ion qubit register will often happen in single shot at the end of an algorithm or simulation, causing the end result to be exponentially sensitive in the state preparation and measurement of the entire register. For a SPAM infidelity $\epsilon \equiv 1 - \mathcal{F}_{SPAM}$, the readout fidelity of the entire register will be $(1-\epsilon)^N$. As an example, with 50 ions and a SPAM infidelity of 1%, the end multi qubit state will be readout correctly only $(99\%)^{50} = 60.5\%$ of the time. It is therefore advantageous in the NISQ

devices to perform high fidelity SPAM, with even an order of magnitude increase providing a serious win ($(99.9\%)^{50} = 95\%$). It will be the main focus of this thesis to improve upon the SPAM fidelity in the $^{171}Yb^{+}$ qubit system, and develop new techniques that may help relax other technological restraints such as the need to low laser background scatter and high numerical aperture imaging systems.

CHAPTER 2

Ions and ion trapping

Most trapped ion based technologies will rely on the ability to operate for extended period of time with long ion crystal lifetimes. These ion traps vary in size, design, and characteristics, but all function to serve a similar purpose: confine ions for a time suitable to perform the desired experiments. Generally, the purpose of the trap will drive the design considerations.

Ion traps can exhibit extremely long trapping lifetimes (> 1 week), and trap large numbers of ions (> 100), making it a suitable technology for many areas of research.

2.1 RF trap

It is a well known result of classical electrostatics that a charged particle trajectory cannot be stably confined with static electric fields alone, a result of Earnshaw's theorem. Visually, if the particle is to remain trapped in equilibrium by some force, any perturbation to its position should cause the force to return the particle to the equilibrium point after some relaxation time. Forces of the form $\mathbf{F} = -k\mathbf{r}$ have this property, known as restorative forces, that direct the particles motion back to the equilibrium position when excursions from the equilibrium point are made.

In order to create a potential that, on average, traps charged particles in stable trajectories, we utilize time dependent electric potentials. The goal is to produce potentials of the form $\phi(\mathbf{r}, t) = \phi_o(\alpha_x x^2 + \alpha_y y^2 + \alpha_z z^2)\cos(\Omega_{rf} t)$, where Ω_{rf} is the frequency of the applied potential and the α_i's are constants that must satisfy Gauss' law in the absence of a charge distribution. Specifically,

$$\begin{aligned} \nabla \cdot \mathbf{E} = -\Delta\phi(\mathbf{r}, t) = -2\phi_0 \cos(\Omega_{rf} t) \sum_{i=x,y,z} \alpha_i = 0 \\ \implies \sum_{i=x,y,z} \alpha_i = 0 \end{aligned} \tag{2.1}$$

where $\Delta = \nabla \cdot \nabla$ is the Laplacian operator. This criteria is satisfied when $\alpha_x + \alpha_y + \alpha_z = 0$. The ion trap used for these experiments is of the ring type geometry, creating an oblate potential with azimuthal symmetry [YSD15]. To determine what the constant coefficients must be, it's easiest to solve the Laplacian equation in cylindrical coordinates (and ignoring the time dependence for the moment). Gauss' law for the potential in cylindrical coordinates is given by

$$\begin{aligned} \Delta\phi(\rho, \varphi, z) = \frac{1}{\rho}\frac{\partial}{\partial\rho}\Big(\rho\frac{\partial\phi}{\partial\rho}\Big) + \frac{1}{\rho^2}\frac{\partial^2\phi}{\partial\varphi^2} + \frac{\partial^2\phi}{\partial z^2} = 0 \\ \phi(\rho, \varphi, z) = \phi_o(\alpha_x \rho^2 \cos^2(\varphi) + \alpha_y \rho^2 \sin^2(\varphi) + \alpha_z z^2) \end{aligned} \tag{2.2}$$

We can immediately set the dependence on variation in φ equal to zero since the solution must be azimuthally symmetric (cannot depend on variations in φ). Ignoring the second term in the Laplacian and performing some simple derivatives, we get

$$\alpha_x \cos^2(\varphi) + \alpha_y \sin^2(\varphi) = -\frac{\alpha_z}{2} \tag{2.3}$$

Since the solution must hold for all values of φ, this indicates that $\alpha_x = \alpha_y$, and therefore

$$\alpha_x = \alpha_y = -\frac{\alpha_z}{2} \tag{2.4}$$

which has solution $(\alpha_x = \alpha_y = 1, \alpha_z = -2)$, giving the potential the form $\phi(\mathbf{r}, t) = \phi_0(x^2 + y^2 - 2z^2)\cos(\Omega_{rf} t)$. In the lab, we will also apply time independent voltages, $\phi_1(\mathbf{r})$, to compensate for any stray electric fields that may be present near the center of the ion trap.

The potential is then

$$\phi(\mathbf{r},t) = \frac{\phi_o}{r_o^2}(x^2+y^2-2z^2)\cos(\Omega_{rf}t) + \frac{\phi_1(\mathbf{r})}{r_o^2} \tag{2.5}$$

where the factor r_o has been introduced and is a scaling factor that accounts for the specific geometry of the ion trap. For our trap, r_o is determined via numerical simulations in Comsol to be 512 μm [YSD15]. The equations of motion can be found for the principle coordinate $r_i(t)$ with $\{r_1, r_2, r_3\} = \{x, y, z\}$, and are

$$\begin{aligned} \ddot{r_i}(t) &= -\frac{2e\alpha_i\phi_0}{mr_0^2}r_i(t)\cos(\Omega_{rf}t) - \frac{2e\alpha_i\phi_1}{mr_0^2}r_i(t) \\ \rightarrow \quad \ddot{r_i}(t) &+ r_i(t)\Big(\frac{2e\alpha_i\phi_0}{mr_0^2}\cos(\Omega_{rf}t) + \frac{2e\alpha_i\phi_1}{mr_0^2}\Big) = 0 \end{aligned} \tag{2.6}$$

The change of variable $\xi = \frac{\Omega t}{2}$ leads to

$$\begin{aligned} &\frac{d^2\tilde{r}_i}{d\xi^2} + \tilde{r}_i(a_i - 2q_i\cos(2\xi)) = 0 \\ &a_i = \frac{8e\alpha_i\phi_1}{m\Omega_{rf}^2 r_0^2} \quad q_i = -\frac{4e\alpha_i\phi_0}{m\Omega_{rf}^2 r_0^2} \end{aligned} \tag{2.7}$$

Where for simplicity it has been assumed that the static potentials are applied to the same electrodes that form the radiofrequency potential. This differential equation is the Mathieu differential equation, for which there are known solutions. The differential equation above describes a simple harmonic oscillator with periodically modulated spring constant. Stable solutions to these equations are of the form [Gho95],

$$\tilde{r}(\xi) = A\sum_{n=-\infty}^{+\infty} C_{2n}\cos(2n\pm\beta)\xi + B\sum_{n=-\infty}^{+\infty} C_{2n}\sin(2n\pm\beta)\xi \tag{2.8}$$

where the coefficients C_{2n} satisfy a recursion relation found by inserting equation 2.8 into equation 2.7.

The trap parameters in table 2.1 are typical values used in our experiment. Using these values, we can see that in our experiment the $|a_i|$'s will be in the range $\{0.0, 0.002\}$ depending

on the applied DC potentials, and the $|q_i|$'s will be in the range $\{0.03, 0.06\}$. Thus, both of these parameters for all principle axis directions will satisfy $a_i \ll q_i \ll 1$. In this limit

Typical ion trap parameters			
ϕ_0	ϕ_1	Ω_{rf}	r_0
300 Volts	<10 Volts	$2\pi\times$ 47 MHz	512μm

Table 2.1: Typical values for ion trap parameters in our lab.

it will be often useful to think of the ion trap in the pseudopotential approximation, where the trapped ion is thought of as located in a harmonic potential well. Following the work in [Gho95], we can make a few assumptions:

1. Solutions will be of the form $\tilde{r}_i = R_i + \mu_i$, where R_i represents the secular motion of the trapped ion and μ_i represents the micromotion for the $i = \{x, y, z\}$

2. The amplitude of the secular motion is much larger than the amplitude of the micromotion, $R_i \gg \mu_i$.

3. The timescales of the motion are such that $\frac{d\mu_i}{dt} \gg \frac{dR_i}{dt}$

With these assumptions it can be shown that the solutions for the secular motion in the i^{th} direction follow the equation of motion

$$\frac{d^2R_i}{dt^2} + \Big(a_i + \frac{q_i^2}{2}\Big)\frac{\Omega_{rf}^2}{4}R_i = 0 \tag{2.9}$$

which is identical to the simple harmonic oscillator with natural frequency $\omega_i = \frac{\Omega_{rf}}{2}\sqrt{a_i + \frac{q_i^2}{2}}$, known as the secular frequency. The solution for the micromotion coordinate is $\mu_i = -\frac{q_i R_i}{2}\cos(2\xi)$. This assumption holds in the limit that $a_i \ll q_i$. Plugging $\mu_i = \tilde{r}_i - R_i$ into the equation for the micromotion coordinate, and solution to the secular motion of the form $R_i(t) = R_i^o\cos(\omega_i t + \phi_o)$, the solution for the ion motion in these limits is

$$\tilde{r}_i = R_i^o\cos(\omega_i t + \phi_o)\Big(1 - \frac{q_i}{2}\cos(\Omega_{rf}t)\Big) \tag{2.10}$$

Where the first term reflects the secular motion of the trapped ion, and the second term represents the intrinsic micromotion of the ion in the trap. This intrinsic micromotion is unavoidable, and in fact necessary for effective trapping of ions.

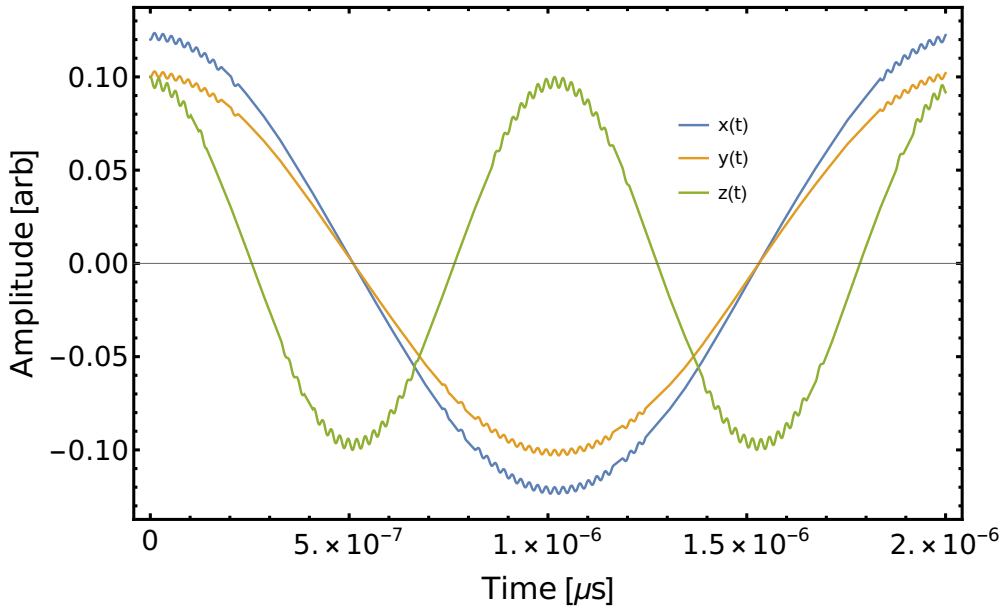

Figure 2.1: Solutions to the ion's equation of motion in the RF trap. The initial displacement in the $\hat{x}$ direction was made slightly different than the $\hat{y}$ direction to prevent overlap of the solutions. The motion exhibits two distinct timescales and amplitudes: the fast motion with small amplitude is *micromotion* that occurs at the trap frequency Ω. The slower oscillatory motion with larger amplitude is the *secular* motion in the trap, whose frequencies are given by $\omega_i = \frac{\Omega_{rf}}{2}\sqrt{a_i + \frac{q_i^2}{2}}$.

If just the large amplitude secular motion is considered, the ion is effectively trapped in a purely three dimensional harmonic oscillator with a potential of the form

$$\Psi = \frac{m}{2}(\omega_x^2 x^2 + \omega_y^2 y^2 + \omega_z^2 z^2) \tag{2.11}$$

where the ω_i's are the secular frequencies. The depth of the pseudopotential for the i^{th} principle coordinate is given by

$$D_i = \frac{m}{2}\omega_i^2 r_o^2 \tag{2.12}$$

2.2 Ion trap loading

Ion traps are "loaded" by introducing the desired ion within the region of the ion trap where laser cooling can be performed. Since the force of the ion trap fields are conservative, the kinetic energy must be below the trap depth for trapping to occur. Given the relatively high trap depth in large ion traps (of order $\sim$ couple eV), the velocity capture range of an ion trap can be quite large. For an ion with m = 171 AMU, 2 eV of kinetic energy corresponds to $\sim$ 1500 m/s, or an external temperature of 23000 K.

There are a few ways to create ions within the trapping region, the most common being photoionization of a thermal beam and ion creation via laser ablation. More sophisticated methods of trap loading are under current investigation to perform fast and efficient trap loading, a likely requirement for large scale trapped in quantum information processors [VAS19, BMC16].

The ion trap in our experiment is loaded by performing 1+1 resonance enhanced multi-photon ionization of ytterbium atoms produced from a thermal source directed at the ion trap center. For ytterbium, this is done by addressing the $^1S_0 \rightarrow {}^1P_0$ transition at 398.9 nm, followed by the absorption of a photon at $\lambda \leq 394$ nm to excite one of the two valence electrons into the continuum, resulting in a singly ionized ytterbium ion. In practice, we use our Doppler cooling laser at 369 nm for the second step for convenience.

The thermal source is a stainless steel tube with $\sim$ 1 mm opening containing natural abundance ytterbium metal which is resistively heated for trap loading. Anywhere from 2-3 Amperes of current are run though the tube to produce a thermal beam directed at the trap.

In order to be isotopically selective, we align the 399 nm laser k-vector perpendicular to the average direction of the thermal beam to reduce Doppler broadening of the 399 nm resonances from each isotope. At a current of 2.2 A, we find that we reliably load a single ion in about 1-5 minutes with 100 μW of 399 nm light focused to a waist of $\omega_0 \approx 40\mu$m at the center of the trap. Much faster loading times have been observed in our system (< 30 s) with the introduction of $\sim$ 0.5 mW of 369 nm mode locked laser, likely due to in increased rate

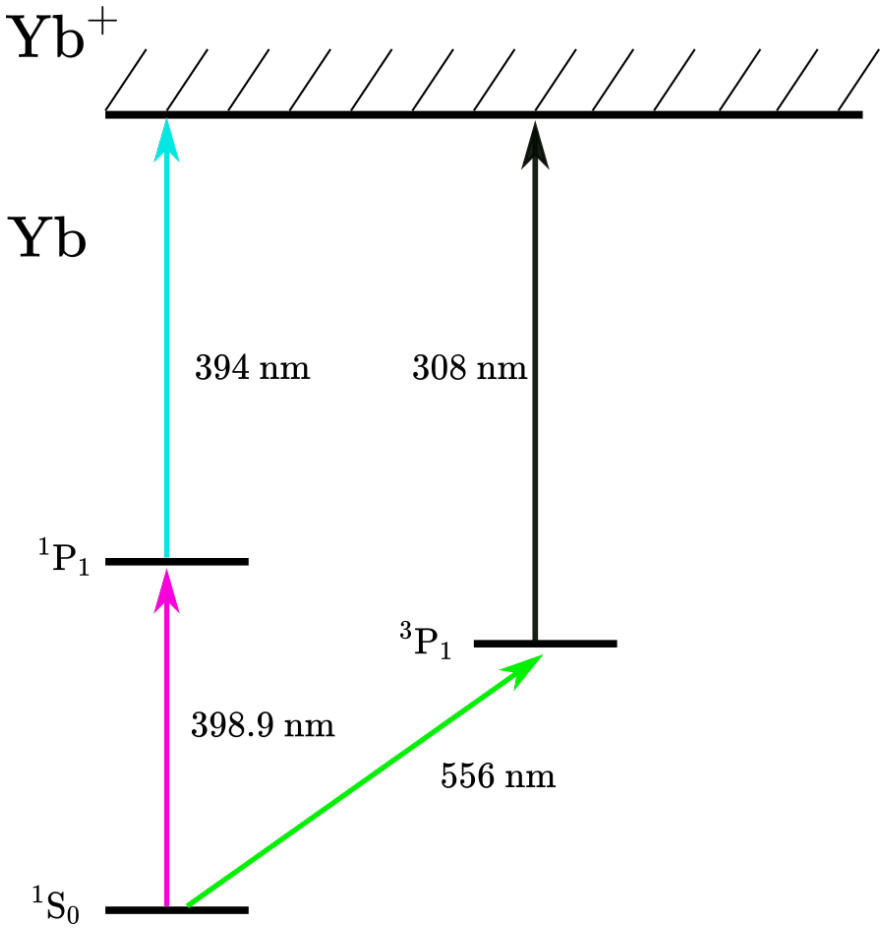

Figure 2.2: Simple energy level diagram of neutral ytterbium atoms. We choose to photoionize on the strong $^1S_0 \rightarrow {}^1P_1$ transition since it only requires one additional laser and is a well established technique.

of ion creation on the second step of photoionization. Faster loading rates have also been observed with mode locked lasers addressing the neutral $^1S_0 \rightarrow {}^1P_1$ transition due to the addressing of a larger number of velocity classes by the laser's broad comb tooth structure [DAB06].

2.3 Doppler cooling

Once the atom has been photoionized it still likely has large amounts of kinetic energy. To cool the ion's external energy to a point suitable for experiments, we apply a velocity dependent force in the form of Doppler cooling. For simplicity, assume the ion is in a 1D

harmonic potential $U_x = \frac{1}{2}m\omega_x^2 x^2$ and that the laser cooling beam propagates in the $\hat{x}$ direction as an infinite plane wave. It is assumed that the timescales of all absorption and spontaneous emission events are much shorter than the oscillation period in the potential, equivalent to the assumption that $\omega_x \ll \Gamma, R_{scatt}$, where Γ is the spontaneous decay rate of the excited state and R_{scatt} is the scattering rate induced by the applied laser. Micromotion will also be neglected, but has been given a formal treatment in [CGB94].

The scattering force exerted on an atom is proportional to how much momentum is transferred to it ($\hbar$k) and the rate at which momentum can be transferred (proportional to the scattering rate). This can be written as $F_{scatt} = \hbar k R_{scatt} = \hbar k \Gamma \rho_{ee}$, where $\hbar k$ is the momentum of a photon with wavelength $\lambda = 2\pi/k$, Γ is the spontaneous decay rate of the excited state, and ρ_{ee} is the excited state probability given by

$$\rho_{ee} = \frac{\Omega^2/\Gamma^2}{1 + \frac{2\Omega^2}{\Gamma^2} + (\frac{2\Delta}{\Gamma})^2} = \frac{1}{2}\frac{s}{1 + s + (\frac{2\Delta}{\Gamma})^2} \tag{2.13}$$

Ω is the resonant Rabi frequency, $\Delta = \omega - \omega_o - \mathbf{k} \cdot \mathbf{v}_x(t)$ is the effective laser detuning from resonance, and $s = 2\Omega^2/\Gamma^2$ is the saturation parameter. Here $v_x(t) = v_o \cos(\omega_x t)$ is the simple harmonic motion of the ion in the $\hat{x}$ direction. The dependence of the laser detuning on the ion velocity causes the scattering force to be higher when the velocity opposes the direction of the laser propagation (in the limit that $kv_x < \omega - \omega_o$). Since the scattering/absorption process is much faster than the ion motion, many events where the ion absorbs momentum $\hbar k$, followed by spontaneous emission in a random direction, can occur, leading to a net damping effect on the ion motion. To see how the damping arises in the limit that the ion velocity is small, the scattering force can be linearized about $v_x = 0$ to get

$$F_{scatt} \approx \hbar k \Gamma \frac{\Omega^2/\Gamma^2}{1 + \frac{2\Omega^2}{\Gamma^2} + (\frac{2\Delta'}{\Gamma})^2} \left(1 + k v_x \frac{8\Delta'/\Gamma^2}{1 + \frac{2\Omega^2}{\Gamma^2} + (\frac{2\Delta'}{\Gamma})^2} \right) \tag{2.14}$$

Where we have redefined the detuning $\Delta' = \omega - \omega_o$ to be the laser detuning from the non-shifted atomic resonance. The second term on the right hand side of equation 2.14 is negative for laser frequencies lower than the natural atomic transition frequency, called "red"

detuned, thereby providing a damping force to the ion motion.

The state of the ion is in equilibrium when the cooling rate due to the damping force is equal to the heating rate due to the randomness of photon absoption and emission. Analysis of these processes is given in many standard texts on laser cooling [MS99, CGB94, WI79], through which an expression for the mean squared velocity of the ion can be determined to be

$$m\langle v^2\rangle = \frac{\hbar\Gamma}{4}\Big(-\frac{\Gamma}{2\Delta}-\frac{2\Delta}{\Gamma}\Big) \tag{2.15}$$

which is minimized when the detuning is $\Delta = -\Gamma/2$. The temperature of the ion inside the harmonic well at the optimal detuning is then

$$T_D = \frac{1}{k_B}\frac{1}{2}m\langle v^2\rangle = \frac{\hbar\Gamma}{2k_B} \tag{2.16}$$

where it has been assumed that the spontaneously emitted photons are emitted in the $\pm\hat{x}$ directions. Small corrections can be made for true emission into three dimensions by an electric dipole.

For a single trapped $^{174}Yb^{+}$ ion, the standard Doppler temperature is 470 μK. For an ion trapped in a 1D harmonic well with secular frequency $\omega = 2\pi \times 1$ MHz, this give a mean thermal phonon number of $\bar{n} \approx 10$.

2.4 Micromotion compensation

In general, without active compensation of stray electric fields, there will be electric fields acting on the ion that displace it from RF null in the trap (the geometric point/line in space where the derivative of the RF electric field is always zero). Voltages are applied to the electrodes on the trap to create electric fields to cancel out these stray electric fields. Here we will list some techniques we have used to determine the location of the RF null.

There are two types of micromotion in an ion trap, usually called *intrinsic* and *excess* micromotion. Intrinsic micromotion is always present, and is the direct result of the second

term in 2.10 due to the secular motion of the ion causing excursions from the RF trap null. Excess micromotion is due to not properly compensating for stray electric fields, resulting in the ion not residing at the three dimensional node of the trap electric field. As shown in [BMB98], an uncompensated stray electric field $\mathbf{E}_{dc}$ will alter the solution to the ion motion to lowest order in a_i, q_i to be

$$\tilde{r}_i(t) \approx \Big(R_i^1 + R_i^o \cos(\omega_i t + \phi_o)\Big)\Big(1 + \frac{q_i}{2}\cos(\Omega_{rf} t)\Big) \tag{2.17}$$

where $R_i^1 = e\mathbf{E}_{dc} \cdot \hat{r}_i / m\omega_i^2$ leads to an overall displacement to the ion position, as well as additional micromotion with amplitude $\sim R_i^1 q_i/2$.

2.4.1 Micromotion modulation of the Doppler cooling transition

The simplest way to detect excess micromotion is to observe its effect on the spectral lineshape of the cooling transition. This method is easily applied when $\Omega_{RF} \geq \Gamma$, and helps for coarse micromotion compensation. The excess micromotion of the ion, in the ion frame, leads to phase modulation of the incident, near resonant laser light that to us, the experimenter, will result in resonances at $\pm n\Omega_{rf}$ in the optical spectrum with $n \in \mathbb{N}_0$. If the spectral lineshape as a function of detuning of a stationary unperturbed ion is given by $\Gamma(\Delta)$, with $\Delta = \omega - \omega_o$, then the micromotion modulated spectra can be approximated as

$$\Gamma(\Delta, \beta) \approx \sum_{n=-\infty}^{\infty} J_n^2(\beta)\Gamma(\Delta + n\Omega_{rf}) \tag{2.18}$$

where β is the modulation depth of the micromotion given by $\beta = \frac{1}{2}\sqrt{(\sum_{i=x,y} k_i R_i^1 q_i)^2} \propto \mathbf{R}^1$, proportional to the displacement from the trap center, and the J_n are Bessel functions of the first kind [BMB98].

The extreme coarse version of this protocol, is to detune the Doppler cooling laser so that it is on resonance with the first order red detuned micromotion sideband, and alter the ion position to decrease the fluorescence observed on the PMT. This works best if the cooling

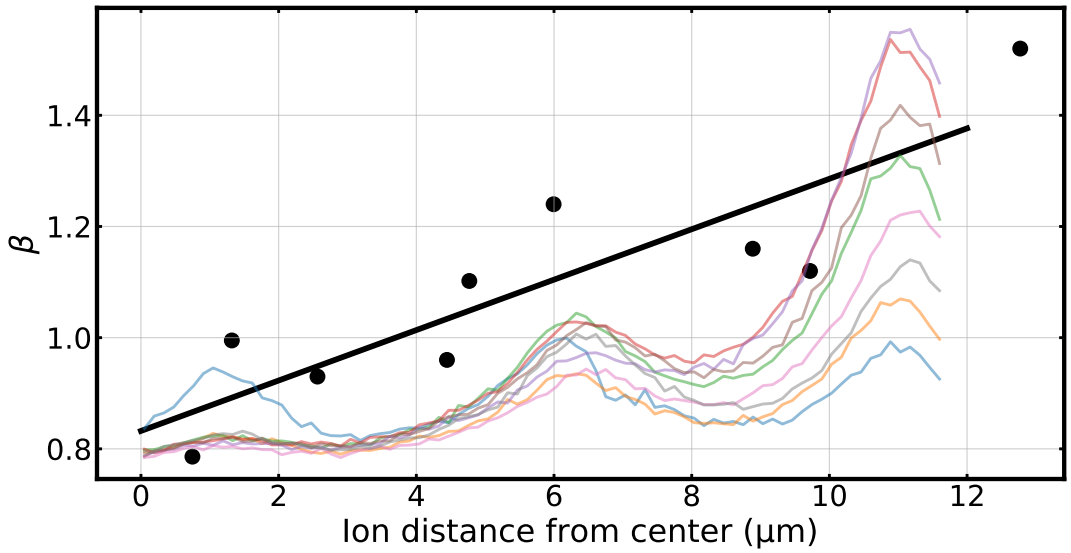

Figure 2.3: Interleaved linescans, and inferred modulation depths as a function of displacement from the trap center. The linear relationship with displacement is clear, with an overall offset from $\beta = 0$ due to a combination of intrinsic micromotion (small effect) and a likely miscalibration of where the true RF null is (large effect). The background shows the linescans of the cooling transition used to determine the micromotion modulation depth. The far right peak is the natural resonance, and the peaks to the left are the n = -1, -2 order micromotion sideband. The total scan width is 120 MHz, spanned by scanning a double passed AOM. Amplitude variation as a function of AOM frequency was not taken into account, but can be with simple calibration.

laser has a relatively large waist at the ion position, and projects onto all principle axes of the trap.

2.4.2 Variation of RF amplitude

A coarse tactic involves variation of the RF amplitude and observing the ion's change in position. The effect of the stray field is to displace the ion from the trap center, and the magnitude of this displacement is proportional to $1/\omega_i^2$. Thus if we increase (decrease) the RF amplitude, we will be decreasing (increasing) the displacement of the ion from the RF null.

While this works in theory to some precision, in our experiment we have found this tactic

unreliable. We believe this is due to a slight DC bias on the RF ring that changes as the RF amplitude is varied, which causes the ion to displace as a function of RF amplitude even when it is well micromotion compensated (up to the precision of our other techniques).

2.4.3 Photon correlation technique

A more sophisticated photon correlation technique can also be used to aid micromotion compensation. In this scheme, a photon time tagging device is triggered on a specific phase of the applied RF signal, and photons detected by a suitable photon counting device are time tagged with respect to a trigger in phase with the applied RF. By binning the photon arrival times from $t = 0$ to $t = 2\pi/\Omega_{rf}$, we can directly observe the effect of micromotion modulation on the photon arrival time. This method has the benefit that it can give explicit information about when the ion crosses the RF null as it is displaced in the trap. See [BMB98] for example traces of the signal. In our lab we use TimeHarp 260P time correlated single photon counter to timetag photon arrival times with 10 ps precision with respect to the trigger from the RF. Example traces of a micromotion compensated ion, and intentional displacements to either side of the RF null are shown in Figure 2.4.

2.4.4 Observation of micromotion on motion sensitive transitions

While not available on our experiment at the time this is written, we soon will have the capability to couple at least one of our qubits in $^{171}Yb^{+}$ to motion via stimulated Raman transitions. With this available, multiple new avenues to micromotion compensation are available, the most straightforward of which would be the direct observation of micromotion sidebands in the qubit spectrum. The micromotion sideband can be scanned over, and the ion displaced throughout the trap to minimize the sideband amplitude. Other experiments that are sensitive to motional heating of the ion may also aid in micromotion compensation.

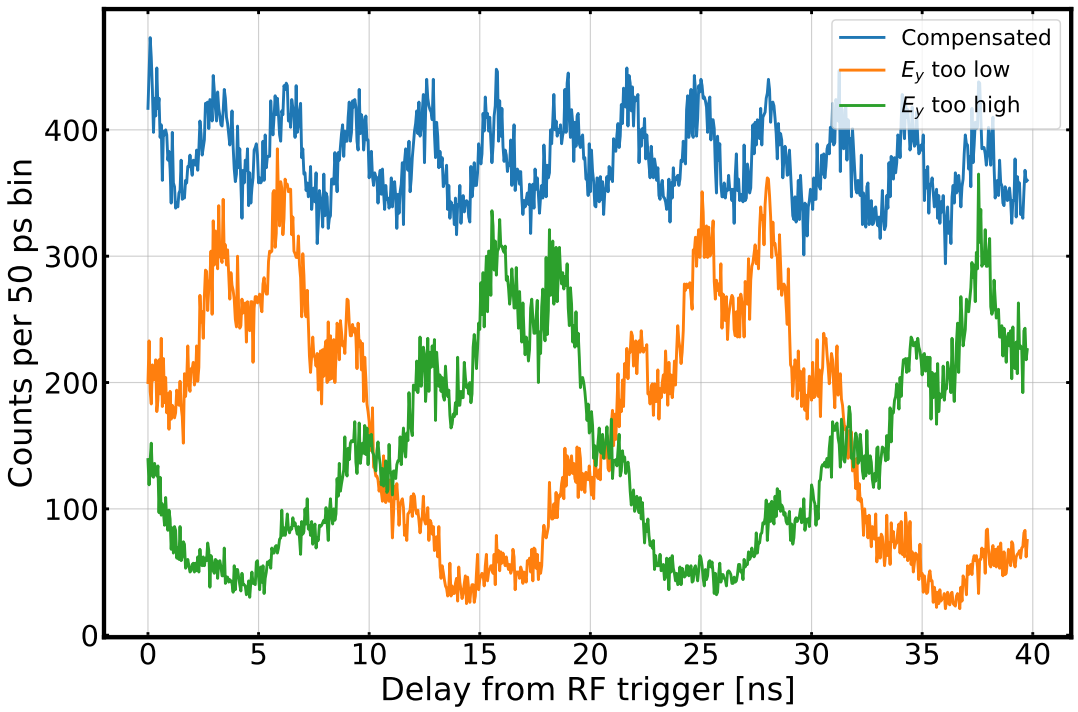

Figure 2.4: TCSPC trace examples. The blue trace shows the case where no micromotion is detected by the Doppler cooling laser. The other two traces show the presence of excess micromotion by moving the ion to either side of the RF null by adjusting the compensating electric field linearly in what we call the y-direction. There is also precise 320 MHz modulation of the photon arrival times that we have not investigated. We suspect it may be related to the frequency of our 935 nm single pass AOM operated at 320 MHz, as no other RF signal in our lab occurs at this precise frequency. The compensated signal is given an artificial offset of +150 counts/bin to separate it from the other two signals.

CHAPTER 3

Light matter interactions

The primary method for controlling the state of a trapped ion is by engineering pulses of electromagnetic radiation to manipulate the electronic state of the ion. Typically this radiation comes in the form of laser light, but sometimes can be longer wavelength radiation in the form of microwave or radiofrequency radiation. We will be interested in both resonant interaction, where the applied radiation is nearly resonant with a particular transition, and off resonant interactions, and how they can affect the state of the ion.

3.1 Electric dipole transitions

The electric dipole interaction can be written as $\mathcal{H}_{E1} = -\mathbf{d} \cdot \mathbf{E}$, with $\mathbf{d} = -e\mathbf{r}$ the dipole moment of the electron and $\mathbf{E}$ an electric field interacting with the electron. Here I have assumed that e is the magnitude of the fundamental charge. The electric field is generally time dependent and can be written as a plane wave $\mathbf{E} = E\hat{\boldsymbol{\epsilon}}\cos(\mathbf{k} \cdot \mathbf{r} - \omega t)$, where $\mathbf{k} = \frac{2\pi}{\lambda}\hat{\mathbf{k}}$ is the wavevector of the electromagnetic wave, $\mathbf{r}$ is the position of the electron, E is the electric field amplitude, and $\hat{\boldsymbol{\epsilon}}$ is the polarization unit vector of the electric field.

The transition matrix element is

$$-\langle e|\,\mathbf{d}\cdot\mathbf{E}\,|g\rangle = \frac{eE}{2}(\langle e|\,\mathbf{r}\cdot\hat{\boldsymbol{\epsilon}}\,|g\rangle\, e^{i(\mathbf{k}\cdot\mathbf{r}-\omega t)} + h.c) \tag{3.1}$$

We can make the electric dipole approximation which states that the wavelength of the radiation is much longer than the length scale associated with the size of the atom, therefore

$e^{i\mathbf{k}\cdot\mathbf{r}} \approx 1$.

$$-\langle e|\,\mathbf{d}\cdot\mathbf{E}\,|g\rangle = \frac{eE}{2}(\langle e|\,\mathbf{r}\cdot\hat{\boldsymbol{\epsilon}}\,|g\rangle\, e^{-i\omega t} + h.c) \tag{3.2}$$

The position vector can be written in terms of spherical harmonics $Y_{l,m}$, which is useful for when we want to compare the relative strengths of transitions. The dot product of the position vector and the laser polarization is

$$\begin{aligned}\mathbf{r}\cdot\hat{\boldsymbol{\epsilon}} &= r\sin(\theta)\cos(\phi)\epsilon_x + r\sin(\theta)\sin(\phi)\epsilon_y + r\cos(\theta)\epsilon_z \\ &= r\sqrt{\frac{4\pi}{3}}\Big(Y_{1,-1}\frac{1}{\sqrt{2}}(\epsilon_x + i\epsilon_y) - Y_{1,1}\frac{1}{\sqrt{2}}(\epsilon_x - i\epsilon_y) + Y_{1,0}\epsilon_z\Big) \\ &= -r\sqrt{\frac{4\pi}{3}}\Big(Y_{1,-1}\hat{\epsilon}_{+1} + Y_{1,1}\hat{\epsilon}_{-1} - Y_{1,0}\hat{\epsilon}_0\Big)\end{aligned} \tag{3.3}$$

Matrix elements of the dipole operator can now be expressed as overlap integrals of the spherical harmonics, which are rank-1 spherical tensors with the equivalence $T^k_q = Y_{l=k,m=q}$.

It will be convenient to evaluate the matrix element of the electric dipole operator between two states in order to determine the coupling strength between the two states, if it exists. A general state which we wish to consider will have quantum numbers $\{n, l, s, I, J, F, m_F\}$. We can write the electronic dipole moment operator $\hat{d}$ as a rank k = 1 spherical tensor operator, T^1_q, which can readily be expressed in terms of the spherical harmonics as shown above. This representation will help us apply the Wigner-Eckart theorem for simplifying the matrix element and comparing relative transition strengths. The Wigner-Eckart theorem can be written for a irreducible spherical tensor operator T^k_q in the $|\gamma, J.m_J\rangle$ basis as

$$\langle\gamma', J', m'_J|\,T^k_q\,|\gamma, J, m_J\rangle = (-1)^{J'-m'_J}\,\langle\gamma', J'|\,|T^k|\,|\gamma, J\rangle \begin{pmatrix} J' & k & J \\ -m'_J & q & m_J \end{pmatrix} \tag{3.4}$$

Where all additional quantum numbers are lumped into $\{\gamma', \gamma\}$. A useful property of the Wigner 3-J symbol for determining an allowed transition is that the sum of the components in the lower row must be zero in order for the 3-J symbol to be non-zero, $m_J - m'_J + q = 0$.

Another helpful relation will be the repeated reduction rule, which is sometimes referred

to as the *spectator theorem*, stemming from the fact that we will remove the dependence of the reduced matrix elements on angular momenta that are not participating in the interaction (hence, they are spectators to the interaction). The spectator theorem can be formulated as follows: if the total angular momentum operator is $\mathbf{J} = \mathbf{J_1} + \mathbf{J_2}$ and $[T^k_q, \mathbf{J}_2] = 0$ for all q, then we can further simplify the reduced matrix element as

$$\langle \gamma', J_1', J_2', J' | \, |T^k| \, | \gamma, J_1, J_2, J \rangle = (-1)^{J_1' + J_2 + J + k} \sqrt{(2J'+1)(2J+1)} \, \langle \gamma', J_1' | \, |T^k| \, | \gamma, J_1 \rangle \begin{Bmatrix} J_1' & J' & J_2 \\ J & J_1 & k \end{Bmatrix} \delta_{J_2', J_2} \quad (3.5)$$

With these tools we can write down a relatively simple formula for the electric dipole matrix element. We will assume that the polarization of laser light is such that only a single arbitrary value of q couples the two states. First we remove the dependence on the magnetic quantum number with the Wigner-Eckart theorem

$$\langle n', l', s', I', J', F', m_F' | \, d^1_q \, | n, l, s, I, J, F, m_F \rangle = (-1)^{F' - m_F'} \, \langle n', l', s', J', I', F' | \, |d^1| \, | n, l, s, J, I, F \rangle \begin{pmatrix} F' & 1 & F \\ -m_F' & q & m_F \end{pmatrix} \quad (3.6)$$

Where we have dropped the subscript q from d to indicate that the magnetic projection dependence is all contained in the Wigner 3-j symbol now. The nuclear spin of the atom does not directly couple to the electric field of the laser, so we can apply the spectator theorem with $(J_1, J_2, J) = (J, I, F)$ and set $I = I'$ to get

$$\langle n', l', s', I, J', F' | \, |d^1| \, | n, l, s, I, J, F \rangle = (-1)^{J' + I + F + 1} \sqrt{(2F+1)(2F'+1)} \begin{Bmatrix} J' & F' & I \\ F & J & 1 \end{Bmatrix} \langle n', l', s', J' | \, |d^1| \, | n, l, s, J \rangle \, \delta_{I', I} \quad (3.7)$$

We could further reduce the reduced matrix element, but it is easier at this point to take advantage of the fact that most strong electric dipole transitions that we use have measured values for the excited state lifetime. It is easier to use this fact, along with results attainable by applying Fermi's golden rule, to write an expression for the reduced matrix element in the above equation in terms of experimental values. The reduced matrix element can be written as [BKD05]

$$\left|\langle n', l', s', J'| \left|d^1\right| |n, l, s, J\rangle\right|^2 = \frac{3\pi\epsilon_0\hbar c^3}{\omega_o^3}(2J'+1)\gamma_p \tag{3.8}$$

where $\gamma_p = \eta\gamma$ is the partial linewidth of the transition $|n', l', s', J'\rangle \leftrightarrow |n, l, s, J\rangle$ given by the total decay rate of the excited state, γ, times the branching ratio of the specific decay path of interest, η. The total expression for the electric dipole matrix element is

$$\begin{aligned}\langle \gamma', I', J', F', m'_F| \, d^1_q \, |\gamma, I, J, F, m_F\rangle = (-1)^{F'-m'_F+J'+I+F+1}\sqrt{(2F+1)(2F'+1)(2J'+1)} \\ \begin{pmatrix} F' & 1 & F \\ -m'_F & q & m_F \end{pmatrix} \begin{Bmatrix} J' & F' & I \\ F & J & 1 \end{Bmatrix} \sqrt{\frac{3\pi\epsilon_0\hbar c^3}{\omega_o^3}\gamma_p}\end{aligned} \tag{3.9}$$

3.2 Electric quadrupole transition

Electric quadrupole transitions are the result of the laser electric field gradient applying a force that couples to the induced quadrupole moment of a given transition. The Hamiltonian governing the transition can be written as

$$\mathcal{H}_{E2} = \hat{Q}\nabla\mathbf{E} \tag{3.10}$$

where $\hat{Q}$ is the induced quadrupole moment. The analysis given here follows the work in [Roo00, Jam98]. The Rabi frequency of the electric quadrupole interaction can be written as [Jam98]

$$\Omega_{E2} = \left|\frac{eE}{2\hbar}\langle e| \, \hat{r}_i\hat{r}_j \, |g\rangle \, \hat{\epsilon}_i k_j\right| = \left|\frac{eE}{2\hbar}\sum_{q=-2}^{2}\langle e| \, r^2 C_q^{(2)} \, |g\rangle \, c_{ij}^{(q)}\hat{\epsilon}_i k_j\right| \tag{3.11}$$

Where $C_q^{(2)}$ are rank-2 spherical tensors and $c_{ij}^{(2)}$ are rank-2 tensors containing geometric information related to the field polarization and propagation direction. $\hat{\epsilon}_i$ are the polarization unit vectors of the applied field and k_j are the components of the laser k-vector. Explicit expressions for $c_{ij}^{(2)}$ are found in the appendix of [Jam98]. For brevity, these matrices can be generated from the spherical basis vectors via the relation

$$\begin{aligned}
\hat{\epsilon}_1 &= -\frac{1}{\sqrt{2}}\{1,-i,0\} \\
\hat{\epsilon}_0 &= \{0,0,1\} \\
\hat{\epsilon}_{-1} &= \frac{1}{\sqrt{2}}\{1,i,0\} \\
\rightarrow c_{ij}^{(q)} &= \sqrt{\frac{10}{3}}(-1)^q \sum_{n=-1}^{1}\sum_{m=-1}^{1} \begin{pmatrix} 1 & 1 & 2 \\ n & m & -q \end{pmatrix} \hat{\epsilon}_{in}\hat{\epsilon}_{jm}
\end{aligned} \tag{3.12}$$

where $\hat{\epsilon}_{jm}$ is the j^{th} component of the m spherical basis vector.

Assuming that the general states of interest have hyperfine structure, and therefore can be expressed as $|\psi\rangle = |\gamma, I, J, F, m_F\rangle$, we can apply the Wiger-Eckart theorem to get

$$\Omega_{E2} = \left| \frac{eE}{2\hbar} \langle \gamma', I', J', F' | \, | r^2 C^{(2)} | \, | \gamma, I, J, F \rangle \sum_{q=-2}^{2} (-1)^{F'-m'_F} \begin{pmatrix} F' & 2 & F \\ -m_F & q & m_F \end{pmatrix} c_{ij}^{(q)} \hat{\epsilon}_i k_j \right| \tag{3.13}$$

Now choosing our coordinate system identically to [Roo00], we define the angle ϕ to be the angle between the laser k-vector and the magnetic field and ψ to be the angle between the laser polarization and the projection of the magnetic field into the plane of incidence. This means our system is, choosing the magnetic field to be in the $\hat{z}$ direction, $\hat{k} = \{\sin(\phi), 0, \cos(\phi)\}$ and $\hat{\epsilon} = \{\cos(\psi)\cos(\phi), \sin(\psi), -\cos(\psi)\sin(\phi)\}$.

The tensor product $\zeta^{(q)} = c_{ij}^{(q)} \hat{\epsilon}_i k_j$ contains all geometric information regarding the relative transition strengths of each $q = \Delta m_F$ transition as a function of the experimental

parameters ψ and ϕ. The tensor products are given by

$$\begin{aligned}
\zeta^{(0)} &= |\cos(\psi)\cos(\phi)\sin(\phi)| \\
\zeta^{(\pm 1)} &= \frac{1}{\sqrt{6}}|\cos(\psi)\cos(2\phi) + i\cos(\phi)\sin(\psi)| \\
\zeta^{(\pm 2)} &= \frac{1}{\sqrt{6}}\left|\Big(\cos(\psi)\cos(\phi) + i\sin(\psi)\Big)\sin(\phi)\right|
\end{aligned} \tag{3.14}$$

The relative strengths as a function of ϕ and ψ are plotted in Figure 3.1. The main electric quadrupole transition driven during experiments in this thesis (when we care about addressing a particular transition) is the $^2S_{1/2} \leftrightarrow {}^2D_{5/2}$ transition, where we try to drive $|\Delta m_F| = 2$ transitions. All lasers in our experiment are incident at a 90 degree angle with respect to

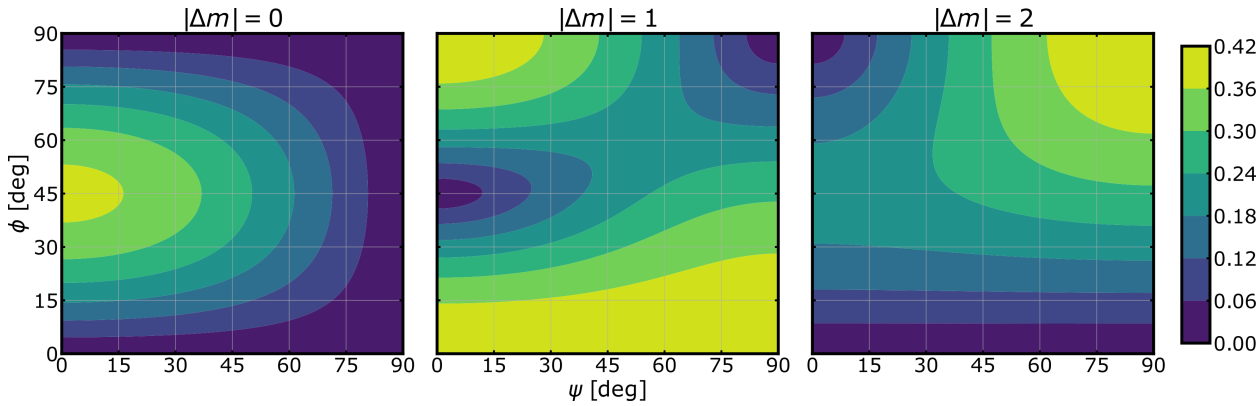

Figure 3.1: Relative strength of the different $|\Delta m_F|$ transitions as a function of the angle ϕ between $\mathbf{k}$ and $\mathbf{B}$, and the angle ψ between the laser polarization $\hat{\boldsymbol{\epsilon}}$ and the projection of $\mathbf{B}$ in the plane of incidence.

the magnetic field ($\phi = 90$).

3.3 Magnetic dipole transitions

In our experiment the primary method for coherent qubit manipulation is via application of resonant microwaves delivered by a standard gain horn antenna. The gain of the horn is quoted in dBi, which is a means of quantifying the directionality of the horn as compared to an isotropic radiator. For our horn, the quoted gain is 20 dBi, which is to say the radiation in the direction of propagation is 100× more intense than if the same amount of microwave

power was radiated by an isotropic radiator (which has 0 dBi gain by definition).

The microwave radiation couples with a non-vanishing magnetic dipole matrix element between two states. Since the qubit states we choose to use are two hyperfine levels within the same fine structure state, an electric dipole moment between the states is parity forbidden ($\Delta L = 0$). The application of microwaves near resonance effectively perturbs the free Hamiltonian by the M1 interaction Hamiltonian

$$\mathcal{H}_{M1} = \boldsymbol{\mu} \cdot \boldsymbol{B}(t, \omega) = -\mu_z B_z \cos(\omega t + \phi) \tag{3.15}$$

Where $\boldsymbol{\mu}$ is the magnetic moment of the atom, ω is the frequency of the applied microwaves, B_z is the amplitude of the magnetic field of the propagating electromagnetic wave at the ions position, and ϕ is the phase of the applied microwaves.

Setting $\hbar = 1$, the Hamiltonian including the qubit states takes the form

$$\mathcal{H}(t) = -\frac{\omega_o}{2} |0\rangle \langle 0| + \frac{\omega_o}{2} |1\rangle \langle 1| - \mathrm{B}_z \cos(\omega t + \phi)\big(\mu_{01} |0\rangle \langle 1| + \mu_{10} |1\rangle \langle 0|\big) \tag{3.16}$$

Where $\mu_{nm} = \langle n| \hat{\mu} |m\rangle$ is the matrix element of the magnetic dipole operator. Then assuming some general two superposition of the two basis states, $|\psi\rangle (t) = c_0(t) |0\rangle + c_1(t) |1\rangle$, we use the time dependent Schrodinger equation to solve for the time dynamics under this Hamiltonian.

$$\begin{aligned} i\dot{c}_0 &= -\frac{\omega_o}{2} c_0 - c_1 \mu_{01} B_z \cos(\omega t + \phi) \\ i\dot{c}_1 &= \frac{\omega_o}{2} c_1 - c_0 \mu_{01}^* B_z \cos(\omega t + \phi) \end{aligned} \tag{3.17}$$

We will now define the Rabi frequency as $\Omega = \mu_{01} B_z$ for convenience. If we now go into the co-rotating frame via the substitution $c_0 = b_0 e^{i\omega_0 t/2}$ and $c_1 = b_1 e^{-i\omega_0 t/2}$, we arrive after algebraic simplification

$$\begin{aligned} \dot{b}_0 &= i\Omega b_1 e^{-i\omega_0 t} \cos(\omega t + \phi) \\ \dot{b}_1 &= i\Omega^* b_0 e^{i\omega_0 t} \cos(\omega t + \phi) \end{aligned} \tag{3.18}$$

Expressing the oscillating field in terms of complex exponentials, and performing the rotating

wave approximation by dropping terms that oscillate at $\omega_0 + \omega$, we get

$$\begin{aligned} \dot{b}_0 &= i\frac{\Omega}{2} b_1 e^{i\phi} e^{i\delta t} \\ \dot{b}_1 &= i\frac{\Omega^*}{2} b_0 e^{-i\phi} e^{-i\delta t} \end{aligned} \tag{3.19}$$

with $\delta = \omega - \omega_0$. To eliminate the time dependence in the system, we can again go into a co-rotating frame via the substitution $b_0 = a_0 e^{i\delta t/2}$ and $b_1 = a_1 e^{-i\delta t/2}$. Inserting these substitutions and performing some simple algebraic simplifications, we get

$$\begin{aligned} \dot{a}_0 &= i\frac{\Omega}{2} a_1 e^{i\phi} - i\frac{\delta}{2} a_0 \\ \dot{a}_1 &= i\frac{\Omega^*}{2} a_0 e^{-i\phi} + i\frac{\delta}{2} a_1 \end{aligned} \tag{3.20}$$

Which have general solutions of the form

$$\begin{aligned} a_0(t) &= A_1 \cos\left(\frac{\Omega_R t}{2}\right) + \frac{1}{\Omega_R}\Big(- i\delta A_1 + i\Omega A_2 \cos(\phi) - \Omega A_2 \sin(\phi)\Big) \sin\left(\frac{\Omega_R t}{2}\right) \\ a_1(t) &= A_3 \cos\left(\frac{\Omega_R t}{2}\right) + \frac{1}{\Omega_R}\Big(i\delta A_3 + i\Omega A_4 \cos(\phi) + \Omega A_4 \sin(\phi)\Big) \sin\left(\frac{\Omega_R t}{2}\right) \end{aligned} \tag{3.21}$$

Where $\Omega_R = \sqrt{\Omega^2 + \delta^2}$ is the generalized Rabi frequency, and the A_i's are constants to be determined by initial conditions. To find the matrix for a general rotation of the initial state $|\psi\rangle = a\,|0\rangle + b\,|1\rangle$, we must find how this matrix should transform the basis state $|0\rangle$ and $|1\rangle$ separately. This is equivalent to asking the question how does this system evolve in time under this interaction when I have initialized the $|0\rangle$ state, or the $|1\rangle$ at t = 0?

Case 1: preparation of the $|0\rangle$ state at t = 0. Under these circumstances, the initial conditions are $a_0(0) = 1$ and $a_1(0) = 0$. Using the latter condition it is easy to show that $A_3 = 0$ and $a_1(t) = \frac{\Omega^*}{\Omega_R} A_4 e^{-i\phi} \sin\big(\frac{\Omega_R t}{2}\big)$. Using this solution, plugging back into 3.20 and evaluating at t = 0, we can easily find that $A_4 = i$, leaving us with $a_1(t) = \frac{i\Omega^*}{\Omega_R} e^{-i\phi} \sin\big(\frac{\Omega_R t}{2}\big)$. We run the exact same procedure for $a_0(t)$, with the exception of using the other differential equation for $\dot{a}_0(t)$ in 3.20 to find $a_0(t) = \cos\big(\frac{\Omega_R t}{2}\big) - i\frac{\delta}{\Omega_R} \sin\big(\frac{\Omega_R t}{2}\big)$

Case 2: preparation of the $|1\rangle$ state at t = 0. With the initial conditions $a_0(0) = 0$ and

$a_1(0) = 1$, we can use the exact same procedure as in case 1 to find $a_0(t) = \frac{i\Omega}{\Omega_R} e^{i\phi} \sin\left(\frac{\Omega_R t}{2}\right)$ and $a_1(t) = \cos\left(\frac{\Omega_R t}{2}\right) + i\frac{\delta}{\Omega_R} \sin\left(\frac{\Omega_R t}{2}\right)$

Now we can fill in a matrix that will evolve any general initial state under the application of this interaction.

$$R(\Omega, \delta, \phi, t) = \begin{pmatrix} \cos\left(\frac{\Omega_R t}{2}\right) - i\frac{\delta}{\Omega_R} \sin\left(\frac{\Omega_R t}{2}\right) & \frac{i\Omega^*}{\Omega_R} e^{-i\phi} \sin\left(\frac{\Omega_R t}{2}\right) \\ \frac{i\Omega^*}{\Omega_R} e^{i\phi} \sin\left(\frac{\Omega_R t}{2}\right) & \cos\left(\frac{\Omega_R t}{2}\right) + i\frac{\delta}{\Omega_R} \sin\left(\frac{\Omega_R t}{2}\right) \end{pmatrix} \tag{3.22}$$

This matrix will allow for the evolution of any initial state given the phase, detuning, and intensity of the applied radiation field, which in our case is typically microwave radiation at 12.642 GHz. Where it will become particularly useful is when we consider more complicated microwave pulse sequences, typically designed to be robust to pulse area ($\theta_{pulse} = \Omega_R t$) errors, detuning errors (δ), or both.

3.3.1 Generalization to four level system

Since our qubit is hosted in the $^2S_{1/2}$ and the nuclear spin of $^{171}Yb^+$ is 1/2, there will be more than just two states in the $^2S_{1/2}$ manifolds that can be coupled by the applied microwave radiation.

These additional states can affect the dynamics of the two approximate two level system if the conditions $\Omega_{02} \ll \delta_B$ and $\Omega_{03} \ll \delta_B$ aren't met. The Hamiltonian for the driven four level system is nearly identical to that of the two level system

$$\mathcal{H}_{M1} = \sum_n \omega_n |n\rangle \langle n| - \Omega_{0n} \cos(\omega t + \phi) \Big(|0\rangle \langle n| + |n\rangle \langle 0| \Big) \tag{3.23}$$

where the energies, in vector form, are $\omega_n = \{-\frac{\omega_0}{2}, \frac{\omega_0}{2}, \frac{\omega_0}{2} - \delta_B, \frac{\omega_0}{2} + \delta_B\}$, and Ω_{0n} are the resonant Rabi frequencies of each transition.

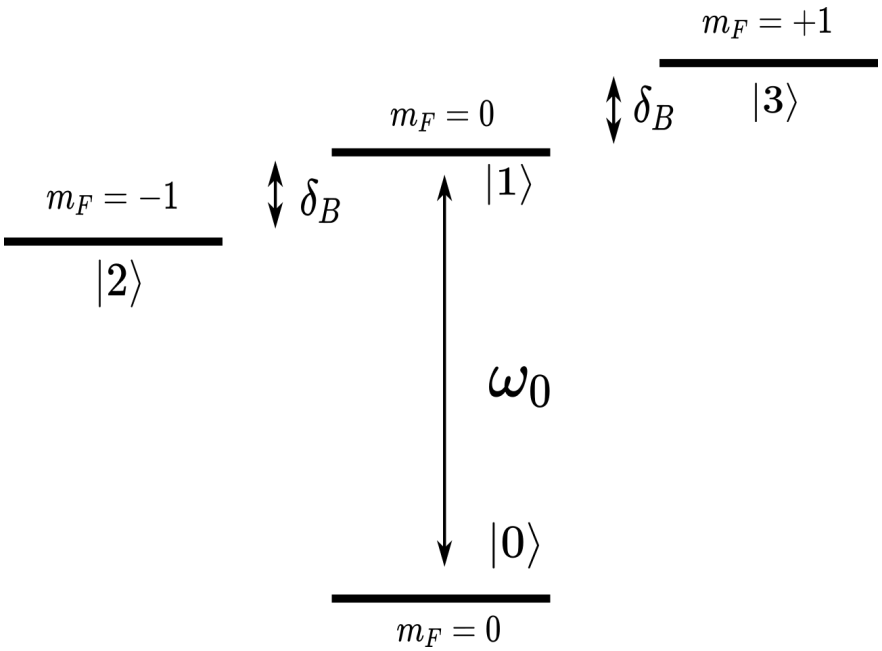

Figure 3.2: Structure of the $^2S_{1/2}$ in $^{171}Yb^+$. The qubit is defined between the zero-field clock states $|0\rangle$ and $|1\rangle$. The magnetic field sensitive states $|2\rangle = |F = 1, m_F = -1\rangle$ and $|3\rangle = |F = 1, m_F = 1\rangle$ are detuned from the qubit frequency by $\delta_B \approx \pm\mu_B|B|$ due to the linear Zeeman shift.

This Hamiltonian can be written in the rotating frame of the qubit as

$$\mathcal{H}_{M1} = \begin{pmatrix} 0 & \frac{\Omega_{01}}{2}e^{i\Delta t}e^{i\phi} & \frac{\Omega_{02}}{2}e^{i\Delta t}e^{i\phi} & \frac{\Omega_{03}}{2}e^{i\Delta t}e^{i\phi} \\ \frac{\Omega_{01}}{2}e^{-i\Delta t}e^{-i\phi} & 0 & 0 & 0 \\ \frac{\Omega_{02}}{2}e^{-i\Delta t}e^{-i\phi} & 0 & -\delta_B & 0 \\ \frac{\Omega_{03}}{2}e^{-i\Delta t}e^{-i\phi} & 0 & 0 & \delta_B \end{pmatrix} \tag{3.24}$$

where it has been assumed that the Rabi frequencies are real. The detuning of the microwaves from the clock qubit resonance is defined as $\Delta = \omega - \omega_0$. To solve this system of equations, the Python package QuTiP is used to numerically solve for the populations in all four states. Input values for the Rabi frequencies are based on experimental measurements, easily determined by performing Rabi flopping scans of each transition.

3.3.2 M1 transition rate

One limitation that every qubit has is the lifetime of the qubit states. Often the qubit state lower in energy is the lowest state available to the electron, and will have an effectively infinite lifetime. The more energetic state though will need to couple to the lower qubit state via some interaction that will allow us to interact the two states. In the case of optical qubits this is often an electric quadrupole interaction (E2), or in the case of hyperfine qubits this is a magnetic dipole (M1) interaction. The lifetime of optical qubits' upper states are often in the 1-60 second range, depending on ion choice (one extreme exception is the $^2\mathrm{S}_{1/2} \leftrightarrow {}^2\mathrm{F}^o_{7/2}$ electric octupole (E3) transition used in a few places around the world as an optical atomic clock, with an upper state lifetime rivaling hyperfine qubits at about 5 years [HSL16]). So what is the lifetime of a hyperfine qubit?

The lifetime of the upper qubit state will depend on the energy separation between that state and any lower energy states it can decay to, and the strength of the coupling to those states. Coupling to the lower states will depend on what moments of the free electromagnetic field the two states couple to, with the lowest order non vanishing moment generally the strongest. For hyperfine qubits defined in the fine structure ground state (often the $^2\mathrm{S}_{1/2}$ for ionic qubits), this lowest order moment is the M1 moment.

The magnetic dipole operator is $\mathbf{M} \propto \mathbf{L} + 2\mathbf{S}$, and can mediate transitions between fine structure states (for instance, $\mathrm{nD}_{5/2} \leftrightarrow \mathrm{nD}_{3/2}$), or between different magnetic states within a particular fine structure state (for instance, $^2\mathrm{S}_{1/2}\,|F=0\rangle \leftrightarrow {}^2\mathrm{S}_{1/2}\,|F=1, m_F\rangle$). The coupling arises from effective magnetic dipole moments of the atom coupling to magnetic fields. Part of the atomic magnet moment is from the intrinsic spin angular momentum of the valence electron, $\mathbf{S}$, and the other is from the orbital magnetic moment of the atom arising from $\mathbf{L}$. The latter idea can be visualized in a classical picture as the electron orbiting around the nucleus as a current loop that itself will have an net magnetic moment.

The transition rate will depend on the reduced magnetic dipole matrix element between the two states of interest, which does not depend on the magnetic quantum number. Assuming the atom has hyperfine structure, we can first remove the dependence on the nuclear

spin, which to lowest order does not partake in the interaction.

$$\langle nJIF|\, L+2S\,|n'J'IF'\rangle = (-1)^{J+I+F'+1}\sqrt{(2F'+1)(2F+1)}\times \begin{Bmatrix} J & F & I \\ F' & J' & 1 \end{Bmatrix} \langle nJ|\,|L+2S|\,|n'J'\rangle \tag{3.25}$$

where now we need to simplify the reduced matrix element of the magnetic moment operator. First we will rewrite $L+2S = J+S$, and the separate matrix elements are

$$\langle nLSJ|\,|S|\,|n'L'S'J'\rangle = (-1)^{S+L'+J'+1}\sqrt{(2J+1)(2J'+1)}\sqrt{S(S+1)(2S+1)}\times \begin{Bmatrix} S & J & L' \\ J' & S & 1 \end{Bmatrix} \delta_{SS'}\delta_{nn'}\delta_{LL'} \tag{3.26}$$

$$\langle nJ|\,|J|\,|n'J'\rangle = \delta_{nn'}\delta_{JJ'}\sqrt{J(J+1)(2J+1)}$$

which can be combined with the previous result that removed the top layer of angular momentum coupling to give the full expression

$$\langle nJIF|\, L+2S\,|n'J'IF'\rangle = -(-1)^{J+I+F'+1}\delta_{SS'}\delta_{nn'}\delta_{LL'}\sqrt{(2F'+1)(2F+1)}\times \begin{Bmatrix} J & F & I \\ F' & J' & 1 \end{Bmatrix} \left(\delta_{JJ'}\sqrt{J(J+1)(2J+1)} + (-1)^{S+L'+J'+1}\sqrt{(2J'+1)(2J+1)}\times \sqrt{S(S+1)(2S+1)} \begin{Bmatrix} S & J & L' \\ J' & S & 1 \end{Bmatrix} \right) \tag{3.27}$$

As a result, magnetic dipole transition selection rules are that $J' = J \pm 1, J$ and that the parity of the initial and final states be the same ($L = L'$). If the orbital angular momentum of the transition cannot change, then it follows that the principal quantum number n must remain unchanged as well due to orthogonality relationships of the hydrogenic radial wavefunctions.

With this matrix element, transition rates between various states where M1 transitions are permitted can be calculated if the energy separation is known. The magnetic dipole

transition rate can be written as [SNM01]

$$A_{i\to j} = \frac{2.69735 \times 10^{10}(\text{Hz nm}^3)}{\lambda^3} \frac{|\langle nJIF| L + 2S |n'J'IF'\rangle|^2}{2F'+1} \tag{3.28}$$

Where the denominator is the degeneracy of the initial state and the wavelength is in nanometers. If a transition in a nuclear spin zero isotope is to be considered, you simply need to neglect (3.25) and just use the results from (3.26), with the degeneracy dictated by the total angular momentum J' rather than F'.

This can now be used to predict the lifetime of the upper qubit state in $^{171}\text{Yb}^+$. The transition frequency is $\omega = 2\pi\times$ 12.642812 GHz, a wavelength in vacuum of 2.37 cm. This gives a transition rate using (3.28) of 2.02×10^{-12} Hz, or a lifetime of about 15600 years.

There will also be interest later in knowing the Einstein A coefficient for the $^2\text{D}_{5/2} \rightarrow {}^2\text{D}_{3/2}$ due to the non vanishing magnetic dipole moment of the transition. Using the energy level values found in the NIST spectral database, the wavelength of the transition can be calculated to be

$$\lambda_D = \frac{1}{\text{E}_{J=5/2} - \text{E}_{J=3/2}} = \frac{1}{24332.69 \text{ cm}^{-1} - 22960.80 \text{ cm}^{-1}} = 7.295 \ \mu m \tag{3.29}$$

We will be particularly interested in the $^2\text{D}_{5/2}\,|F=3\rangle \rightarrow {}^2\text{D}_{3/2}\,|F=2\rangle$ decay path, a small error channel in the electron shelving scheme to be described later. Using the calculated wavelength, the Einstein A coefficient is $A_{i\to j} = 28$ mHz. With an upper state lifetime of $\tau_{5/2} = 7.2$ ms, the branching ratio to the $^2\text{D}_{3/2}\,|F=2\rangle$ is $\xi = (A_{i\to j})(\tau_{5/2}) = 2\times10^{-4}$.

3.4 Stimulated Raman transitions

In order to drive coherent rotation of a microwave frequency qubit with laser fields, two laser fields with a frequency difference near the qubit frequency can be used. Consider the system shown in Figure 3.3: the qubit states are $\{|0\rangle, |1\rangle\}$ with energies $E = \hbar\{\omega_0, \omega_1\}$ (the energy

zero is defined at $\omega = 0$), and are separately coupled to the excited state $|e\rangle$ with energy $E = \hbar\omega_e$. The unperturbed Hamiltonian is (setting $\hbar = 1$),

$$\mathcal{H}_0 = \omega_0 |0\rangle \langle 0| + \omega_1 |1\rangle \langle 1| + \omega_e |e\rangle \langle e| \tag{3.30}$$

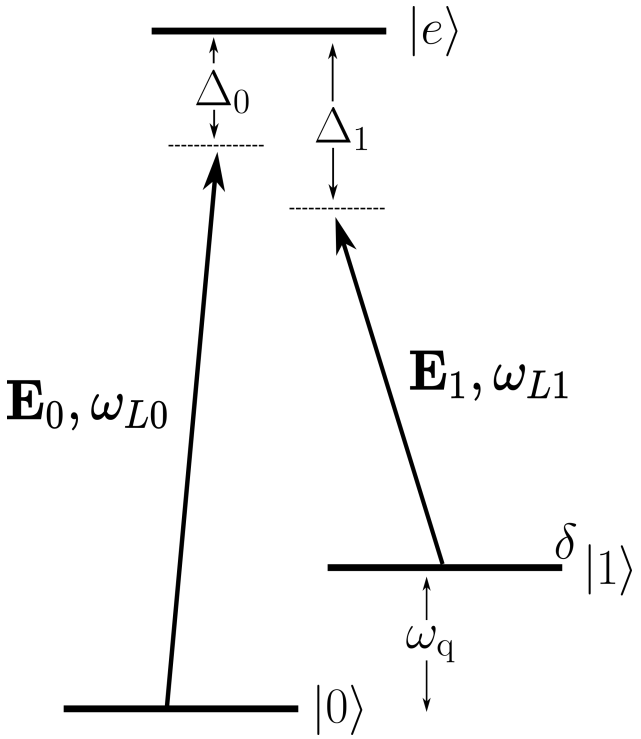

Figure 3.3: Three level system interacting with two far detuned lasers. The qubit is defined between the $|0\rangle$ and $|1\rangle$ states with separation $\mathrm{E}_q = \hbar\omega_q = \hbar(\omega_1 - \omega_0)$. Each qubit states is separately coupled to the excited state $|e\rangle$ via separate laser beams with frequencies ω_{L0} and ω_{L1}. The two lasers are detuned by different amounts from the excited state, indicated as Δ_0 and Δ_1

The low lying states $|0\rangle$ and $|1\rangle$ are coupled to the excited state $|e\rangle$ by two separate lasers with electric fields $\mathbf{E}_0$ and $\mathbf{E}_1$ via interaction with the electric dipole moment of the transition. The electric fields can be expressed as

$$\boldsymbol{E}_i(t) = \boldsymbol{E}_i \cos\left(\boldsymbol{k}_i \cdot \boldsymbol{r} - \omega_{Li} t\right) = \frac{E_i}{2}\left(\hat{\epsilon}_i e^{i(\boldsymbol{k}_i \cdot \boldsymbol{r} - \omega_{Li} t)} + \hat{\epsilon}_i^* e^{-i(\boldsymbol{k}_i \cdot \boldsymbol{r} - \omega_{Li} t)}\right) \tag{3.31}$$

where I have assumed the field amplitudes to be real. The coupling of the applied fields to

the ion are via the electric dipole interaction given by $\mathcal{H}_{int} = -\boldsymbol{d}\cdot\boldsymbol{E}$, which can be expanded in the basis states of the problem. I will assume that the interaction does not couple $|0\rangle$ and $|1\rangle$ directly, so the terms $\langle 0|\,\mathcal{H}_{int}\,|1\rangle = \langle 1|\,\mathcal{H}_{int}\,|0\rangle = 0$.

$$\begin{aligned}\mathcal{H}_{int} = &-\sum_i\sum_j |i\rangle\langle i|\,\boldsymbol{d}\cdot\boldsymbol{E}\,|j\rangle\langle j| = \\ &-\langle 0|\,\boldsymbol{d}\cdot\boldsymbol{E}\,|e\rangle\,|0\rangle\langle e| - \langle e|\,\boldsymbol{d}\cdot\boldsymbol{E}\,|0\rangle\,|e\rangle\langle 0| \\ &-\langle 1|\,\boldsymbol{d}\cdot\boldsymbol{E}\,|e\rangle\,|1\rangle\langle e| - \langle e|\,\boldsymbol{d}\cdot\boldsymbol{E}\,|1\rangle\,|e\rangle\langle 1|\end{aligned} \tag{3.32}$$

Recognizing that there will be two applied fields, such that $\boldsymbol{E} = \boldsymbol{E}_0 + \boldsymbol{E}_1$ (which are implicitly time dependent), and that our beginning assumption that each field only couples one ground state to the excited state, this expression can be simplified to

$$\begin{aligned}\mathcal{H}_{int} &= -\langle 0|\,\boldsymbol{d}\cdot\boldsymbol{E}_0\,|e\rangle\,|0\rangle\langle e| - \langle e|\,\boldsymbol{d}\cdot\boldsymbol{E}_0\,|0\rangle\,|e\rangle\langle 0| \\ &\quad -\langle 1|\,\boldsymbol{d}\cdot\boldsymbol{E}_1\,|e\rangle\,|1\rangle\langle e| - \langle e|\,\boldsymbol{d}\cdot\boldsymbol{E}_1\,|1\rangle\,|e\rangle\langle 1| \\ &= -\mathcal{H}_{0e}\,|0\rangle\langle e| - \mathcal{H}_{e0}\,|e\rangle\langle 0| - \mathcal{H}_{1e}\,|1\rangle\langle e| - \mathcal{H}_{e1}\,|e\rangle\langle 1|\end{aligned} \tag{3.33}$$

The total Hamiltonian of the system is then given by

$$\begin{aligned}\mathcal{H} = \mathcal{H}_0 + \mathcal{H}_{int} = &\omega_0\,|0\rangle\langle 0| + \omega_1\,|1\rangle\langle 1| + \omega_e\,|e\rangle\langle e| \\ &-\mathcal{H}_{0e}\,|0\rangle\langle e| - \mathcal{H}_{e0}\,|e\rangle\langle 0| - \mathcal{H}_{1e}\,|1\rangle\langle e| - \mathcal{H}_{e1}\,|e\rangle\langle 1|\end{aligned} \tag{3.34}$$

We will begin with the time dependent Schrodinger equation, $i\partial_t\,|\psi\rangle = \mathcal{H}\,|\psi\rangle$, to an arbitrary state $|\psi\rangle = c_0\,|0\rangle + c_1\,|1\rangle + c_e\,|e\rangle$, where the coefficients are time dependent and evolve according to the Hamiltonian. The resulting partial differential equations are

$$\begin{aligned}i\dot{c_0} &= \omega_0 c_0 - \mathcal{H}_{0e}c_e \\ i\dot{c_1} &= \omega_1 c_1 - \mathcal{H}_{1e}c_e \\ i\dot{c_e} &= \omega_e c_e - \mathcal{H}_{e0}c_0 - \mathcal{H}_{e1}c_1\end{aligned} \tag{3.35}$$

The first rotation we will make is to rotate each solution at its natural unperturbed frequency, $c_n = b_n e^{-i\omega_n t}$ for $n = \{0, 1, e\}$, which results in the new coupled partial differential equations

$$\begin{aligned} i\dot{b_0} &= -\mathcal{H}_{0e} b_e e^{-i(\omega_e - \omega_0)t} \\ i\dot{b_1} &= -\mathcal{H}_{1e} b_e e^{-i(\omega_e - \omega_1)t} \\ i\dot{b_e} &= -\mathcal{H}_{e0} b_0 e^{i(\omega_e - \omega_0)t} - \mathcal{H}_{e1} b_1 e^{i(\omega_e - \omega_1)t} \end{aligned} \tag{3.36}$$

Looking at Figure 3.3, we can relate the frequencies above to experimentally controllable parameters: $\omega_e - \omega_0 = \omega_{L0} + \Delta_0$ and $\omega_e - \omega_1 = \omega_{L1} + \Delta_1$. At this point we need to provide a more explicit representation of the interaction matrix elements. Generally,the matrix element will look like

$$\begin{aligned} \mathcal{H}_{nm} &= \langle n| \boldsymbol{d} \cdot \boldsymbol{E}_i |m\rangle \\ &= \frac{E_i}{2}\Big(\langle n| \boldsymbol{d} \cdot \hat{\epsilon}_i |m\rangle e^{i(\boldsymbol{k}_i \cdot \boldsymbol{r} - \omega_{Li} t)} + \langle n| \boldsymbol{d} \cdot \hat{\epsilon}_i^* |m\rangle e^{-i(\boldsymbol{k}_i \cdot \boldsymbol{r} - \omega_{Li} t)} \Big) \end{aligned} \tag{3.37}$$

Entering this into the partial differential equations, we will find that certain terms oscillate at Δ_i, and others will oscillate at twice the laser frequencies. Since after integration, the parts of the solution that go as $e^{i2\omega_{Li}}$ will pick up a factor of $\frac{1}{2\omega_{Li}} << \frac{1}{\Delta_i}$, we will drop terms that oscillate at optical frequencies an retain the slower evolving terms that should represent the relevant dynamics of the system.

$$\begin{aligned} i\dot{b_0} &= -b_e \frac{E_0}{2} \langle 0| \boldsymbol{d} \cdot \hat{\epsilon}_0^* |e\rangle e^{-i\Delta_0 t} e^{-i\boldsymbol{k}_0 \cdot \boldsymbol{r}} \\ i\dot{b_1} &= -b_e \frac{E_1}{2} \langle 1| \boldsymbol{d} \cdot \hat{\epsilon}_1^* |e\rangle e^{-i\Delta_1 t} e^{-i\boldsymbol{k}_1 \cdot \boldsymbol{r}} \\ i\dot{b_e} &= -b_0 \frac{E_0}{2} \langle e| \boldsymbol{d} \cdot \hat{\epsilon}_0 |0\rangle e^{i\Delta_0 t} e^{i\boldsymbol{k}_0 \cdot \boldsymbol{r}} - b_1 \frac{E_1}{2} \langle e| \boldsymbol{d} \cdot \hat{\epsilon}_1 |1\rangle e^{i\Delta_1 t} e^{i\boldsymbol{k}_1 \cdot \boldsymbol{r}} \end{aligned} \tag{3.38}$$

Defining the single photon Rabi frequency as $\Omega_n = -E_n \langle n| \boldsymbol{d} \cdot \hat{\epsilon}_n^* |e\rangle$ and noting that $\langle n| \boldsymbol{d} \cdot$

$\hat{\epsilon}_n^* |e\rangle = \langle e| \boldsymbol{d} \cdot \hat{\epsilon}_n |n\rangle$, the above equations become

$$\begin{aligned} i\dot{b_0} &= b_e \frac{\Omega_0}{2} e^{-i\Delta_0 t} e^{-i\boldsymbol{k}_0 \cdot \boldsymbol{r}} \\ i\dot{b_1} &= b_e \frac{\Omega_1}{2} e^{-i\Delta_1 t} e^{-i\boldsymbol{k}_1 \cdot \boldsymbol{r}} \\ i\dot{b_e} &= b_0 \frac{\Omega_0}{2} e^{i\Delta_0 t} e^{i\boldsymbol{k}_0 \cdot \boldsymbol{r}} + b_1 \frac{\Omega_1}{2} e^{i\Delta_1 t} e^{i\boldsymbol{k}_1 \cdot \boldsymbol{r}} \end{aligned} \tag{3.39}$$

Now we will want to eliminate the excited state from the dynamics, which we can do by adiabatic elimination. This is done by directly integrating the equation for $\dot{b}_e$, under the assumption that the dynamics are dominated by the terms that oscillate at $\Delta_{0,1}$, implying the time dependent populations $b_{0,1}$ remain approximately constant over these timescales. As long as the detuning from the excited states of the Raman laser is sufficiently larger than the two photon Rabi frequency, this approximation remains valid. Direct integration therefore gives us

$$b_e = b_0 \frac{\Omega_0}{2} \frac{(1 - e^{i\Delta_0 t})}{\Delta_0} e^{i\boldsymbol{k}_0 \cdot \boldsymbol{r}} + b_1 \frac{\Omega_1}{2} \frac{(1 - e^{i\Delta_1 t})}{\Delta_1} e^{i\boldsymbol{k}_1 \cdot \boldsymbol{r}} \tag{3.40}$$

Inserting equation 3.40 into the previous coupled differential equations effectively decouples the dynamics of the ground states from the excited states. We get

$$\begin{aligned} i\dot{b_0} &= b_0 \frac{\Omega_0^2}{4\Delta_0} e^{-i\Delta_0 t}(1 - e^{i\Delta_0 t}) + b_1 \frac{\Omega_0 \Omega_1}{4\Delta_1} e^{-i\Delta_0 t}(1 - e^{i\Delta_1 t}) e^{-i(\mathbf{k}_0 - \mathbf{k}_1)\cdot \mathbf{r}} \\ i\dot{b_1} &= b_1 \frac{\Omega_1^2}{4\Delta_1} e^{-i\Delta_1 t}(1 - e^{i\Delta_1 t}) + b_0 \frac{\Omega_0 \Omega_1}{4\Delta_0} e^{-i\Delta_1 t}(1 - e^{i\Delta_0 t}) e^{i(\mathbf{k}_0 - \mathbf{k}_1)\cdot \mathbf{r}} \end{aligned} \tag{3.41}$$

The rotating wave approximation can be made such that terms that oscillate at $\Delta_{0,1}$ can be eliminated as they will average out over the timescales associated with the coherent evolution of $b_{0,1}$. To make this assumption work, we will now assume that the Raman lasers are equally detuned from the excited state ($\Delta_0 = \Delta_1 \equiv \Delta$). This gives

$$\begin{aligned} i\dot{b_0} &= -b_0 \frac{\Omega_0^2}{4\Delta} - b_1 \frac{\Omega_0 \Omega_1}{4\Delta} e^{-i(\mathbf{k}_0 - \mathbf{k}_1)\cdot \mathbf{r}} \\ i\dot{b_1} &= -b_1 \frac{\Omega_1^2}{4\Delta} - b_0 \frac{\Omega_0 \Omega_1}{4\Delta} e^{i(\mathbf{k}_0 - \mathbf{k}_1)\cdot \mathbf{r}} \end{aligned} \tag{3.42}$$

Identifying $\delta_i = \Omega_i^2/4\Delta$ and $\tilde{\Omega} = \Omega_0\Omega_1/2\Delta$, the effective two level Hamiltonian matrix can be written

$$\mathcal{H}_{eff} = \begin{pmatrix} -\delta_0 & -\frac{\tilde{\Omega}}{2}e^{-i(\mathbf{k}_0-\mathbf{k}_1)\cdot\mathbf{r}} \\ -\frac{\tilde{\Omega}}{2}e^{i(\mathbf{k}_0-\mathbf{k}_1)\cdot\mathbf{r}} & -\delta_1 \end{pmatrix} \tag{3.43}$$

3.4.1 Spontaneous scattering rate due to Raman lasers

We can get an estimate of the spontaneous emission rate due to populating the excited state by looking at the excited state population in equation 3.40. We will make the simplifications $\Omega_0 = \Omega_1 \equiv \Omega$, and $\Delta_0 = \Delta_1 \equiv \Delta$, and the assumption that the timescale of a gate $t_{gate} \sim \pi/\tilde{\Omega}$ is much slower than $1/\Delta$ so that we can ignore terms in 3.40 that oscillate at Δ. These terms will oscillate rapidly over the time t_{gate} and average to zero. With these assumptions, the excited state population can be expressed as

$$\begin{aligned} |b_e|^2 &= \frac{\tilde{\Omega}^2}{4\Delta^2}(|b_0|^2 + |b_1|^2 + b_0 b_1^* e^{i(\boldsymbol{k}_0-\boldsymbol{k}_1)\cdot\boldsymbol{r}} + b_0^* b_1 e^{-i(\boldsymbol{k}_0-\boldsymbol{k}_1)\cdot\boldsymbol{r}}) \\ &= \frac{\tilde{\Omega}^2}{4\Delta^2}(\rho_{00} + \rho_{11} + \rho_{01}e^{i(\boldsymbol{k}_0-\boldsymbol{k}_1)\cdot\boldsymbol{r}} + \rho_{10}e^{-i(\boldsymbol{k}_0-\boldsymbol{k}_1)\cdot\boldsymbol{r}}) \end{aligned} \tag{3.44}$$

The spontaneous emission rate can then be expressed as $R_{spon} = \Gamma|b_e|^2 = \Gamma\rho_{ee}$.

CHAPTER 4

The ytterbium ion

Our ion species of choice are the various isotopes of element 70, ytterbium. There are 7 isotopes of ytterbium with stable nuclei, and the m = 171 isotope with a nuclear spin I = 1/2 is the workhorse qubit in many quantum information experiments. The only other stable isotope with non-zero nuclear spin is the m = 173 isotope with a nuclear spin I = 5/2. Throughout this thesis, the primary isotopes that we work with are $^{174}Yb^{+}$, $^{171}Yb^{+}$, and $^{173}Yb^{+}$.

4.1 Relevant states, branching ratios, and linewidths

The energetic ground state of Yb^{+} has electron configuration $4f^{14}6s$ ($^{2}S_{1/2}$), a filled 4f inner shell and a single valence electron in the outer 6s shell. The other hydrogen like states in Yb^{+} are the different fine structure components of the $4f^{14}6p$ ($^{2}P^{o}_{1/2}$, $^{2}P^{o}_{3/2}$) and $4f^{14}5d$ ($^{2}D_{3/2}$, $^{2}D_{5/2}$) electron configurations.

Most remaining electronic states that are utilized in the Yb^{+} ion are not composed of a full shell and a single valence electron, but instead an unfilled core shell ($4f^{13}$) and two valence electrons. These states arise due to the fact that it takes less energy to promote one of the core electrons to outer electron orbitals than to second ionize the Yb ion. In most ion species, the amount of energy necessary to remove a core electron exceeds the second ionization energy of the ion. In the Yb^{+} isotopes, the required energy is only 2.65 eV (467 nm from the ground state) to reach the lowest lying state with an unfilled core, well below the 12.18 eV needed for second ionization and creation of Yb^{2+}. It should be noted that there are other levels with signle valence electron and closed core shell and higher principle

quantum number n, but the next level is $4f^{14}6d\ ^2D_{3/2}$ at $\sim 62100\ cm^{-1}$, more energetic than any state considered throughout this thesis.

The $^2F^o_{7/2}$ is the lowest lying of these states with electron configuration $4f^{13}6s^2$.

Relevant states in Yb^+			
State	Lifetime	Daughter states	Branching ratio
$^2S_{1/2}$	∞ ns	n/a	n/a
$^2P^o_{1/2}$	8.12(2) ns [OHM09]	$\{^2S_{1/2}, ^2D_{3/2}\}$	{0.995, 0.005} [OYM07]
$^2P^o_{3/2}$	6.15(9) ns [PRK97]	$\{^2S_{1/2}, ^2D_{3/2}, ^2D_{5/2}\}$	{0.9875 0.0017, 0.0108} [FFE18]
$^2D_{3/2}$	52.7(2.4) ms [YM00]	$\{^2S_{1/2}\}$	{1.0}
$^2D_{5/2}$	7.2(3) ms [TRG97]	$\{^2S_{1/2}, ^2F^o_{7/2}, ^2D_{3/2}\}$	$\{0.17, 0.83, 2\times10^{-4^*}\}$ [TRG97]
$^3[3/2]^o_{1/2}$	37.7 ns	$\{^2S_{1/2}, ^2D_{3/2}\}$	{0.982, 0.018}
$^1[3/2]^o_{3/2}$	29.3 ns **	$\{^2S_{1/2}, ^2D_{3/2}, ^2D_{5/2}\}$	{0.975, 0.003, 0.022}**
$^2F^o_{7/2}$	$\sim$5 yrs	$\{^2S_{1/2}\}$	{1.0}

Table 4.1: * This value is from theoretical calculations of the M1 decay rate, not from [TRG97]. ** These values are calculated from theoretical Einstein A coefficients provided by the DREAM collaboration at Mons University. Error bars for the branching ratios from publications can be found in the provide citations.

4.2 Hyperfine structure

Atoms that possess non-zero nuclear spin ($\mathcal{I} \neq 0$) will exhibit additional structure within each fine structure state due to the interaction of the nuclear spin and the orbital angular momentum of the valence electron (with the exception of when $J = 0$, as in the $^1S_0$ state in ^{171}Yb). This interaction splits each fine structure state into sublevels with frequency splittings ranging anywhere from 10's of MHz to 10's of GHz. A rule of thumb is that electron orbitals with larger overlap with the nucleus exhibit stronger interaction with the nucleus (in particular the ground $^2S_{1/2}$ state in alkali earth like atoms).

In general, an atom with nuclear spin $\mathbf{I}$ may exhibit $2I + 1$ nuclear moments, with the $I = 0$ case the trivial electric monopole moment [Cas36, Ste20]. At low field strengths, the hyperfine interaction can be treated as a perturbation to the spin-orbit interaction, and the total angular momentum of the atom that is constant within a single state is $\mathbf{F} = \mathbf{I} + \mathbf{J}$. The good eigenstates of the system are then $|\gamma, J, I, F, m_F\rangle$, and within a fine structure state the

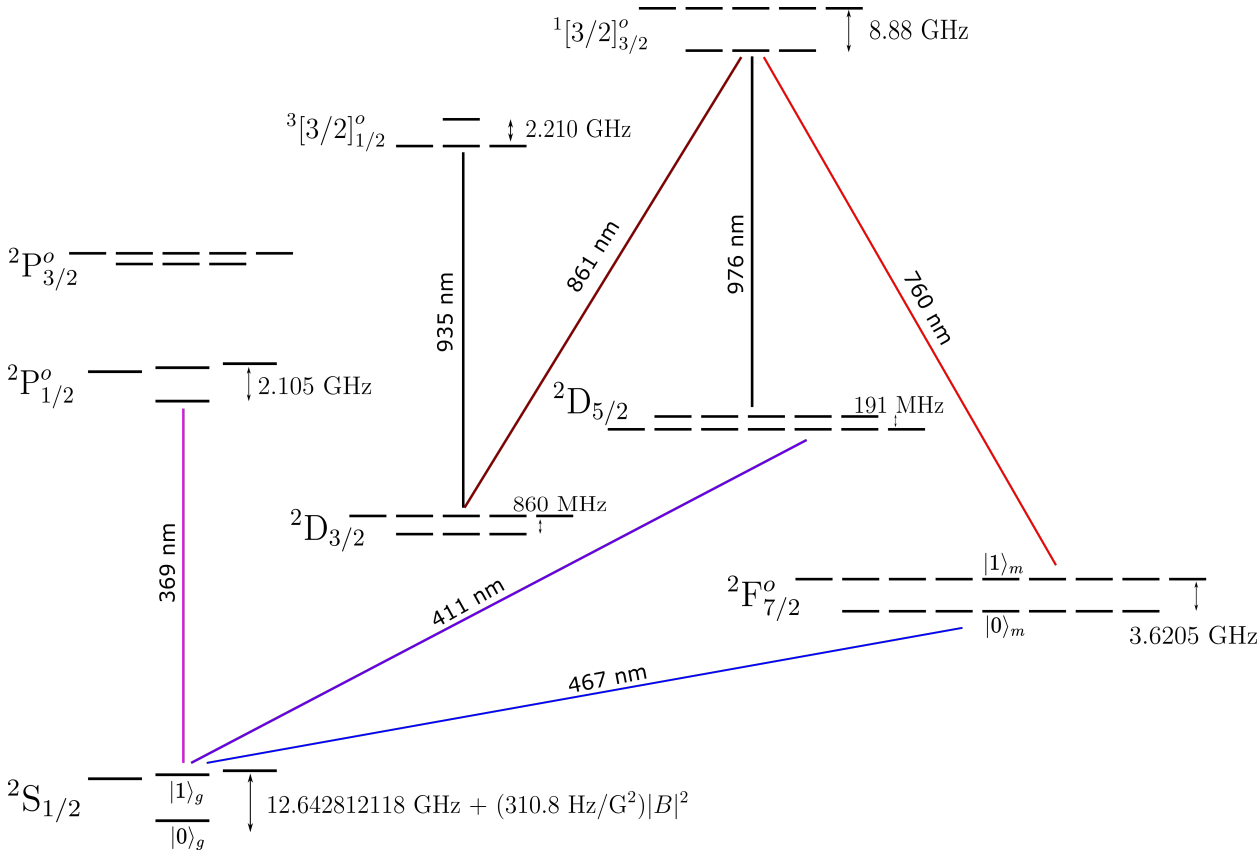

Figure 4.1: Diagram of most relevant levels in the $^{171}Yb^+$ ion for this thesis. Superscript "o" on term symbols is used to indicate that the state has odd parity. All above transitions with the exception of the 467 nm $^2S_{1/2} \leftrightarrow ^2F^o_{7/2}$ electric octupole transition have been driven in our lab.

total angular momentum can take on values from $F \in \{|J-I|, |J-I|+1, ..., J+I-1, J+I\}$, and within a hyperfine level $m_F \in \{-F, -F+1, ..., F-1, F\}$.

4.2.1 Magnetic dipole hyperfine interaction

The first non-trivial moment for non-zero nuclear spin is the magnetic dipole interaction. The magnetic moment of the nucleus is

$$\boldsymbol{\mu}_I = g_I \mu_N \mathbf{I} \tag{4.1}$$

where μ_N is the nuclear magneton and g_I is the nuclear g-factor. The nuclear magneton is related to the Bohr magneton by the mass ratio of the electron to the proton, which is (in experimentalist units)

$$\mu_N = \frac{m_e}{m_p}\mu_B = 762 \text{ Hz/Gauss} \tag{4.2}$$

And the nuclear g-factors for the two Yb isotopes with nuclear spin are[1]

$$\begin{aligned} g_I(^{171}\text{Yb}^+) &= +0.98734 \\ g_I(^{173}\text{Yb}^+) &= -0.2592 \end{aligned} \tag{4.3}$$

The interaction of the nuclear magnetic moment with the magnetic field $\mathbf{B}_{el}$ created by the electrons at the the location of the nucleus is

$$\mathcal{H}_{m.dipole} = \boldsymbol{\mu}_I \cdot \mathbf{B}_{el} \equiv A_{M1}\mathbf{I}\cdot\mathbf{J} \tag{4.4}$$

where the equivalence is made recognizing that the nuclear magnetic dipole moment scales as $\mathbf{I}$ and that the magnetic field produced by the valence electrons at the core scales as $\mathbf{J}$ [Woo80]. This simplifies the problem to measuring the hyperfine splitting (equivalent to measuring the magnetic dipole hyperfine constant, A_{M1}).

The operators in equation 4.4 can be rewritten as

$$\mathbf{I}\cdot\mathbf{J} = \frac{1}{2}(\mathbf{F}^2 - \mathbf{I}^2 - \mathbf{J}^2) \tag{4.5}$$

which in turn gives the diagonal elements of the magneitc dipole hyperfine interaction Hamiltonian as

$$\Delta E = \frac{1}{2}A_{M1}\Big[F(F+1) - I(I+1) - J(J+1)\Big] \tag{4.6}$$

In the absence of higher order hyperfine interaction, the so called *interval rule* holds, which is that the energy splitting between the level with total angular momentum F and level with total angular momentum $F-1$ is given by $\Delta E(F) = A_{M1}F$. Below is a table of

[1] https://easyspin.org/documentation/isotopetable.html

experimentally measured A_{M1} for various states in $^{171}Yb^+$ and $^{173}Yb^+$.

A_{M1} in various fine structure states of Yb^+		
State	Hyperfine Levels (isotope)	A_{M1}
$^2S_{1/2}$	F = 0, 1 (171)	12.642812118 GHz [FSL97]
	F = 2, 3 (173)	3.497240079 GHz [MBG87]
$^2P^o_{1/2}$	F = 0, 1 (171)	2.105 Ghz [MGH94]
	F = 2, 3 (173)	-581 MHz [MGH94]
$^2P^o_{3/2}$	F = 1, 2 (171)	875.4 MHz [FFE18]
	F = 3, 4 (173)	-245 MHz [BM92]
$^2D_{3/2}$	F = 1, 2 (171)	430 MHz [ET96]
	F = 1, 2, 3, 4 (173)	-110 MHz ∗∗ [Ita06]
$^2D_{5/2}$	F = 2, 3 (171)	-63.368 MHz [TEM21]
	F = 0, 1, 2, 3, 4, 5 (173)	3.47 MHz ∗∗ [Ita06]
$^2F^o_{7/2}$	F = 3, 4 (171)	905.1 MHz ∗
	F = 1, 2, 3, 4, 5, 6 (173)	-240 MHz ∗∗ [DF16]
$^1[5/2]_{5/2}$	F = 0, 1, 2, 3, 4, 5 (173)	-55 MHz ∗∗ [PSW12]

Table 4.2: Summary of measured hyperfine magnetic dipole coefficients. Uncertainties have been left out and can be found in the respective citations. Note that m = 173 fine structure levels with $J \geq 3/2$ will have higher order contributions from the electric quadrupole (B_{E2}) and magnetic octupole (C_{M3}) hyperfine interactions, discussed below. $*$ $^2F^o_{7/2}$ interval measured in our lab, unpublished. $**$ Theoretical prediction.

4.2.2 Higher order hyperfine interactions

For atoms with nuclear spin $I > 1/2$ and fine structure state with $J > 1/2$, there can be higher order interactions between the electron and the nuclear moments. The next two higher order moments are due to the nuclear electric quadrupole moment (B_{E2}) and the magnetic octupole moment (C_{M3}). Includng these terms, the hyperfine interaction Hamiltonian can be written as [Arm71, Ste20]

$$\mathcal{H}_{HFS} = A_{M1}\mathbf{I}\cdot\mathbf{J} + B_{E2}f_{E2}(\mathbf{I}\cdot\mathbf{J}) + C_{M3}f_{M3}(\mathbf{I}\cdot\mathbf{J}) \tag{4.7}$$

where the coefficients are functions of the nuclear spin and electron angular momentum

J, given in [Arm71, Ste20] as

$$f_{E2} = \frac{3(\mathbf{I}\cdot\mathbf{J})^2 + \frac{3}{2}\mathbf{I}\cdot\mathbf{J} - I(I+1)J(J+1)}{2I(2I-1)J(2J-1)}$$
$$f_{M3} = \Bigg[10(\mathbf{I}\cdot\mathbf{J})^3 + 20(\mathbf{I}\cdot\mathbf{J})^2 + 2(\mathbf{I}\cdot\mathbf{J})\Big[-3I(I+1)J(J+1) + I(I+1) + J(J+1) + 3\Big]$$
$$- 5I(I+1)J(J+1)\Bigg] / \Big[I(I-1)(2I-1)J(J-1)(2J-1)\Big] \tag{4.8}$$

For the stable ytterbium isotopes, these higher order interactions only apply to $^{173}Yb^+$ with nuclear spin I=5/2. Very few of these higher order moments have been measured in the ionic 173 isotope, but some theoretical estimates have been made. The energy shift from the energetic centroid can be written as [Ste20]

$$\Delta E_{HFS} = \frac{1}{2}A_{M1}K + \frac{\frac{3}{2}K(K+1) - 2I(I+1)J(J+1)}{4I(2I-1)J(2J-1)}B_{E2} +$$
$$\frac{\frac{5}{4}K^2(K+4) + K[I(I+1) + J(J+1) + 3 - 3I(I+1)J(J+1)] - 5I(I+1)J(J+1)}{I(I-1)(2I-1)J(J-1)(2J-1)}C_{M3} \tag{4.9}$$

where $K = F(F+1) - I(I+1) - J(J+1)$.

Higher order hyperfine coefficients in $^{173}Yb^+$		
State	B_{E2}	C_{M3}
$^2P^o_{3/2}$	1460 MHz (*meas*) [BM92]	
$^2D_{3/2}$	951 MHz [Ita06]	
$^2D_{5/2}$	1190 MHz [Ita06]	
$^2F^o_{7/2}$	-4762 [DF16]	
	-5330 MHz [XLC20]	4.53×10^{-4} MHz/(b $\times\mu_N$) [XLC20]
	-3680 MHz [PSW12]	
$^1[5/2]_{5/2}$	-1720 MHz [PSW12]	

Table 4.3: Unless denoted as an experimental measurement, all above numbers are theoretical calculations.

4.3 Laser cooling Yb^+

Laser cooling of any of the Yb^+ isotopes only requires two lasers: a 369 nm laser and a 935 nm laser. Strong photon scattering on the $^2S_{1/2}$ to $^2P^o_{1/2}$ transition is achieved at 369 nm, and repumping of the metastable $^2D_{3/2}$ is performed at 935 nm. This repumper is necessary to facilitate continuous photon scattering (and hence cooling) on the stronger transition because the $^2P^o_{1/2}$ can decay to the relatively long lived $^2D_{3/2}$ about 1 out of every 200 scattered photons, corresponding to a branching ratio of 0.005.

To trap individual ions for extended periods of time, an additional repump laser is necessary to depopulate the long lived $^2F^o_{7/2}$, which can be populated without direct laser coupling. It is believed that various collisional pathways exist that can transfer an electron during Doppler cooling to the $^2F^o_{7/2}$ [SDN09], and it was shown that the transition rate to the long lived state is a function of the background pressure of buffer gasses. Various repumping schemes have been explored for returning an ion in the $^2F^o_{7/2}$ to the cooling cycle [Sug99]. A laser at 3.4 μm can be used to couple the $^2F^o_{7/2}$ to the $^2D_{5/2}$, but the relatively long lifetime (7.2 ms) and unfavorable branching ratio to the $^2S_{1/2}$ (0.17) make this inefficient. A common choice is to use a 638 nm laser to couple $^2F^o_{7/2}$ to $^1[5/2]^o_{5/2}$, which can in principle decay to either low lying ^2D_J state. In our lab, we repump the $^2F^o_{7/2}$ at 760 nm, coupling to the $^1[3/2]^o_{3/2}$, which has the advantage that it has electric dipole coupling to the $^2S_{1/2}$, producing a favorable branching ratio (0.975) to $^2S_{1/2}$ and short lifetime (29.3 ns). The 760 nm laser couples the two states via an electric quadrupole transition amplitude, and therefore has an extremely small branching fraction. Even with 10's of mW of 760 nm laser and reasonable beam waists ($\omega_0 \sim 30\mu$m) at the ion's position, the transition remains well under saturated. This means that more laser power would be a win and speed up the repumping of the $^2F^o_{7/2}$.

Laser cooling of the non-spin zero isotopes require extra optical tones due to the presence of hyperfine structure. For $^{171}Yb^+$, a free space resonant EOM [2] at 7.379 GHz is used to

[2]New Focus Model 4851, 3W microwave power

produce a second order sideband +14.758 GHz from the laser carrier, which is set to be -10 MHz from the $^2S_{1/2}\ |F=1\rangle \leftrightarrow {}^2P^o_{1/2}\ |F=0\rangle$ transition. The second order sideband repumps the $^2S_{1/2}\ |F=0\rangle$ state to the $^2P^o_{1/2}\ |F=1\rangle$ transition, which is populated by off resonant excitation to the $^2P^o_{1/2}\ |F=1\rangle$ by the laser carrier tone. The modulation frequency is set to be on resonance with the repump transition when the carrier is -10 MHz of the transition for optimal Doppler cooling.

An additional laser tone at -3.07 Ghz is necessary on the 935 nm laser for repumping of the $^2D_{3/2}\ |F=2\rangle$ state, which is only populated via 369 nm coupling to the $^2P^o_{1/2}\ |F=1\rangle$ state. This tone is applied with a fiber EOM [3].

4.4 The ground state qubit

The ground state qubit in $^{171}Yb^+$ is a hyperfine zero-field clock state qubit within the $^2S_{1/2}$ manifold. Specifically, the qubit states are $|0\rangle_g = {}^2S_{1/2}\ |F=0, m_F=0\rangle$ and $|1\rangle_g = {}^2S_{1/2}\ |F=1, m_F=0\rangle$. While any of the three m_F states in the $^2S_{1/2}\ |F=1\rangle$ manifold is a suitable choice for a qubit along with $|0\rangle_g$, the $|1\rangle_g$ state is chosen due magnetic insensitivity near zero field. This means that when the external magnetic field at the ion's position is zero, there is no linear Zeeman shift of the qubit frequency. The quadratic shift of the qubit frequency is $\delta_2 = (310.8\text{Hz/G}^2)|B|^2$.

In order to lift the degeneracy of the Zeeman states in the ground and all excited states, a small magnetic field is applied by applying current to a coil mounted directly to the vacuum chamber. This is done to avoid coherent dark states on the cooling transitions that would suppress laser scatter on the $^2S_{1/2} \leftrightarrow {}^2P^o_{1/2}$ transition, and therefore our cooling power [JG02]. While this added external field does mean we operate the ground state qubit away from the clock condition, the field is small enough that only a small linear sensitivity to magnetic field fluctuations remains.

[3] AdvR, $\sim$ 20 mW microwave power

4.4.1 $|0\rangle_g$ state preparation

The $|0\rangle_g$ state can be prepared extremely fast in the $^{171}Yb^+$ ground state qubit due to electric dipole selection rules on the $^2S_{1/2} \rightarrow {}^2P^o_{1/2}$ transition. Application of laser light driving the $^2S_{1/2}\ |F=1\rangle \rightarrow {}^2P^o_{1/2}\ |F=1\rangle$ transition will cause population to quickly fall into the $|0\rangle_g$ state. This laser tone should be +2.105 GHz of the laser carrier, which is created by phase modulation of the laser by a free space EOM [4].

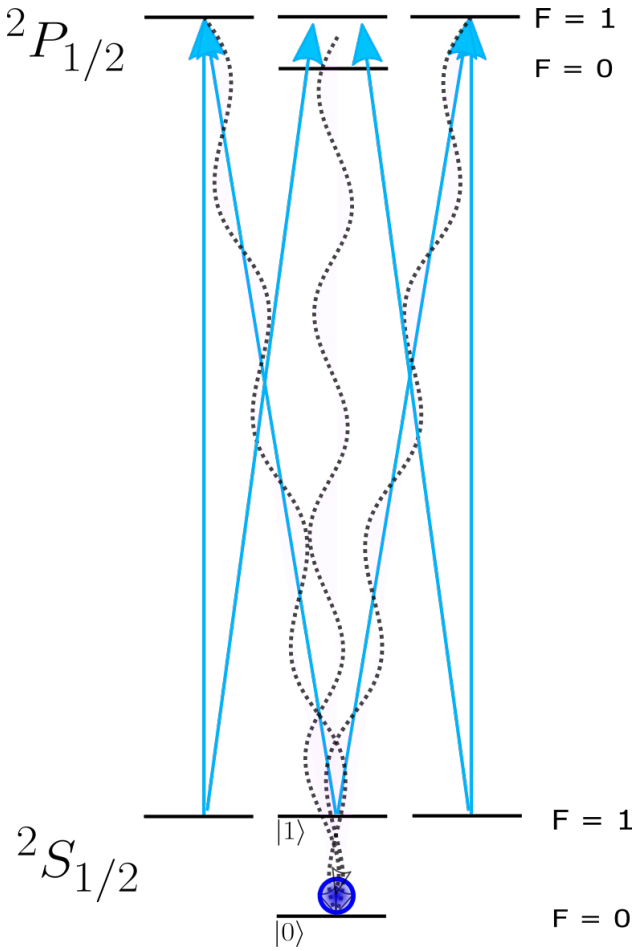

Figure 4.2: Diagram of laser tones and driven transitions for incoherent preparation of the $|0\rangle_g$ state.

The polarization of the optical pumping beam is chosen so that all transitions are driven so no population is stranded in any of the three magnetic sub-levels of the $^2S_{1/2}\ |F=1\rangle$.

[4] New Focus Model 4431, 2W microwave power

Once excited to the $^2P^o_{1/2}$ $|F=1\rangle$, the electron will decay to $|0\rangle_g$ 1/3 of the time, and back into one of the $^2S_{1/2}$ $|F=1\rangle$ sub-levels 2/3 of the time. The polarization of the 935 nm laser beam is set such that all dipole allowed transitions are driven to prevent population trapping in the $^2D_{3/2}$ $|F=2\rangle$.

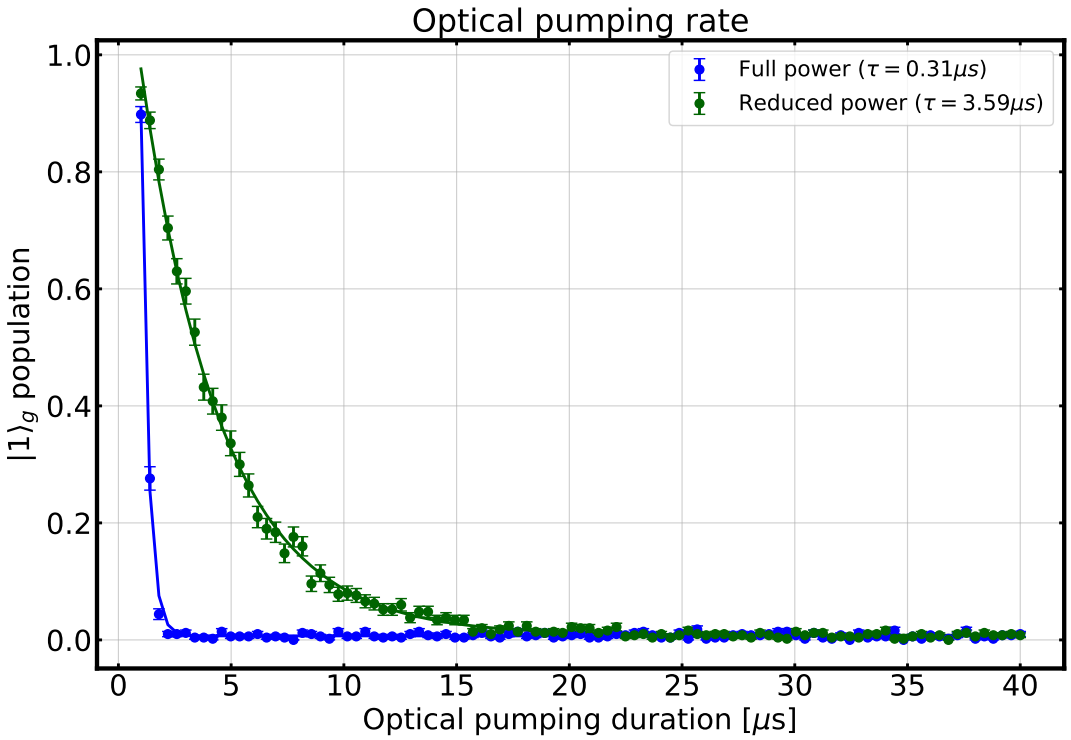

Figure 4.3: Preparation of the $|0\rangle_g$ state as a function of optical pumping duration. Two different optical intensities are shown here as examples. High fidelity state preparation of the $|0\rangle_g$ state can be achieved in just a few microseconds.

4.4.2 $|1\rangle_g$ state preparation

Preparation of the $|1\rangle_g$ state is a two step process: first the $|0\rangle_g$ state is prepared via incoherent optical pumping as described above, followed by a $\theta_p = \pi$ rotation of the qubit with resonant microwaves. Here θ_p is the pulse area of the (typically) rectangular microwave pulse given by $\theta_p = \Omega t$, where Ω is the resonant Rabi frequency, and corresponds to the polar angle on the Bloch sphere through which the qubit state is rotated. So, to perform a

full rotation from $|0\rangle_g$ to $|1\rangle_g$, the pulse area needs to be π, and thus the radiation applied for a time $t_\pi = \pi/\Omega$.

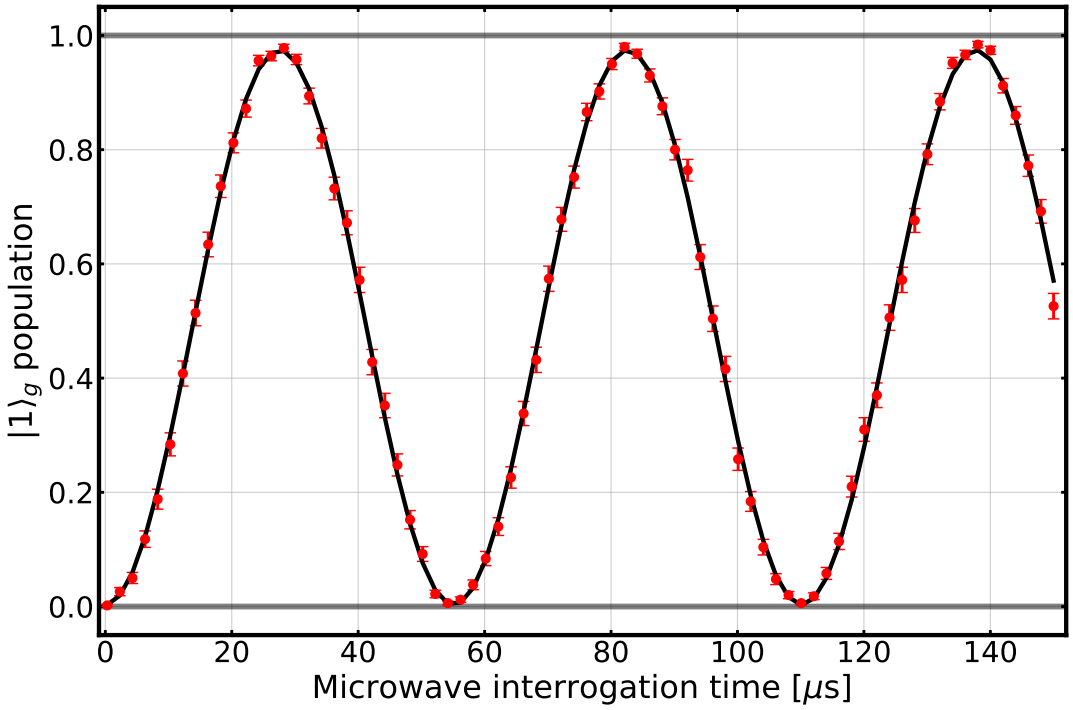

Figure 4.4: Microwave Rabi flopping of the ground state qubit. Population in the $|1\rangle_g$ state as a function of microwave interrogation duration. The optimal time for a $\theta_p = \pi$ rotation here is about 27 μs. Each data point is the result of 500 experiments.

Preparation of the $|1\rangle_g$ state is done in this way because there is not a high fidelity avenue to preparing the state incoherently. If there was, that would likely be the method of choice, just like the $|0\rangle_g$ state.

4.4.3 Qubit state readout

Readout is performed by applying laser light resonant with the $^2\mathrm{S}_{1/2}\ |F=1\rangle \rightarrow {}^2\mathrm{P}^o_{1/2}\ |F=0\rangle$ transition, with polarization such that the bright state ($|1\rangle_g$) produces the maximal number of photons. If we assume the laser used for detection is linearly polarized and has propagation direction perpendicular to the applied magnetic field, the excited $^2\mathrm{P}^o_{1/2}\ |F=0\rangle$ state

population can be analytically solved for [ETH10] (slight modification of similar equation from [JG02]),

$$\begin{aligned} P_e &= \frac{3}{4}\frac{\Omega^2}{3}\frac{\cos^2\theta\sin^2\theta}{1+3\cos^2\theta}\frac{1}{(\gamma'/2)^2+\Delta^2} \\ \left(\frac{\gamma'}{2}\right)^2 &= \left(\frac{\gamma}{2}\right)^2 + \frac{\Omega^2}{3}\cos^2\theta\frac{1-3\cos^2\theta}{1+3\cos^2\theta} + \frac{\cos^2\theta}{1+3\cos^2\theta}\left(\frac{\Omega^4}{36\delta_B^2}+4\delta_B^2\right) \end{aligned} \tag{4.10}$$

Where Ω is the resonant Rabi frequency as defined in [ETH10] ([JG02] has a slight difference in definition), $\delta_B = \mu_B|B|$ is the energy shift of the $^2\mathrm{S}_{1/2}\,|F=1,m_F=\pm1\rangle$ states due to the linear Zeeman effect, Δ is the detuning from the $m_F = 0 \leftrightarrow m_F = 0$ transition, $\gamma = 2\pi \times 19.6$ MHz is the natural linewidth of the transition, and θ is the angle between the laser electric field polarization and the quantization axis. Generally speaking, since the relative strength of the three $^2\mathrm{S}_{1/2}\,|F=1,m_F\rangle \rightarrow {}^2\mathrm{P}^o_{1/2}\,|F=0\rangle$ transitions are the same, the optimal polarization will have about equal amounts of σ^-, σ^+, and π polarization. This occurs when the the laser polarization is at an angle of $\theta = \arccos\frac{1}{\sqrt{3}} = 54.7^\circ$ with respect to the applied magnetic field, such that the projection onto B is 1/3 (resulting in 1/3 π contribution) and projection perpendicular to B is 2/3 (resulting in 1/3 σ_- and 1/3 σ_+). In the limit of large magnetic field, the excited state population can approach 1/4, as expected in a fully saturated multilevel driven system with three ground states and one excited state (all states become equally populated in the limit of infinite saturation). Optimization of resonant Rabi frequency as a function of the applied magnetic field is discussed in various publications [JG02, ETH10], with the optimized resonant scattering rate given by [NVG13],

$$\Gamma_{opt} = \frac{\gamma}{6}\frac{s}{1+\frac{2}{3}s+(\frac{2\Delta}{\gamma})^2} \tag{4.11}$$

where $s = 2\Omega^2/\gamma^2$ is the on resonance saturation parameter and the result assumes the on resonance Rabi frequency has been set to match the optimal given in [JG02], $\Omega = 2\delta_B$.

This transition, along with repumping of the $^2\mathrm{D}_{3/2}\,|F=1\rangle \rightarrow {}^3[3/2]^o_{1/2}\,|F=0\rangle$, forms a

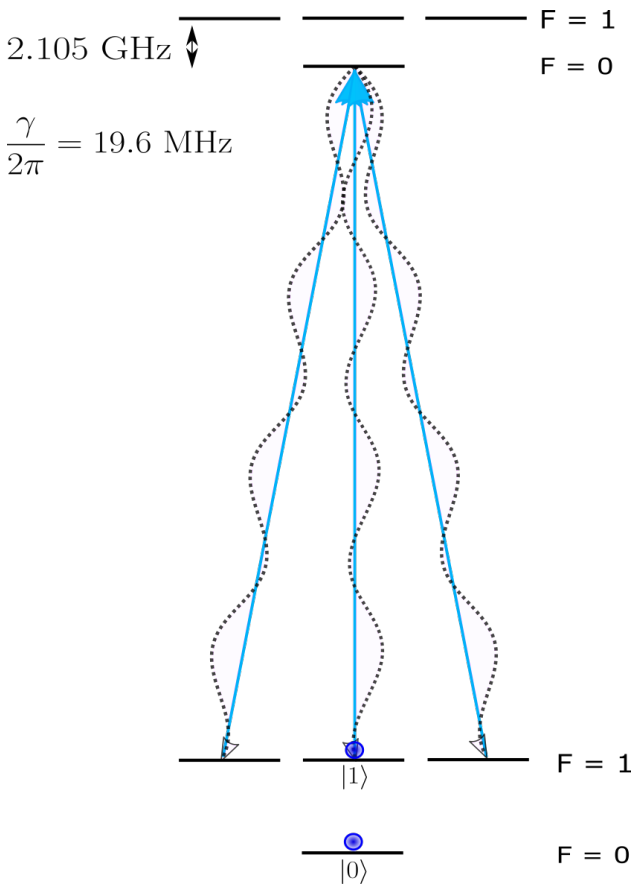

Figure 4.5: Diagram of laser polarization and frequency used to perform closed cycling of the $|1\rangle_g$ state for state readout.

closed cycling transition that includes the $|1\rangle_g$ state, and not the $|0\rangle_g$ state. If the qubit is projected into the $|1\rangle_g$ state, many photons are scattered, collected, and counted by photon time tagging electronics. Conversely, if the qubit projects into $|0\rangle_g$, no photons are scattered and no photons should be scattered. Results from a state preparation and measurement (SPAM) experiment of the ground state qubit using this readout scheme are shown in Figure 4.6.

This method for qubit readout has the advantage of scattering on a strong electric dipole transition, making it fast and efficient. The large hyperfine splitting in the $^2P^o_{1/2}$ (2.105 GHz) relative to the atomic linewidth (19.6 MHz [OHM09]) allows for high fidelity readout in a short period of time before qubit states begin to mix. This mixing sets a fundamental limit to the measurement fidelity if the histogram discrimination technique is used for state

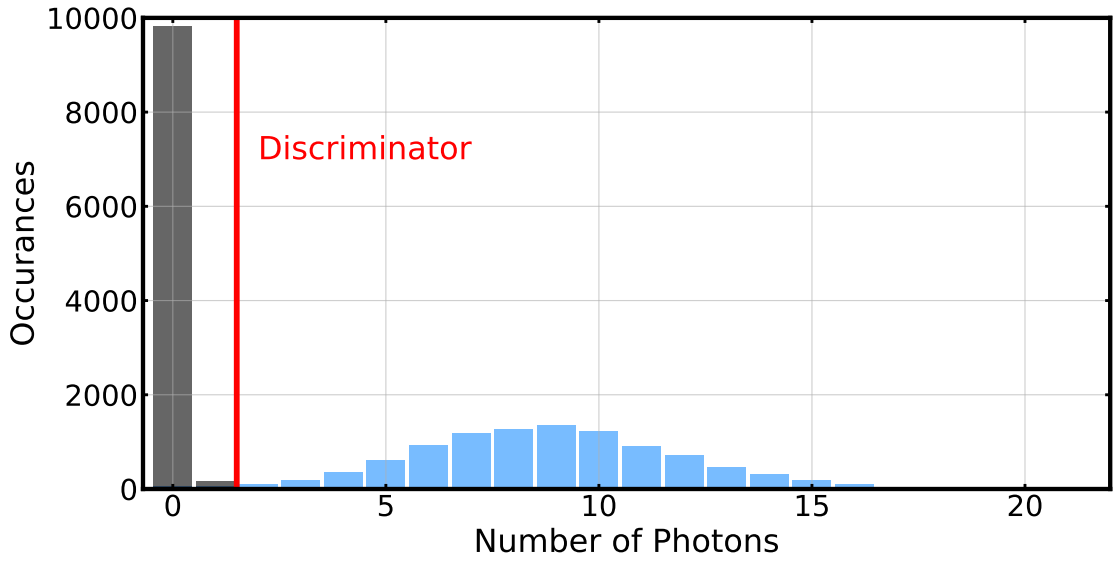

Figure 4.6: Histograms resulting from the individual state preparation and measurement of both qubit states using the standard I = 1/2 hyperfine qubit readout scheme. In this particular histogram, light collecting objectives on both sides of the ion trap are used to increase the photon detection efficiency. The state preparation and measurement fidelity of $|0\rangle_g$ is $\mathcal{F}_{|0\rangle_g} = 0.9970(5)$, and the $|1\rangle_g$ state is $\mathcal{F}_{|0\rangle_g} = 0.9905(9)$, resulting in a total fidelity $\mathcal{F}_q = 0.9937(8)$. Each histogram is the result of 10000 attempts.

detection. Following the work in [ABH06] with updated values for the atomic properties, if ideal photon detection efficiency was possible (unit efficiency), state readout fidelity of $\mathcal{F}_{ideal} = 1 - 5 \times 10^{-6}$ is in theory possible.

Despite the relatively large ratio $\omega_{HFP}/\Gamma_P \approx 100$, the off resonant excitation to the upper hyperfine manifold is what limits the state detection fidelity in $^{171}\mathrm{Yb}^+$. In a realistic experiment, there will be two rates: there will be a rate at which population in the $^2\mathrm{S}_{1/2}$ $|F = 1\rangle$ is pumped dark during state detection, and also a rate at which the $|0\rangle_g$ is pumped bright, both via coupling to the $^2\mathrm{P}^o_{1/2}$ $|F = 1\rangle$. The latter rate is smaller by nearly an order of magnitude due a larger detuning of $\omega_{HFS} + \omega_{HFP} \approx 14.7$ GHz.

Proper treatment of these effects for both detection via the $^2\mathrm{P}^o_{1/2}$ (hyperfine selective, all polarizations) and via the $^2\mathrm{P}^o_{3/2}$ (hyperfine selective, polarization $\sigma_\pm$) can be found in [ABH06], with additional treatment of the former case specifically related to $^{171}\mathrm{Yb}^+$ in [ETH10].

4.5 Readout statistics

When we perform a state preparation and measurement experiment, we are attempting to create a pure state, and detect it via laser induced fluorescence (the states being $\{|0\rangle, |1\rangle\}$). The goal of the experiment is to determine the binomial distribution parameters that result from the combined state preparation and measurement sequence, where each time we ask the binary output question "was the ion in $|1\rangle$?" (or for shelving state detection, "was the ion in $|0\rangle$?"). Each attempt at state preparation and measurement is a Bernoulli process, where the result is either a success or a failure, typically determined by prior knowledge of the attempted state and the number of photons detected. At the end of the experiment, we are provided with a two key parameters: the number of trials (n_t), the number of failures (n_f), the interpretation of which can change based on the experiment. For instance

- In a SPAM measurement, a "failure" is when we attempt to prepare a qubit basis state, measure the result, and find that we did not measure or prepare that state properly. This could mean we attempted to prepare $|0\rangle_g$, but detected a number of photons $N_\gamma > d$, where d is the histogram discriminator. Conversely, this could mean we attempted to prepare $|1\rangle_g$, but detected a number of photons $N_\gamma < d$. Both scenarios are failures.

- In a Rabi experiment, we will select one of the basis states to be out definition of "success", and any event that fails to create that state is a "failure". For instance, at the $t_{Rabi} = \pi/2\Omega_{Rabi}$ time on a Rabi flop, we expect to "fail" 50% of the time since we are attempting to create the state $|\psi\rangle = \frac{1}{\sqrt{2}}(|0\rangle_g + |1\rangle_g)$.

When the number of experimental trails n_t and the number of successes, n_t - n_f, are known, the probability of success can be estimated as $p = \frac{n_t - n_f}{n_t} = 1 - n_f/n_t$. Now we want to assess *our confidence in this measurement* by placing a confidence interval around p. Intuitively, the more trials that are performed the more confident we can be that the mean outcome of our experiment accurately represents the true value of p since we have sampled from the

distribution a larger number of times. A common method of assigning a confidence interval about p is to assume the error is normally distributed about the observed value of p. This gives the simple result,

$$p \pm \sqrt{\frac{p(1-p)}{n_t}} \tag{4.12}$$

It turns out that the normal approximation does not hold well when the success probabilities are close to 0 or 1, where the binomial distribution becomes asymmetric and non-Gaussian. In this case, we need a new way to assign a confidence interval. This will often be useful for us when performing SPAM experiments with electron shelving, or using shelving state detection to perform some other experiment since we will often not perform enough experiments to significantly sample from our distribution of errors near the extremes (0 or 1). The Wilson score interval can be expressed as

$$p_{\pm} = \frac{n_s + \frac{z^2}{2}}{n_t + z^2} \pm \frac{z}{n_t + z^2}\sqrt{\frac{n_s n_f}{n_t} + \left(\frac{z}{2}\right)^2} \tag{4.13}$$

where $p_{\pm}$ is the value at the edge of the confidence interval $\pm$ from the mean, at a desired confidence level set by the z-score value z (where z = number of standard deviations from the mean to contained within the confidence interval). If we were to report a measured values as (lower bound, mean, upper bound), then it would be reported as (p_-, p, p_+). The Wilson interval remains reliable when the success probabilities are near the extreme and when the number of samples are low [Wal13].

4.6 Spectroscopy

Throughout this thesis we will utilize transitions that either need to be periodically calibrated, such as out 369 nm and 935 nm transitions for laser cooling, or frequencies established since they are new transitions that we have never driven before. Here we will detail some of the spectroscopy we have done. In most cases below, the quoted frequencies are

read off from our wavemeter [5] as the laser software lock is used to scan the laser frequency. The corresponding ion fluorescence and wavemeter reading is recorded every 100-200 ms (depending on the laser) and the results are plotted.

4.6.1 $^2\mathbf{S}_{1/2} \rightarrow {}^2\mathbf{P}^o_{1/2}$

We routinely perform an experiment to calibrate the line center for the 369 nm laser by performing an experiment where we interleave Doppler cooling of the ion with interrogations of the electric dipole transition at variable detunings. By interleaving the cooling and interrogation of the ion, we can observe the spectral line shape on the blue side of resonance and produce full Lorentzian line shapes that would not be possible by simply scanning the laser frequency from red to blue over resonance.

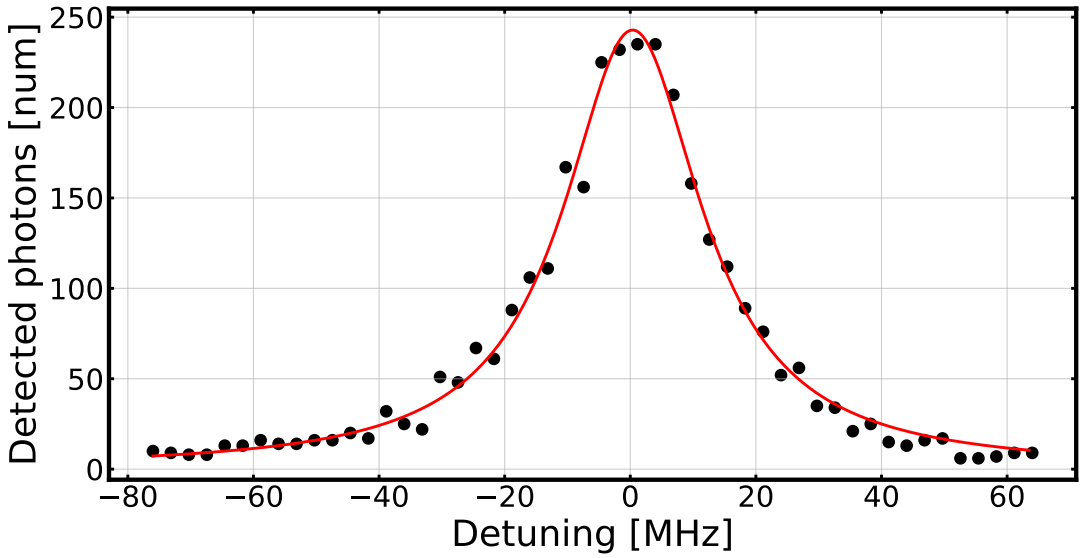

Figure 4.7: Interleaved line scan of a single $^{171}Yb^+$ ion. The detuning on the x-axis is controlled by a double pass acousto-optic modulator, and is referenced to the center frequency of the AOM.

The ion is Doppler cooled for 1 ms at Δ = - 10 MHz, followed by interrogation for 100 μs at a fixed detuning during which time photons are counted. Each data point is the result of

[5] High Finesse WS-U

repeating this procedure 100 times at a fixed detuning. Observed spectral line widths (full width half maximum) on a typical day are in the range $\Gamma' \in 2\pi \times [22, 30]$ MHz, determined by fitting the data to a Lorentzian profile. Broader line widths typically indicate power broadening or poor Doppler cooling.

This experiment, when run, is designed to automatically run the scan and perform a fitting routine to update the location of the line center in our global parameters shared amongst the various experiments. This makes it easy to ensure that we are always applying 369 nm laser light at the desired detuning from resonance. For longer experiments, we have the ability to integrate these tracking diagnostic experiments within the longer experiment for tracking of drifts in the lab.

4.6.2 $^2\mathbf{F}^o_{7/2} \leftrightarrow {}^1[3/2]^o_{3/2}$

The transition from the $^2\mathrm{F}^o_{7/2}$ state to the $^1[3/2]^o_{3/2}$ state is a critical one throughout this thesis. It is an electric octupole transition that we use to transfer population back to the $^2\mathrm{S}_{1/2}$ from the $^2\mathrm{F}^o_{7/2}$. Despite the weakness of the transition moment, the fast decay of the excited state ($\sim$29 ns) and favorable branching to the ground state (0.975) makes it an attractive pathway for retrieving population stranded in the $^2\mathrm{F}^o_{7/2}$.

To perform spectroscopy of the transition, we load multiple $^{171}\mathrm{Yb}^+$ ions in the trap. The ions are continuously pumped into the $^2\mathrm{F}^o_{7/2}$ while Doppler cooling by applying 411 nm light resonant with the $^2\mathrm{S}_{1/2}\ |F = 1\rangle \rightarrow {}^2\mathrm{D}_{5/2}\ |F = 3\rangle$ transition, which will populate both hyperfine manifolds in the $^2\mathrm{F}^o_{7/2}$. On separate scans, the 760 nm laser are scanned in frequency around the known center frequency, and we observe a decrease in fluorescence as the laser becomes off resonant due to population trapping in the $^2\mathrm{F}^o_{7/2}$.

Both lasers are shifted in frequency by +160 MHz by separate acousto-optic modulators, which is not taken into account on the frequency axis in Figure 4.8.

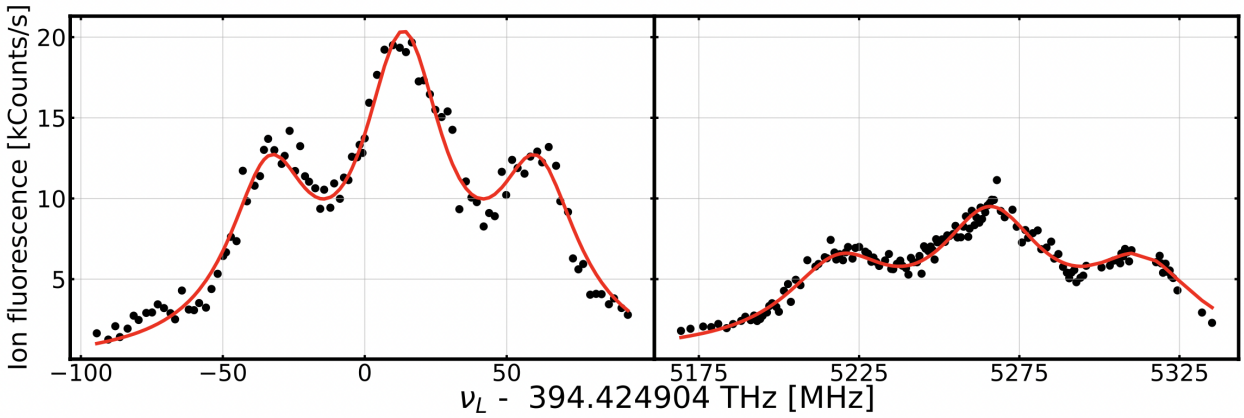

Figure 4.8: The ${}^2\mathrm{F}^o_{7/2}\,|F=3\rangle \rightarrow {}^1[3/2]^o_{3/2}\,|F=1\rangle$ transition is shown on the left, and the ${}^2\mathrm{F}^o_{7/2}\,|F=4\rangle \rightarrow {}^1[3/2]^o_{3/2}\,|F=2\rangle$ transition is shown on the right. The resulting lineshapes are fit to a micromotion modulated spectrum since large amounts of excess micromotion was present during these scans. The difference in overall fluorescence is because a different number of ions were in the trap for each scan, leading to differing overall peak fluorescences.

4.6.3 ${}^2\mathbf{D}_{5/2} \leftrightarrow {}^1[3/2]^o_{3/2}$

The ${}^2\mathrm{D}_{5/2} \leftrightarrow {}^1[3/2]^o_{3/2}$ transition at 976 nm will be used to aid in depopulating the ${}^2\mathrm{F}^o_{7/2}$ by quenching the ${}^1[3/2]^o_{3/2} \rightarrow {}^2\mathrm{D}_{5/2} \rightarrow {}^2\mathrm{F}^o_{7/2}$ decay path. It will also serve as a critical tool for enhancing our preparation of the $|0\rangle_g$ state via as second incoherent optical pumping step along with the 411 nm laser (which will be address in later chapters).

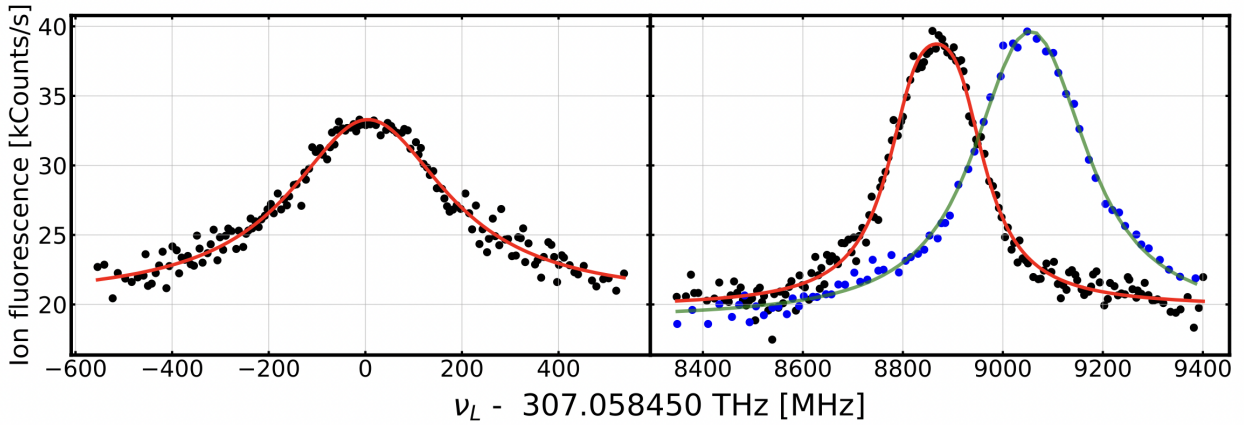

Figure 4.9: All three allowed transitions are shown in this figure. The ${}^2\mathrm{D}_{5/2}\,|F=2\rangle \leftrightarrow {}^1[3/2]^o_{3/2}\,|F=1\rangle$ is shown on the left, and the ${}^2\mathrm{D}_{5/2}\,|F=2\rangle \leftrightarrow {}^1[3/2]^o_{3/2}\,|F=2\rangle$ is shown on the right in black. The ${}^2\mathrm{D}_{5/2}\,|F=3\rangle \leftrightarrow {}^1[3/2]^o_{3/2}\,|F=2\rangle$ is shown in blue, shifted from the neighboring transition by the ${}^2\mathrm{D}_{5/2}$ hyperfine splitting.

The above scans are taken by Doppler cooling multiple ions in the trap while driving the $^2S_{1/2}\ |F=1\rangle \rightarrow {}^2D_{5/2}\ |F=2,3\rangle$ transition, while also illuminating the ion with 760 nm laser light to help depopulate the $^2F^o_{7/2}$. As the 976 nm laser is scanned over the two resonances, the coupling induced to the $^1[3/2]^o_{3/2}$ quenches the electric dipole decay to the $^2F^o_{7/2}$ from the $^2D_{5/2}$ state, resulting in an increase in fluorescence. The two transitions in black in Figure 4.9 are separated by the bracket state hyperfine splitting, which these scans imply is $\Delta_{HFB} = 2\pi\times$ 8.861(3) GHz. The difference in center frequency for the two resonances on the right hand side of Figure 4.9 is due to the $^2D_{5/2}$ hyperfine splitting. From the data, we measure the splitting to be $\Delta_{HFD} = 2\pi\times$ 188(2) MHz.

The 976 nm laser is shifted in frequency by +320 MHz by an acousto-optic modulator, which has not been taken into account on the frequency axis in Figure 4.9.

4.6.4 $^2\mathbf{D}_{3/2} \leftrightarrow {}^1[3/2]^o_{3/2}$

The $^2D_{3/2} \leftrightarrow {}^1[3/2]^o_{3/2}$ will be of interest when performing electron shelved state detection of the ground state qubit in $^{171}Yb^+$. This transition can be used to repump a particular rare decay from the $^2D_{5/2}$ to the $^2D_{3/2}$ that can cause errors during state detection. This transition is around $\lambda = 861$ nm, and we used the output of a continuous wave titanium sapphire laser to perform the spectroscopy with approximately 100 μW of laser light.

To perform the spectroscopy, a single $^{171}Yb^+$ ion was loaded into the trap. The intensity of the 935 nm repump laser is reduced well below saturation such that the ion fluorescence is reduced by a factor of ~ 10. The 861 nm laser can aid the repumping of the $^2D_{3/2}$ during laser cooling by driving population to $^1[3/2]^o_{3/2}$, which predominantly decays back to the $^2S_{1/2}$ state. Due to potential decays to $^2D_{5/2}$ that can populate $^2F^o_{7/2}$ during the spectroscopy, lasers at 976 nm and 760 nm are used to depopulate $^2D_{5/2}$ and $^2F^o_{7/2}$ directly. As the 861 nm laser is scanned over resonance while Doppler cooling, we see an increase in fluorescence due to an increased rate of population depletion from $^2D_{3/2}$.

The measured hyperfine splitting of the $^1[3/2]^o_{3/2}$ state based on this spectroscopy is $\Delta_{HFB} = 2\pi\times$ 8.876(2) GHz. This measured splitting is inconsistent with the above mea-

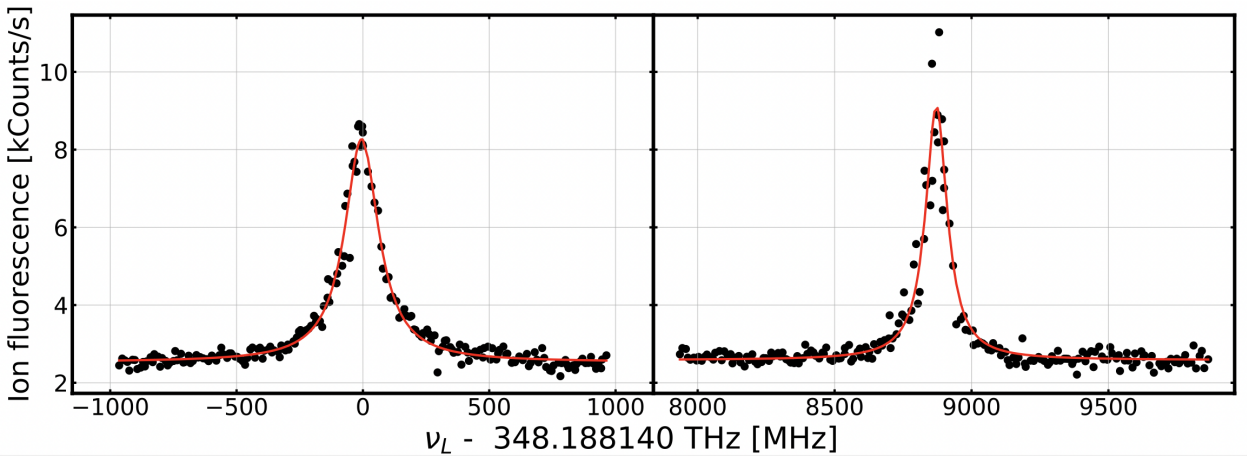

Figure 4.10: Spectroscopy of the 861 nm laser transition. The clear increase in fluorescence is due to an increased repump rate of the $^2\mathrm{D}_{3/2}$. The two transition shown are $^2\mathrm{D}_{3/2}\,|F=1\rangle \rightarrow {}^1[3/2]^o_{3/2}\,|F=1\rangle$ (left) and $^2\mathrm{D}_{3/2}\,|F=1\rangle \rightarrow {}^1[3/2]^o_{3/2}\,|F=2\rangle$ (right). We do not directly observe the transitions from $^2\mathrm{D}_{3/2}\,|F=2\rangle$ performing the scans in this way due to the very small amount of population that resides there in steady state laser cooling.

surement performed on the $^2\mathrm{D}_{5/2}\,|F=2\rangle \rightarrow {}^1[3/2]^o_{3/2}\,|F=1,2\rangle$ transitions. The cause of this discrepancy is unknown, but could be due to some uncalibrated systematic effects such as an AC Stark shift of the $^2\mathrm{D}_{3/2}$ due to continuous illumination with the 935 nm laser.

CHAPTER 5

The Experiment

Most trapped ion quantum information systems have many common components necessary for day to day operation. A short, but by no means comprehensive, list of some components is: an ion trap housed in a ultra-high vacuum system, lasers, optical modulators, radio-frequency and microwave-frequency synthesizers, and some form of experimental control. Here I will go through the main aspects of our experimental setup and try to highlight why certain design choices were made.

5.1 The trap

The trap used in all experiments throughout this thesis is an oblate Paul trap, or a "ring" trap, whose potential is formed by applying a radiofrequency potential to a ring. In fact two of these traps, identical in design and fabricated at the same time, were used: the first one experienced damage that I will briefly discuss later. Many of the details of this trap are addressed in [YSD15]. This particular geometry results in strong confinement in all three dimensions without the need for static fields.

The ion trap was fabricated by Translume. The base is a monolithic 1 mm thick piece of fused silica. For conductive regions of the trap, the layering process began with 20 nm thick layer of titanium, followed by a 500 nm thick layer of gold, with gaps in the coating between the separate conducting regions. In the side of the trap there are trenches with 200 μm diameter openings that taper down conically to 100 μm in diameter at the RF ring for delivery of laser beams and neutral Yb atoms.

Typical secular frequencies in our ion trap are $\{\omega_x, \omega_y, \omega_z\} \approx 2\pi \times \{0.5, 0.5, 1.0\}$ MHz. The

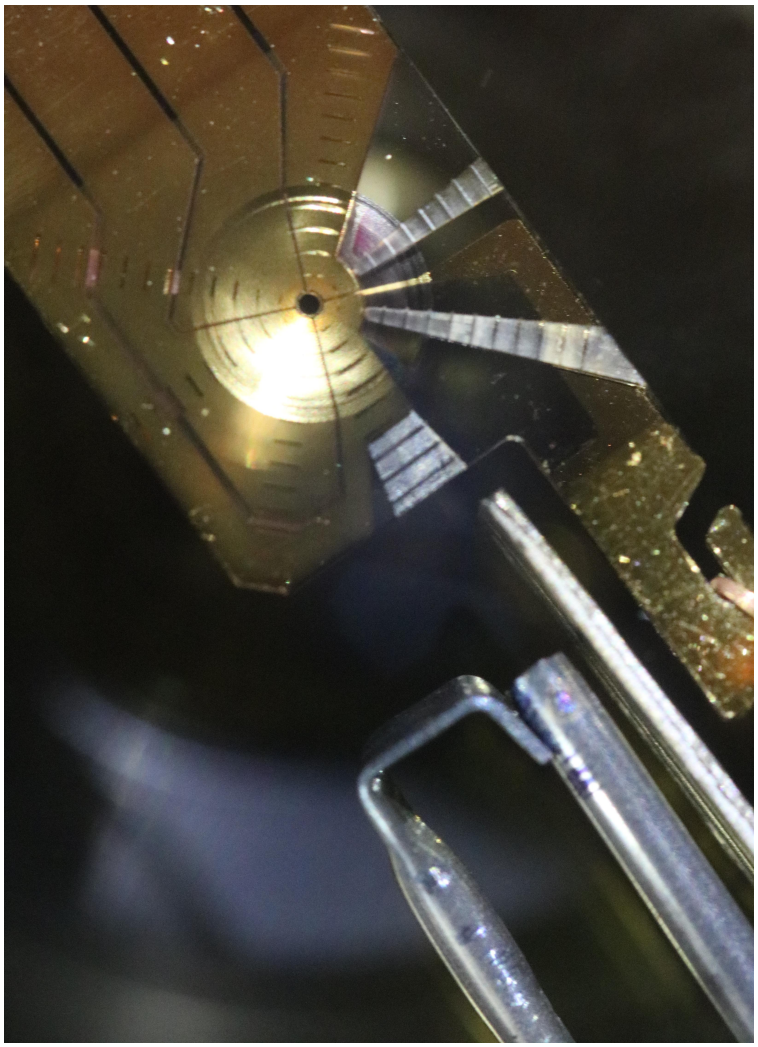

Figure 5.1: Ion trap used throughout this work. The RF is connected to the hook on the right hand side, and the trace leads to the ring at the middle. The stainless steel tube in the bottom right is the neutral Yb oven directed through a laser etched conical section in the side of the trap, and on opposing side is a trench for neutral Yb atoms to be deposited into. A metallic guard is placed between the oven and RF feedthrough to prevent Yb deposition on the RF trace.

strong confinement in the z-direction causes ion crystals to form in 2 dimensional triangular lattices as shown in Figure 5.2.

The ion trap is housed in a 6" stainless steel octagon with recessed UV grade fused silica re-entrant viewports on top and bottom. This was done to allow for high numerical aperture (NA) optical access from both sides of the trap. The windows on the sides of the chamber are 2.75" UV grade fused silica viewports AR coated at 369 nm to avoid stray scatter of 369

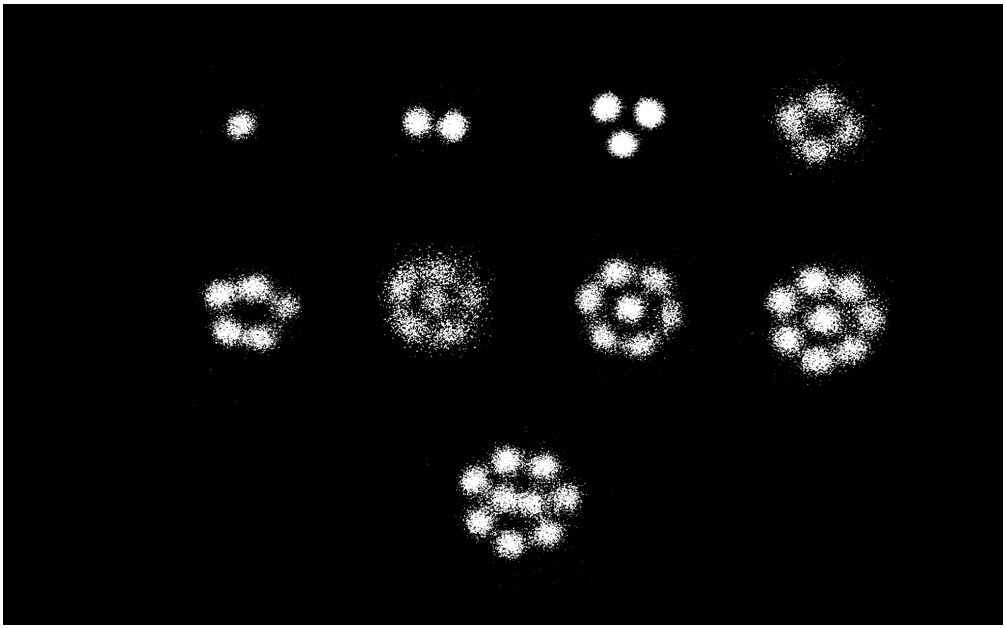

Figure 5.2: Various ion crystal structures observed in our trap. Each image is composed of a different number of $^{174}Yb^{+}$ ions ranging from 1 to 9. Larger ion crystals have been loaded, but are hard to keep crystallized due to excess micromotion experienced by all ions not residing at the center.

nm light.

5.1.1 Trap breakage

The first iteration of this ion trap trapped ions quite well for over 5 years. Over time, the application of high voltage RF caused degradation of the gold lamination on the RF ring, and a portion of the ring became delaminated from the surface. Even though this happened, the trap still created a suitable potential for trapping ions, but with degraded stability.

The initial sign that something was in fact wrong was ion position drifting around in the trap, indicating some sort of time dependent phenomena in the local electric field (either the stray fields were changing, or something about the RF was changing). The ion drift eventually became large enough to cause ion loss, limiting our lifetime to m̃inutes and the trap often un-loadable.

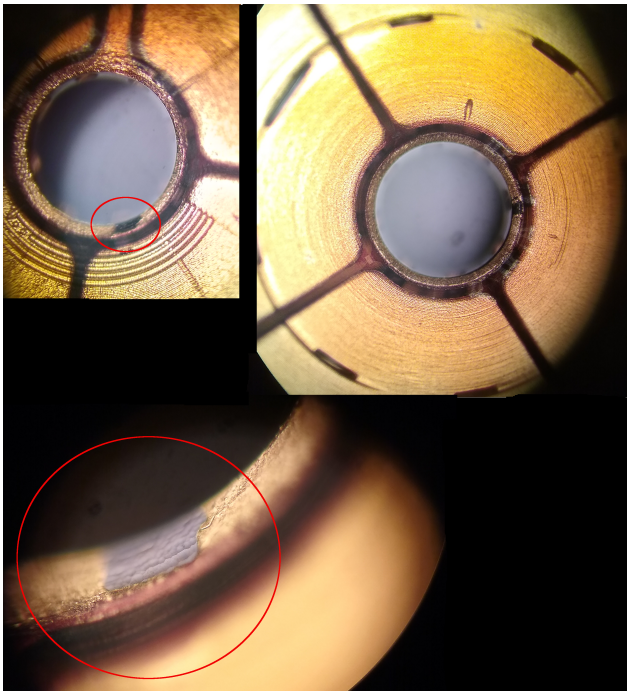

Figure 5.3: Images taken of the broken ion trap once removed from the vacuum chamber. A part of the RF ring gold coating is missing and shows the exposed titanium beneath. These images were taken through a microscope objective with a standard cell phone camera.

5.2 Vacuum chamber

The ion trap is housed in a 6" stainless steel octagon with recessed UV grade fused silica rentrant viewports on top and bottom. This was done to allow for high numerical aperture (NA) optical access from both sides of the trap. The windows on the sides of the chamber are 2.75" UV grade fused silica viewports AR coated at 369 nm to avoid stray scatter of 369 nm light.

We utilize three separate pumps that remain attached to the chamber: a 20 L/s ion pump from Agilent, a titanium sublimation pump housed in a 6" diameter nipple (TiSub), and a non-evaporable getter from SAES (NEG).

5.2.1 Trap replacement

When we replaced the broken ion trap, the chamber was entirely disassembled and slightly rearranged so that each part could be cleaned before baking the chamber. Most standard stainless steel components were cleaned in three stages: deionized water with Alcanox, followed by acetone, and lastly methanol. All step were performed by submerging the part in an ultrasonic bath with the solvent for about 30 minutes each. After cleaning, each part was wrapped in clean UHV grade foil and stored before assembly in a clean area. The exceptions were the main octogon, and the TiSub nipple due to their size and various parts that were already mounted and inside that we did not wish to remove.

Once assembled, the chamber was places inside a convection oven and evacuated by a turbopump. The oven was ramped at a rate of 2° C every 5 minutes until reaching 205° C, limited by the fused silica - stainless steel seal on the chamber windows. Background gas constituents were monitored with a residual gas analyzer. With the turbopump operating, many components were outgassed by applying current: the TiSub, the NEG, and the neutral Yb oven.

The NEG was also activated while the turbopump was on, as it has been observed that NEG activation can cause extreme outgassing that can make an ion pump inoperable if it is the only other pump used to clean out the debris from the NEG [Huc15]. The NEG was activated once at the beginning of the bake (heated to $\sim$ 500° C), and conditioned various times (heated to $\sim$ 200° C) before closing the bakeable valve. Each time the NEG was conditioned, we observed a spike in the H_2 partial pressure on an RGA, followed by an exponential decay to a baseline below the previous baseline. This was repeated until the baseline remained unchanged.

The bakeable valve was closed with the ion pump activated, and the chamber continued to bake for $\sim$ 2 weeks. Once the chamber temperature was ramped back down to room temperature, the pressure read by our ion gauge was 1.6×10^{-10} Torr. Repeated firing of the TiSub over the course of the next two weeks reduced the pressure to a final value of 3×10^{-11} Torr.

5.3 The lasers

The quick list of lasers used in this experiment is: 369 nm, 399 nm, 411 nm, 760 nm, 935 nm, 976 nm, and a mode locked laser. The purpose of all these lasers is briefly covered below. Then the lasers will each be detailed in their own subsections with more specifics.

Practical trapping of Yb^+ ions only requires three lasers at 399 nm, 369 nm, and 935 nm. The 399 nm laser is the first step in 1+1 REMPI of neutral Yb atoms, the second step being facilitated by the 369 nm laser. Once the neutral Yb atom has been photoionized, the 369 nm and 935 nm lasers facilitate laser cooling in the $\{^2S_{1/2} \leftrightarrow {}^2P^o_{1/2} \rightarrow {}^2D_{3/2} \leftrightarrow {}^3[3/2]^o_{1/2}$ $\}$ cycle, where the right arrow is meant to emphasize that this is a four level laser cooling cycle.

In reality, we have quite a few additional lasers. Two 760 nm lasers separated by 5.257 GHz are needed to deplete population that becomes trapped in the $^2F^o_{7/2}$ state via the $^1[3/2]^o_{3/2}$ state. This state is thought to be populated during standard laser cooling via collisional transfer of $^2D_{3/2} \rightarrow {}^2D_{5/2}$, which decays strongly to the metastable state via a 3.4 μm photon. Due to the extreme lifetime of the $^2F^o_{7/2}$ ($\sim$ 5 years), an ion that ends up in this state will not be recovered via spontaneous emission back to the ground state without laser assisted repumping. Additionally, for electron shelving in Yb^+ the 760 nm lasers are necessary at moderate intensities to achieve fast retrieval of population in the metastable state back into the cooling cycle.

The other key laser for electron shelving is the 411 nm laser, which drives the $^2S_{1/2} \leftrightarrow {}^2D_{5/2}$ electric quadrupole transition. In reality we will want the ability to drive separate hyperfine transitions during the course of a shelving experiment, so we will require two 411 nm beams separated by the $^2D_{5/2}$ hyperfine splitting of 191 MHz.

Two lasers that facilitate more specific tasks in the electron shelving experiment are the 861 nm and 976 nm lasers. The 976 nm laser repumps population in the $^2D_{5/2}$ to the $^1[3/2]^o_{3/2}$. This will be useful for two reasons: it will speed up recovery of $^2F^o_{7/2}$ population by suppressing the $^1[3/2]^o_{3/2} \rightarrow {}^2D_{5/2} \rightarrow {}^2F^o_{7/2}$ decay channel, and it will also facilitate a second

method for incoherent preparation of the $|0\rangle_g$ state. The 861 nm laser addresses the $^2D_{3/2} \rightarrow {}^1[3/2]^o_{3/2}$ transition, which is used to suppress errors in dark state population readout caused by $^2D_{5/2} \rightarrow {}^2D_{3/2}$ magnetic dipole decay during electron shelving. This error channel will be discussed in more detail when covering the electron shelving scheme.

The mode locked laser served various purposes throughout this thesis, first used for direct laser cooling of Yb ions, and second for background free state detection of the $^{171}Yb^+$ qubit.

5.3.1 The 369 nm system

The 369 nm laser is a MogLabs ECDL direct diode laser. The laser provides about 7 mW of laser light directly out of the laser head, and a large power hit is taken by using an anamorphic prism pair to clean up the laser mode extra-cavity. After an optical isolator, a little over 3 mW of laser light is available for three purposes: fiber to a wavemeter, locking to an optical cavity, and to deliver to the experiment.

The laser is first split on a polarizing beam splitter, with the majority of the light coupled into a single mode fiber and delivers typically 1 mW to the main optical table. The remaining light is split on a 45/55 pellicle, one portion going to the wavemeter and the other through a second optical isolator to the optical cavity. The second optical isolator is there to prevent feedback of optical cavity to the laser, which we discovered was necessary after initially setting up the cavity.

The portion of the light delivered to the experiment is first passed through a double pass AOM setup, for a total frequency shift of +400 MHz. The zeroth order of the first pass of the double pass is picked off with a D-mirror, and sent through a single pass AOM at about +350 MHz and delivered to the experiment as a protection beam.

The double passed light is then delivered through a series of three AOMs set up in a parallel configuration: the zeroth order of AOM *n* goes directly into the *n+1* AOM. All three AOMs have a fixed frequency shift of +110 MHz.

The first of the three is sent through a resonant free space electro optic phase modula-

tor (EOM) with a resonant frequency of 7.379 GHz[1]. The positive second order sideband frequency is chosen such that when the 369 nm laser carrier frequency is set 10 MHz red detuned of the $^2S_{1/2}\,|F=1\rangle \rightarrow {}^2P^o_{1/2}\,|F=0\rangle$ cooling line, the sideband will have zero detuning from the $^2S_{1/2}\,|F=0\rangle \rightarrow {}^2P^o_{1/2}\,|F=1\rangle$ repump line. This beam facilitates efficient Doppler cooling of all Yb^+ isotopes, with the exception of $^{173}Yb^+$, which due to a different hyperfine structure requires a separate phase modulator for laser cooling.

The second AOM is passed through a similar resonant free space EOM with resonant frequency 2.105 GHz[2]. The positive first order sideband will resonantly drive the $^2S_{1/2}\,|F=1\rangle \rightarrow {}^2P^o_{1/2}\,|F=1\rangle$ transition which will optically pump population to the $|0\rangle_g$ state.

The third AOM is simply sinlge passed at +110 MHz to provide laser light resonant with the $^2S_{1/2}\,|F=1\rangle \rightarrow {}^2P^o_{1/2}\,|F=0\rangle$ transition for CW state detection of the ground state qubit in the standard $I=1/2$ scheme.

All beams are delivered to the ion trap via single mode optical fibers.

5.3.2 The 399 nm system

The 399 nm laser is a Toptica DL 100 Pro ECDL, which outputs about 20 mW of laser power directly out of the laser head. The optical setup for this laser is far simpler than the 369 nm laser: the laser output is first shaped with an anamorphic prism pair, passed through an isolator, and split between delivery to the ion trap and the wavemeter. The laser has no active or passive frequency stabilization, so before loading the trap we simply adjust the laser frequency on the wavemeter by hand.

[1]New Focus Model 4851, ∼3W of microwave power used

[2]New Focus Model 4431, microwave power set to optimize positive first order sideband intensity

5.3.3 The 935 nm system

The 935 nm laser is a distributed Bragg reflector (DBR) laser from Toptica. The laser outputs about 10 mW of laser power, which is passed through an anamoprhic prism pair and an optical isolator. The light is then split on a PBS, with one leg going to the wavemeter and the other through a fiber KTP crystal phase modulator[3] that exhibits large bandwidth modulation with little microwave power. This modulator is generally driven at 3.070 GHz for efficient laser cooling of $^{171}Yb^{+}$ due to off resonant population of the $^{2}D_{3/2}\,|F=2\rangle$ level during laser cooling, and direct population of the same level during $|0\rangle_g$ state preparation.

The output of the fiber modulator is passed through a +320 MHz single pass AOM which is then subsequently coupled into a fiber to the ion trap. The frequency of this laser is software locked with the built in DACs in our wavemeter[4].

5.3.4 The 760 nm laser systems

Since we require significant optical intensity of two 760 nm laser tones separated by about 5 GHz, we use two separate DBR lasers for each tone[5]. Each laser outputs about 50 mW of laser power, with each passing through a anamorphic prism pair and an optical isolator. A small portion of each laser's power is sent to the wavemeter for software locking, with the remaining power for both lasers separately passed through +160 MHz AOMs. The positive first order from both AOMs are combined on a PBS and overlaid with the 935 nm laser on a 45° dichroic beam splitter[6] into the fiber to the trap. Each of the lasers delivers about 15 mW to the ion, for a total of about 30 mW of laser power.

The frequencies for the two lasers are set so that the red and blue beams drive the $^{2}F^{o}_{7/2}\,|F=3\rangle \rightarrow {}^{1}[3/2]^{o}_{3/2}\,|F=1\rangle$ and $^{2}F^{o}_{7/2}\,|F=4\rangle \rightarrow {}^{1}[3/2]^{o}_{3/2}\,|F=2\rangle$ transitions respec-

[3]AdvR KTP Phase Modulator

[4]High Finesse WS-U, 8 channel fiber switch

[5]Photodigm PH760DBR080T8, TO-8 packaging

[6]Semrock FF776-Di01-25x36

tively.

5.3.5 The 976 nm system

The 976 nm laser is a fiber output butterfly packaged DBR laser from ThorLabs that provides about 30 mW out of the fiber. The laser is split directly out of the laser with a PBS, with a small amount of power going to the wavemeter and the majority delivered through a +320 MHz single pass AOM. The laser is then combined on a 50/50 beamsplitter with the 861 nm laser, and subsequently overlaid with the 935 nm laser on a PBS before being overlaid with the 760 nm lasers.

This laser is generally set to drive the $^2\mathrm{D}_{5/2}\,|F=2\rangle \rightarrow {}^1[3/2]^o_{3/2}\,|F=1\rangle$ transition for incoherent preparation of the $|0\rangle_g$ state. This is achieved by applying 411 nm laser light driving the $^2\mathrm{S}_{1/2}\,|F=1\rangle \rightarrow {}^2\mathrm{D}_{5/2}\,|F=2\rangle$ transition, along with the 976 nm laser. This will cause population to eventually decay directly into the $|0\rangle_g$ qubit state.

5.3.6 The mode-locked laser

The mode locked laser is a Spectra Physics Tsunami laser head pumped with a Spectra Physics Millenia eV 532 nm pump laser (15W max ouput power). The Tsunami system is a Ti:Sapph mode locked laser capable of broad center frequency tuning via an intracavity birefringent filter. We always operate the laser in the picosecond pulse width regime, where the Tsunami laser head is operated as an active mode locked laser (as opposed to a passive mode locked laser, like many femtosecond mode locked lasers). A part within the laser head called the GTI (Gires-Tournois interferometer) controls the pulse width of the picosecond system, and in our lab we have separate GTIs for providing 30 ps, 10 ps, and 1 ps pulse widths. On the Yb^+ experiment, the 10 ps GTI was used for the cooling and detection experiments, and was converted to the 1 ps GTI for stimulated Raman transitions.

5.4 The electronics

5.4.1 The "pulser"

The main device in our lab that controls the experiment is what we call *the pulser*. It is a FPGA controlled system with 16 phase coherent direct digital synthesizers (DDSs), 32 TTL output channels, and photon counting capabilities with 10 ns photon time-tagging resolution [PK15]. The DDSs can generate RF frequencies up to 800 MHz, limited in part by the 2 GHz reference clock for the system. The DDSs are used for three main purposes in the experiment: one provides the radiofrequency necessary for the ion trap, two are dedicated to driving microwave qubit transitions of the m and g type qubits, and the rest are used to drive AOMs.

The pulser system is controlled by the master FPGA[7]. Pulse sequences are loaded onto the master FPGA before an experiment executes, and distributes the pulse sequence to local FPGA chips on each of the DDS boards [8]. The DDS boards can be switched in amplitdue, phase, and frequency with 40 ns resolution, while the TTLs can be generated with 10 ns resolution. The specifics of DDS performance can be found in [PK15], and the resolutions of each setting are briefly listed below, taken from [PK15].

Characteristic	Resolution	Range
Frequency	0.1 pHz	0 o 800 MHz
Amplitude	0.004 dB	-60 to 0 dBm
Phase	0.0055 deg	0 to 360 deg
Frequency ramp rate	113 Hz/ms	max 7.45 MHz/ms
Amplitude ramp rate	0.0017 dB/ms	max 22.9 dB/ms

Table 5.1: Resolution and range of each programmable feature of each DDS. Data is transferred to each DDS FPGA as a 128 bit number, with memory allocation of {64, 14, 16, 16, 16 } bits per characteristic, from top to bottom above. All numbers taken from [PK15]

A number of the features of these DDS boards will be important when we consider implementing composite pulse sequences for high fidelity population transfer of $|0\rangle_g \rightarrow |1\rangle_g$.

[7] Opal Kelly XEM6010

[8] Altera Cylcone IV

5.4.2 Trap DC voltages

The DC voltages applied to the 8 trap electrodes are provided by Analog Devices AD660 DAC chips. The chips are controlled by a master FPGA, same one as the pulser. Each DAC chip is passed through a 4 stage RC filter board, the outputs of which are connected directly to feedthrough pins on the vacuum chamber with short wires. Electrical ground for the chips is provided on one of the feedthrough pins near the trapping region.

5.4.3 Microwave sources

We have two main microwave sources in our lab: one PXIe module from MagiQ that provides microwave tones at 7.37 GHz, 2.105 GHz, and 3.07 GHz for our various electro optic modulators needed for laser cooling and qubit operations in $^{171}Yb^{+}$, and an HP 8672A for qubit operations.

To make a phase agile source for qubit manipulation, we mix a DDS from the pulser with the 8672A output to produce a tone at the qubit splitting. Band pass filters are used to filter out unwanted frequencies produced in the mixing process at $\approx$ + 400 MHz and + 800 MHz from the carrier tone. We have also built but not yet implemented a circuit that multiplies a DDS input by 32 to produce a microwave signal reosnant with the qubit. The design was based on the design outlined in [Har13]. The main downside of the frequency multiplied device is a loss in phase resolution due to the frequency multiplication process. That being said, the resulting phase resolution of 0.176 deg should be sufficient for most applications.

5.5 The experimental control

The workhorse of the experiment is the pulser, which performs all programmed pulse sequences and counts and timetags photons.

Nearly all experimental control software is written within the LabRAD framework created

at UCSB [9]. LabRAD allows for control of nearly any piece of hardware on our experiment that is connected to any computer on the local area network. In general, each device may have a *server* and a *client*. The server wraps the hardware commands in Python and creates easily used functions to communicate with the hardware. The clients are Python GUIs that communicate with the servers to provide an easy way to interface with the hardware.

Lastly there are the scripts that we write to perform experiments, within which we can communicate with any device connected to our local LabRAD instance, program and execute pulse sequences with the pulser, and retrieve and analyze data. For more details regarding LabRAD in our experiment, please see [Ran20, Chr20] and various online resources on GitHub.

[9] https://github.com/labrad

CHAPTER 6

Laser cooling with mode locked lasers

Strong optical transitions in singly ionized atoms often require laser light in the ultraviolet (UV) to drive, and can even be energetically separated enough to necessitate vacuum-ultraviolet photons (< 200 nm) [WD75, HS75, NHT78, WDW78]. Continuous wave laser light becomes increasingly hard to produce in quantity at these wavelengths, and adds significant complexity to any experiment wishing to address transitions at these wavelengths. One of the advantages of mode-locked lasers is their high instantaneous intensity, which can be used for efficient frequency doubling via single passes though non-linear crystals. Mode locked lasers have even been used to reach deep regions of the extreme ultraviolet (EUV) ($<$ 100 nm) via a process known as high-harmonic generation.

In our work here, we aimed to demonstrate efficient laser cooling of a trapped ion with only a single mode of a resonant mode-locked laser. In order to efficiently Doppler cool the ion's motion in the trap, we must be able to apply a strong velocity dependent force with the laser and scatter many photons to achieve reasonable cooling rates. This is most efficiently achieved by addressing the atomic transition with a single longitudinal mode of the mode locked laser (a single "comb tooth").

6.1 Scattering rate

In order to Doppler cool a trapped ion, we need to scatter photons on a strong transition. The scattering rate of a stationary atom due to illumination with a resonant mode locked laser is [FBA03]

$$\Gamma_{comb}(\Delta) = \frac{1}{T_r} \frac{\sin^2(\frac{\theta}{2}) \sinh\left(\frac{T_r}{2\tau}\right)}{\cosh\left(\frac{T_r}{2\tau}\right) - \cos^2(\frac{\theta}{2}) \cos(\Delta T_r)} \tag{6.1}$$

where T_r is the repetition period of the mode locked laser, τ is the lifetime of the excited state, $\theta = \int \Omega(t)dt$ is the pulse area defined as the integral of the instantaneous Rabi frequency over the length of the interaction time with a single pulse, and $\Delta = \omega_{tooth} - \omega_{atom}$ is the detuning of a reference comb tooth from the atomic transition. This equation was derived under the assumption of a comb of optical teeth with uniform intensity, equivalent to the assumption that the pulse duration τ_p is much shorter than the repetition period T_r.

First thing to note in eq 6.1 is that the maximum scattering rate is $\Gamma_{max} = \frac{\tanh(T_r/2\tau)}{T_r}$ achieved when $\theta = \pi$. This will not be optimal for laser cooling though, as when the pulse area is π the dependence on comb tooth detuning, and therefore the atom's velocity, is removed. Throughout this experiment we generally worked in the regime where $\theta < \pi/2$.

In order to address the ion with a single comb tooth, coherences between the ion and the laser must build up by interacting with multiple pulses in a pulse train. Visualized on a Bloch sphere, the first pulse at $t = 0$ will create an excitation by an angle θ, followed by a time T_r of free evolution. As the next pulse arrives at $t = T_r$, the relative phase of the Bloch vector and the optical phase of the pulse will determine what happens. If a longitudinal mode of the mode locked laser is near resonance with the atomic transition, then the ion will continue to get further excited. If there is a detuning between the longitudinal mode and the ion, then rotation will occur about a different axis and the excitation will be suppressed. It is this build up of pulse-to-pulse coherence that is necessary to address the atomic transition with a single comb tooth. In our system, the excited state lifetime of the Yb^+ $^2P^o_{1/2}$ state is $\tau = 8.12$ ns [OHM09], and after a pulse excited an ion initially in the $^2S_{1/2}$, it has a 78% chance of spontaneously emitting a photon by the time the next pulse arrives $T_r = 12.3$ ns later. This means that by the time the second pulse arrives, more often than not the ion will lose all information about the optical phase of the previous pulse.

To help understand the importance of the two pictures of this interaction (comb teeth vs broadband pulses), we consider the comb tooth visibility, defined as $V = (\Gamma_{max} -$

$\Gamma_{min})/(\Gamma_{max} + \Gamma_{min})$, where $\Gamma_{max/min}$ are the maximum and minimum scattering rates from eq 6.1 as the reference comb tooth is scanned over a range $\delta f = 1/T_r \equiv f_r$. The visibility turns out to be

$$V = \cos^2\left(\frac{\theta}{2}\right) \operatorname{sech}\left(\frac{T_r}{2\tau}\right) \tag{6.2}$$

which remains surprisingly high at 0.77 in the $\theta \to 0$ limit with our system parameters despite the previous argument. This occurs because the coherence of a superposition between two states decays at half the rate compared to the populations within the excited state due to spontaneous emission, and therefore coherences actually can build up when $\tau \sim T_r$.

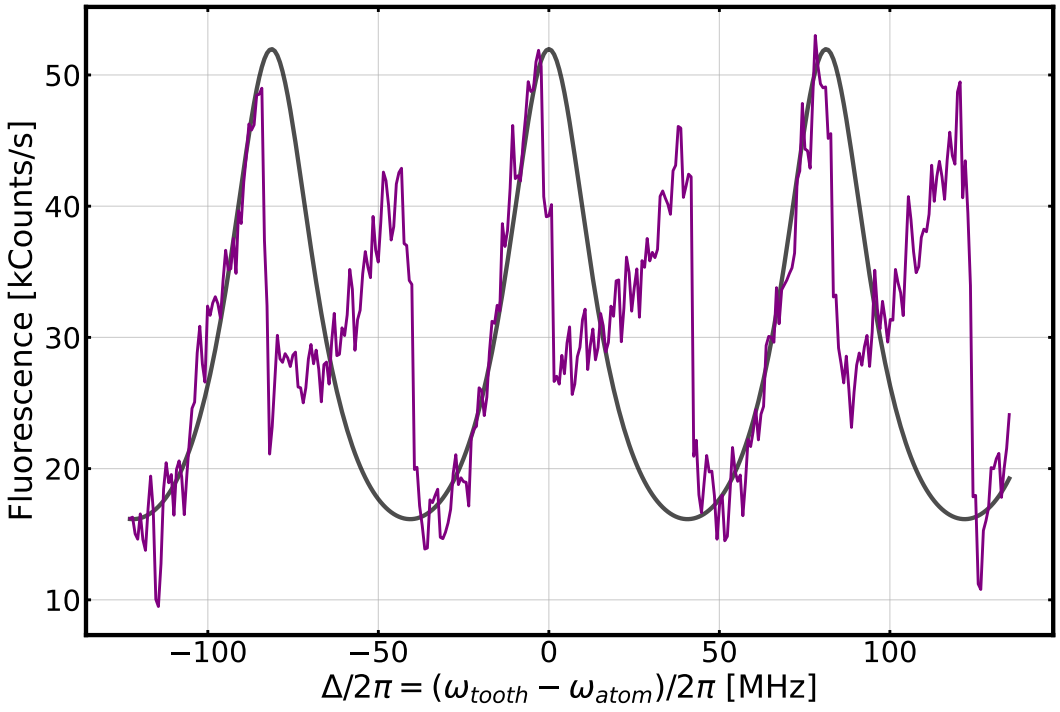

Figure 6.1: Collected fluorescence as the comb teeth are scanned over resonance. In the scattering rate predicted from equation 6.1 is shown in grey, clearly deviating from the theoretical model when the nearest comb tooth is blue detuned from resonance. In the theory plot $\theta = 0.38\pi$, and the overall rate is scaled for photon detection efficiency.

6.2 The experiment

The laser used is a Spectra Physics Tsunami Ti:Sapph tunable mode-locked laser set to 405.645 THz ($\sim$ 740 nm), and subsequently frequency doubled to match the resonance of the $^2S_{1/2}$ to $^2P^o_{1/2}$ transition in Yb^+. The repetition period of the laser is tunable within a small range, and was $\sim$ 12.3 ns for these experiments. The pulse width was $\tau_p = 10$ ps, corresponding to an optical bandwidth of $\approx$ 100 GHz.

Ions are loaded into the trap with the standard Doppler cooling lasers, and then illuminated with the UV mode locked laser light to observe its effect on the ion. When observing the ion fluorescence rate due to the interaction with the mode locked laser, the continuous wave 369 nm laser is removed from the trap and the 935 nm laser remains to repump the $^2D_{3/2}$. To see how well eq 6.1 models the scattering rate in our system, we vary the location of comb teeth relative to atomic resonance. This is done by varying a voltage on an intracavity piezoelectric actuator behind one of the mirrors inside the mode locked laser cavity. This piezo causes the repetition rate of the laser to change by small amounts, causing a change in the comb tooth spacing in frequency space. Scanning the repetition rate effectively scans the teeth over resonance in the optical regime. Data from a scan performed with a single trapped $^{174}Yb^+$ ion is shown in Figure 6.1. The data is taken by switching the 935 nm laser on/off every 100ms, the difference of which results in a signal that is mainly from the ion with the $\sim$ 170 kCounts/s of background scatter from the mode locked laser removed. The collected fluorescence from the ion is well modeled by equation 6.1 when the detuning of the nearest comb tooth is red detuned ($\Delta < 0$), but exhibits deviation from theory when blue detuned ($\Delta > 0$).

To see what is happening blue of resonance, we perform the same scan but observe the ion on an EMCCD camera instead of collecting fluorescence with the PMT. Images of the ion are taken when the nearest comb tooth was red detuned from resonance (at approximately $\Delta = -2\pi \times 15$ MHz in Figure 6.1) and blue detuned from resonance (at approximately $\Delta = 2\pi \times 30$ MHz in Figure 6.1)

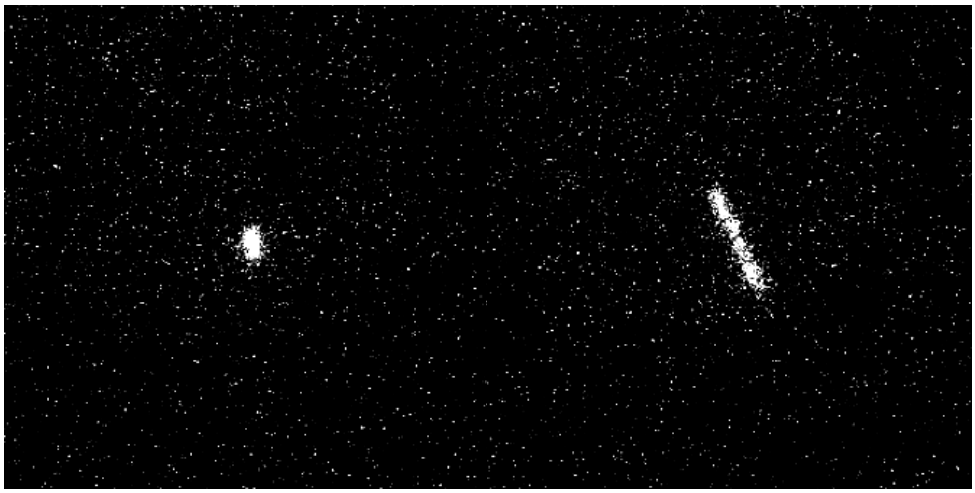

Figure 6.2: Images taken of the ion when the nearest comb tooth is red detuned from resonance (left) and blue detuned from resonance (right). The ion is oscillating with significant amplitude along the principle axis of the trap we designate as $\hat{x}$.

To model the interaction between the ion and the mode locked laser, we consider the energy transfer to to the ion due to the laser-ion interaction, including spontaneous emission and classical harmonic motion of the ion. All the following work will consider secular cycle averaged values instead of instantaneous, as the secular motion is slow compared to all other timescales in the experiment. The energy in the harmonic motion of the ion is $E = \frac{1}{2}m\omega_x^2 x_o^2$, where x_o is the amplitude of oscillation and ω_x is the oscillation frequency. The rate of energy transfer from the laser to the ion is

$$\frac{dE}{dt} = -\beta(E)\frac{2E}{m} + S(E) \tag{6.3}$$

where S(E) is the stochastic heating term from spontaneous emission and randomness in absorption, and $\beta(E)$ is a damping coefficient resulting from the laser-ion interaction. We

will model these two terms as

$$\begin{aligned} S(E) &= (1+\xi)\frac{\hbar^2|\mathbf{k}|^2}{2m}\Gamma(\Delta, x_o) \\ -\frac{2E}{m}\beta(E) &= \langle \mathbf{F}\cdot\mathbf{v}_{sec}\rangle_{T_{sec}} \end{aligned} \tag{6.4}$$

where $\Gamma(\Delta, x_o)$ is the secular cycle averaged scattering rate for an ion with harmonic amplitude x_o, $\xi = 2/5$ is a geometric factor taking into account the dipole radiation pattern of spontaneous emission [LBM03], $\mathbf{F} = \hbar\mathbf{k}\Gamma_{comb}$ is the scattering force, and $\mathbf{v}_{sec}$ is the instantaneous secular velocity.

6.3 Modeling scattering rate data

To average over the secular motion, we need to take into account how it effects the relevant parameters governing the laser-ion scattering rate. If the ion is oscillating, it will be taking excursions from the RF null of the trap (assuming stray electric fields had already been compensated for), which can cause excess micromotion. Thus, we include the effects of micromotion modulation of the scattering rate. Additionally, the ion will be oscillating with peak speed $v_x = \omega_x x_0$ at $x = 0$, creating a time dependent Doppler shift that should be taking into account. The time dependent Doppler shift will be $\delta\omega = \mathbf{k}\cdot\mathbf{v}_x = k\omega_x x_o \sin(\omega_x t)$, where k is the projection of the mode locked laser k-vector onto the principle axis of motion. The secular averaged scattering rate, included the effects of micromotion and setting $\phi = 0$, can be written as

$$\Gamma(\Delta, x_o) = \frac{1}{2\pi}\int_0^{2\pi} d\chi \sum_n J_n^2\Big(kx_o\frac{q}{2}\cos\xi\Big)\Gamma(\Delta + n\Omega_{rf} + k\omega_x x_o \sin\chi) \tag{6.5}$$

where J_n is the n^{th} Bessel function of the first kind, $q \approx 2\sqrt{2}\omega_x/\Omega_{rf} = 0.03$ is the Mathieu q parameter, Ω_{rf} is the RF frequency applied to the ion trap, and $\chi = \omega_x t$. The argument in the Bessel function is the time dependent modulation depth of the ion motion [BMB98].

Using the above equation with $x_0 = 0$ when the nearest comb tooth is red detuned, and

$x_0 = 4.9\mu$m when the nearest comb tooth is blue detuned to reflect the change in oscillation amplitude, we find a better quantitative agreement with the observed line scan.

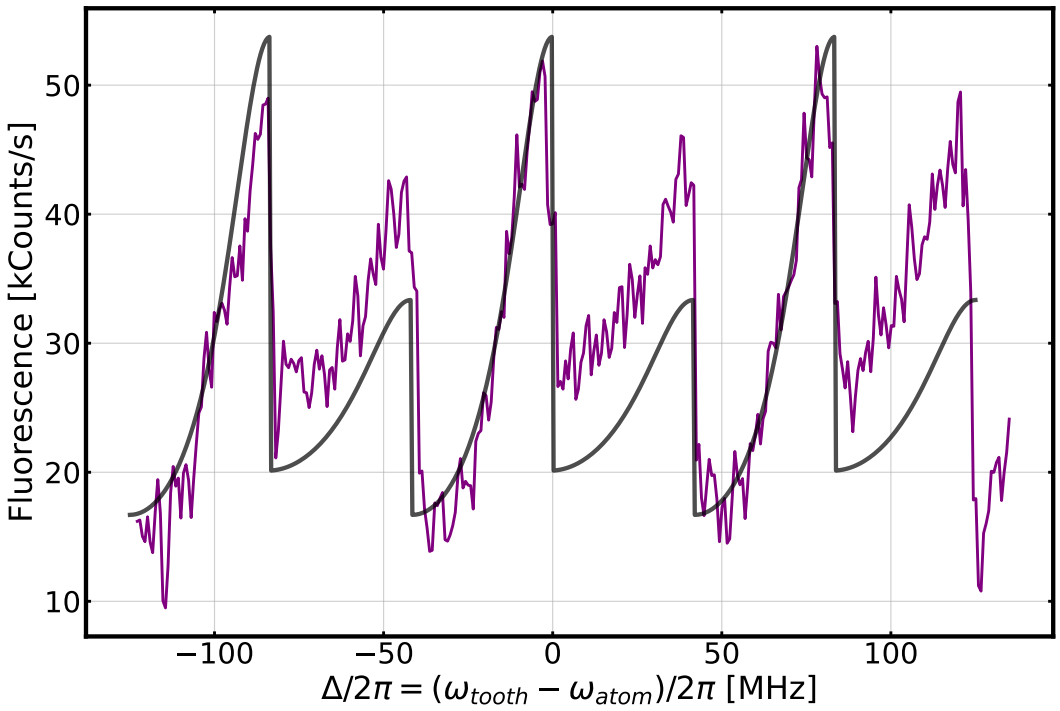

Figure 6.3: Collected fluorescence as the comb teeth are scanned over resonance. In the scattering rate predicted from equation 6.5 is shown in grey, agreeing significantly better with the observed line shape. The theoretical plot is not a fit, and is scaled by eye with no offset.

Qualitatively, once the nearest comb tooth is blue detuned it amplifies the motion of the ion in the trap in the direction the k-vector projects onto most strongly (in our case the direction we are calling $\hat{x}$). This causes the secular motion of the ion to be excited to an amplitude such that the Doppler shift at $x = 0$ shifts the ion into resonance with a tooth that is red detuned in that frame. Once the motion is damped enough, it is on resonance on the blue side with the other tooth again, and the process continues.

6.4 Dynamics of the interaction

To determine the oscillation amplitude of the ion motion in the trap and understand why the ion remains in the trap when the nearest optical tone is blue detuned, we can investigate the dynamics of equation 6.3. In particular, we will be interested in two things: for fixed detuning, what values of x_o will cause the power delivered to the ion to vanish, and what is the behavior in the small oscillation limit.

The secular cycle averaged amplitude damping coefficient $\beta(E)$ is given by

$$\beta(E) = \frac{\hbar k}{2\pi\omega_x x_o}\int_0^{2\pi} d\chi \sin(\chi)\sum_n J_n^2\Big(kx_o\frac{q}{2}\cos\xi\Big)\Gamma(\Delta + n\Omega_{rf} + k\omega_x x_o \sin\chi) \tag{6.6}$$

Rewriting 6.3 as

$$\frac{dE}{dt} = -\beta(x_0)\omega_x^2 x_o^2 + S(x_o) \tag{6.7}$$

by allowing $E = \frac{1}{2}m\omega_x^2 x_o^2$. The terms on the right hand side can now be numerically integrated over a secular cycle for a fixed detuning as a function of the oscillation amplitude. The results of the numerical integration with our experimental parameters are shown in Figure 6.4.

There are clearly many solutions for $\frac{dE}{dt} = 0$, and of particular interest are oscillation amplitudes x_k at which $\frac{dE}{dt}|_{x_k} = 0$ and $\frac{d^2E}{dtdx_0}|_{x_k} < 0$. At these locations, the oscillation will be stable and maintained. Since the derivative with respect to oscillation amplitude is negative, if the amplitude decreases more energy is pumped in to the ion motion to return it to the zero crossing. Conversely, if the amplitude increases, the amplitude will be damped and returned back to the zero crossing.

When the reference tooth is red detuned from resonance, the model predicts an oscillation amplitude of $x_0^* \approx 90$ nm for $\Delta = -\pi/2T_r$, far below the resolution of our imaging system ($\approx 1\mu$m). High order oscillation amplitudes are resolvable by our imaging, so we can investigate them and compared to theory.

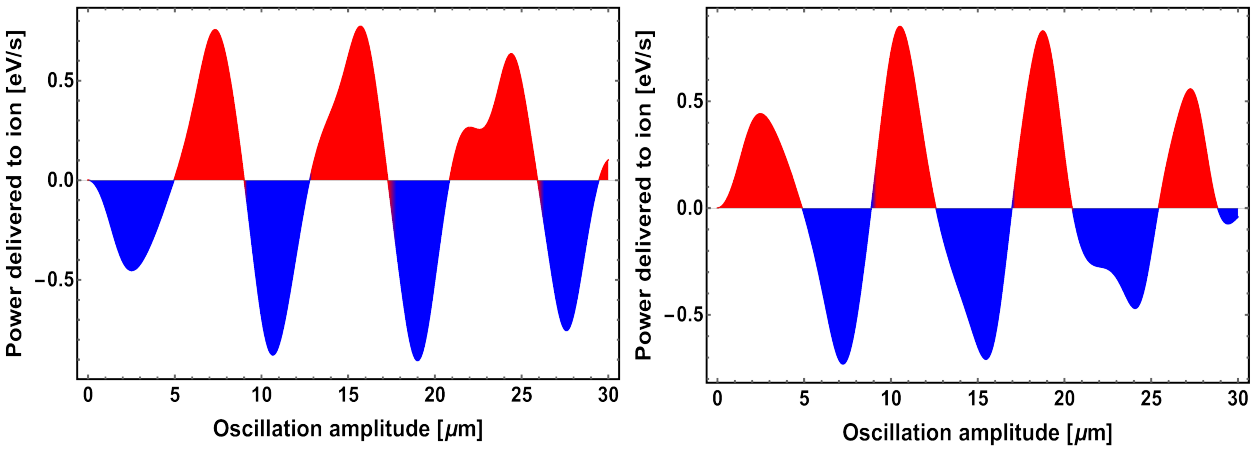

Figure 6.4: The power delivered to the ion, averaged over a secular cycle, shown $\Delta = -2\pi\times15$ MHz (left) and $\Delta = 2\pi \times 15$ MHz (right). For the purpose of these plots, only the first order micromotion sideband is included. Blue shading indicates oscillation amplitudes where the laser-ion interaction has a net damping effect, and red shading indicates amplitudes where the interaction has a net amplification effect. Bleeding of the shading near zero crossings is artificial and should be ignored.

To create these larger oscillation amplitude states, we connect a signal generator to one of the trap DC electrodes to "tickle" the ion. The frequency of the applied electric field is chosen to be close to ω_x so that energy is transferred into that particular mode of motion. The process of creating the higher order oscillating modes is stochastic and not deterministic when done this way. Averaged images of the ions in higher oscillatory fixed points are shown in Figure 6.5, with the corresponding vertical column sums of those images show in Figure 6.6.

To determine the classical turning point of these fixed oscillations, we fit the column summed data to a convolution of the simple harmonic oscillator probability density function (SHO PDF) and a Gaussian profile. The SHO PDF, which is the probability of finding the ion at position x in a window dx at a random time t, is given by

$$P_{sho}(x, x_o) = \frac{1}{\pi}\frac{1}{\sqrt{x_o^2 - x^2}} \tag{6.8}$$

We numerically convolve a Gaussian profile with $P_{sho}(x, x_o)$ and fit the data to extract x_o, the classical turning point where the ion has vanishing velocity.

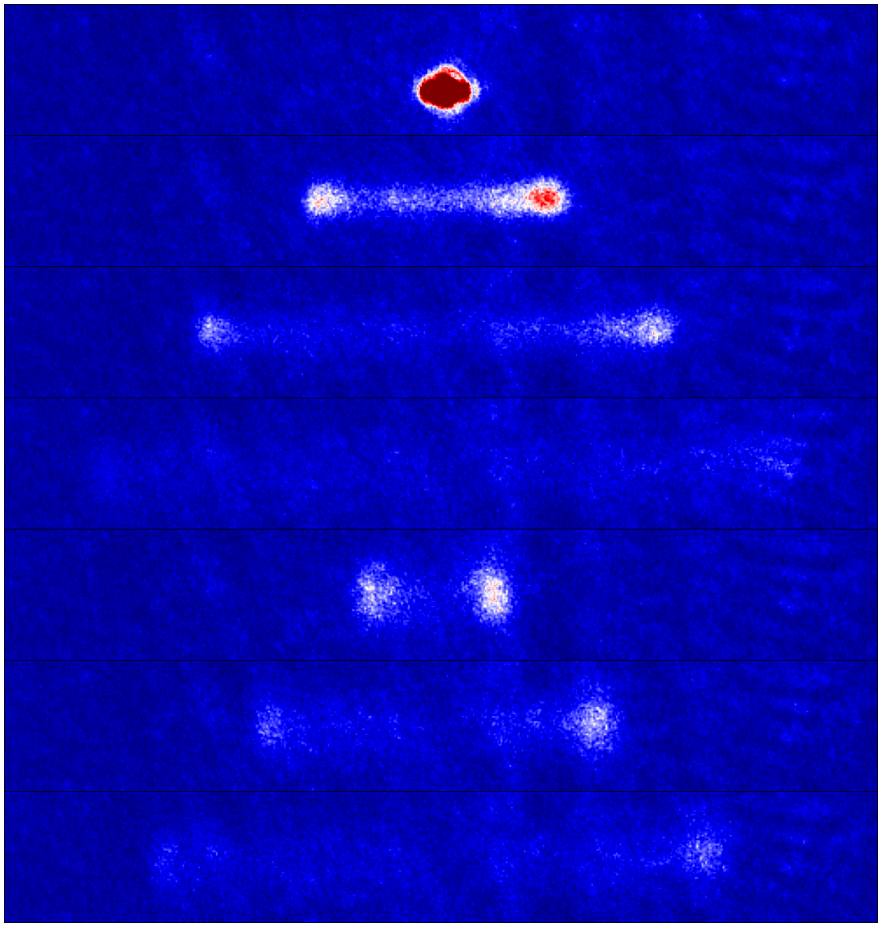

Figure 6.5: Integrated camera images of different velocity classes at fixed oscillation amplitudes while illuminating the ion with the mode locked laser alone. The top 4 images are the first 4 stable amplitudes when the nearest comb tooth is red detuned from resonance. The lower 3 are the first 3 fixed amplitudes when the nearest comb tooth is blue detuned from resonance.

6.5 Temperature derivation

In the limit of small oscillation amplitude ($E \to 0$) and with the nearest comb tooth red detuned from the cooling transition, an expression for the Doppler temperature can be derived. At this point, the power delivered to the ion will be vanishing, indicating that the damping and stochastic terms in equation 6.3 are equal to one another. With that we can write

$$\frac{dE}{dt} \to 0 : E = \frac{1}{2} m \frac{S(E)}{\beta(E)} \tag{6.9}$$

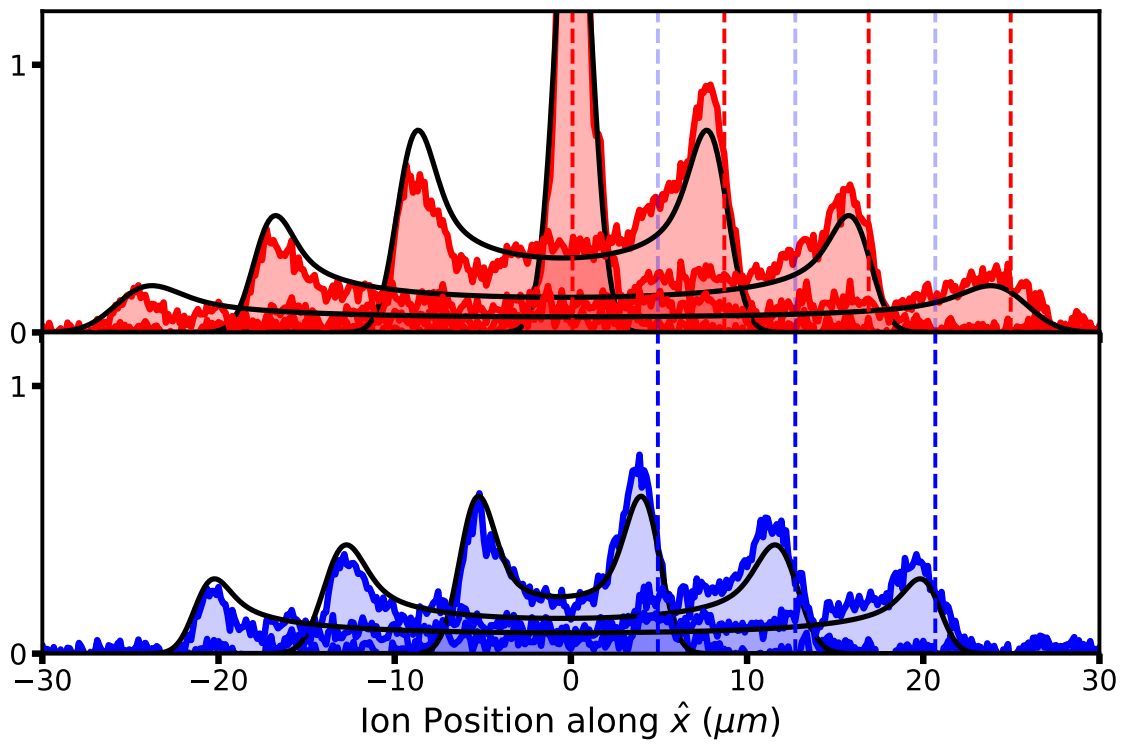

Figure 6.6: Column sums of the images shown in Figure 6.5. By calibrating our imaging system we can convert pixels to microns and fit the fluorescence to the convolution of a Gaussian and the probability density function of a simple harmonic oscillator. Vertical dashed lines indicate the fitted classical turning point of the harmonic motion. The turning points in red are $x_r^* = \{0.09, 8.71, 16.90, 24.96\}\mu$m, and turning points in blue are $x_b^* = \{4.94, 12.74, 20.68\}\mu$m.

where the expressions for the stochastic heating and damping must be evaluated in the $x_o \to 0$ limit. We will start with the stochastic term.

6.5.1 Small oscillation amplitude limit of stochastic heating

The stochastic heating term written out in full is given by

$$S(E) = \frac{\hbar^2 k^2}{2m}(1+\xi)\frac{1}{2\pi}\int_0^{2\pi} d\chi \sum_n J_n^2\Big(kx_o\frac{q}{2}\cos\xi\Big)\Gamma(\Delta + n\Omega_{rf} + k\omega_x x_o \sin\chi) \tag{6.10}$$

As x_0 tends to 0, the argument of the Bessel function will tend to 0 as well. In this limit only the 0^{th} order Bessel function will survive, with all higher orders vanishing in the small argument limit. This physically makes sense as well: as the oscillation amplitude, and

therefore the excursions from the RF null, tend to zero, the effects of excess micromotion will also vanish. We now have, setting n = 0,

$$S(E) = \frac{\hbar^2 k^2}{2m}(1+\xi)\frac{1}{2\pi}\int_0^{2\pi} d\chi \Gamma(\Delta + k\omega_x x_o \sin\chi) \tag{6.11}$$

The scattering rate within the integrand is

$$\Gamma(\Delta + k\omega_x x_o \sin\chi) = \frac{1}{T_r}\frac{\sin^2(\frac{\theta}{2})\sinh\left(\frac{T_r}{2\tau}\right)}{\cosh\left(\frac{T_r}{2\tau}\right) - \cos^2(\frac{\theta}{2})\cos(\Delta T_r + T_r k\omega_x x_o \sin\chi)} \tag{6.12}$$

which can be simplified by expanding the term $\cos(a+\epsilon)$ in the denominator about $\epsilon = 0$ to get

$$\Gamma(\Delta + k\omega_x x_o \sin\chi) = \frac{1}{T_r}\frac{\sin^2(\frac{\theta}{2})\sinh\left(\frac{T_r}{2\tau}\right)}{\cosh\left(\frac{T_r}{2\tau}\right) - \cos^2(\frac{\theta}{2})\cos(\Delta T_r) + T_r k\omega_x x_o \sin\chi\cos^2(\frac{\theta}{2})\sin(\Delta T_r)} \tag{6.13}$$

This expression can be expanded to second order in x_o as $a/(b+\epsilon)$ about $\epsilon = 0$. This gives

$$\Gamma(\Delta + k\omega_x x_o \sin\chi) = \Gamma(\Delta) - \Gamma(\Delta)\frac{T_r k\omega_x x_o \sin\chi\cos^2(\frac{\theta}{2})\sin(\Delta T_r)}{\cosh\left(\frac{T_r}{2\tau}\right) - \cos^2(\frac{\theta}{2})\cos(\Delta T_r)} \tag{6.14}$$

Using this expression for the scattering rate in the integrand for the stochastic heating term, the second term vanishes since $\int_0^{2\pi}\sin\chi d\chi = 0$, and we get

$$S(E) = \frac{\hbar^2 k^2}{2m}(1+\xi)\Gamma(\Delta) \tag{6.15}$$

6.5.2 Small oscillation limit of damping term

Starting from equation 6.6 and applying the identical approximation to the cycle averaged scattering rate, we get

$$\beta(E) = \frac{\hbar k}{2\pi\omega_x x_o}\int_0^{2\pi} d\chi \sin\chi\left(\Gamma(\Delta) - \Gamma(\Delta)\frac{T_r k\omega_x x_o \sin\chi\cos^2(\frac{\theta}{2})\sin(\Delta T_r)}{\cosh\left(\frac{T_r}{2\tau}\right) - \cos^2(\frac{\theta}{2})\cos(\Delta T_r)}\right) \tag{6.16}$$

The first term integrates to 0, and the second term goes as $\int_0^{2\pi} \sin^2\chi d\chi = \pi$, which gives us the final expression for the damping coefficient in the small amplitude limit as

$$\beta(E) = -\frac{\hbar k^2}{2} T_r \Gamma(\Delta) \frac{\cos^2(\frac{\theta}{2})\sin(\Delta T_r)}{\cosh\left(\frac{T_r}{2\tau}\right) - \cos^2(\frac{\theta}{2})\cos(\Delta T_r)} \tag{6.17}$$

6.5.3 Temperature expression and limits

Putting the two expressions above together with equation 6.9, we can form an expression for the steady state temperature of the ion while being cooled by the mode locked laser.

$$T_D = \frac{\hbar}{2k_B T_r}(1+\xi)\Big(\cot(\Delta T_r) - \frac{\cosh\left(\frac{T_r}{2\tau}\right)}{\cos^2(\frac{\theta}{2})\sin(\Delta T_r)}\Big) \tag{6.18}$$

The detuning red of resonance that minimizes the temperature of the ion can readily be solved for by setting $\frac{dT_D}{d\Delta} = 0$ and solving for the detuning, which gives

$$\Delta_{opt} = -\frac{1}{T_r}\arccos\left(\frac{\cos^2(\frac{\theta}{2})}{\cosh\left(\frac{T_r}{2\tau}\right)}\right) \tag{6.19}$$

We can make equivalence arguments about mode locked lasers and continuous wave lasers and take appropriate limits of the above equations to ensure that they reduce to the well known formulas for the Doppler temperature and optimal detuning for laser cooling in the continuous wave limit.

In the limit where the repetition period of the mode locked laser tends to 0 (comb tooth spacing, $f_{rep} \to \infty$) and the pulse area tends to $\theta^2 \to s_o T_r^2/2\tau^2$. In both of these limits, the Doppler temperature reduces to $T_D \to \hbar/(2k_B\tau)$ and the optimal detuning reduces to $\Delta_{opt} \to -1/2\tau$, precisely the result obtained in the continuous wave limit.

CHAPTER 7

Mode-locked lasers for background-free qubit state readout

As quantum processors continue to scale to larger number of qubits, it is natural that many system components will be miniaturized along the way. One such system is the photon collection and detection systems in trapped ion quantum processors, which in many experimental setups are large and bulky. Current research aims to forego the large ex-vacuo imaging for trap integrated photon detection systems, such as avalanche photodiodes (APDs) and superconducting nanowire single photon detectors (SNSPDs) [TVM21]. These detectors would be integrated into the surface of a 2D surface trap, and ions would reside directly above the detector during qubit state readout. The close proximity to the detector ($\sim 100\mu$m) provides large solid angle photon detection, but the system lacks the large imaging setup used for spatially filtering background scatter from the excitation lasers.

Other optical cycling schemes have been proposed where the detected fluorescence is at a different wavelength than the excitation lasers, which is limited to ions with low lying D_J states [LAS12, HSC08]. These schemes suffer from reduced collection rate of detection photons while still being subject to the same off resonant errors. In the case of Ref. [HSC08], large amounts of laser power (~ 0.25 W) are needed to quickly drive an electric quadrupole transition, a roadblock for the scheme as a scalable solution.

A potential solution to this background scatter is the use of temporal filtering of the excitation light, instead of spatial filtering [BN97]. If excitation on the detection transition can occur in a period substantially shorter than the excited state lifetime, then the excitation can occur periodically in pulses, with photon detection and counting only occurring during

the period between excitation pulses when the laser light is not present. The spontaneous decay rate of excited states used for detection of trapped ion qubits are typically of order 100 MHz, making use of standard optical devices such as acousto-optic modulators for fast excitation difficult. Instead of modulated CW lasers, we can use a resonant mode-locked laser for the fast excitation with pulse width $\mathcal{O}(1\text{ps})$ and pulse separation $\mathcal{O}(10\text{ns})$ that is suitable for efficient excitation and high duty cycle photon detection.

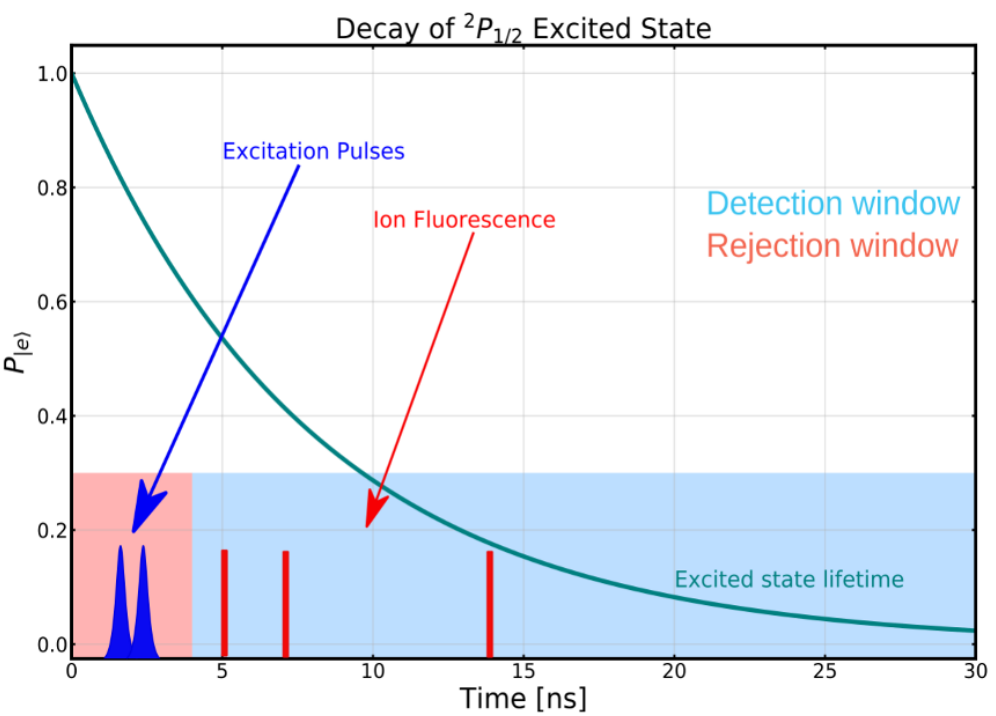

Figure 7.1: Time domain picture of background free state detection scheme. The excitation pulses (blue) enter the trap, excite the ion, and leave before the ion spontaneously emits. After the pulses leave, we collect and count photons emitted by the ion (maximum of 1 per excitation pulse) until the next excitation pulse arrives. The probability of finding the ion in the excited state as a function of time is shown in green following a full excitation to $|e\rangle$.

The essence of the background free state detection with mode-locked lasers is shown in Figure 7.1. Ground state population is excited near $t = 0$ by a pulse or pulse pair from the mode-locked laser, after which spontaneous emission can occur. If the spontaneous emission event occurs in the dead time between excitation pulses, it is most likely that the photon came from the ion and not from the excitation laser. Photons that are detected near the time when the pulse was in the ion trap region are rejected and filtered out. This filtering

could be accomplished by gating a PMT signal in phase with the repetition rate of the mode-locked laser, such that no photon clicks are registered while the pulse is present in the trap. Instead, we utilize a time correlated single photon counter (TCSPC) that can time tag photon arrival times with 10 ps precision with respect to a periodic trigger signal. This device will register all collected photons and allow for temporal filtering of the photons based on their arrival time relative to a trigger from the mode-locked laser. The device takes two inputs: a reference clock and the photon signals to be time tagged. The TCSPC [1]. will begin its time tagging clock once it receives a trigger from the reference clock, and time stamp signals it receives from the photon detector until the next clock trigger occurs.

The mode locked laser we use is a Spectra Physics Tsunami laser oscillator operating at 740 nm. The pulses from the laser are frequency doubled to 369.5 nm by single passing through a critically phase matched LBO crystal, and subsequently directed through a single pass AOM and directed to the ion via single mode fiber. During the direct hyperfine qubit readout section outlined below, the 740 nm pulses are first passed through the Mach-Zehnder interferometer before frequency doubling.

We want to reference the photon arrival times to the mode lock laser pulse repetition rate, so a small amount of the 740 nm mode locked laser light is focused onto a photodiode with 1 GHz bandwidth, and the signal is sent as the clock to the TCSPC. The remaining pulsed is light frequency doubled to $\sim$ 369 nm and delivered to the ion. The ion and background laser scatter at 369 nm is imaged onto a photon counting PMT [2] by an off the shelf laser focusing objective [3]. When the PMT successfully detects a photon, it outputs TTL pulses 10 ns in length. We measure the timing jitter of the produced TTL pulses by observing the spread in photon arrival times due to the pulsed laser alone. Since the laser pulse duration of 10 ps is equivalent to the timing resolution of the TCSPC (10 ps), the pulses are effectively delta function impulses we can use to measure the response of the PMT. The timing jitter is

[1] PicoQuant TimeHarp 260p

[2] Hamamatsu H10682-210

[3] Special Optics 54-17-29-λ

found to be approximately 400 ps, determined by estimating the full width half maximum of the observed signal due to the pulses alone (see black trace in Figure 7.2. The timing jitter is often referred to in literature as the transient time spread (TTS).

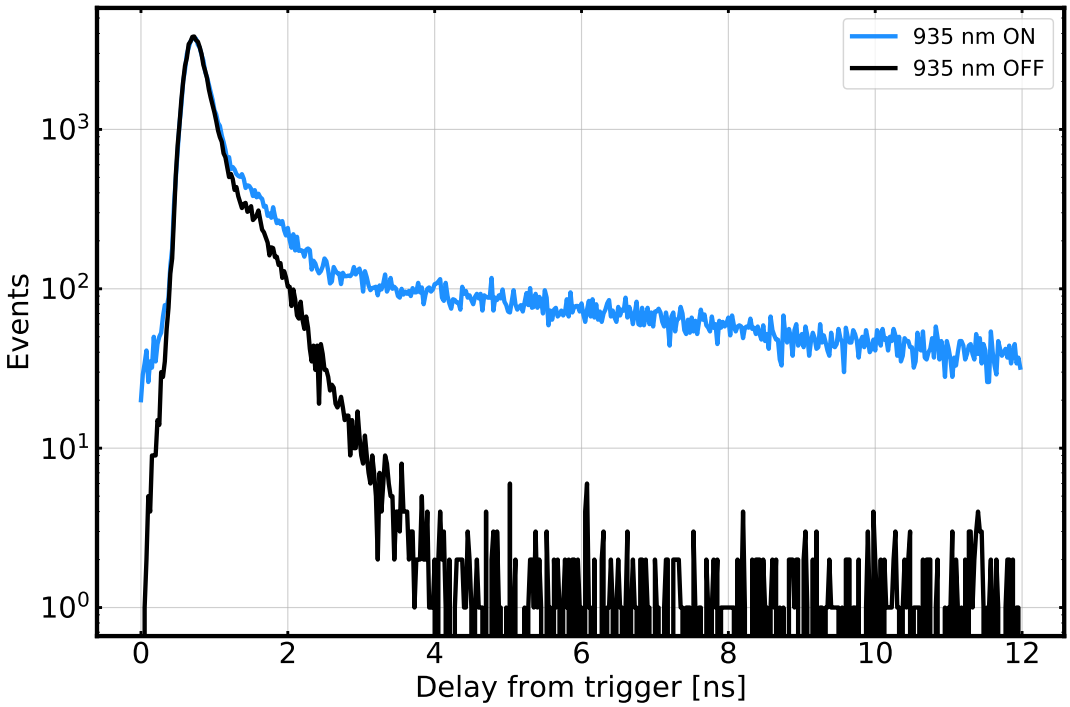

Figure 7.2: Example traces from the TCSPC. A single trapped $^{174}Yb^+$ ion is laser cooled with the mode locked laser, and the detected photons are timetagged by the TCSPC. Example traces where the 935 nm laser is on/off are shown above, the off situation is meant to emulate the electron shelved qubit by leaving population stranded in the $^2D_{3/2}$.

We perform initial characterization of the system with a trapped $^{174}Yb^+$ ion as seen in Figure 7.2. In the trace without the repump laser on, the prompt scatter at t $\approx$ 1 ns is due to the mode locked laser scatter, and by t = 4 ns the detected counts are dominated by the dark counts of the PMT ($\sim$40 Hz). With the repump laser on, the same incident laser scatter is observed followed by the exponential decay of the excited state with lifetime $\tau = 8.12$ ns [OHM09]. Standard time tagging of photons by our FPGA system would contain no phase information about the arrival times with respect to the arrival of the mode locked laser pulses, so we wouldnt be able to distinguish pulsed laser photons from ion produced

photons. With this temporal information provided by the TCSPC, we can apply a temporal filter that chooses which region of time relative to the trigger to count photons for qubit state readout.

7.1 Direct hyperfine qubit readout

Continuous wave laser readout of a nuclear spin 1/2 hyperfine qubit can be performed on the closed cycling transition $^2\mathrm{S}_{1/2}\ |F=1\rangle \rightarrow {}^2\mathrm{P}^o_{1/2}\ |F=0\rangle$, which works well due to the large hyperfine splittings in the $^2\mathrm{S}_{1/2}$ and $^2\mathrm{P}^o_{1/2}$ relative to the natural linewdith of the transition. The mode-locked laser we use has a pulse width of $\tau_p = 10$ ps, corresponding to a bandwidth of ~ 100 GHz, which will drive all allowed transitions between the $^2\mathrm{S}_{1/2}$ and $^2\mathrm{P}^o_{1/2}$. Thus if we attempted just to use the mode locked laser for state detection, both the $|1\rangle_g$ and $|0\rangle_g$ states would produce approximately the same number of laser induced fluorescence photons, making the states indistinguishable measuring this way.

To circumvent this problem, a simple pulse shaping scheme can be used to coherently drive the desired transition and coherently suppress the undesired ones. This is achieved by passing the mode locked laser pulses through a single pass, unbalanced Mach-Zehnder interferometer, effectively turning each 10 ps pulse into two 10 ps pulses separated in time by $\delta t = \delta L/c$, where δL is the optical path length difference between the two arms of the interferometer. The alteration of the mode-locked laser pulse train by the interferometer can be thought of as an optical frequency filter acting on the broadband comb spectrum. If we imagine an optical frequency comb with infinite bandwidth, and pass that through the aforementioned unbalanced Mach-Zehnder inteferometer, the output ports of the interferometer will contain copies of the input with the optical spectrum modulated by $\cos\left(\frac{c}{\delta L} + \phi_i\right)^2$ and $\sin\left(\frac{c}{\delta L} + \phi_i\right)^2$. The phase difference between the two ports, ϕ_i, is controlled by altering the optical phase difference between the two arms.

As a first test with the interferometer, we perform a resonant Ramsey experiment on the $^2\mathrm{S}_{1/2} \leftrightarrow {}^2\mathrm{P}^o_{1/2}$ transition of a single trapped $^{174}\mathrm{Yb}^+$ ion. The center frequency of the laser is

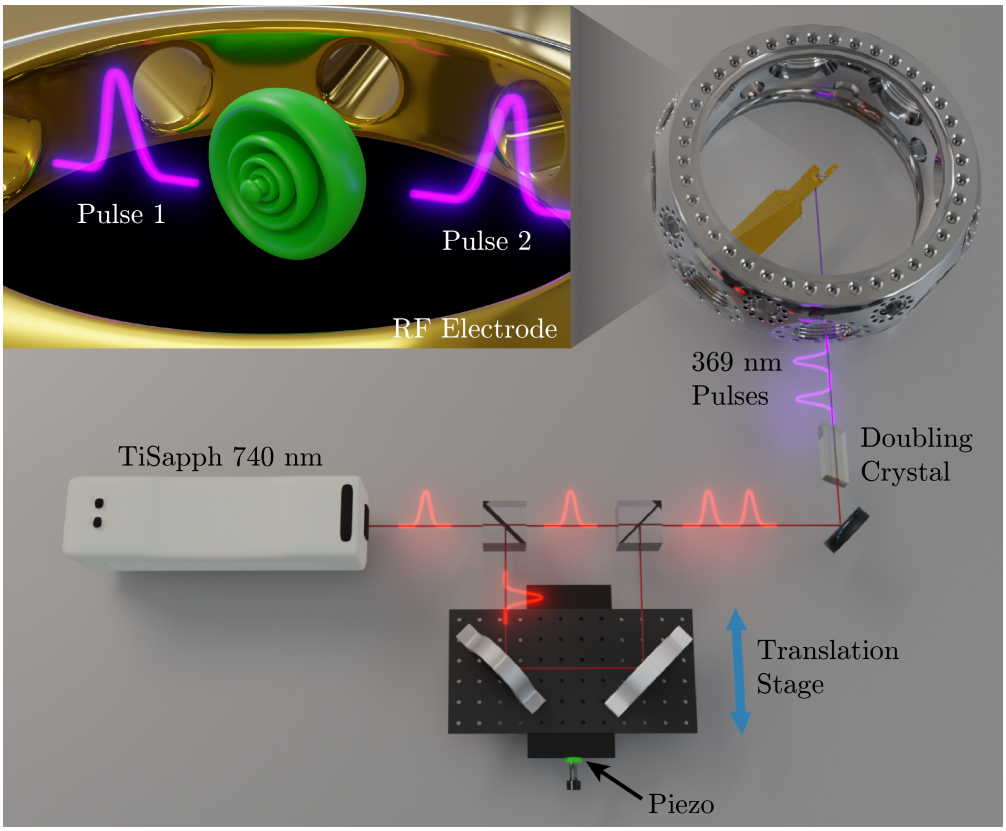

Figure 7.3: Simplified diagram of the experimental setup for direct detection of the hyperfine qubit with mode locked laser pulses.

first tuned to resonance by illuminating the ion with single pulses, and adjusting the center frequency to maximize the laser fluorescence via direct Doppler cooling with a single comb tooth [IRJ18]. Pulse pairs separated in time by $\approx$ 237 ps are then let into the trap, with all continuous wave 369 nm laser light removed. Photons are timetagged by the TCSPC, and background scatter from the laser is filtered out by only recording the number of photons detected between 4 ns and T_{rep} =12.5 ns. Voltage applied to a piezoelectric actuator in the interferometer changes the pulse pair temporal separation by 10s of attoseconds. Resulting Ramsey fringes are shown in Figure 7.4.

In $^{171}Yb^{+}$, we can think of the four hyperfine manifolds of the $^{2}S_{1/2}$ and $^{2}P^{o}_{1/2}$ states as a simple four level model in order to determine what the delay time between pulses should be. We will assume that the three allowed transitions (all except $^{2}S_{1/2}\ |F=0\rangle \leftrightarrow {}^{2}P^{o}_{1/2}\ |F=0\rangle$) here are approximately uncoupled two level systems, which is to say that the dynamics of each

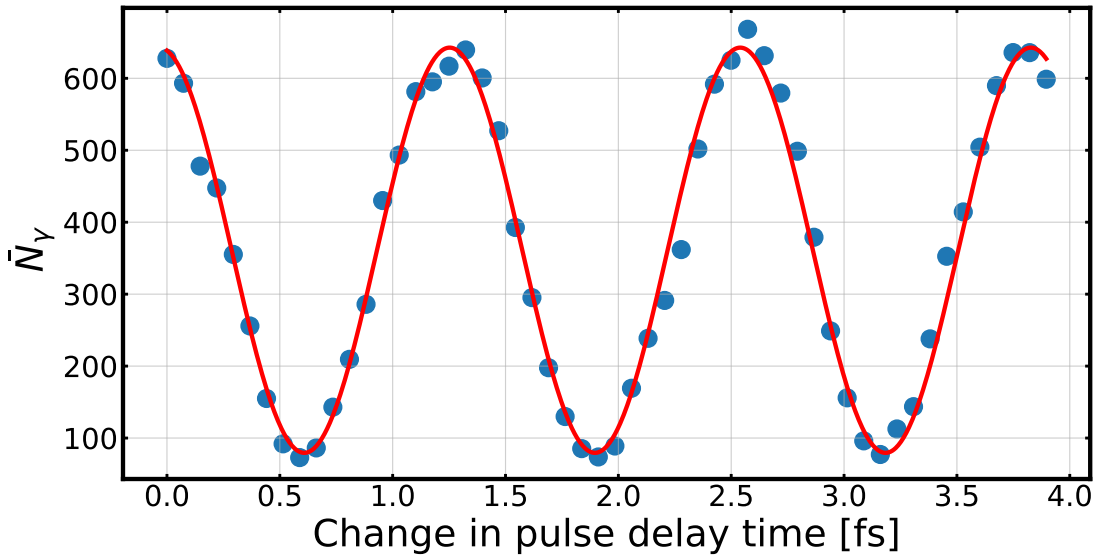

Figure 7.4: Optical Ramsey fringe of a single trapped $^{174}Yb^+$ ion. The vertical axis is the average number of background free detected photons emitted from the ion in a 3000 attempts of 80 μs interrogation with the pulsed laser.

system are independent of each other. The hyperfine splittings are, approximately, $\omega_{HFS} = 2\pi \times 12.6$ GHz and $\omega_{HFP} = 2\pi \times 2.1$ GHz. If we are rotating at $\omega_o = \omega_{P,F=0} - \omega_{S,F=1}$ and the qubit was prepared in some arbitrary superposition, then after the first pulse hits the ion all allowed transitions are driven. For this to remain coherent (not affected by spontaneous emission), we want the delay between the pulses to be much shorter than the excited state lifetime, so $\delta t \ll 8.12$ ns. If that condition is held, then by the time the second pulse interacts with the ion the superpositions of the undesired excitations will have acquired phases $e^{i\omega_{HFP}\delta t}$ ($^2S_{1/2}\ |F=1\rangle \leftrightarrow {}^2P^o_{1/2}\ |F=1\rangle$) and $e^{i(\omega_{HFP}+\omega_{HFS})\delta t}$ ($^2S_{1/2}\ |F=0\rangle \leftrightarrow {}^2P^o_{1/2}\ |F=1\rangle$), while the desired transition in the rotating frame has acquired no additional phase.

If the delay time is chosen appropriately, we can make it so that the accumulated phase of the desired superposition is zero, while the two undesired superpositions accumulate a minus sign. This is equivalent to the condition that $\omega_{HFP}\delta t = (2n+1)\pi$ and $(\omega_{HFS} + \omega_{HFP})\delta t = (2m+1)\pi$ for any two integers $n, m \in \mathcal{Z}$. Due to the fact that the hyperfine splittings are near integer multiples of each other ($\omega_{HFS}/\omega_{HFP} = 6.006$), with only a two pulse sequence we can satisfy the above conditions by waiting for a time $\delta t = 237$ ps.

This logic allows for identifying the coarse delay time between the pulse pairs necessary to ensure that the relative phase relationship of the desired and undesired transitions is met ($\delta\phi = \pi$), but the fine optical phase difference between the pulses still needs to be adjusted. Setting the coarse delay correctly ensures that the superpositions have the correct relative phase, but setting the optical phase shift correctly ensures that the desired transition experiences a coherent excitation and the undesired ones experience a coherent suppression of excitation. As in Figure 7.4, we want to fine tune the delay so that the desired cycling transition is at the top of a fringe, while the two undesired transitions are simultaneously at the bottom of a fringe.

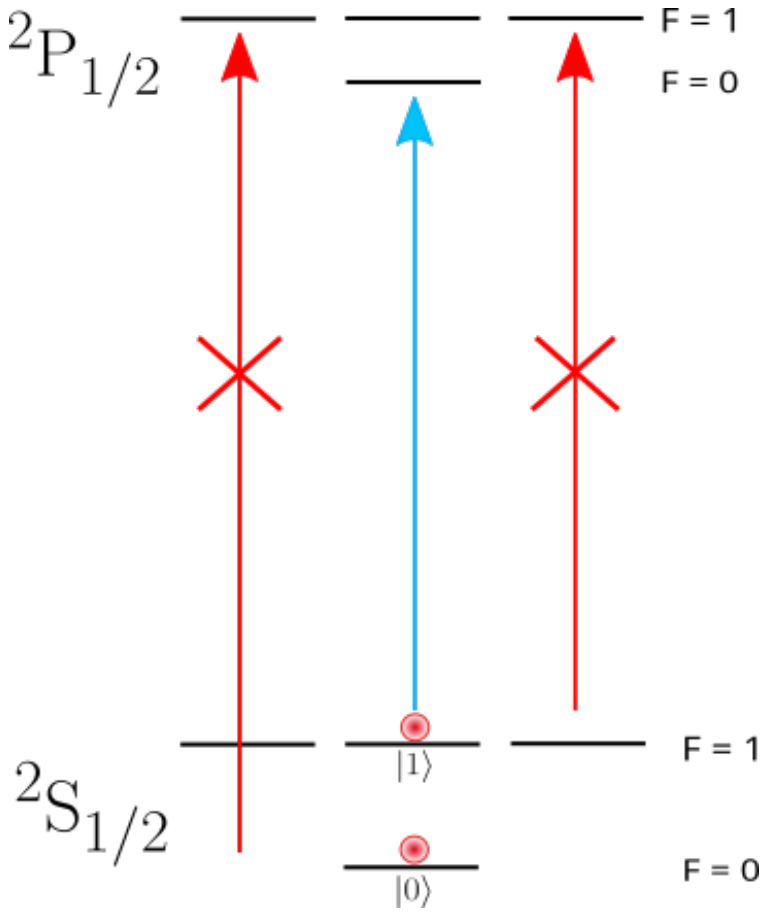

Figure 7.5: Diagram of three (approximately) uncoupled two level systems. The undesired transitions are indicated with red arrowd, where the desired transtion is in blue.

An initial experiment we developed to set the optical phase between pulse pairs began with state preparation of both $|0\rangle_g$ and $|1\rangle_g$, interrogated the ion for a variable amount

of time by pulse pairs at a fixed pulse separation, and then measured the qubit population at the end. If the optical phase difference is set appropriately, excitations on the $^2\mathrm{S}_{1/2}\ |F=0\rangle \rightarrow {}^2\mathrm{P}^o_{1/2}\ |F=1\rangle$ and $^2\mathrm{S}_{1/2}\ |F=1\rangle \rightarrow {}^2\mathrm{P}^o_{1/2}\ |F=1\rangle$ transitions should be suppressed. Therefore, population prepared in $|0\rangle_g$ should remain in $|0\rangle_g$ and population prepared in $|1\rangle_g$ should remain in the $^2\mathrm{S}_{1/2}\ |F=1\rangle$ manifold, as scattering on the $^2\mathrm{S}_{1/2}\ |F=1\rangle \rightarrow {}^2\mathrm{P}^o_{1/2}\ |F=0\rangle$ transition is what we desire and will mix popuation throughout the manifold. Example traces are shown in Figure 7.6 for different interferometer settings near 237 ps.

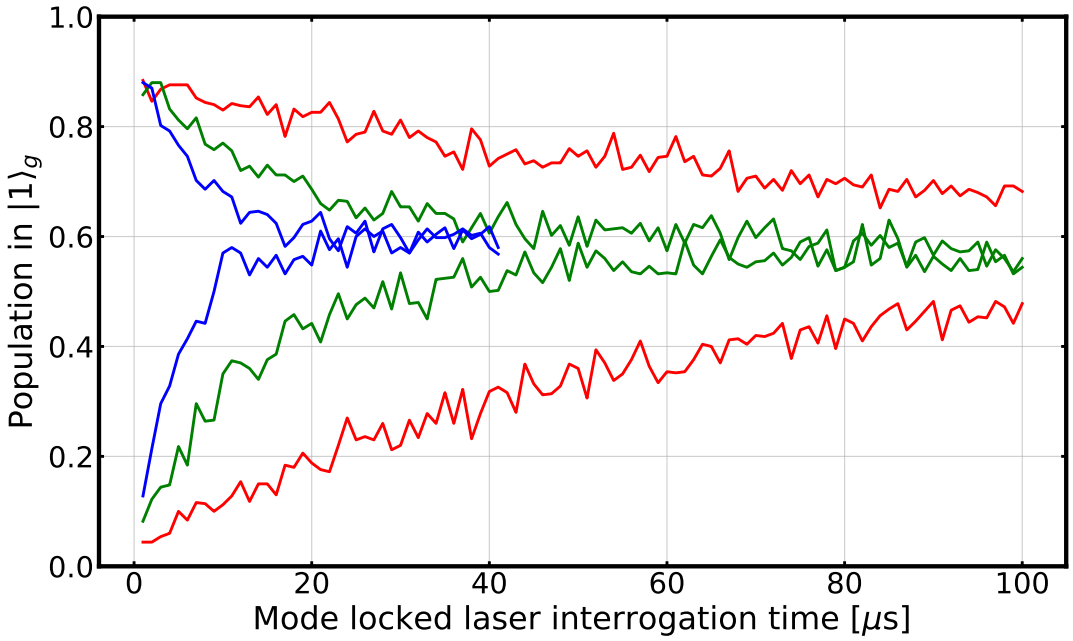

Figure 7.6: Example traces from mode locked laser population mixing experiment. Each color represents a different voltage setting on the interferometer. Traces that begin near 0 had $|0\rangle_g$ as the initial state, and traces that begin near 1 has $|1\rangle_g$ as the initial state. As the interrogation time increases, so does the state mixing.

This experiment can be performed at various piezo voltages. The decay in contrast between the two states as a function of time is fit to an exponential decay at each piezo voltage. As we scan the interferometer over a full free spectral range (1 FSR = 4.21 GHz), we see two optimal settings of the optical phase difference, corresponding to nearly equivalent

settings where the undesired transitions are suppressed, and the desired one is excited. In practice, the interferometer distance is locked by passing a 760 nm laser through at a slightly different elevation than the pulsed laser, and locking the interferometer length to the side of an interference fringe. The length is locked by feeding back to the piezo, and the length is scanned by adjusting the wavemeter software lock set point of the 760 nm laser.

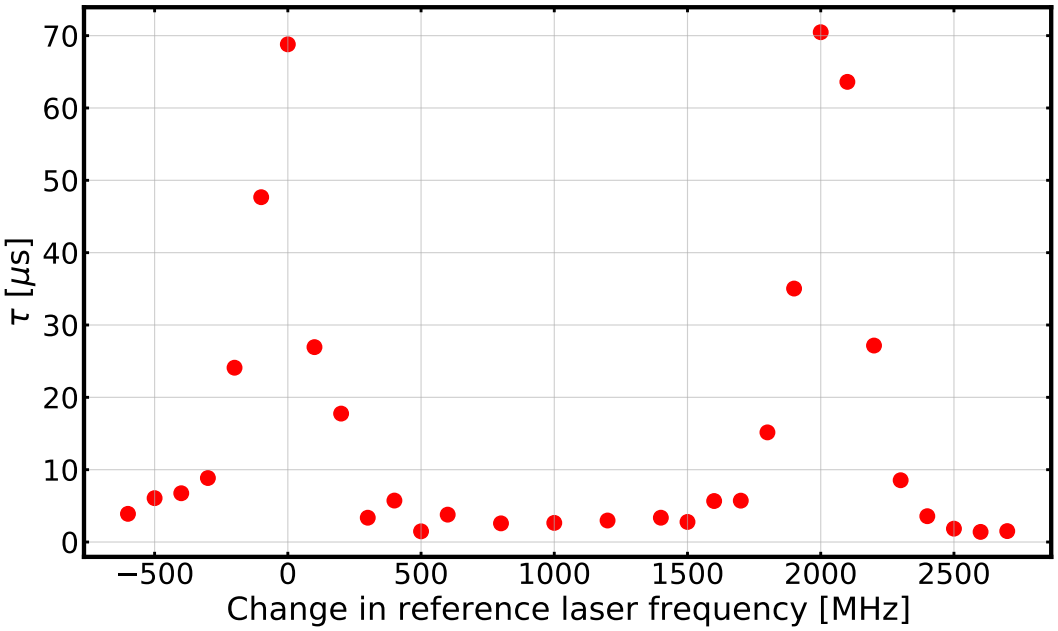

Figure 7.7: Contrast decay time constant (τ) as a function of 760 nm laser lock frequency, referenced to a lock point of minimal state mixing. The IR laser only needs to be changed by ~ 2.1 GHz to change the frequency domain dynamics of the pulse pairs delivered to the ions because the IR ML laser pulses are passed through the interferometer, and then frequency doubled, resulting in a factor of 2.

7.1.1 Results

With the interferometer set appropriately, we can begin to perform direct detection of the qubit with mode locked laser pulses. The initial experiment we run is to observe the TCSPC time traces due to illumination by the mode-locked laser after preparation of the qubit basis states ($|1\rangle_g$ and $|0\rangle_g$), with the interferometer locked at the appropriate phase. If we have

any hope of state discrimination, we must be able to distinguish between the trace produced after $|0\rangle_g$ preparation and the trace produced after $|1\rangle_g$ preparation. The accumulation of many such timetraces is shown in Figure 7.8. Although we do have clear discrimination

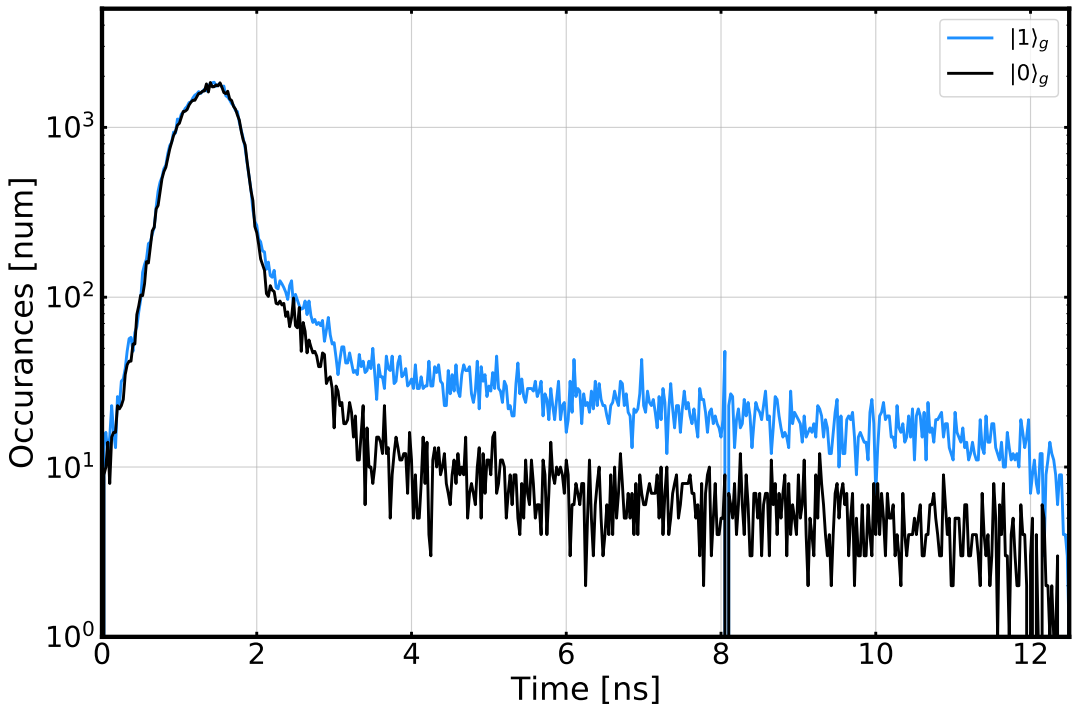

Figure 7.8: TCSPC time traces resulting from multiple preparations and interrogations of the $|1\rangle_g$ and $|0\rangle_g$ states, separately.

between the $|1\rangle_g$ and $|0\rangle_g$ state in Figure 7.8, it is also clear that the trace for $|0\rangle_g$ does not bottom out at the PMT dark counts as the traces in Figure 7.2 did for the "dark" ion. This is due to the fact that even with the interferometer set optimally, we still experience a significant number of scattered photons on the undesired transitions.

We can directly observe the effect of the interferometer setting on the qubit state discrimination by detecting Rabi flopping of the qubit with the pulse pairs in two instances: with the interferometer set at the correct phase (desired transition at top of a fringe, undesired transitions at bottom of fringes), and with the interferometer at the least optimal phase (desired bottom of fringe, undesired top of fringes).

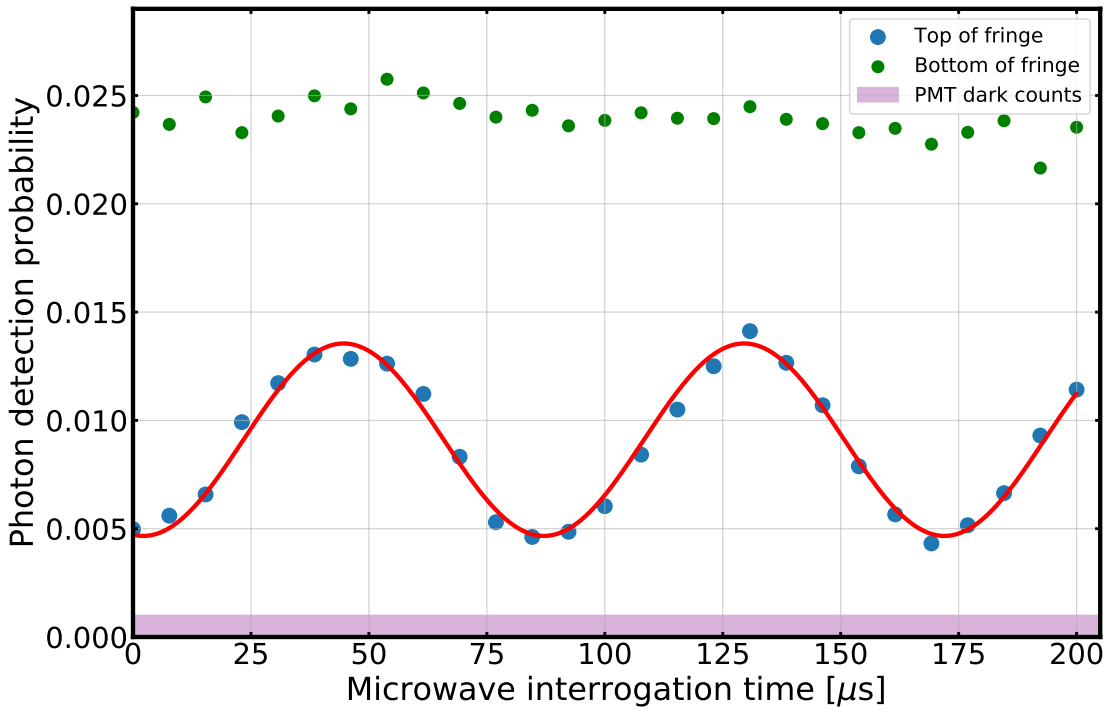

Figure 7.9: Direct detection of Rabi flopping the ground state qubit with resonant mode locked laser pulse pairs. The vertical axis is the average probability of detecting a photon on a single experiment. The mode-locked laser interrogation time for detection is set to $t = 25\mu$s.

The data is taken by recording timetags from the TCSPC on each experiment, and counting how many occur between 2.5 ns and 12.6 ns with respect to the trigger pulse. Each data point is repeated 10000 times, with the total number of detection photons returned. Single shot state detection of the qubit is not performed because we cannot collect enough state dependent scattered photons before state mixing occurs.

Rotations of the qubit are clearly observed when the interferometer phase is set correctly. The baseline of the Rabi curve does not bottom out at the PMT dark counts due to finite state mixing, as discussed earlier. When the interferometer phase is set $\delta\phi = \pm\pi$ from the optimal setting, no qubit rotations are observed due to poor state discrimination. The overall number of photons scattered is also higher because all ground state levels produce laser-induced fluorescence.

7.1.2 Ramsey fringes and approximate two level systems

To see more precisely what is happening to the three allowed transitions as the optical phase difference of the two pulses is changed, we developed a way to observe each of the three fringes separately, similar to the fringe obtained in Figure 7.4. To isolate the three, approximately separate two level systems relevant for for direct detection of the $^{171}Yb^{+}$ hyperfine qubit, three different schemes for state preparation and readout (with cw lasers) before and after the mode locked Ramsey zones are utilized. For each, we limit the pulsed laser interrogation duration and strength to the regime where approximately 1 photon is emitted since subsequent emission can mix the qubit states.

State preparation of the desired ground state (either $|0\rangle_g$ or $|1\rangle_g$) is followed by a short ($\approx 4\mu s$) interrogation of low pulse area Ramsey pairs prepared by a fixed fine delay of the Mach-Zehnder interferometer. Standard state detection is then performed to reveal any population residing in the $^2S_{1/2}\ |F=1\rangle$ manifold. This sequence is repeated as the delay stage piezo voltage is scanned to produce the individual Ramsey fringes. Depending on which Ramsey fringe is being probed, an additional microwave π pulse may be used before state readout to reorganize population in the ground state. For all fringes, the mode locked laser is π-polarized so that only $\delta m_F = 0$ transitions are driven.

The schemes for acquiring the three separate fringes are outlined below, each designed to ideally leave the electron in the $^2S_{1/2}\ |F=1\rangle$ manifold 2/3 of the time at the top of a fringe, while ideal execution at the bottom of a fringe will leave the population in $|0\rangle_g$. These values are then used to convert measured populations to excitation probability.

- $|0\rangle_g \rightarrow {}^2P^o_{1/2}\ |F=1\rangle$: the only allowed transition is to the $^2P^o_{1/2}\ |F=1, m_F=0\rangle$ state. Spontaneous emission from this state will distribute 1/3 of the population to $|0\rangle_g$, and 2/3 to the $^2S_{1/2}\ |F=1\rangle$ manifold.

- $^2S_{1/2}\ |F=1\rangle \rightarrow {}^2P^o_{1/2}\ |F=1\rangle$: the $^2S_{1/2}\ |F=1, m_F=-1\rangle$ state is prepared initially. The mode locked laser can excite the electron to the $^2P^o_{1/2}\ |F=1, m_F=-1\rangle$ state, after which the population is evenly distributed amongst the $^2S_{1/2}\ |F=1, m_F=-1\rangle$,

$|1\rangle_g$, and $|0\rangle_g$ states. Before state readout, a microwave π-pulse is applied between the $|0\rangle_g$ and $^2\mathrm{S}_{1/2}$ $|F=1, m_F=-1\rangle$ states.

- $|1\rangle_g \rightarrow {}^2\mathrm{P}^o_{1/2}$ $|F=0\rangle$: $|1\rangle_g$ is prepared initially, and the only allowed transition is the one of interest. Successful excitation and subsequent spontaneous emission will leave the electron population evenly distributed amongst the $^2\mathrm{S}_{1/2}$ $|F=1\rangle$ states. Before state readout, a microwave π-pulse is applied on the $m_F = 0 \rightarrow m_F = 0$ transition.

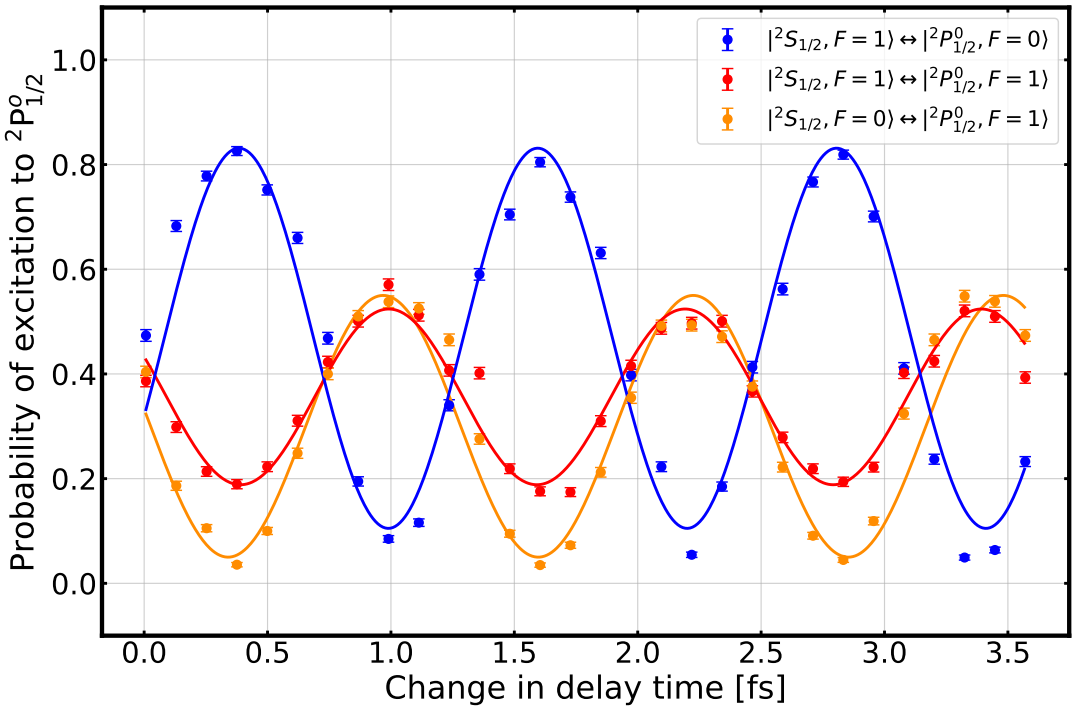

Figure 7.10: Pulsed Ramsey experiment of the individual allowed $^2\mathrm{S}_{1/2} \leftrightarrow {}^2\mathrm{P}^o_{1/2}$ hyperfine transitions. The coarse delay between the pulses is set to approximately 237 ps, corresponding to an interferometer free spectral range of 4.21 GHz. As can be seen here, the target transition (blue) is nearly exactly π out of phase with the transitions we wish to suppress (red, orange). By locking the interferometer at a location where the $^2\mathrm{P}^o_{1/2}$ is maximally excited to the $F=0$, and minimally to the $F=1$, we can perform state selective readout of the qubit with these pulses.

An example acquisition of the three Ramsey fringes with the coarse pulse delay set to 237 ps is shown in Figure 7.10. The phase shift between the electron wave packets is clearly

observable, and validates our choice of coarse delay time.

7.2 Shelved hyperfine qubit readout

Instead of reading out the ground state qubit populations with the mode locked laser immediately following state preparation, we can first shelve the population in $|1\rangle_g$ to the long lived $^2F^o_{7/2}$ state, as described in other chapters. By mapping population in $|1\rangle_g$ to a separate electronic state 100's of THz detuned from our cycling transition, we can perform state readout with the mode locked laser without pulse shaping and directly interrogate the cycling transition. Higher laser intensity can be used now to scatter more state dependent photons since we are no longer concerned with population mixing, all while still taking advantage of the background free readout provided by this scheme.

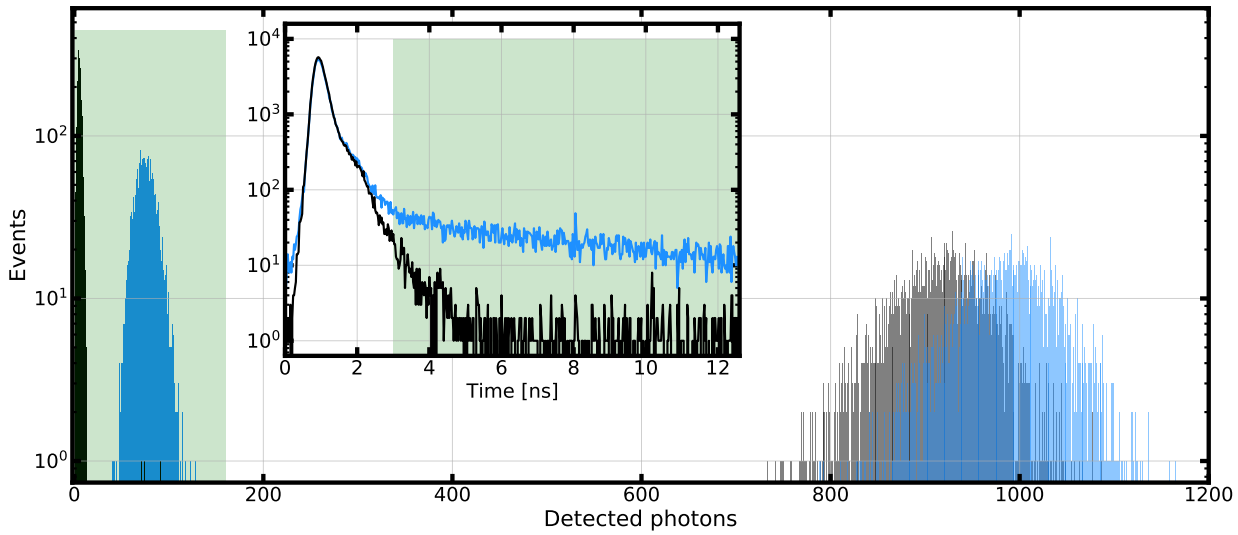

Figure 7.11: Comparison of electron shelved state detection with a mode locked laser with and without temporal filtering. The green shaded region on the inset indicates the photons that were used for the histograms on the left.

In this experiment the ion is either prepared in the $|1\rangle_g$ or $|0\rangle_g$ state, after which the $^2S_{1/2} \leftrightarrow {}^2D_{5/2}$ is driven at 411 nm to shelve the $|1\rangle_g$ population to the $^2F^o_{7/2}$. After shelving, the ion is illuminated with the resonant mode locked laser and 935 nm light. Time traces are collected by the TCSPC and offloaded at the end of an experiment for analysis. To illustrate

the power of temporal filtering, Figure 7.11 shows histograms of the same timetraces: one where temporal filtering is not employed, the other where the photon counting window is chosen to eliminate photons from the mode locked laser.

Without temporal filtering, the histograms exhibit significant overlap, yielding a low state preparation and measurement fidelity of $\mathcal{F} = 0.76 \pm 0.01$. Instead, if we only count the photons that arrive from t = 3 ns until the next trigger, the background scatter from the mode locked laser is filtered out and the state preparation and measurement fidelity is increased to $\mathcal{F} = 0.9993^{+3}_{-6}$.

To illustrate the use of this detection technique, we detect ground state qubit Rabi flopping in the presence of large amounts of background scatter. After electorn shelving, we detect the remaining population in $|0\rangle_g$ with resonant pulses from the mode-locked laser.

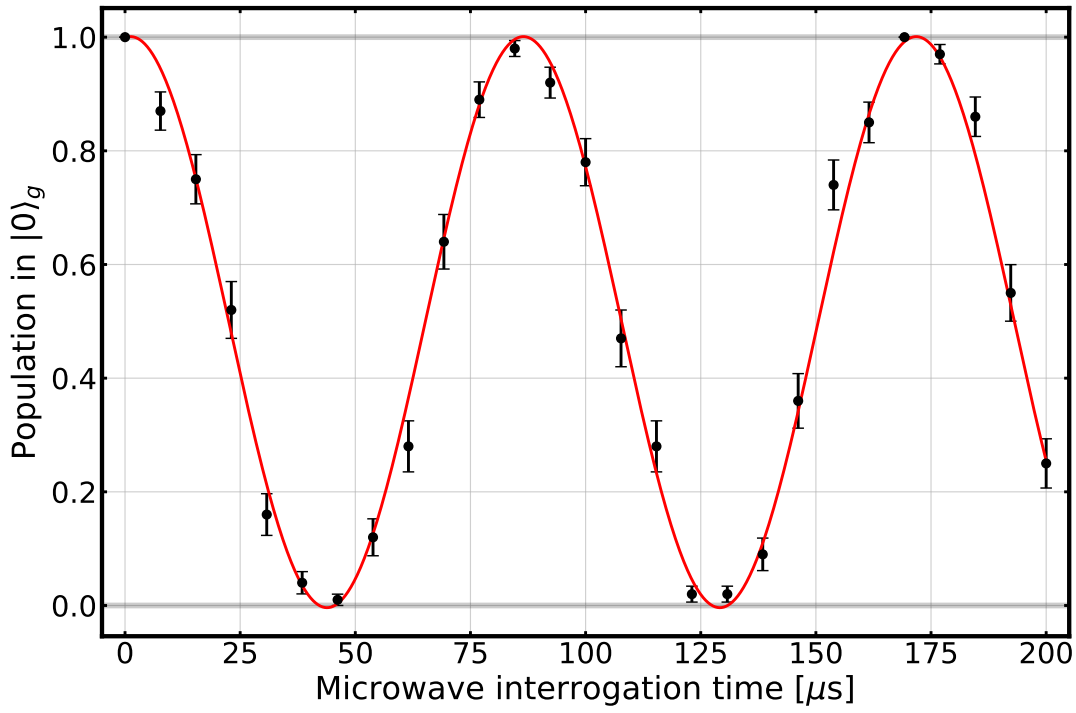

Figure 7.12: Rabi flopping observed by a combination of electron shelving and background free state detection with the mode locked laser.

CHAPTER 8

Electron Shelving in Yb^+

Electron shelving is a technique for readout of a quantum state in multi level atoms. In quantum information related experiments, it involves the transfer of population in a computational basis state to an auxiliary state that is outside the cycling transition used for laser induced fluorescence. After population transfer, if the qubit projects into the unshelved state, it will scatter many photons during laser induced fluorescence. Conversely, if the qubit projects into the shelved state, it resides outside the cylcing transition and produces no photons. Electron shelving detection of a trapped ion was first demonstrated in [NSD86] with a single trapped Ba^+ ion.

8.1 Electron shelving

The essence of electron shelving of trapped ions is to take quantum information encoded somewhere in an atom, and "shelve" it to a different electronic state that does not scatter photons during the readout process. Two common ways that this is achieved:

- Shelve to a detuned hyperfine state that, due to polarization and frequency selectivity, does not scatter photons during the readout process (e.g. Be^+, Mg^+). This is typically employed in ions lacking low lying metastable D states.
- Shelve to a long lived excited state that is optically separated from the cycling transition used for detection (e.g. Ca^+, Ba^+, Sr^+, Ra^+). The metastable state typically used is the $^2D_{5/2}$ state.

The advantage of shelved stated detection, as opposed to hyperfine selective readout in

$I = 1/2$ ions, is that transfer of population to a long lived state allows for longer periods of laser induced fluorescence.. As with any other method for qubit state readout, the detection process must be state selective and desirably high fidelity. So, we must have a way to selectively transfer one of the qubit states to the metastable manifold, after which laser induced fluorescence will reveal which computational basis state we projected into.

8.2 Electron shelving in $^{171}Yb^{+}$

8.2.1 A quick note on SPAM

In this chapter, we will be distinguishing between the two essential parts of a SPAM measurement: *state preparation* and *measurement*. The electron shelving scheme that will be described below is a method for *measurement*, not state preparation. The population transfer process will project the qubit, and transfer the population to the shelved state.

State preparation is the process through which we prepare the separate computational basis states, in this case $|1\rangle_g$ and $|0\rangle_g$. Many states outside of the qubit subspace will be used to perform the some aspect of qubit state preparation, but in the end an (ideally) pure electronic state will be prepared before the electron shelving process begins. With how well the electron shelving scheme in $^{171}Yb^{+}$ works, it turns out that this is the harder part of the SPAM measurement.

8.2.2 Shelving to the $^2D_{5/2}$

It is possible to utilize the low lying $^2D_{5/2}$ in $^{171}Yb^{+}$ as a shelved manifold, and has recently been demonstrated in [LRR21]. In other ions where the $^2D_{5/2}$ is the shelved manifold, the only decay paths are via an electric quadrupole coupling to the ground state and a magnetic dipole coupling to the $^2D_{3/2}$. Since both of these couplings are much weaker ($\lesssim$ Hz) than electric dipole couplings ($\sim$ MHz), the lifetime of the shelved manifold is generally long ($\sim$ seconds). This is not the case in Yb^{+}, though, due to the presence of the low lying $^2F^o_{7/2}$, which provides an electric dipole coupling decay pathway via spontaneous emission of a 3.4

μm photon.

The presence of the electric dipole pathway from the $^2\mathrm{F}^o_{7/2}$ causes the lifetime of the $^2\mathrm{D}_{5/2}$ to be 7.2 ms, and therefore a challenging pathway to electron shelving. In [LRR21], a state preparation and measurement fidelity of 99.8% was achieved via $^2\mathrm{D}_{5/2}$ electron shelving. The shelving was performed by concatenating a series of five π pulses on the $|0\rangle_g \rightarrow$ $^2\mathrm{D}_{5/2}$ $|F=2\rangle$ transition at 411 nm, with each pulse addressing a different magnetic sublevel in the hyperfine manifold. This was followed by 100 μs of Doppler cooling laser light to detect the remaining population in the ground state.

Just like standard $I = 1/2$ hyperfine qubit state detection, this method requires high numerical aperture lenses for light collection so that the detection time can be reduced for effective histogram separation and suppression of $^2\mathrm{D}_{5/2}$ spontaneous emission errors. It also adds the complication of necessitating fast and coherent optical qubit operations for electron shelving, which may be hard to scale to large multi-ion systems.

8.2.3 Shelving to the $^2\mathbf{F}^o_{7/2}$

Shelving to the $^2\mathrm{F}^o_{7/2}$ is achieved via incoherent narrow band optical pumping of the $|1\rangle_g$ state to the $^2\mathrm{F}^o_{7/2}$ via the $^2\mathrm{D}_{5/2}$ $|F=3\rangle$ at 411 nm. The method relies on the spontaneous emission of the $^2\mathrm{D}_{5/2}$ to the $^2\mathrm{F}^o_{7/2}$ for population transfer, so the speed limit is set by the $^2\mathrm{D}_{5/2}$ lifetime (7.2 ms) and branching to the $^2\mathrm{F}^o_{7/2}$ (0.83) [TRG97].

A benefit of using this transition in I = 1/2 ions is that the g-factors of $^2\mathrm{S}_{1/2}$ $|F=1\rangle$ and $^2\mathrm{D}_{5/2}$ $|F=3\rangle$ are both equal to 1. What this means is that to first order we cannot resolve transitions with the same change in magnetic quantum number m_F. The second order Zeeman effect will break this degeneracy, but this is of order kHz which we cannot resolve in our experiments. After the first scattered photon from $^2\mathrm{D}_{5/2}$ during population transfer, population that decays back to $^2\mathrm{S}_{1/2}$ $|F=1\rangle$ can reside in any of the magnetic sub-levels, but since $g_F(^2\mathrm{S}_{1/2}) = g_F(^2\mathrm{D}_{5/2})$, all transitions with the same Δm_F are nearly degenerate.

To see how long we need to optically pump to achieve the desired level of population transfer, we can look at some simple rate equations and develop them with increasing levels of complexity.

Basic three level model: We will assume this is a three level system, where the lowest state has an infinite lifetime, the shelved manifold has a lifetime of 5 years, and the excited state has a lifetime of $\tau_D = 7.2$ ms. The branching ratio of the excited state to the $^2S_{1/2}$ is 0.17, and to the $^2F^o_{7/2}$ is 0.83.

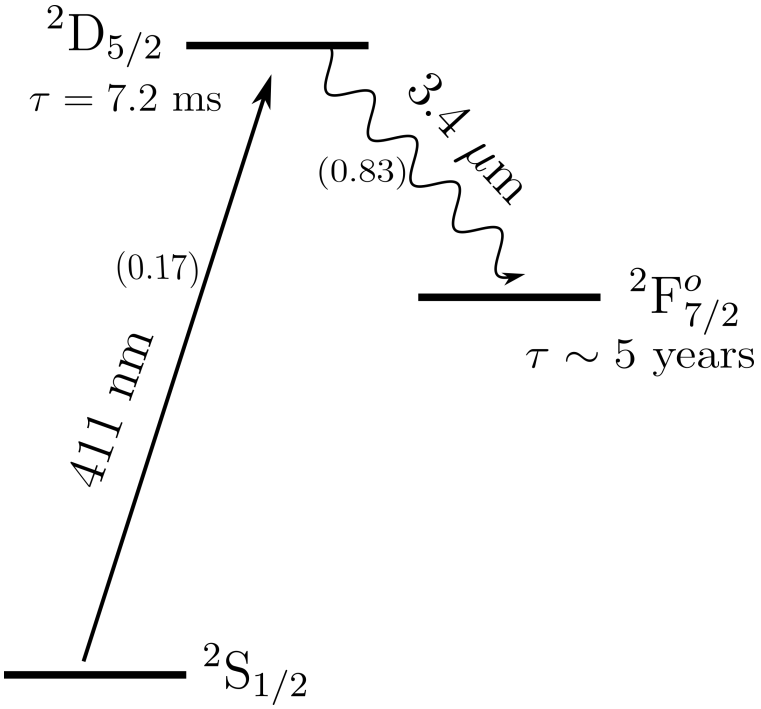

Figure 8.1: Simplified grotrian diagram of relevant states for electron shelving. The 411 nm laser drives population in the $^2S_{1/2}$ to the $^2D_{5/2}$, which can decay directly to the $^2F^o_{7/2}$ for long term storage.

If all population starts in the ground state, then the population in the shelved manifold will evolve as

$$\dot{p}_F = \gamma_D \zeta p_D \tag{8.1}$$

where $\zeta = 0.83$ is the branching to the shelved manifold, γ_D is the decay rate of the intermediate D state, and p_i is the population in the state "i" (which are implicitly assumed to be time dependent). Since we are not coherently populating the $^2D_{5/2}$, there will be no popu-

lation inversion, but instead the transition will be saturated by the 411 nm laser ($p_S = p_D$). This condition, along with the fact that population is conserved ($p_D + p_S + p_F = 1$), means we can eliminate p_D from the above equation and get

$$\dot{p}_F = \frac{1}{2}\gamma_D \zeta (1 - p_F) \tag{8.2}$$

This can be readily integrated with the initial condition $p_F(t = 0) = 0$ to get

$$p_F(t) = 1 - e^{-t\frac{\gamma_D \zeta}{2}} = 1 - e^{-t\frac{\zeta}{2\tau_D}} \tag{8.3}$$

In this model, the effective time constant of the shelved state population is $\tau = \frac{2}{\gamma_D \zeta} = 17.3$ ms. The fidelity of the population transfer can be written as

$$\mathcal{F}(t) = p_F(t) + \zeta p_D(t) = p_F(t) + \frac{\zeta}{2}(1 - p_F(t)) \tag{8.4}$$

where the second term arises from the fact that at the time when shelving is stopped, 83% of any remaining $^2\mathrm{D}_{5/2}$ population will emit to the $^2\mathrm{F}^o_{7/2}$ and result in successful population transfer. While this model is appropriate for determining population transfer fidelity for moderate shelving times (< 500 ms), the finite lifetime of the $^2\mathrm{F}^o_{7/2}$ will come into play at some point.

Including finite lifetime of $^2\mathbf{F}^o_{7/2}$: To include the finite lifetime of the $^2\mathrm{F}^o_{7/2}$ into the model, we incorporate a term for spontaneous emission of population to $^2\mathrm{S}_{1/2}$ from $^2\mathrm{F}^o_{7/2}$. We will also now incorporate a term R_0 that represents the population transfer rate between $^2\mathrm{S}_{1/2}$ and $^2\mathrm{D}_{5/2}$.

$$\begin{aligned}
\dot{p}_S &= -R_0 p_S + (R_0 + (1 - \zeta)\gamma_D) p_D + \gamma_F p_F \\
\dot{p}_F &= \gamma_D \zeta p_D - \gamma_F p_F \\
\dot{p}_D &= R_0 p_S - (R_0 + \gamma_D) p_D
\end{aligned} \tag{8.5}$$

While symbolic integration software (Mathematica) can find analytic solutions to these equa-

tions, I have not found them to be particularly enlightening or useful. The key here is that the limit on the population transfer fidelity is set by the competing rates of population transfer into ($\zeta\gamma_D$) and out of (γ_F) $^2\mathrm{F}^o_{7/2}$. The $t \to \infty$ limit of equation 8.4 using the solutions above can be found to be

$$\lim_{t\to\infty} \mathcal{F}(t) = 1 - \frac{\gamma_F((1+\zeta)R_0 + \gamma_D)}{\gamma_D\gamma_F + R_0(\zeta\gamma_D + 2\gamma_F)} \tag{8.6}$$

This suggests that the population transfer limit via incoherent narrow band optical pumping is $\sim 1 - 10^{-10}$.

This model suggests that if we shelve for 200 ms, we will achieve population transfer better than 0.99999, which will be the minimum population transfer fidelity we want to work with for high fidelity operation so that the contribution to the error budget is minimal. In principle, shelving can be performed for a longer period of time to get better population transfer.

The models discussed above will describe the shelving process in even isotopes of Yb^+ fairly well. As we will show below, there will be other decay processes that will limit the fidelity of population transfer for qubit measurement in $^{171}\mathrm{Yb}^+$.

Accounting for magnetic dipole decay during population transfer: In $^{171}\mathrm{Yb}^+$, there exists a magnetic dipole transition moment between $^2\mathrm{D}_{5/2}\ |F=3\rangle$ and $^2\mathrm{D}_{3/2}\ |F=2\rangle$ discussed in the next section that will need to be taken into account when performing qubit state selective population transfer of $|1\rangle_g$ to $^2\mathrm{F}^o_{7/2}$. The theoretical branching of $^2\mathrm{D}_{5/2}\ |F=3\rangle$ to $^2\mathrm{D}_{3/2}\ |F=2\rangle$ is 2×10^{-4}, implied from the theoretical magnetic dipole transition rate of 28 mHz. This decay is repumped to the ground state with the 935 nm laser and will branch to the $^2\mathrm{S}_{1/2}\ |F=0\rangle$ and $|F=1\rangle$ with probability 1/3 and 2/3 respectively. For simplicity in the model, we will ignore the details of the repumping and treat the repump events as instantaneous so that $^2\mathrm{D}_{5/2}\ |F=3\rangle$ branches to the ground state hyperfine manifolds directly. This approximation is valid in the regime where the repumping rate ($< 1\mu$s) is much faster than the decay rate of $^2\mathrm{D}_{5/2}$ (7.2 ms), which is true in the

$^{171}Yb^{+}$ system. Additionally, we will treat all decays from $^2F^o_{7/2}$ as errors that populate $|0\rangle_g$ so we can avoid modeling the hyperfine structure in the $^2F^o_{7/2}$. Since the attainable fidelity is limited primarily by the M1 decay, changing the state to which $^2F^o_{7/2}$ population decays has no observable effect on the numerical results. The system of equations is

$$\begin{aligned}
\dot{p}_{S1} &= -R_0 p_{S1} + (R_0 + (1-\zeta)\gamma_D + \frac{2}{3}\chi\gamma_D)p_D + \gamma_F p_F \\
\dot{p}_{S0} &= \frac{1}{3}\chi\gamma_D p_D \\
\dot{p}_F &= \gamma_D(\zeta - \chi)p_D - \gamma_F p_F \\
\dot{p}_D &= R_0 p_S - (R_0 + \gamma_D)p_D
\end{aligned} \tag{8.7}$$

where $\chi = 2\times10^{-4}$ is the branching ratio to $^2D_{3/2}\ |F=2\rangle$, and S1 and S0 are the $F=1$ and $F=0$ hyperfine manifolds in the ground state, respectively. The addition of the magnetic dipole decay channel is modeled as a channel that weakens the decay path to $^2F^o_{7/2}$, which has little effect on the overall dynamics. This decay channel quickly populates $|0\rangle_g$, and limits state selective population transfer of $|1\rangle_g$ to $^2F^o_{7/2}$ to 0.99992 for times $t > 0.2$ ms.

We measure population transfer fidelity of the $^2S_{1/2}\ |F=1\rangle$ manifold to the $^2F^o_{7/2}$ state by first preparing $|0\rangle_g$, followed by a series of three microwave π-pulses: first on the $|0\rangle_g \rightarrow |1\rangle_g$ transition, followed by one each on the $|0\rangle_g \rightarrow {}^2S_{1/2}\ |F=1, m_F=\pm1\rangle$ transitions. This is followed by manifold selective population transfer at 411 nm for variable times up to $t_{shelve} = 300$ ms. We measure combined $^2S_{1/2}\ |F=1\rangle$ manifold and population transfer fidelities of 0.99991^{+3}_{-4} at 200 ms, and 0.99992^{+3}_{-4} at 300 ms. Both results are consistent with the aforementioned limits set by the magnetic dipole decay.

8.2.4 Sources of infidelity during population transfer

There will be two main sources of error during an attempt to transfer the $|1\rangle_g$ population to the $^2F^o_{7/2}$: off resonant excitation to the $^2D_{5/2}\ |F=2\rangle$ hyperfine level, and a non vanishing magnetic dipole moment between $^2D_{5/2}\ |F=3\rangle$ and $^2D_{3/2}\ |F=2\rangle$.

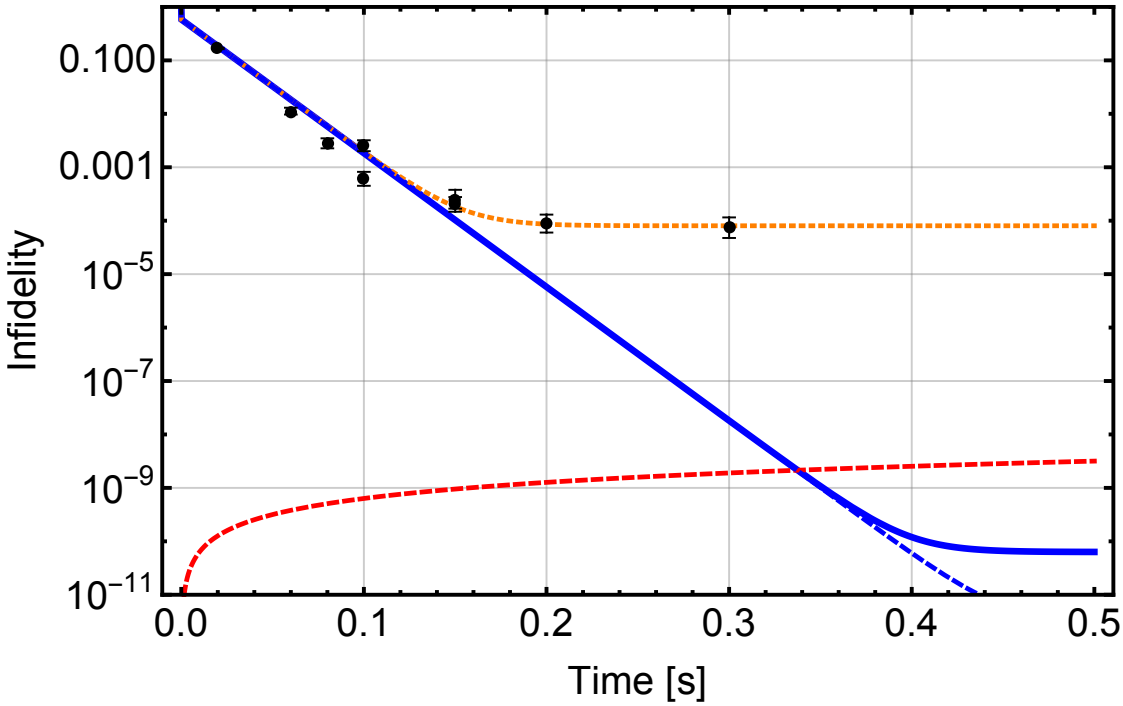

Figure 8.2: Shelving infidelity as a function of time, with all above models shown. Blue dotted line ignores the finite lifetime of $^2\mathrm{F}^o_{7/2}$, solid blue line includes it. The orange curve includes the magnetic dipole decay channel, and the red curve is $1 - e^{-\gamma_F t}$. Data taken at variable shelving times shown on plot. For long shelving times, the data agrees quite well with the basic rate model. Experimental data at times $\leq$ 100 ms tend to perform better than the simple rate model, which could be explained by a slight asymmetry of the $^2\mathrm{S}_{1/2}$ and $^2\mathrm{D}_{5/2}$ populations.

To estimate an upper bound on the error caused by off resonant scatter to the incorrect hyperfine manifold, we will look at the ratio of the scattering rates. There will be two sets of parameters: one characterizing the $^2\mathrm{S}_{1/2}\ |F=1\rangle \rightarrow {}^2\mathrm{D}_{5/2}\ |F=3\rangle$ transition and another characterizing the $^2\mathrm{S}_{1/2}\ |F=1\rangle \rightarrow {}^2\mathrm{D}_{5/2}\ |F=2\rangle$ transition. This is necessary since the relative coupling strengths are different by about a factor of 3 [TEM21]. The saturation intensity for the two transitions are

$$\begin{aligned} I_{sat,3} &= \frac{\pi hc}{3\lambda^3}\eta_3\gamma = 70.4\ \mu\mathrm{W/m}^2 \\ I_{sat,2} &= \frac{\pi hc}{3\lambda^3}\eta_2\gamma = 28.9\ \mu\mathrm{W/m}^2 \end{aligned} \tag{8.8}$$

Where $\lambda = 411$ nm, $\gamma = 1/\tau = 2\pi \times 22$ Hz, and $(\eta_3, \eta_2) = (0.17, 0.07)$ are the branching ratios

of the two upper hyperfine manifolds back to the lower ground state manifold [TEM21]. An upper bound on the amount of power used during the experiments is P = 2 mW, and an estimated beam waist $\omega_0 = 40\mu$m. This gives

$$\begin{aligned} I &= \frac{2P}{\pi\omega_0^2} = 796 \text{ kW/m}^2 \\ s_3 &\approx 1.1 \times 10^{10} \\ s_2 &\approx 2.7 \times 10^{10} \end{aligned} \tag{8.9}$$

and a resonant Rabi frequency on the shelving line of $\Omega = 2\pi \times 281$ kHz. This is calculated under the assumption that the ion is located radially at the center of an ideal Gaussian beam profile, and at z = 0 where the intensity is the highest. In practice, we have not observed Rabi frequencies this high, determined coarsely by detuning the laser and observing the AC Stark shift of the $|1\rangle_g$ state via Ramsey spectroscopy.

The ratio of the off resonant scattering rate to the resonant scattering rate is

$$\frac{R(\Delta = 2\pi \times 191 \text{ MHz}, s = s_2)}{R(\Delta = 0, s = s_3)} = 1.8 \times 10^{-7} \tag{8.10}$$

This is even further suppressed by the fact that even if an off resonant excitation occurs, it still correctly shelves the population 83% of the time, and only mixes population into the $|0\rangle_g$ 11% of the time. The off resonant scattering rate is calculated with these parameters to be $\sim 30\mu$Hz, which should be no issue during electron shelving. Given this scattering rate, the probability of an off resonant scattering event in 200 ms is 6×10^{-6} without taking into account the decreasing population as a function of time in $^2\text{S}_{1/2}\ |F = 1\rangle$. This limit is user-tunable, and can be suppressed by narrowing of the 411 nm laser and decreasing the laser intensity.

The more important effect turns out to be the magnetic dipole decay between the two D_J states, an often overlooked effect due to its relatively small strength. The transition rate was derived in Section 3.3.2, resulting in a M1 transition rate of 28 mHz. Electric quadrupole contributions to this rate are about 3 orders of magnitude smaller, and therefore are neg-

ligible. This transition rate results in a branching ratio of 2×10^{-4} to the $^2\mathrm{D}_{3/2}\,|F=2\rangle$. This state is typically repumped to the $^3[3/2]^o_{1/2}\,|F=1\rangle$, which will branch to the ground state F = 1 and F = 0 manifolds with probabilities 2/3 and 1/3 respectively. Therefore, the contribution to our population transfer fidelity is $\sum_{n=0}^{\infty}\eta_3^n(1/3)(2\times10^{-4}) = 8\times10^{-5}$, our largest "physics limited" source of infidelity. The form of this infidelity stems from the fact that there will be multiple spontaneous emission events from the $^2\mathrm{D}_{5/2}$ during the population transfer process, each of which has a finite probability of mixing the qubit states due to an M1 decay.

There are multiple ways this error channel can be avoided or suppressed. The most straightforward method is to depopulate the $^2\mathrm{D}_{3/2}\,|F=2\rangle$ manifold via an electric dipole transition to an odd parity electronic state with $J = 3/2$ and total angular momentum $F = 2$. This can be readily achieved by driving population to $^2\mathrm{P}^o_{3/2}$ at 1.35 μm, or to $^1[3/2]^o_{3/2}$ at 861 nm. While both of these schemes do not completely eliminate the potential for state mixing, they highly suppress the error channel to less than 1×10^{-6}. Alternatively, one can attempt to depopulate the intermediate $^2\mathrm{D}_{5/2}\,|F=3\rangle$ manifold in a state selective way before a spontaneous emission event can occur. This can be achieved with the addition of a 3.4 μm laser to drive population between the intermediate manifold and the target metastable manifold.

8.3 Optical pumping, preparation of $|0\rangle_g$

The first step in state preparation is the start in a simple state that we can prepare with high fidelity and speed. For nuclear spin 1/2 ions, this is typically the $^2\mathrm{S}_{1/2}\,|F=0\rangle = |0\rangle_g$ due to the ease of incoherent optical pumping. This is achieved by illuminating the ion with laser light resonant with the $^2\mathrm{S}_{1/2}\,|F=1\rangle \leftrightarrow {}^2\mathrm{P}_{1/2}\,|F=1\rangle$ transition. After excitation to the $^2\mathrm{P}_{1/2}$, the ion will decay into the $|0\rangle_g$ state 1/3 of the time. The laser light can simply be left on for a suitable amount of time until the desired state has been prepared with high certainty, which typically takes on the order of ~ 10 μs.

The question we aim to answer is how high is that certainty, and what are the limits to this scheme? If we had the ability to provide a spectrally pure laser resonant with the optical pumping transition, the limit of that process would be the competing rate at which population is pumped *out* of the $|0\rangle_g$ state by that same laser light via the only allowed transition to the $^2\mathrm{P}_{1/2}\,|F=1\rangle$ manifold. The scattering rate of optical pumping and the off resonant out-pumping are given by

$$\mathrm{R}_{in} = \left(\frac{1}{3}\right)\left(\frac{2}{3}\right)\frac{\Gamma}{2}\frac{s}{1+s} \tag{8.11}$$

$$\mathrm{R}_{out} = \left(\frac{2}{3}\right)\frac{\Gamma}{2}\frac{s}{1+s+(\frac{2\Delta}{\Gamma})^2} \tag{8.12}$$

where the detuning of the out coupling light is $\Delta = 2\pi \times 12.6$ GHz, and the natural linewidth of the transition $\Gamma = 2\pi \times 19.7$ MHz. The ratio of these rates will give us an answer for the steady state population that we can expect in the $F = 1$ manifold of the ground state.

$$\frac{\mathrm{R}_{out}}{\mathrm{R}_{in}} = \frac{2(1+s)}{1+s+(\frac{2\Delta}{\Gamma})^2} \xrightarrow{s\to 0} \frac{2}{1+(\frac{2\Delta}{\Gamma})^2} \tag{8.13}$$

This gives a steady state population of 1.8×10^{-6}, or a $|0_g\rangle$ state preparation fidelity $\mathcal{F}_{|0\rangle_g} \approx 0.999998$.

Without the availability of a separate UV laser, typically an electro-optic modulator (EOM) is used to produce laser light for optical pumping. As the laser propagates through the EOM, it will undergo phase modulation at the applied modulation frequency that results in optical sidebands with intensity $\propto \mathrm{I}_0|J_n(\beta)|^2$, where β is the modulation depth determined by the intensity of the applied modulation electric field.

The population dynamics during optical pumping can be approximated by a set of rate equations modeling the populations of the $^2\mathrm{S}_{1/2}\,|F=1\rangle$ and $^2\mathrm{S}_{1/2}\,|F=0\rangle$ while interacting with laser light exiting the EOM. If we allow no population to reside in the excited state and ignore the effect of the $^2\mathrm{D}_{3/2}$, which is approximately true given the short lifetime of the

excited state ($\sim$ 8 ns) and weak branching to the metastable manifold (0.005), we can use a two level model to find the dynamics. The rate equations can be approximated by

$$\begin{aligned}\dot{p}_0(t) &= \left(\frac{2}{3}\right)\left(\frac{1}{3}\right)p_1(t)\Big[R(0, s_{OP}) + R(\omega_{HFP}, s_C)\Big] - \\ &\quad \left(\frac{2}{3}\right)p_0(t)\sum_n R(\Delta_n,\ |J_n(\beta)|^2 s_0) \\ \dot{p}_1(t) &= -\dot{p}_0(t)\end{aligned} \tag{8.14}$$

Where $R(\Delta, s)$ is the scattering rate induced by one of the accounted for laser tones. The sum is over n = 0 to 8, and the Δ_n is the detuning of the positive n$^{\text{th}}$ order sideband from the $^2\mathrm{S}_{1/2}\,|F=0\rangle \rightarrow {}^2\mathrm{P}^o_{1/2}\,|F=1\rangle$ transition that would move population out of the $|0\rangle_g$ state. The factor of 2/3 in the first term reflects that at any point, one of the three $^2\mathrm{S}_{1/2}\,|F=1\rangle \rightarrow {}^2\mathrm{P}^o_{1/2}\,|F=1\rangle$ transitions is a coherent dark state of the system [NVG13], and the factor of 1/3 is the branching back to the $|0\rangle_g$ state. Likewise, the factor of 2/3 in the second term is the branching back to the $|1\rangle_g$ state.

It was observed by addition of extra terms that included other sidebands in the first term of the rate equations above did not result in a significant change in the optimal modulation depth or the infidelity of the process. Another detail to take into account is the possibility that our EOM does not phase modulate all input laser light and full carrier suppression is not possible. We will use the parameter η to model this, defined as the fraction of the carrier that goes unmodulated. There will be two effects here: the first is that for $\eta = 0$, the equations should reduced to the original model, and for $\eta = 1$ all terms except for the carrier should have zero intensity. This is modeled by letting $s_c = |J_0(\beta_{opt})|^2 s_0(1-\eta) + \eta s_0$, and $s_0 \rightarrow (1-\eta)s_0$ for all other terms, where η is the fraction of the input light that goes unaffected by the modulation process (i.e. if the zeroeth order Bessel function was zeroed out, this is how much carrier light would still pass through the modulator). Setting the modulation depth to the numerical optimal of $\beta = 1.75$ and scanning η we find unsurprisingly that the optical pumping gets worse as η increases.

This model fails to take into account the effect of laser polarization of the optical pumping

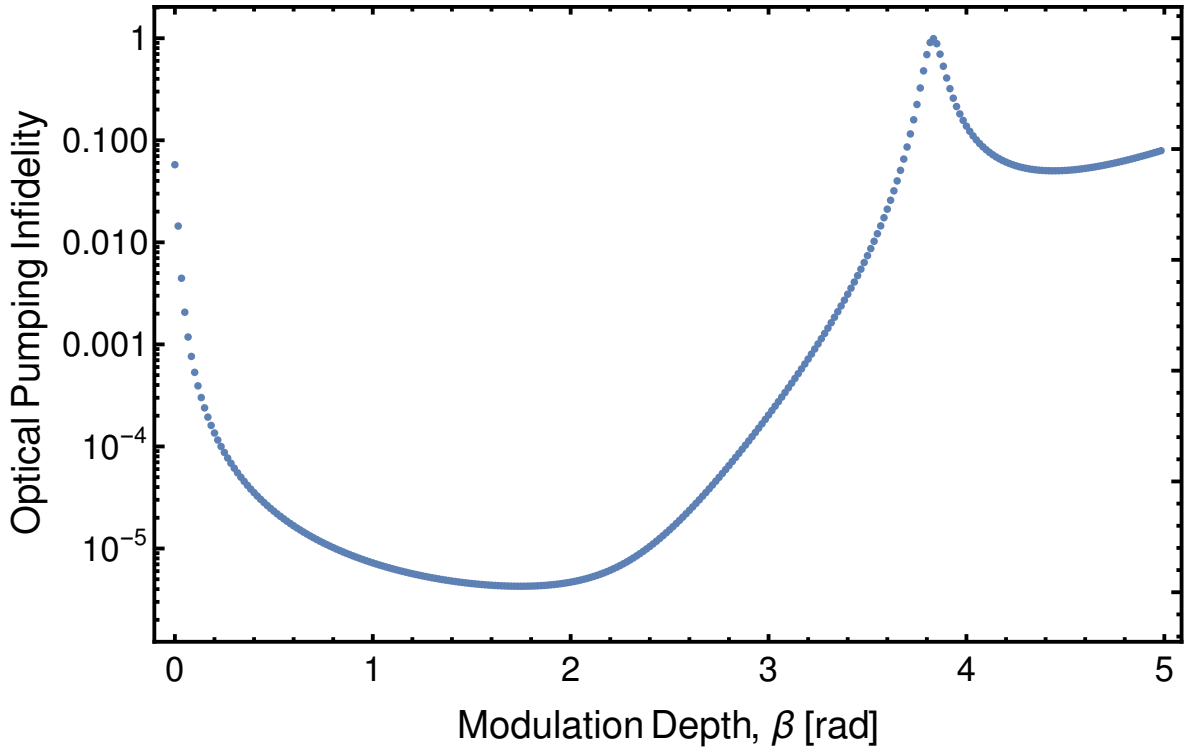

Figure 8.3: Optical pumping infidelity as a function of EOM modulation depth, β. The optimal modulation depth is $\beta = 1.75$ given an input saturation intensity s_0 =1. This value of the modulation depth is just below the maximum value of $|J_1(\beta)|$ at β =1.84 that optimizes the optical pumping intensity.

beam, along with the Zeeman substructure of both fine structure states. In order to take these effects into account, an 8 level system would need to be simulated with arbitrary couplings between the states (which gets more difficult when trying to account for all the EOM sidebands). Another issue with this simulation is its speed: since the full Hamiltonian will have to take into account the hyperfine splittings, we will not be able to rotate out the time dependence at the hyperfine energy splittings, which means that numerical simulations will need to take step sizes on the order of $\delta t \sim 1/\omega_{HFS} \sim 80$ picoseconds.

With this model, it seems clear that the E1 optical pumping scheme is fairly insensitive to the input microwave power. So long as the modulation depth is set in the neighborhood of $\beta = 1.75$, and the unmodulated index η remains moderately small, infidelities below around 10^{-5} should be easily achievable, in theory. What this does not take into account is all

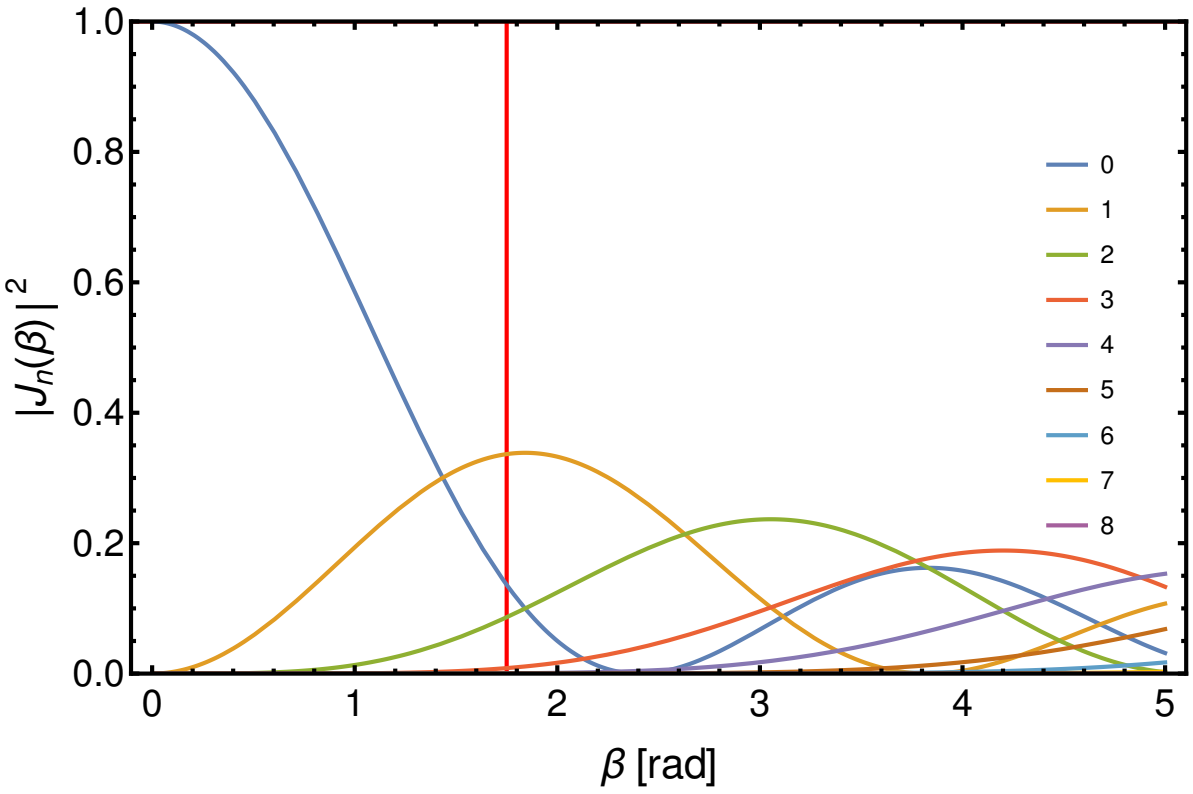

Figure 8.4: Bessel functions plotted as a function of the modulation depth, β. The solid vertical line indicates the numerically solved optimal modulation depth for optical pumping with high fidelity.

the experimental complexity that goes into performing these experiments, and potential not obvious sources of error. Some of these, to name a few, are RF pickup on AOMs, leak-through light on unwanted lasers (in particular the Doppler cooling AOM), and ion heating during the shelving process.

In order to improve upon this standard E1 mediated optical pumping, additional techniques are necessary to improve the $|0\rangle_g$ preparation. The limiting factor in the above scheme is the large linewidth of the dipole transition, and the ratio of that linewidth to the respective hyperfine splittings. Since there is nothing we can do to change the inherent structure of the ion, we need to take advantage of other transitions. The ideal situation would be the following:

1. An excited state connected to the $^2S_{1/2}\,|F=1\rangle$ states via a moderately weak transition

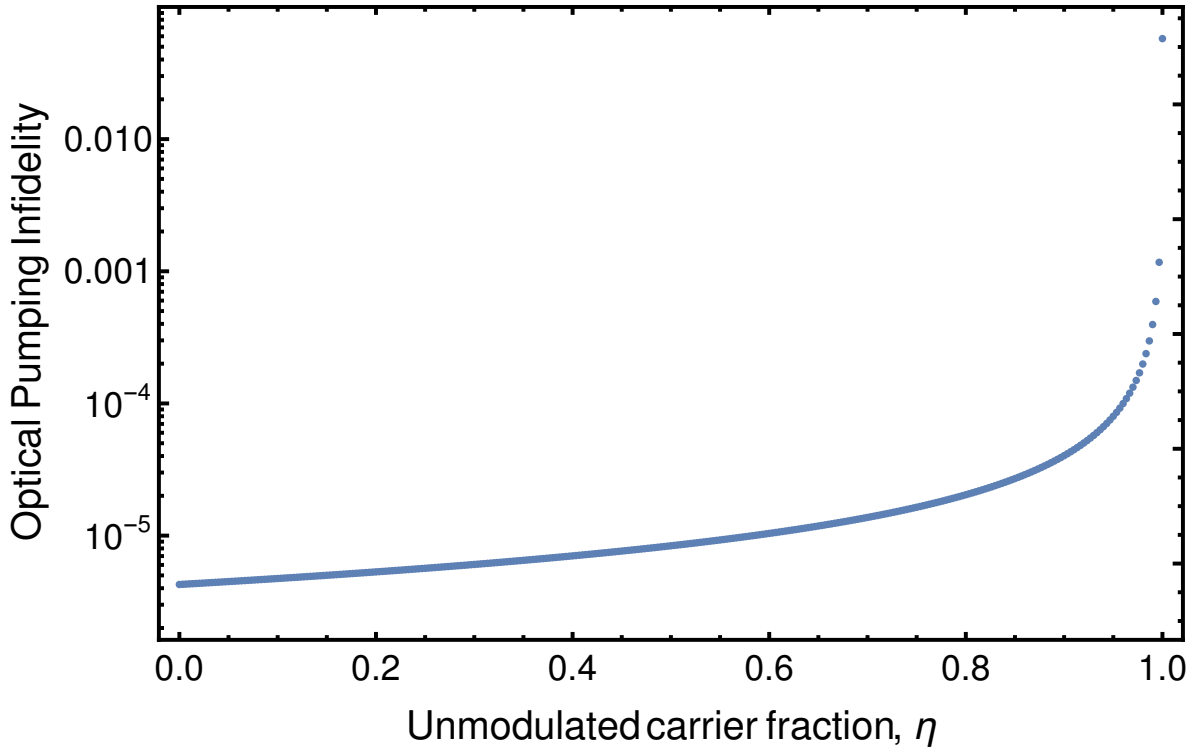

Figure 8.5: Infidelity of optical pumping as a function of the unmodulated carrier fraction, η, with an input saturation parameter of $s_0 = 1$.. The minimum occurs at $\eta = 0$ with an optical pumping infidelity of 4.2×10^{-6}, and the maximum occurs at $\eta = 1$ where the optical pumping fidelity is 0.943, corresponding to optical pumping with the carrier tone alone. This was simulated at the numerical optimal modulation depth of $\beta = 1.75$, which assumed a perfect modulator ($\eta = 0$).

(E2 or M1 for instance). The low lying $^2\mathrm{D_J}$ states are candidates for some ions.

2. A second excited that has a couple properties:

   - Decays quickly and with high probability to the ground state
   - Has the correct grand total angular momentum F to allow for optical pumping to the $|0\rangle_g$ state.

These last two requirements limit us to excited states that have a strong dipole moment with the $^2\mathrm{S}_{1/2}$ ground state, and thus must have odd parity. If the decay is to be via an electric dipole transition, then the grand total angular momentum must also be $F = 1$ so that decays to the $|0\rangle_g$ qubit state is possible. Luckily in Yb^+, there are many relatively low

lying odd parity states that we can use, so there are a few schemes to achieve this goal:

1. Step 1: ${}^2\mathrm{S}_{1/2}\,|F=1\rangle \leftrightarrow {}^2\mathrm{D}_{3/2}\,|F=2\rangle$ (E2 at 435 nm), followed by Step 2: ${}^2\mathrm{D}_{3/2}\,|F=2\rangle \leftrightarrow {}^3[3/2]^o_{1/2}\,|F=1\rangle$ (E1 at 935 nm)

2. Step 1: ${}^2\mathrm{S}_{1/2}\,|F=1\rangle \leftrightarrow {}^2\mathrm{D}_{5/2}\,|F=2\rangle$ (E2 at 411 nm), followed by Step 2: ${}^2\mathrm{D}_{5/2}\,|F=2\rangle \leftrightarrow {}^1[3/2]^o_{3/2}\,|F=1\rangle$ (E1 at 976 nm)

Since we are already implementing the E2 transition at 411 nm to perform electron shelving, this is the natural choice in our lab. This method for optical pumping is used as a secondary method following standard electric dipole mediated optical pumping. If the first stage of optical pumping can be performed with infidelity ϵ, where we assume the error is population residing in the upper hyperfine manifold, then the second stage of optical pumping should improve preparation of the $|0\rangle_g$ state to $\mathcal{F}_{|0\rangle_g} = 1-(1-\mathcal{F}_2)\epsilon$ where $\mathcal{F}_2$ is the fidelity of the second stage. We have separately quantified our ability to perform this second state of optical pumping, and have found that $|0\rangle_g$ state preparation fidelities > 0.999 are easily achieved in less than a few milliseconds.

There are other sources of experimental infidelity as well. One of the more important ones is leak-through laser light from other laser paths that should not be activated during the optical pumping sequence of the experiment. In particular, we should be very concerned about the path used for Doppler cooling of ions because leak-through of light on this path *may* have light resonant with the $|0\rangle_g \rightarrow {}^2\mathrm{P}^o_{1/2}\,|F=1\rangle$ transition which would actively depopulate the $|0\rangle_g$ state. I say *may* because there may be two mechanisms for this leak-through laser light: the first is some sort of specular scatter in the AOM crystal causing the laser wavevector to be identical to that of the AOM's first order diffracted light, the other being RF pickup in the cables causing actual first order deflection of the Doppler cooling light into the fiber (and hence to the ion). The first scenario we have observed in the lab, and should cause photons that are -110 MHz detuned from the line to leak into the trap. The second scenario has also been observed, but can be solved by shifting the operating frequencies of other AOMs on during optical pumping. We therefore shifted the optical pumping AOM from +110 MHz

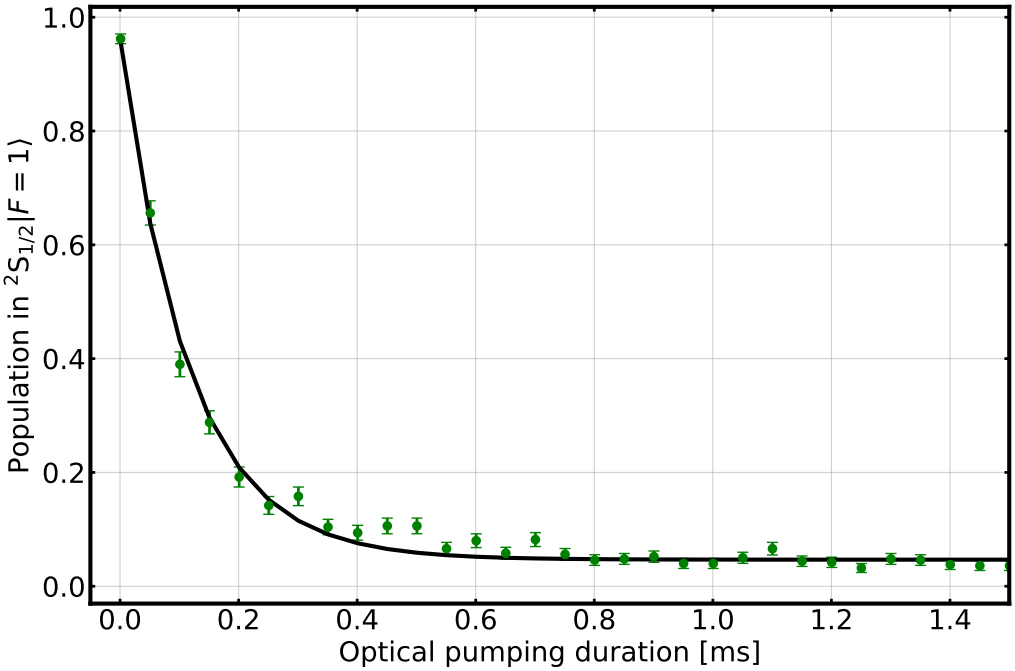

Figure 8.6: Optical pumping rate experiment measuring the population in $|1\rangle_g$ as a function of the time the 411 nm + 976 nm lasers are applied for $|0\rangle_g$ state preparation. The measured time constant in this instance is $\tau = 115$ μs. Standard spin 1/2 hyperfine qubit measurement is used here, so an overall offset to the exponential fit is allowed to account for the measurement fidelity of the $|0\rangle_g$ state.

to +120 MHz, and compensated for the frequency shift with the double pass during optical pumping. Optical intensities of the leak through laser light are too small to measure with out optical power meter, and are not visible by eye on the output of the fiber.

Both of these effects can be checked by running the following experiment: prepare the $|0\rangle_g$ state as well as possible, and then allow for a variable dead time between the end of optical pumping and the beginning of shelving and see how the fidelity scales as a function of the wait time. This works, in principle, but is hindered by the effects of heating on the experiment. If we leave the ion in the dark for long periods of time (> 100 ms), significant heating can occur and degrade the effectiveness of shelving. It is therefore hard to deconvolve the effects of leak-through light and ineffective shelving at long wait times.

8.4 Preparation of $|1\rangle_g$

To perform a SPAM measurement, we need to show our ability to prepare and detect *both* of qubit basis states. We have shown that state preparation (SP of SPAM) of the $|0\rangle_g$ state in our lab is, in theory, feasible at the 1 - 10^{-8} level, and further investigation for state preparation of the $|1\rangle_g$ state is now necessary.

In nuclear spin 1/2 ions, when the qubit basis states are the ground state hyperfine clock states, it is typical to prepare the $|1\rangle_g$ state by first preparing $|0\rangle_g$ and performing a single qubit gate to rotate $|0\rangle_g \rightarrow |1\rangle_g$. This is done primarily because no simple method of incoherent optical pumping is available to prepare the $|1\rangle_g$ state, and most quantum information laboratories have all the tools to perform arbitrary single qubit gates at reasonable fidelities.

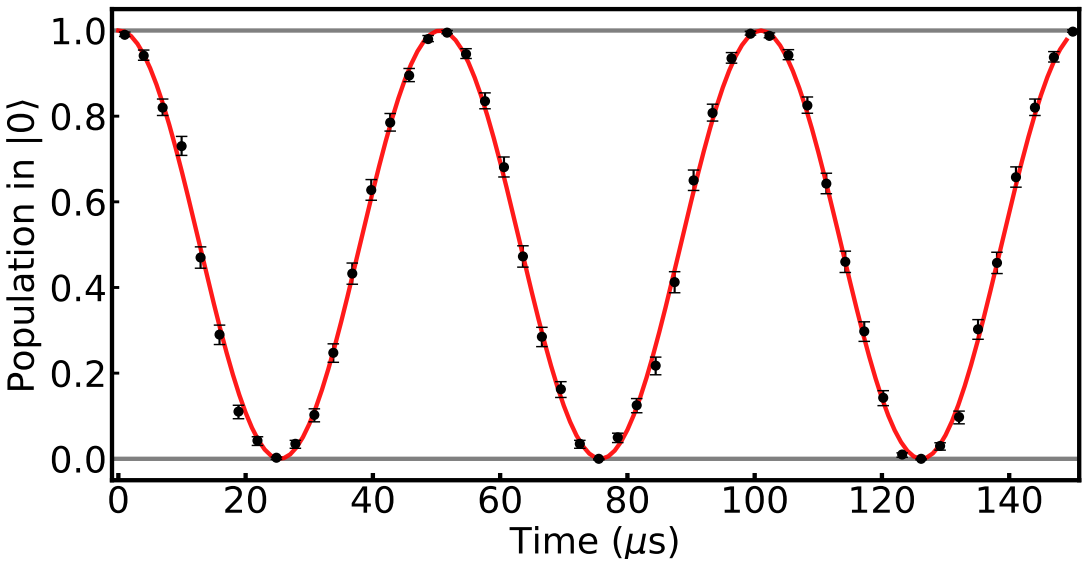

Figure 8.7: Rabi flopping of the ground state qubit, with measurement performed via electron shelving. Each point is the result of 400 experimental trials.

After state initialization and performing a single qubit rotation for time t, with resonant Rabi frequency Ω and detuning Δ from the qubit transition, the population in the $|1\rangle_g$ is given by solving the standard two level Rabi problem,

$$
\begin{aligned}
|c_1(t)|^2 = P_1(t) &= \frac{\Omega^2}{\Omega^2+\Delta^2}\sin^2\left(\frac{t}{2}\sqrt{\Omega^2+\Delta^2}\right) \\
&= \frac{1}{1+(\Delta/\Omega)^2}\sin^2\left(\frac{\Omega t}{2}\sqrt{1+(\Delta/\Omega)^2}\right)
\end{aligned}
\tag{8.15}
$$

The challenge experimentally is to maintain small errors in the applied microwave frequency and amplitude at the location of the ion. Determining the correct transition frequency is often relatively easy by implementing a variable delay Ramsey experiment at a fixed detuning, through which the resonant frequency of the qubit can be determined to $\sim$ Hz accuracy and precision, or about a part in 10^9 for qubits in the GHz range.

Correctly determining the appropriate interaction time is often more difficult, as it is influenced by additional experimental factors. To accomplish a π rotation (for full preparation of the $|1\rangle_g$), the interaction must be applied for a time $t = \pi/\Omega$ at zero detuning. Due to thermal drifts of high power amplifiers, often Ω cannot be considered a constant in time, and can often vary temporally and with the duty cycle of a particular experiment. This makes it challenging to accurately determine Ω to the desired precision, which in turn leaves uncertainty in setting the interaction time.

Taking the $\Delta \to 0$ limit of 8.15 we get

$$
P_1(t) = \sin^2\left(\frac{\Omega t}{2}\right) \tag{8.16}
$$

where we have dropped terms $\mathcal{O}((\Delta/\Omega)^2)$. Typical values for the resonant Rabi frequnecy on our experiment are $\Omega = 2\pi\times$ (2-20) kHz, so if the detuning is calibrated to better than 10 Hz, a typical ratio of the detuning to the resonant Rabi frequency is of order 10^{-3}. The quantity $\Omega t \equiv \theta$ is often referred to as the pulse area, and the parameter θ is chosen as it represents the polar angle on the two level Bloch sphere. Expanding 8.16 around $\theta = \pi$, we

get

$$\begin{aligned} P_1(t) &\approx 1 - \frac{1}{4}(\theta - \pi)^2 \\ &= 1 - \frac{\delta\theta^2}{4} \end{aligned} \tag{8.17}$$

where $\delta\theta$ is the pulse area error in radians. In order to perform a population transfer to $|1\rangle$ better than $\mathcal{F}_{|1\rangle} = 1 - 10^{-5}$ we need to maintain a pulse area error below 0.6%. For a fixed Rabi frequency of 10 kHz, this means timing the microwave application time to $\pm$100 ns. The pulse area error can conveniently be expressed in terms of the programmed t_π and a timing error δt as $\delta\theta = \frac{\pi\delta t}{t_\pi}$, where the timing error could be the result of misidentifying the Rabi frequency or a result of limitations of our pulse sequencer which can only supply TTL signals in increments of 40 ns.

We characterize our π-pulse fidelity by concatenating N_p π-pulses with random phases, where the set of random phases for a fixed N_p is regenerated every 100 experiments to ensure sufficient randomization. Numerical simulations suggest that using at least 100 different sets of randomly generated phases is enough to simulate a random walk about the poles of the Bloch sphere. If a pulse has constant pulse area error $\delta\theta$, after N_p π-pulses with random phases, on average the angular displacement of the Bloch vector from the pole will be $\sqrt{N_p}\delta\theta$. Since equation 8.17 scales quadratically with small angular displacements from the pole, the measured process fidelity should scale linearly with the number of concatenated π-pulses.

We perform this measurement for $N_p = \{2, 12, 16, 22, 28, 32, 42\}$, and fit the resulting process fidelities to the function $\mathcal{I}(N_p) = N_p\epsilon_\pi + \epsilon_{SPAM}$, where we interpret the y-intercept as the state preparation and measurement error for $N_p = 0$ pulses. The results are shown in Figure 8.8. Since we only perform even numbers of pulses, we expect to always begin and end the experiment in $|0\rangle_g$. This means the interpretation of the y-intercept is the SPAM of the $|0\rangle_g$ state, and is consistent with auxiliary measurements of the $|0\rangle_g$ SPAM fidelity with standard state detection.

To further validate our single qubit gate fidelity, we perform randomized benchmarking of

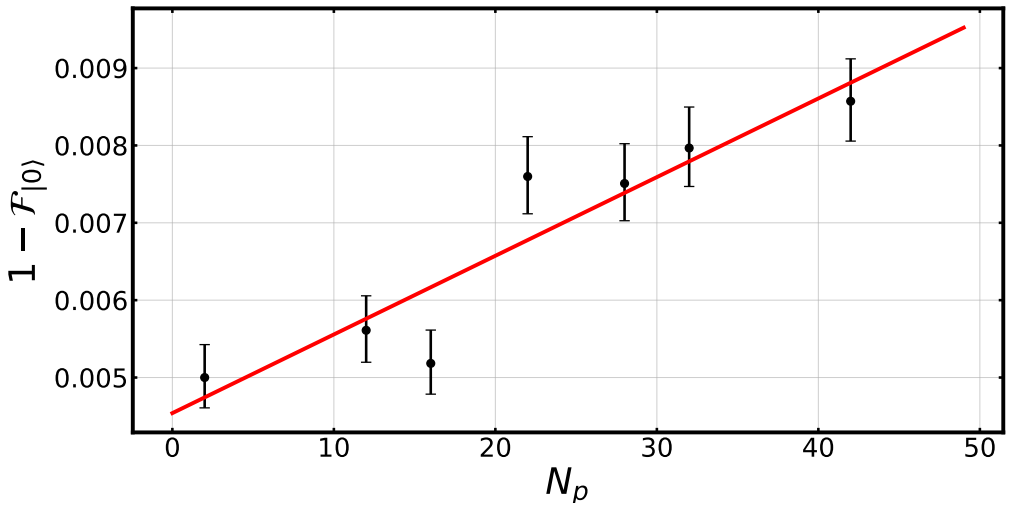

Figure 8.8: Results of concatenating π-pulses. The results of this experiment imply a single π-pulse infidelity of $\epsilon_\pi = 1.0(2) \times 10^{-4}$ and a SPAM intercept of $4.5(5) \times 10^{-3}$.

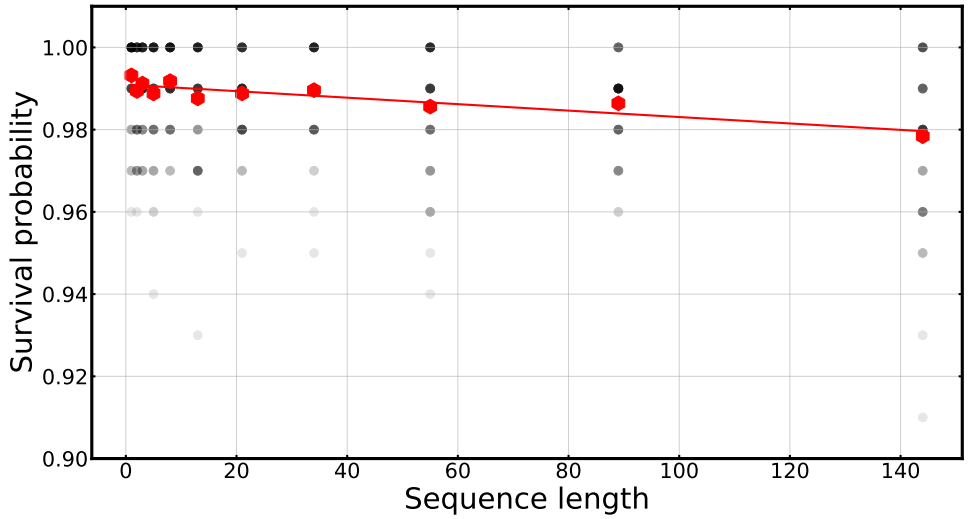

Figure 8.9: Results of single qubit randomized benchmarking experiment. The alpha channeled black datapoints are the results of each individual sequence, and the red hexagons are the mean result for each sequence length. We find a resulting error per random computational gate of $\epsilon_g = 8(2) \times 10^{-5}$ and a SPAM intercept of $\epsilon_{spam} = 9.1(7) \times 10^{-3}$.

our single qubit gates following the prescription in [KLR08]. Sequences of length N are composed of N-1 random computational gates, where each random computational gate is composed of a Pauli gate chosen uniformly at random from the set $\mathcal{P} \in \{\pm X(\pi), \pm Y(\pi), \pm Z(\pi),$

$\pm I(\pi)\}$ followed by a Clifford gate chosen uniformly at random from the set $\mathcal{C} \in \{\pm X(\pi/2), \pm Y(\pi/2)\}$. The Pauli gates are $e^{\pm i\pi\sigma_p/2}$, implemented as pulses with area π rotating the qubit about the corresponding axis of the Bloch sphere. Similarly, the Clifford gates are $e^{\pm i\pi\sigma_c/4}$, implemented as pulses with area $\pi/2$ rotating the qubit about the corresponding axis of the Bloch sphere. The first N-1 computational gates are randomly generated, at which point the resulting computational basis state to end the sequence in is chosen at random from $\{|0\rangle_g, |1\rangle_g\}$, and the the Nth computational gate is chosen such that the qubit is rotated to the chosen computational basis state. The Clifford Z gate is only used in the Nth computational gate if the qubit already resides in the computational basis after the first N-1 random computational gates. Pauli $\pm I$ gates are implemented as an empty sequence of duration t_π, and Pauli $\pm Z$ gates are implemented as an empty sequence of duration t_π with a rotation of the logical frame for subsequent pulses.

The sequence lengths chosen are the Fibonacci sequence as suggested in [Mei13] since the lengths were unlikely to hide errors due to use of only odd or even length sequences and their general exponential increase in separation. We use sequence lengths N = $\{1, 2, 3, 5, 8, 13, 21, 34, 55, 89, 144\}$, terminating at length 144 only due to limitations of our pulse sequencer. Ideally for confirming random computational gate infidelities of order ϵ_g, one should perform sequences up to length $N_{max} \sim 1/\epsilon_g$ in order to observe the exponential decrease in survival probability. If a sufficient number of randomly generated sequences for each length are explored, the resulting process fidelity as a function of the sequence length should follow the form

$$\mathcal{F}(N) = \frac{1}{2} + \frac{1}{2}(1 - 2\epsilon_{spam})(1 - 2\epsilon_g)^N \tag{8.18}$$

We perform 100 experiments per point shown in Figure 8.9, where we use $N_c = 5$ unique sequences of Clifford gates each of which is randomized by $N_p = 10$ unique sets of Pauli gates, for a total of $length(N)N_cN_p = 550$ unique sequences. We find a resulting error per random computational gate of $\epsilon_g = 8(2) \times 10^{-5}$ and a SPAM intercept of $\epsilon_{spam} = 9.1(7) \times 10^{-3}$, consistent with our state preparation and measurement fidelity measured through auxiliary experiments. The mean survival probability for each sequence length is fit via a least squares

algorithm provided by the Python SciPy package to equation 8.18. A potential interpretation of this result is provided in [KLR08]: all Clifford gates are of real pulse area $\pi/2$ and half of the utilized Pauli operators are of pulse area π, so that ϵ_g may be interpreted at the error rate of random gates of action π.

8.4.1 Deshelving

When electron shelving, deshelving population stranded in the metastable manifold is an essential part of the operation. Efficient deshelving both ensures that stranded population after state detection is quickly retrieved, and that at any other necessary point in the experiment erroneous population transfer to the metastable manifold is not detrimental (e.g. during quadrupole optical pumping).

Deshelving of $^2\mathrm{F}^o_{7/2}$ population is achieved with a pair of 760 nm DBR lasers separated in frequency by 5.257 GHz. The large frequency difference owes in part to the large hyperfine splittings in both the $^2\mathrm{F}^o_{7/2}$ and the $^1[3/2]^o_{3/2}$ fine structure levels. The $^2\mathrm{F}^o_{7/2}$ hyperfine splitting we have measured to be $\omega_{HFF} = 2\pi \times 3.6205$ GHz by direct resonant microwave spectroscopy, and the $^1[3/2]^o_{3/2}$ hyperfine splitting we have measured to be about 8.88 GHz. The bracket state splitting was measured both via direct measurement of the two 760 nm laser laser transitions, as well as the 861 nm transitions.

A second laser at 976 nm is also applied to prevent population excited to $^1[3/2]^o_{3/2}$ from decaying back to $^2\mathrm{F}^o_{7/2}$ via $^2\mathrm{D}_{5/2}$.

8.5 The SPAM measurement

The experiment that measures state preparation and measurement fidelity interleaves preparation of the $|0\rangle_g$ and $|1\rangle_g$ state every 100 experiments. This is done to make sure no systematic effect is causing the measurement of one of the states to be better than it should be. The qubit frequency is measured every hour to track its drift, and the resonant Rabi rate is measured every $\sim$2000 experiments to track drifts.

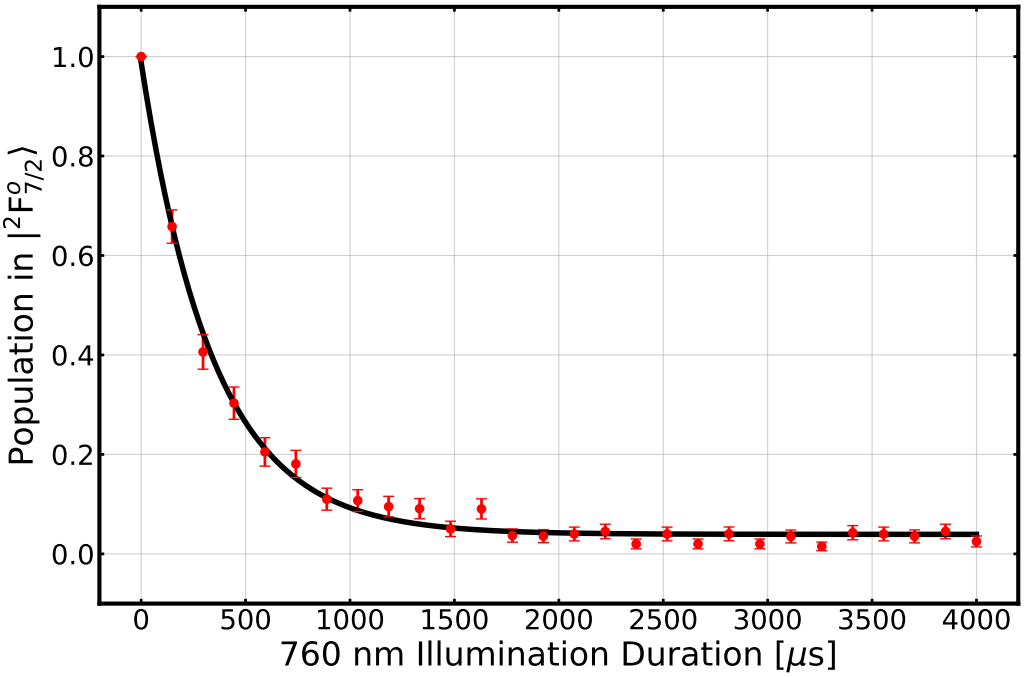

Figure 8.10: Deshelving rate experiment. Population in the metastable state is inferred from $^2S_{1/2}$ population measurement after a variable amount of deshelving time. During deshelving, both 760 nm lasers along with the 976 nm laser and 935 nm laser are applied so the metastable ^2D_J states are depopulated efficiently. With $\sim$ 15 mW per 760 nm laser, the observed deshelving time constant is $\tau = 350$ μs.

Throughout the measurement, our wavemeter is calibrated to a saturated absoprtion locked 780 nm laser every 5 minutes to minimize drifts in the software frequency locks. All lasers are locked in this way, except for our 369 nm ECDL which is stabilized to an optical cavity via the Pound-Drever-Hall method. This is particularly important for the 822 nm laser lock, where drifts on the order of MHz can affect the population transfer process.

In the process of taking data, we log the number of scattered photons during state detection and Doppler cooling. We use the Doppler cooling counts to ensure that at the beginning of an experiment the ion is present and properly cooled, and use the counts as a filter for experiments where the ion was not properly cooled beforehand.

We define a successful attempt at SPAM as having found the ion properly cooled before

and after the SPAM attempt. We have found experimentally that the majority of our $|0\rangle_g$ SPAM errors occur preceding a failed Doppler cooling test, which we label as ion storage errors. To verify that the storage errors are not related to the population transfer process, we perform state preparation and measurement $|0\rangle_g$ without applying 411 nm laser light during the shelving step, but instead leaving the ion in the dark for the identical amount of time (200 ms). If not filtered, the contribution of storage errors to our SPAM is determined to be $3^{+0.7}_{-0.5} \times 10^{-4}$ (27 errors in 88474 attempts). When filtering for storage errors, we see a contribution to our infidelity of $1.1^{+2.9}_{-0.6} \times 10^{-5}$ (1 error in 88403 attempts), in line with the measured SPAM with application of the shelving laser light.

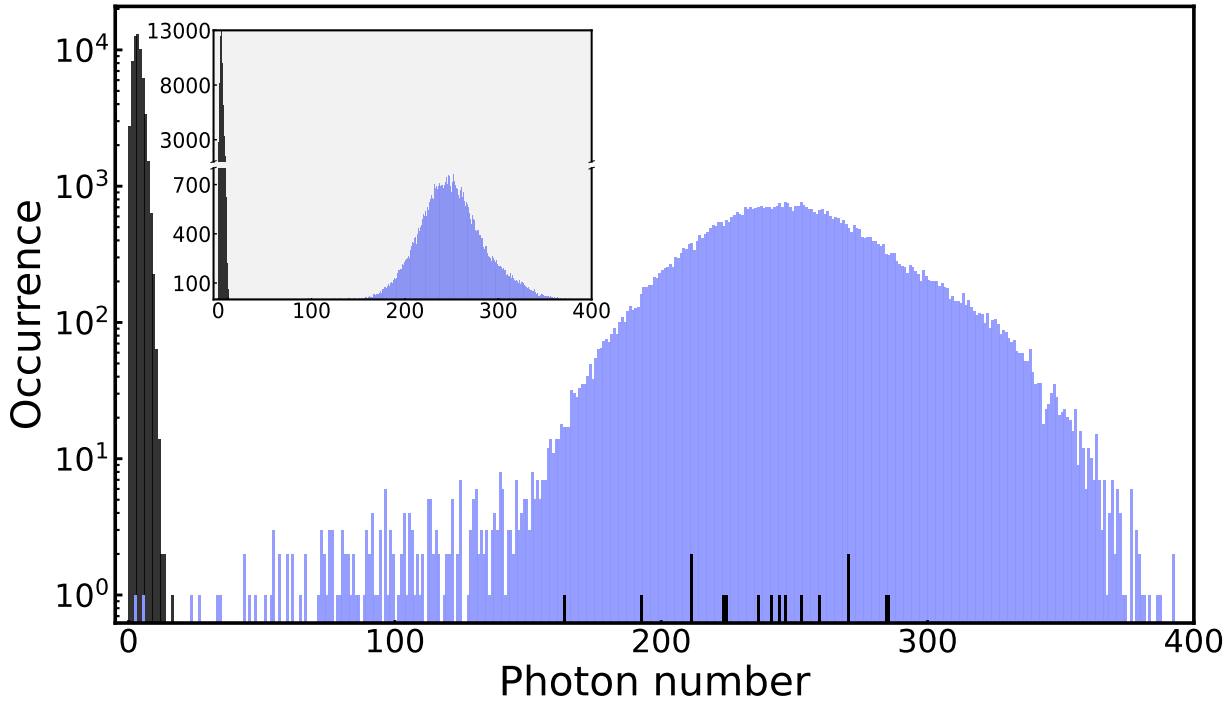

Figure 8.11: Results of the SPAM measurement. The measured state preparation and measurement infidelity is $\epsilon_{\text{SPAM}} = 1.5^{+0.4}_{-0.3} \times 10^{-4}$, where the main contribution is single qubit gate errors in preparation of $|1\rangle_g$.

The total state preparation and measurement fidelity of the ground state qubit is $\epsilon_{\text{SPAM}} = 1.5^{+0.4}_{-0.3} \times 10^{-4}$. The state preparation and measurement fidelity of $|0\rangle_g$ is $\epsilon_{|0\rangle_g} = 3.4^{+3.4}_{-1.7} \times 10^{-5}$, and the state preparation and measurement fidelity of $|1\rangle_g$ is $\epsilon_{|1\rangle_g} = 2.7^{+0.8}_{-0.6} \times 10^{-4}$. The main contribution to the infidelity is error in our single qubit gates throughout the measurement,

consistent with an average π-pulse infidelity of $\epsilon_\pi \cong 1.9 \times 10^{-4}$.

8.5.1 Achievable SPAM

While our SPAM measurement fidelity is limited by our ability to perform a single qubit gate, this is not the limit of the scheme. To determine the true potential SPAM fidelity achievable with 200 ms of narrow-band optical pumping, we can take the $|0\rangle_g$ data from above and combine it with the $^2\mathrm{S}_{1/2}\ |F=1\rangle$ manifold preparation data from earlier and gather a pseudo-SPAM fidelity. The "fidelity" is the combine SPAM fidelity of the $|0\rangle_g$ state combined with our ability to prepare the $^2\mathrm{S}_{1/2}\ |F=1\rangle$ manifold with three separate π-pulses to the separate magnetic sub-levels after preparation of $|0\rangle_g$. This results in a pseudo-SPAM fidelity of $\mathcal{F} = 0.99993^{+2}_{-3}$.

8.6 Shelving speed up options

Here we will go over some potential pathways to faster population transfer to the $^2\mathrm{F}^o_{7/2}$ of in general the $|1\rangle_g$ state in a qubit basis selective way. Each scheme will be worked out in moderate detail.

8.6.1 Shelving via $^1[5/2]^o_{5/2}$

The idea behind this scheme is for population to spontaneously emit photons via an M1 or E2 amplitude from the $^1[5/2]^o_{5/2}$ state to the $^2\mathrm{F}^o_{7/2}$. To achieve this, a two step excitation can be performed via the intermediate ^2D_J states. Either driving $|1\rangle_g \rightarrow {}^2\mathrm{D}_{3/2}\ |F=2\rangle \rightarrow {}^1[5/2]^o_{5/2}\,|F=3\rangle$ at 435 nm and 410 nm respectively, or driving $|1\rangle_g \rightarrow {}^2\mathrm{D}_{5/2}\ |F=3\rangle \rightarrow {}^1[5/2]^o_{5/2}\,|F=3\rangle$ at 411 nm and 436 nm respectively, can achieve the same goal. Since lingering population in the $^2\mathrm{D}_{5/2}$ will decay to the $^2\mathrm{F}^o_{7/2}$ directly with branching ratio 0.83, the latter scheme seems favorable.

The issue with this scheme is twofold: appropriate repumping of the other ^2D_J hyperfine levels must be done to avoid population mixing, and the Einstien A coefficient of the bracket

state to the metastable manifold must be greater than 19 Hz for this scheme to be faster than using the $^2\mathrm{D}_{5/2}$ directly.

Repumping of the ^2D_J would be done at 861 nm and 976 nm via the $^1[3/2]^o_{3/2}\,|F=2\rangle$ state. This would ensure that population would either couple back to the $^2\mathrm{S}_{1/2}\,|F=1\rangle$ manifold, or back to any of the ^2D_J hyperfine manifolds, all of which are either being repumped or shelved. This rempumping applies to either of the shelving pathways mentioned above, with just a slight adjustments of which hyperfine manifolds are addressed.

The transition rate A_{BF} of the bracket state to the shelved manifold will have two contributions: M1 and E2. Based on the electron configuration of the two states, it makes it seem like the core electrons are undergoing an M1 like transition ($4f^{13}(^2\mathrm{F}^o_{5/2}) \rightarrow 4f^{132}\mathrm{F}^o_{7/2}$) and the outer electrons will undergo an E2 like transition ($6s5d(^1\mathrm{D}) \rightarrow 6s^2(^1\mathrm{S})$). Since approaching a multi-electron transition likely necessitates a more formal approach for a precise answer, we can modify out approach to set a bound on the rate. For optical transitions, magnetic dipole rates are typically stronger than E2 rates, so if we treat the transition as if the core was the only contributor (as in the M1 moment is the only contribution to the transition moment), this should set an upper bound on A_{BF} (which will likely be further reduced by the addition of the E2 moment).

The transition occurs at 385.4 nm, leading to a rate of 258.4 Hz. This suggests that this could be a potential pathway to faster shelving if the appropriate repump lasers are used.

8.6.2 Addition of 3.4 μm laser

There is potential for using a 3.4 μm laser to drive the $^2\mathrm{D}_{5/2} \leftrightarrow {}^2\mathrm{F}^o_{7/2}$ transition to speed up the population transfer process. A number of ideas have been discussed as to how this would be performed, a few of which are outlined below.

- Perform multiple population transfer steps in the form of a coherent π-pulse with the 411 nm laser, followed by a coherent π-pulse with the 3.4 μm laser to the $^2\mathrm{F}^o_{7/2}$. This can be repeated many times, each time the population is transferred to a new magnetic

sublevel in the $^2F^o_{7/2}$. The difficulty here is the effective need for two operational optical qubits just for electron shelving.

- Stimulated Raman adiabatic passage (STIRAP)

- Instead of performing sequential π-pulses at 411 nm and 3.4 μm, an off resonant two photon stimulated Raman transition transition could be performed directly from $^2S_{1/2}$ to $^2F^o_{7/2}$.

CHAPTER 9

The Metastable Qubit

9.1 The metastable qubit platform

In laser cool-able trapped ion species with non-zero nuclear spin, there can exist excited states that have moderately long lifetimes ($>$ 1s) which exist outside of the standard cycling transition and possess hyperfine structure. The hyperfine interaction generates convenient energy intervals in these excited states, between which we can define a qubit.

These species are required, in this scheme, to possess a suitable ground state qubit (g-type), a moderately long lived metastable state ($>$ 1s) with a convenient metastable state qubit (m-type), and a means of performing coherent population transfer via an optical transition between the g and m qubit types (o-type). In $^{171}Yb^{+}$, the OMG (**O**ptical, **M**etastable, and **G**round) qubits are detailed below

- **g-type**: hyperfine zero-field clock qubit defined between the $^2S_{1/2}\,|F=0\rangle \leftrightarrow {}^2S_{1/2}\,|F=1, m_F=0\rangle$ states.
- **m-type**: hyperfine zero-field clock qubit defined between the $^2F^o_{7/2}\,|F=3, m_F=0\rangle \leftrightarrow {}^2F^o_{7/2}\,|F=4, m_F=0\rangle$ states. Like the ground state, there are other options for defining a qubit in this excited manifold, but the clock state is chosen for its low magnetic field sensitivity.
- **o-type**: Electric octupole transition between the $^2S_{1/2}$ g-type states and the $^2F^o_{7/2}$ m-type states. This is the proposed o-type scheme, but there may be other options for performing two step coherent transfer via less restrictive transitions.

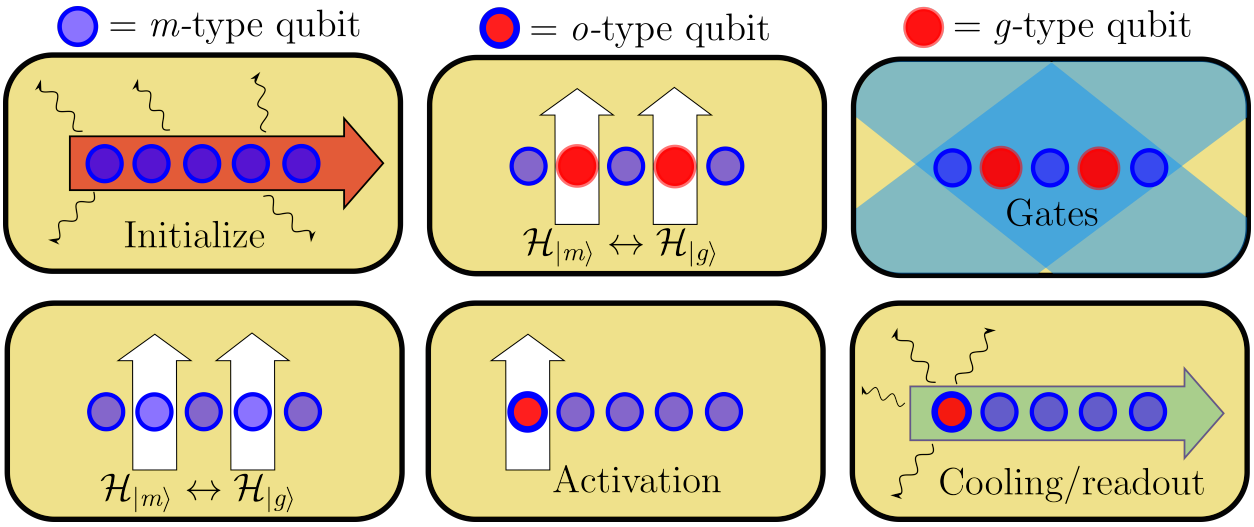

Figure 9.1: The $^{171}Yb^{+}$ metastable qubit scheme. Each primitive operation is performed in one of the three qubit types, all three are necessary for full operation of the o-m-g qubit quantum information processor.

Let's run through the 6 steps outlined in Figure 9.1:

- **Initialization**: all qubits can be prepared in one of the basis states of the m-type Hilbert space. This can be done in a heralded fashion by utilizing dissipative population transfer to the metastable manifold along with a few additional operations, but that may be slow and scales poorly to many qubits. A preferable method would be to first prepare the g-type qubit in $|0\rangle_g$, and utilize the o-type operation to map the g-type Hilbert space to the m-type Hilbert space. Then, the state preparation can be heralded via laser induced fluorescence in the g-type manifold.

- **Activation**: multi-qubit gates can be performed in the g-type qubit, so individually addresses o-type operations will perform the desired m-type to g-type Hilbert space shuttling ($\mathcal{H}_{|m\rangle} \leftrightarrow \mathcal{H}_{|g\rangle}$) prior to the multi-qubit gate. This will either be achieved by the one step 467 nm E3 transition, or potentially a multi step coherent population transfer (3.43 μm followed by 411 nm, for instance)

- **Gates**: multi-qubit gates, as well as single qubit gates if necessary, will be driven in the g-type Hilbert space via stimulated Raman transitions coupling the g-type qubit to the motion of the crystal.

- **Archive**: Following g-type gate operations, the quantum information in the g-type qubits will be shuttled in Hilbert space ($\mathcal{H}_{|m\rangle} \leftrightarrow \mathcal{H}_{|g\rangle}$) to the m-type manifold for storage. This is essential so that subsequent multi-qubit gates not containing those particular physical qubits can be performed without cross-talk with the m-type Hilbert space (although the motion of the collective crystal can still be excited).

- **Activation**: prior to dissipative state readout or conversion of a physical qubit into a refrigerant ion, an m-type qubit can be mapped to the g-type qubit via individually addressed o-type operations.

- **Cooling/readout**: o-type operation can perform full/partial m-to-g Hilbert space mapping for qubit state readout. This can in fact be performed by either coherent operation with the o-type qubit, or entropically (yet still state selectively) with the 760 nm lasers.

This scheme takes advantage of the various properties of the m-type and g-type qubit and utilizes both Hilbert spaces to perform flexible operations.

9.1.1 Alternative scheme for $^{171}Yb^{+}$

The $^{171}Yb^{+}$ metastable qubit platform is unique in the fact that the "metastable" manifold is more of a "stable" manifold, acting almost like a second ground state due to its extreme lifetime ($\tau \sim 5$ years). This provides the opportunity to potentially operate the $^{171}Yb^{+}$ system in a different way, where all qubit (unitary) operations are performed in the m-type qubit, and all dissipative operations are performed in the g-type manifold (which in this case is not utilized as a computational qubit).

This configuration removes the need for coherent o-type operations, replacing them with m-type qubit state selective dissipative population transfer to the g-type manifold. An outline is given below in Figure 9.2.

- **Initialize**: ions to be used as physical qubits are initialized into one of the m-type

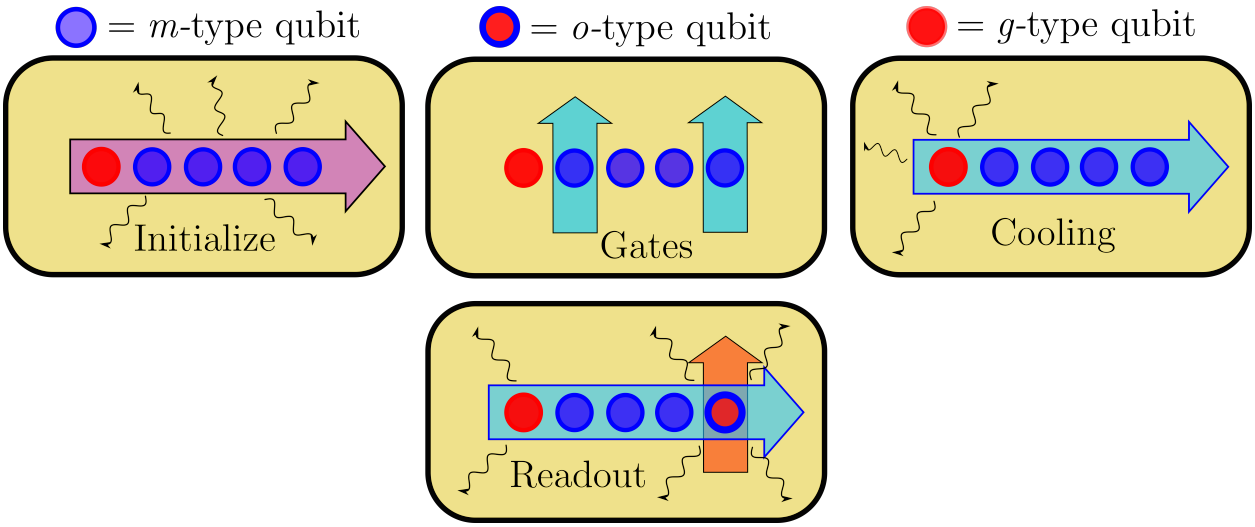

Figure 9.2: Alternate scheme for $^{171}Yb^{+}$ metastable qubit

qubit basis states, which can be done as described in the previous section. Ions that are to remain as refrigerant ions can remain in the g-type manifold.

- **Gates**: both single qubit and multi qubit gates will be performed by individually addressed lasers in the m-type manifold. Options for these gates will be discussed later.

- **Cooling**: ions initialized in the ground state will remain as refrigerant ions, where standard Doppler cooling and resolved sideband cooling can be performed to cool the motional modes of the crystal. The arrangement of refrigerant ions within the chain of physical qubits is flexible and can be optimized for a particular system.

- **Readout**: Either m-type qubit computational basis state can be state selectively returned to the g-type manifold with the application of 760 nm and 976 nm laser light (other options exist).

9.2 Single and multi *m*-qubit gates

The metastable qubit will be hosted in the $^{2}F^{o}_{7/2}$ excited state in Yb^{+}. If the isotope of choice is $^{171}Yb^{+}$, some choices could be

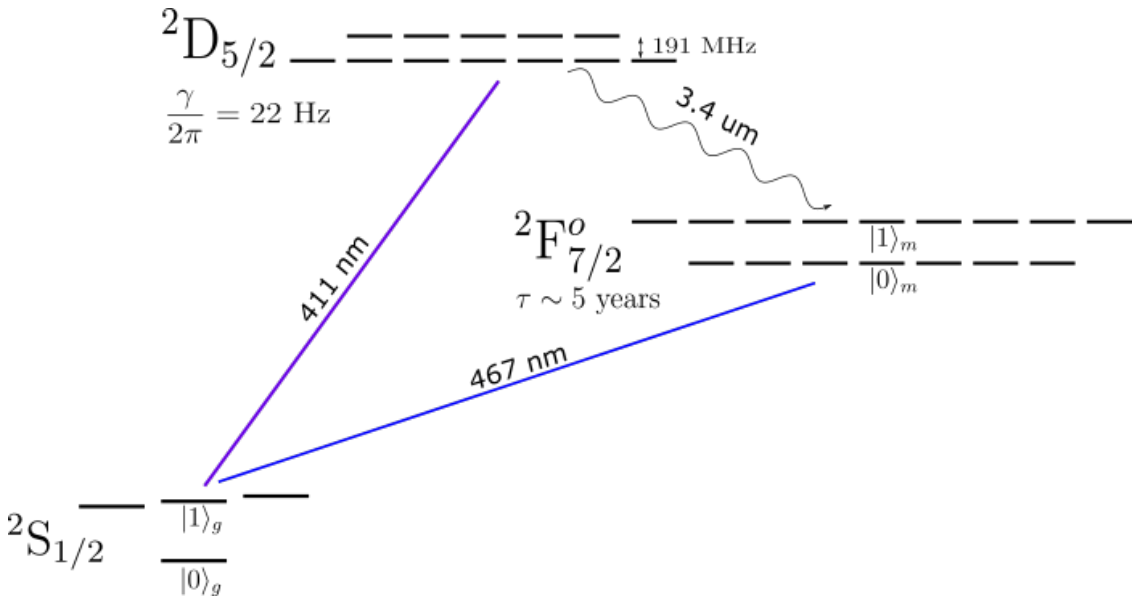

Figure 9.3: Diagram of the OMG system in $^{171}Yb^+$. The ground state qubit is hosted in the $^2S_{1/2}$, and the metastable qubit is hosted in the $^2F^o_{7/2}$. The o-type qubit can be operated at 467 nm by directly driving the $^2S_{1/2} \leftrightarrow ^2F^o_{7/2}$ electric octupole transition, or by performing a stimulated Raman transition mediated by the $^2D_{5/2}$. In the latter case, the 411 nm leg of the transition is mediated by an electric quadrupole moment, and the 3.4 μm leg is mediated by an electric dipole moment.

- Hyperfine clock states: $^2F^o_{7/2}|F=3, m_F=0\rangle$ and $^2F^o_{7/2}|F=4, m_F=0\rangle$
- Stretched hyperfine qubit: $^2F^o_{7/2}|F=3, m_F=\pm 3\rangle$ and $^2F^o_{7/2}|F=4, m_F=\pm 4\rangle$
- Any other combination of allowed M1 transitions: $^2F^o_{7/2}|F=3, m_F\rangle$ and $^2F^o_{7/2}|F=4, m_F=m_{F'}\rangle$

If utilizing $^{173}Yb^+$, there are numerous choices since there will exist 6 hyperfine manifolds. Regardless of the choice, we want to know what laser will best allow us to perform individually addressed single qubit gates (with good motional coupling), and multi qubit gates in the metastable qubit. If we wish to couple the qubit to a strong transition our options are

- Single qubit gate: stimulated Raman process with E1 coupling
- Multi qubit gate: MS ($\sigma_X\sigma_X$) gate coupled to same E1 transition

Alternatively, we can couple our qubit to a weaker transition, likely an electric quadrupole transition. If this path is chosen, the options are

- Single qubit gate: stimulated Raman process with E2 coupling
- Multi qubit gate: light-shift gate ($\sigma_Z\sigma_Z$) coupled to same E2 transition

Alternatively, a suitable E2 transition can also be used as an optical based qubit. There are also a multitude of optical M1 transitions that should exhibit stronger couplings than the E2 transitions, but most seem to have short lifetimes due to E1 coupling to less energetic levels such as the D_J states.

9.2.1 Strong transitions

Data from the NIST spectral database the the DREAM project databases will show that there are only a few options for coupling the metastable qubit to a strong transition. The table below summarizes all E1 allowed transitions with $\lambda > 320$ nm.

Electric Dipole Allowed Transitions from $^2F_{7/2}$			
State	Wavelength [nm]	Partial Linewidth [MHz]	Lifetime [ns]
$(7/2, 0)_{7/2}$	377.45	$2\pi\times$ 0.101	41.5
$(7/2, 1)_{7/2}$	363.88	$2\pi\times$ 1.21	31.8
$(7/2, 1)_{9/2}$	358.65	$2\pi\times$ 1.98	29.2
$(7/2, 1)_{5/2}$	356.13	$2\pi\times$ 2.46	28.8

Table 9.1: Electric dipole transitions: listed above are the lowest lying E1-allowed transitions excluding the transition to the $^2D_{5/2}$. Partial linewidths are given by the corresponding Einstein A coefficient from the DREAM database. Lifetimes of the excited states are calculated via $\tau = \frac{1}{\sum_j A_{ij}}$ for an excited state i and all states j to which an E1 decay is allowed from excited state i.

There will be a few questions we want to answer about these potential candidates: what is the laser technology like at these wavelengths, and with that technology what are the attainable Rabi frequencies and error rates. With the given range of wavelengths of the available E1 transitions, it seems natural to ask if there is an optimum for using a single

laser for gates in the ground state qubit *and* the metastable qubit. The ground state qubit can be flexible, and gates can be operated ± 20 nm from 369 nm, so it is worth considering if there is a certain wavelength selection that would work well for both qubits.

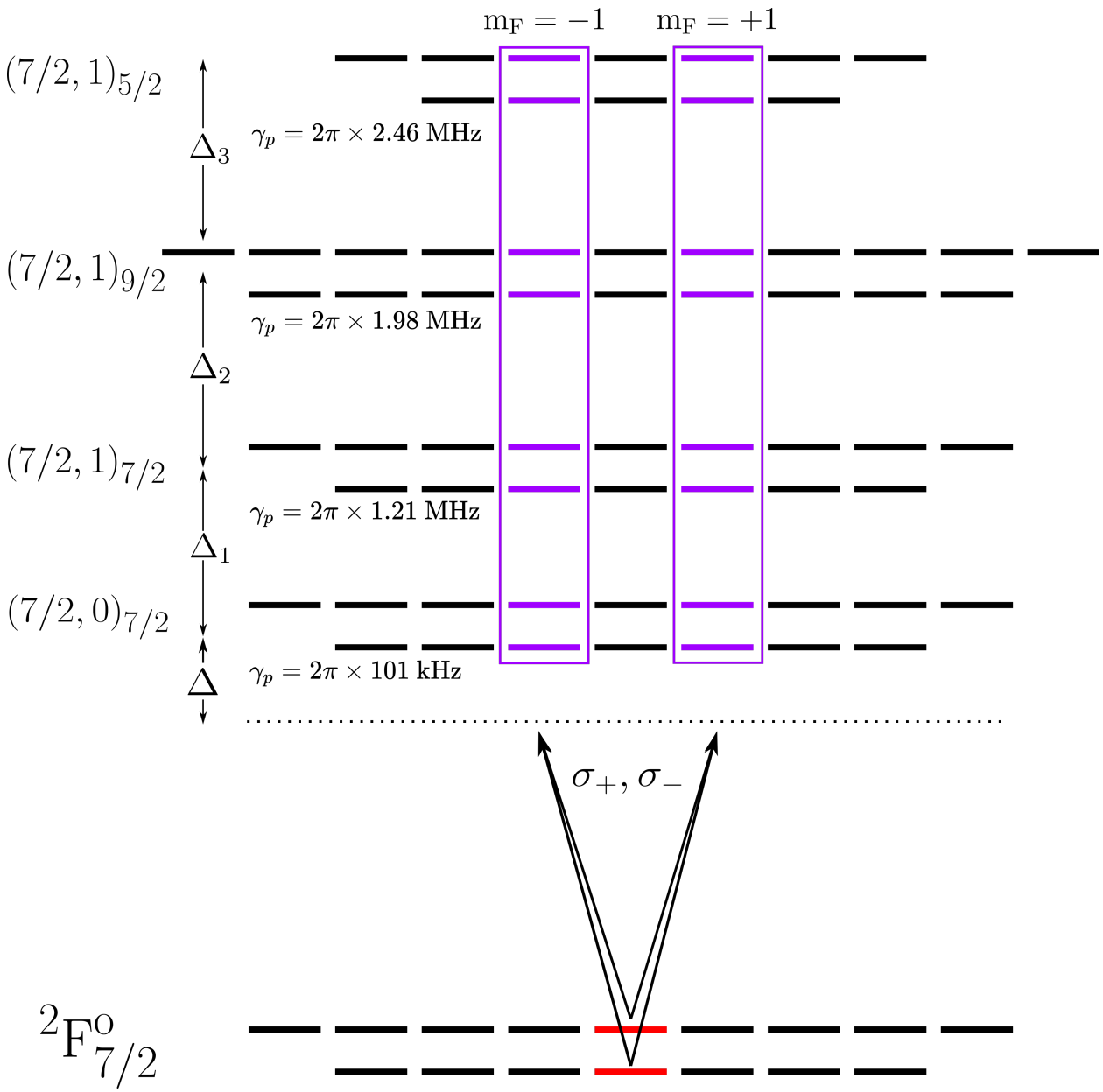

Figure 9.4: Relevant levels for E1 mediated stimulated Raman transitions between metastable qubit states. Each state is labeled with the partial linewidth, γ_p. A pair of Raman beams with σ_+, σ_- polarization in equal amounts will drive metastable qubit transitions via a beatnote at the qubit frequency and coupled to the excited states. The Raman lasers have equal detunings below the lowest level by an amount Δ, and the excited states have fine structure splittings $\{\Delta_1, \Delta_2, \Delta_3\} = 2\pi \times \{29.62, 12.02, 5.9\}$ THz.

An important quantity when considering stimulated Raman transitions mediated by electric dipole transitions will be the dipole matrix element between the ground and excited states. In this case, the electric dipole interaction Hamiltonian is $\mathcal{H}_{E1} = \mathbf{d} \cdot \mathbf{E}$. Here, $\mathbf{d} = e\mathbf{r}$ is the electron dipole moment and $\mathbf{E} = \mathcal{E}\hat{\epsilon}$ is the applied electric field with field strength $\mathcal{E}$ and polarization unit vector $\hat{\epsilon}$. A general state that we will be considering will have quantum numbers {F, m_F, J, L, S, I}. These are still good quantum numbers for the ground state ($^2F_{7/2}$), but **LS** coupling is no longer the good coupling scheme for all the excited states under consideration here. These excited states are best represented in the J_1J_2 basis. All four of these states consist of an unfilled $4f$ shell with 13 electrons, a single electron in an outer $6s$ shell, and an excited electron in a outer $6p$ shell. The J_1J_2 coupling scheme first couples the spin and orbital angular momenta of the core and outer electrons separately, and then couples the core total angular momentum to the outer total angular momentum.

$$\begin{aligned} J_c &= l_c + s_c \\ J_o &= l_o + s_o \\ J &= J_c + J_o \end{aligned} \tag{9.1}$$

Parentheses states $(J_c, J_o)_J$			
Term symbol	Electron Configuration	(l_c, s_c)	(l_o, s_o)
$(7/2, 0)_{7/2}$	$4f^{13}(^2F^o_{7/2})6s6p(^3P^o_0)$	(3, 1/2)	(1, 1)
$(7/2, 1)_{7/2}$	$4f^{13}(^2F^o_{7/2})6s6p(^3P^o_1)$	(3, 1/2)	(1, 0)
$(7/2, 1)_{9/2}$	$4f^{13}(^2F^o_{7/2})6s6p(^3P^o_1)$	(3, 1/2)	(1, 0)
$(7/2, 1)_{5/2}$	$4f^{13}(^2F^o_{7/2})6s6p(^3P^o_1)$	(3, 1/2)	(1, 0)

Table 9.2: Parentheses states under consideration for E1 mediated stimulated Raman transitions. The two outer electrons are in the spin triplet state in the lowest lying level, and in the spin singlet state for the three excited states. There also exist $(7/2, 2)_J$ states when the outer electrons are in the spin triplet state and $J_o = |l_o + s_o| = 2$ as apposed to $J_o = |l_o - s_o| = 0$.

It is worth looking at is what is happening in these transitions at the electron orbital level. The initial state the $^2F^o_{7/2}$ where the electron configuration is $4f^{13}(^2F_{7/2})6s^2$ and we

transfer to states that look like $4f^{13}(^2\mathrm{F}_{7/2})6s6p(^3\mathrm{P}_J)$. This is a bit similar to a Helium-like transition from a filled valence S shell ($^1\mathrm{S}_0$) to an excited two electron configuration with an electron in the s orbital and the other excited to a p orbital ($^{2S+1}\mathrm{P}_J$). The electron spin does not partake in the electric dipole interaction, so $\Delta S = 0$. The electron configurations for the aforementioned parentheses states will reveal that the leading order term in the wavefunctions are all $^3\mathrm{P}_J$ for the valence electrons, which would seem to indicate all of these transitions are dipole forbidden to leading order. A deeper dive will reveal that there are in fact higher order terms contributing to the wavefunction, listed below.

$$\begin{aligned}
(7/2,0)_{7/2} &= (86.8\%)\{^2F_{7/2},^3P_0\} + (9.1\%)\{^2F_{7/2},^3P_1\} + (2.2\%)\{^2F_{7/2},^3P_2\} \\
(7/2,1)_{7/2} &= (84.2\%)\{^2F_{7/2},^3P_1\} + (10.1\%)\{^2F_{7/2},^3P_0\} + (\mathbf{2.8}\%)\{\mathbf{^2F_{7/2},^1P_1}\} \\
(7/2,1)_{9/2} &= (90.8\%)\{^2F_{7/2},^3P_1\} + (\mathbf{4.4}\%)\{\mathbf{^2F_{7/2},^1P_1}\} + (1.7\%)\{^2F_{7/2},^3P_1\} \\
(7/2,1)_{5/2} &= (85.1\%)\{^2F_{7/2},^3P_1\} + (\mathbf{5.2}\%)\{\mathbf{^2F_{7/2},^1P_1}\} + (4.8\%)\{^2F_{7/2},^3P_2\}
\end{aligned} \tag{9.2}$$

The percentages to not total up to 100% because there exist smaller contributions from other electron configurations not included in the literature. As can be seen, the states with outer electrons in a spin singlet configuration ($s_o = 0$) have overlap with a $^1\mathrm{P}_1$ like wavefunction, which would possibly provide a non-vanishing contribution to the electric dipole moment between the metatstable manifolds and these excited states.

One potentially insightful option is to express the states expressed in the J_1J_2 basis in the LS basis, just like the lower state. This may help provide some intuitive reasoning as to what kind of interaction may couple these states. Recoupling of four angular momenta is covered in many texts (see for example *Zare*).

$$|(j_1 j_4) j_{14} (j_2 j_3) j_{23} j m_j\rangle = \sum_{j_{12}, j_{34}} \sqrt{(2j_{12}+1)(2j_{34}+1)(2j_{14}+1)(2j_{34}+1)} \times \begin{Bmatrix} j_1 & j_2 & j_3 \\ j_4 & j_5 & j_6 \\ j_7 & j_8 & j_9 \end{Bmatrix} |(j_1 j_2) j_{12} (j_3 j_4) j_{34} j m_j\rangle \tag{9.3}$$

Where the term in $\{\cdots\}$ is a Wigner 9-j symbol. Most programs do not have built in functions for the 9-j symbol, but regularly do for the Wigner 3-j and 6-j symbols (i.e. python, Mathematica). It will be useful then to relate the 9-j symbol to a sum over 6-j symbols, which is

$$\begin{Bmatrix} j_1 & j_2 & j_3 \\ j_4 & j_5 & j_6 \\ j_7 & j_8 & j_9 \end{Bmatrix} = \sum_{k_{min}}^{k_{max}} (-1)^{2k} (2k+1) \begin{Bmatrix} j_1 & j_4 & j_7 \\ j_8 & j_9 & k \end{Bmatrix} \begin{Bmatrix} j_2 & j_5 & j_8 \\ j_4 & k & j_6 \end{Bmatrix} \begin{Bmatrix} j_3 & j_6 & j_9 \\ k & j_1 & j_2 \end{Bmatrix} \tag{9.4}$$

Where $k_{min} = max(|j_1 - j_9|, |j_4 - j_8|, |j_2 - j_6|)$ and $k_{max} = min(|j_1 + j_9|, |j_4 + j_8|, |j_2 + j_6|)$. Using these relationships we can now expand the $J_1 J_2$ coupled states of interest in the LS basis.

$$\begin{aligned}
\left|(7/2,0)_{7/2}\right\rangle &= -\frac{1}{2\sqrt{3}} \left|^2 F_{7/2}\right\rangle - \frac{1}{2} \left|^2 G_{7/2}\right\rangle + \sqrt{\frac{5}{21}} \left|^4 D_{7/2}\right\rangle + \frac{1}{2} \left|^4 F_{7/2}\right\rangle + \frac{1}{2}\sqrt{\frac{5}{7}} \left|^4 G_{7/2}\right\rangle \\
\left|(7/2,1)_{5/2}\right\rangle &= 2\sqrt{\frac{5}{21}} \left|^2 D_{5/2}\right\rangle + \frac{1}{\sqrt{21}} \left|^2 F_{5/2}\right\rangle \\
\left|(7/2,1)_{7/2}\right\rangle &= \frac{3}{2}\sqrt{\frac{3}{7}} \left|^2 F_{7/2}\right\rangle + \frac{1}{2\sqrt{7}} \left|^2 G_{7/2}\right\rangle \\
\left|(7/2,1)_{9/2}\right\rangle &= \left|^2 G_{9/2}\right\rangle
\end{aligned} \tag{9.5}$$

Another insight from (9.2) is that in any of these transitions, the core electrons remain unaffected. Both the $^2\mathrm{F}_{7/2}$ and the excited states under consideration have a core configuration with $(l_c, s_c, J_c) = (3, 1/2, 7/2)$, which can all be ascertained from the core electron term

symbol for each state. When we consider the matrix element between the metastable ground state and the excited states, it will be the outer electrons that facilitate a non-vanishing matrix element. What we can do then is decouple the angular momenta of the ground and excited states into three parts: the nuclear spin wavefunction, the core wavefunction, and the outer electron wavefunctions. This is done with a series of angular momenta decoupling steps. First we decouple the total electron angular momentum from the nuclear spin, and then we decouple the total electron angular momentum into the core and outer angular total angular momenta. The end result is

$$
\begin{aligned}
|J_c, J_o, J, I, F, m_F\rangle &= \sum_{m_I, m_J} (-1)^{J-I+m_F} \sqrt{2F+1} \begin{pmatrix} J & I & F \\ m_J & m_I & -m_F \end{pmatrix} \\
&\left(\sum_{m_c, m_o} (-1)^{J_c - J_o + m_J} \sqrt{2J+1} \begin{pmatrix} J_c & J_o & J \\ m_c & m_o & -m_J \end{pmatrix} |J_c, m_c\rangle \, |J_o, m_o\rangle \right) |I, m_I\rangle \\
&= \sum_{\substack{m_I, m_J \\ m_c, m_o}} (-1)^{J+J_c-J_o-I+m_F+m_J} \sqrt{(2J+1)(2F+1)} \begin{pmatrix} J & I & F \\ m_J & m_I & -m_F \end{pmatrix} \\
&\begin{pmatrix} J_c & J_o & J \\ m_c & m_o & -m_J \end{pmatrix} |J_c, m_c\rangle \, |I, m_I\rangle \, |J_o, m_o\rangle
\end{aligned}
\tag{9.6}
$$

If we now consider a electric dipole matrix element between two states decomposed in identical ways, the matrix element will look like

$$
\begin{aligned}
&\langle J_c', J_o', J', I', F', m_F'| \, \mu_q^1 \, |J_c, J_o, J, I, F, m_F\rangle = \\
&= \sum_{(m',m)} f'(\{j'm'\}) f(\{jm\}) \Big(\langle J_c', m_c'| \, \langle I', m_I'| \, \langle J_o', m_o'| \, \Big) \mu_q^1 \Big(\, |J_o, m_o\rangle \, |I, m_I\rangle \, |J_c, m_c\rangle \, \Big) \\
&= \sum_{(m',m)} f'(\{j'm'\}) f(\{jm\}) \, \langle J_o', m_o'| \, \mu_q^1 \, |J_o, m_o\rangle \, \delta_{J_c', J_c} \delta_{m_c', m_c} \delta_{I', I} \delta_{m_I', m_I} \\
&= \sum_{(m',m)} f'(\{j'm'\}) f(\{jm\}) (-1)^{J_o' - m_o'} \begin{pmatrix} J_o' & 1 & J_o \\ -m_o' & q & m_o \end{pmatrix} \langle J_o'| \, |\mu^1| \, |J_o\rangle \, \delta_{J_c', J_c} \delta_{m_c', m_c} \delta_{I', I} \delta_{m_I', m_I}
\end{aligned}
\tag{9.7}
$$

where the $f(\{jm\})$ are the geometric factors in equation 9.6 and the sum over $\{m', m\}$ includes all the magnetic subcomponents from 9.6. The above procedure works, but will require some slick angular momentum algebra to end up at a result that could be obtained a bit simpler. Instead of working in the uncoupled basis from the beginning, we can begin in the $J_1 J_2$ basis, and utilize the repeated reduction formula. This is appropriate when a spherical tensor operator T_{kq} acts within one of the angular momentum sub-spaces of the total angular momentum (i.e. S_x operating on the state $|\gamma, L, S, J, m_J\rangle$). The procedure allows for the reduction of the matrix element to a single reduced matrix element dependent only on the angular momentum partaking in the interaction. In the case of the stimulated Raman transitions we are concerned with here, the assertion will be that only the outer total angular momentum, J_o, partakes in the interaction. The expression for the matrix element can be written as

$$
\begin{aligned}
&\langle J_c' J_o' J' I' F' m_f' | T_{kq} | J_c J_o J I F m_f \rangle = \\
&(-1)^{F' - m_F' + F + J' + I + J + J_o' + J_c + 2k} \sqrt{(2F+1)(2F'+1)(2J+1)(2J'+1)} \\
&\begin{Bmatrix} J' & F' & I \\ F & J & k \end{Bmatrix} \begin{Bmatrix} J_o' & J' & J_c \\ J & J_o & k \end{Bmatrix} \begin{pmatrix} F' & k & F \\ -m_F' & q & m_F \end{pmatrix} \langle J_o' || T_k || J_o \rangle
\end{aligned}
\tag{9.8}
$$

where the reduced matrix element now only depends on the total angular momentum of the outer electrons (and potentially l_o, s_o). Following the procedure from [BKD05], we can relate the reduced matrix element to the Einstein A coefficient (a.k.a. the transition partial linewidth) via

$$|\langle J_o'| \, |\mu_1| \, |J_o\rangle|^2 = \frac{3\pi\epsilon_0\hbar c^3}{\omega_o^3}(2J_o'+1)\gamma_p \tag{9.9}$$

Where μ_1 is the reduced electric dipole operator. We have now identified the spherical tensor operator as the electric dipole operator, and γ_p is the partial linewidth of the transition. This combined with equation 9.8 gives us a value for the electric dipole transition moment between any two states in the $|J_c J_o JIFm_F\rangle$ basis, given that our assumptions hold and the partial linewidth of the transition is known or has been calculated.

$$\begin{aligned}
&\langle J_c' J_o' J' I' F' m_f' | \mu_q^1 | J_c J_o JIF m_f\rangle = \\
&(-1)^{F'-m_F'+F+J'+I+J+J_o'+J_c}\sqrt{(2F+1)(2F'+1)(2J+1)(2J'+1)(2J_o'+1)} \\
&\begin{Bmatrix} J' & F' & I \\ F & J & 1 \end{Bmatrix} \begin{Bmatrix} J_o' & J' & J_c \\ J & J_o & 1 \end{Bmatrix} \begin{pmatrix} F' & 1 & F \\ -m_F' & q & m_F \end{pmatrix} \sqrt{\frac{3\pi\epsilon_0\hbar c^3}{\omega_o^3}\gamma_p}
\end{aligned} \tag{9.10}$$

A sanity check we can make here is to look at the stretched state transition, for which all the angular momentum factors should evaluate to 1 (including the $\sqrt{2J_o'+1}$ picked up from the reduced matrix element). For the states considered here, the stretched state transition is the ${}^2F_{7/2}\,|F=4, m_F=4\rangle \leftrightarrow (7/2,1)_{9/2}\,|F=5, m_F=5\rangle$ transition, which indeed does evaluate to 1.

Using this to evaluate the electric dipole matrix elements, the results of some basic analysis of the stimulated Raman transitions are shown in Figures 9.5 and 9.6. All plots where relevant are made assuming $P = 1$ mW per laser in a Gaussian beam with $\omega_o = 1$ μm,

The two photon Raman Rabi frequency is calculated by summing over all couplings to excited states, assuming the Raman lasers are σ_+ polarized. An expression for the Raman

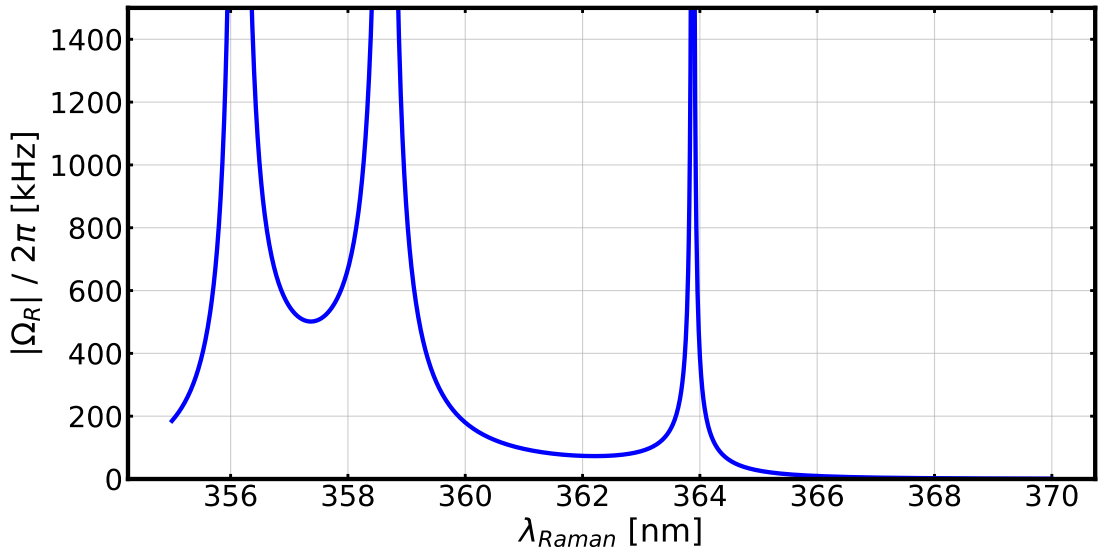

Figure 9.5: Magnitude of the two photon Raman Rabi frequency as a function of wavelength. Constructive interference occurs in the fine structure interval between the $(7/2, 1)_{5/2}$ and $(7/2, 1)_{9/2}$ states, where the optimal wavelength is found to be $\lambda_{opt} \approx 357.2$ nm.

Rabi frequency is given by

$$\Omega_R = \frac{1}{2}\mathcal{E}^2 \sum_e \frac{\langle 1| \mathbf{d} \cdot \epsilon_2 |e\rangle \langle e| \mathbf{d} \cdot \epsilon_1 |0\rangle}{\Delta_e} \tag{9.11}$$

where it has been assumed that the two laser fields have equal amplitude $\mathcal{E}$ and phase difference $\phi_1 - \phi_2 = 0$. This expression for the Rabi frequency is such that the time to make a full qubit rotation is given by $t_\pi = \pi/\Omega_R$.

A common quantity of interest is the the gate error due to spontaneous emission during a π-rotation of the qubit. This conveniently does not scale with laser power (at least not in our treatment), and thus is only a function of the atomic structure. The spontaneous emission rate from the excited state will scale as the population in the excited state, ρ_{ee}, time the spontaneous decay rate of that state, γ_e. In the large detuning limit ($\Delta_e \gg \gamma_e$), this can be written as

$$\Gamma_{SE} = \mathcal{E}^2 \sum_e \sum_{q=0,1} \sum_{i=1,2} \frac{\gamma_e}{2} p_q \frac{|\langle q| \mathbf{d} \cdot \epsilon_i |e\rangle|^2}{\Delta_e^2} \tag{9.12}$$

where the sum over q is over the qubit states, p_q is the population in a given qubit state, the sum over i is over the two raman lasers, and the sum over e is over all excited states that can be coupled to either of the qubit states by either Raman laser. For the purpose of our analysis, we assume $p_0 = p_1 = 1/2$ so that all potential laser couplings to the excited states are accounted for. The probability of spontaneous emission during a π-pulse is the just the

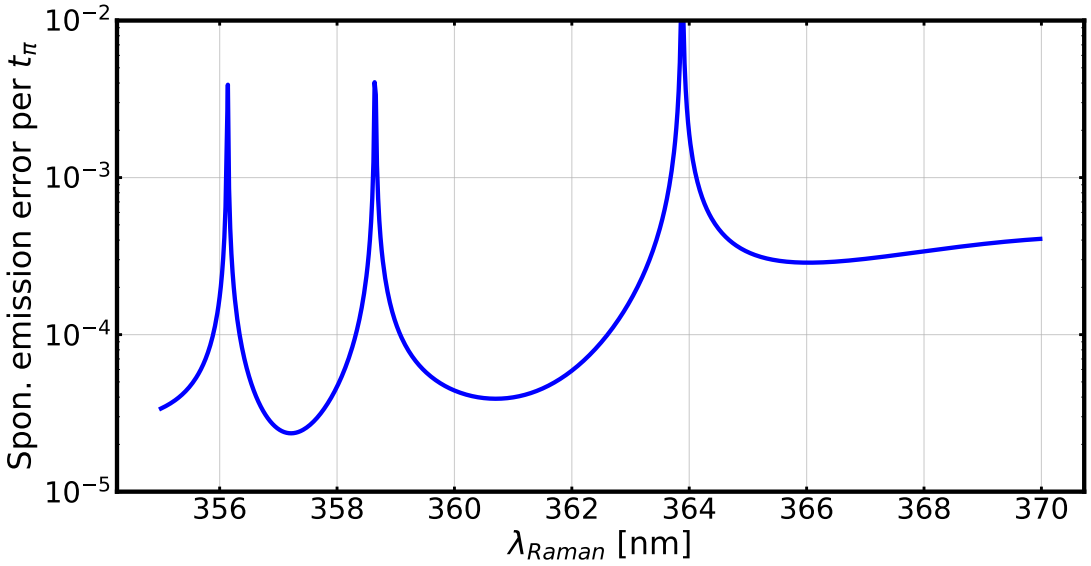

Figure 9.6

time it takes to perform the rotation times the scattering rate, $P_{SE} = t_\pi \Gamma_{SE}$. P_{SE} exhibits a minimum of 2.3×10^{-5} at $\lambda = 355.17$ nm.

9.3 Experimental progress

Below we will detail, somewhat chronologically, our experimental progress in developing primitive operations for the OMG system. As we currently have the g-type qubit well under control with the exception of resolved sideband cooling and multi qubit gates, most of our focus will be on initial spectroscopy in the $^2\mathrm{F}^o_{7/2}$ of $^{171}\mathrm{Yb}^+$ and some characterization of qubit

properties.

9.3.1 State preparation: initial scheme

In our system we do not have a way of preparing a pure state incoherently in the $^2\mathrm{F}^o_{7/2}$, so to initially find the microwave transitions we incoherently prepare multiple magnetic sublevels of the $^2\mathrm{F}^o_{7/2}\ |F=3\rangle$ by applying 411 nm laser light to drive $|0\rangle_g \rightarrow {}^2\mathrm{D}_{5/2}\ |F=2\rangle$. The polarization of the 411 nm light is chosen such that it will predominantly drive $|\Delta m_F| = 1$ transitions ($\mathbf{k} \perp \mathbf{B} \parallel \hat{\epsilon}$). This is chosen to maximally populate the $^2\mathrm{F}^o_{7/2}\ |F=3, m_F=0\rangle$ state without making and drastic changes to our system. The ion is shelved at 411 nm for 40-80 ms with the addition of our 369 nm optical pumping beam to prevent population trapping in the $^2\mathrm{S}_{1/2}\ |F=1\rangle$ levels.

Resonant microwaves are delivered to the ion via a standard ex-vacuo gain horn antenna, providing up to 16 W [1] of microwave radiation at $\omega_m \approx 2\pi \times 3.620$ GHz [2]. Microwaves are applied for a duration of $\sim$ 100 - 200 μs, and the frequency is scanned around ω_m. At the end of each interrogation, population is transferred out of the $^2\mathrm{F}^o_{7/2}\ |F=3\rangle$ manifold at 760 nm to return any population back to the ground state, where laser induced fluorescence reveals population that projected into the $^2\mathrm{F}^o_{7/2}\ |F=3\rangle$ manifold. Any successful population transfer to the $^2\mathrm{F}^o_{7/2}\ |F=4\rangle$ manifold will result in a dark ion during laser-induced fluorescence (LIF), and indicate that we are driving one of the desired microwave transitions. Early results are shown in Figure 9.7

As outlined earlier, we expect to populate the $^2\mathrm{F}^o_{7/2}\ |F=3, m_F=0\rangle$ more than any other state with our given scheme, so we focused first on the transition at $\Delta/2\pi = +534$ kHz which appears to be about 50% more populated than the other transitions (assuming that the resonant Rabi frequency of all transitions are equal, which is typically not the case). To verify that this is in fact the zero-field clock state, we perform qubit scans of this transition

[1] ZHL-16W-43-S+

[2] Signal generator is either a RF Consultant TPI-1001-B synthesizer, or a frequency octupled DDS from the Pulser operating at $f_{DDS} = 452.5$ MHz

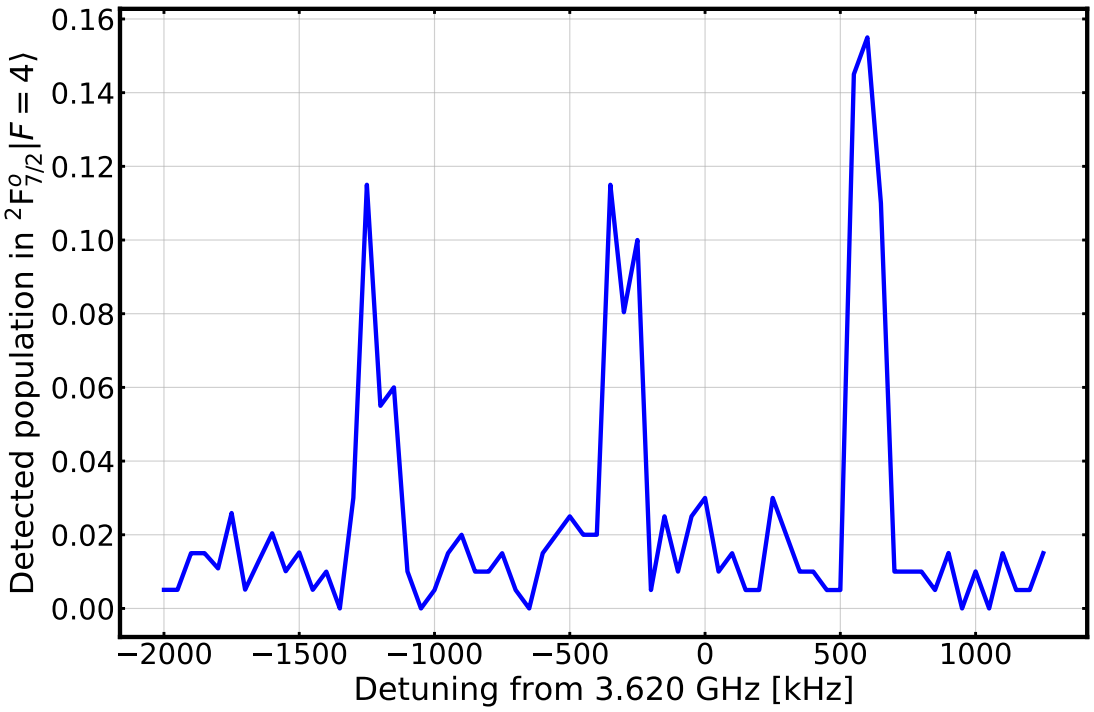

Figure 9.7: First set of microwave linescans in the $^2F^o_{7/2}$. We are able to identify the transition at $\Delta/2\pi = +534$ kHz as the clock qubit by varying the magnetic field and performing additional scans. The transitions at $\Delta/2\pi \approx -350, -1250$ kHz are identified as the $|F = 3, m_F = 3\rangle \rightarrow |F = 4, m_F = 4\rangle$ and the $|F = 3, m_F = -1\rangle \rightarrow |F = 4, m_F = -1\rangle$ transitions, respectively.

and the ground state $|0\rangle_g \rightarrow |F = 1, m_F = +1\rangle$ transition at two distinct magnetic fields to compare the energy shifts as a function of the applied magnetic field strength. As can be seen in Figure 9.8, there is no observable shift in the transition frequency for the $\Delta/2\pi = +534$ kHz transition as compared to the shift in the magnetic sensitive ground state transition, indicating this is likely the zero-field clock state transition.

With the transition frequency identified, we can perform Rabi flopping of the qubit and attempt to optimize the position of our microwave horn to maximize the Rabi frequency. Despite the additional power provided by our amplifier, we can only achieve Rabi frequencies of a few kHz in our system. This is likely due to the fact that at 3.6 GHz is it hard to deliver high intensity microwave radiation with a gain horn antenna, since the active aperture of

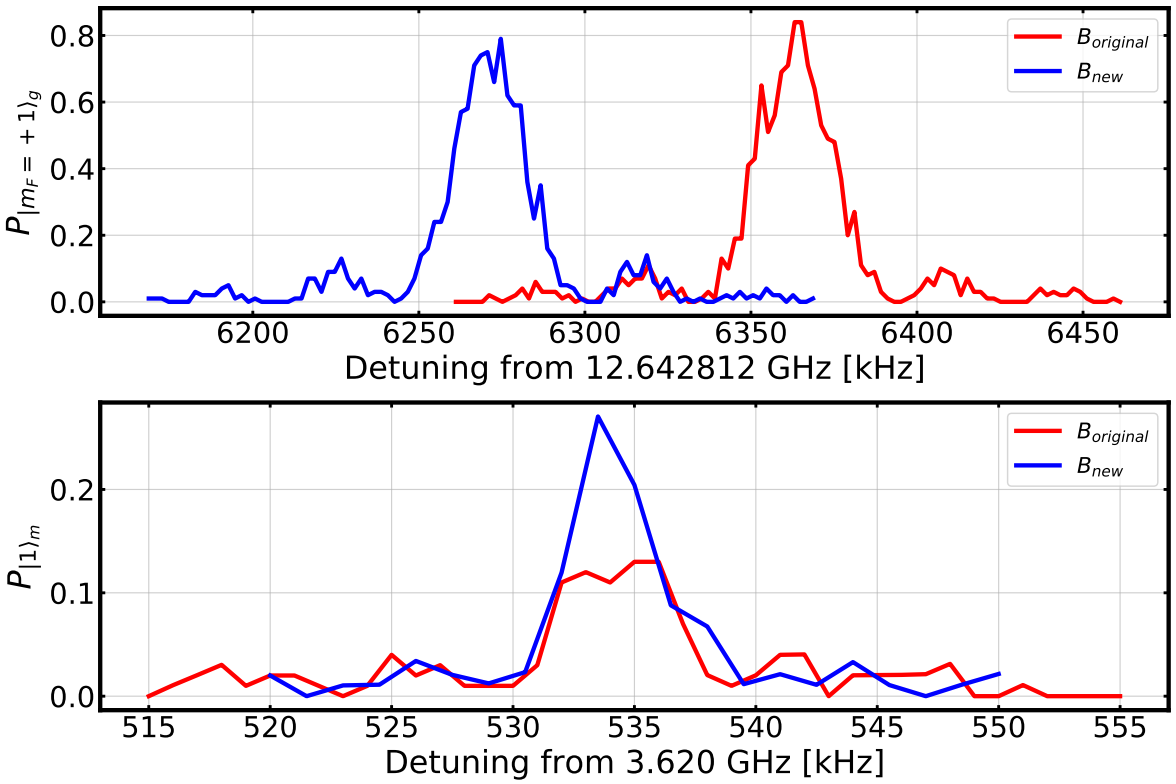

Figure 9.8: Verification of the zero-field clock state qubit transition frequency. For a magnetic field change of ≈ 70 mG, we observe no noticeable change in the metastable transition frequency. Change in transition frequency this small is also inconsistent with $m_F \neq 0, \Delta m_F = 0$ transitions that only have suppressed first order magnetic field sensitivity to the order of $\sim 0.28\mu_B$ in the $^2\mathrm{F}^o_{7/2}$ state.

the antenna (and therefore the area over which the power is delivered) is significantly larger for a 3.6 GHz antenna (87.9 mm $\times$ 110.0 mm) vs. our 12.6 GHz antenna (53.6 mm $\times$ 73.1 mm).

9.3.2 State preparation: heralding

With the ability to perform single qubit gates, we can start to think about other scheme for state preparation. We will be interesting in quantifying various qubit properties such as coherence time, precise qubit frequency, and state preparation and measurement fidelity. Generally these experiments will require or be aided by high fidelity state initialization, which is also a general quality we want to develop for any qubit.

In order to prepare a single qubit state with a high degree of certainty, we can take advantage of the fact that we can return population from either qubit manifold in a state selective way to the ground state, after which LIF can provide us with additional information. It is worth noting briefly how we deshelve each manifold in the $^2\mathrm{F}^o_{7/2}$ in a state selective way:

- $^2\mathrm{F}^o_{7/2}\,|F=3\rangle$: Application of a 760 nm laser to couple the $|F=3\rangle$ to $^1[3/2]^o_{3/2}\,|F=1\rangle$ is already state selective and will not mix into the $^2\mathrm{F}^o_{7/2}\,|F=4\rangle$ manifold. The excited state can decay to the $^2\mathrm{S}_{1/2}$ with high probability, the $^2\mathrm{D}_{3/2}$ which is repumped with a 935 nm laser directly back to the $^2\mathrm{S}_{1/2}$, or to $^2\mathrm{D}_{5/2}\,|F=2\rangle$ via an electric dipole moment, which cannot mix into the $^2\mathrm{F}^o_{7/2}\,|F=4\rangle$ manifold.

- $^2\mathrm{F}^o_{7/2}\,|F=4\rangle$: Application of 760 nm laser to couple the $|F=4\rangle$ to the $^1[3/2]^o_{3/2}\,|F=2\rangle$ is not perfectly state selective. Spontaneous emission to either $^2\mathrm{D}_{5/2}$ hyperfine manifold can cause population mixing into the $^2\mathrm{F}^o_{7/2}\,|F=3\rangle$. This effect can be highly suppressed by applying 976 nm laser light coupling both $^2\mathrm{D}_{5/2}\,|F=2,3\rangle$ manifolds to the $^1[3/2]^o_{3/2}\,|F=2\rangle$ state, suppressing the decay channel into the $^2\mathrm{F}^o_{7/2}$. In theory this is ideally done with two separate resonant laser tones on the 976 nm laser with frequency difference of 191 MHz, but in practice we place the 976 nm laser between the two $^2\mathrm{D}_{5/2}$ hyperfine manifolds to off resonantly couple to both.

To herald state preparation of the m-type qubit, we start by incoherently preparing the $^2\mathrm{F}^o_{7/2}\,|F=3\rangle$ manifold just as before. We then perform a microwave pulse with pulse area $\theta=\pi$ on the qubit transition. Subsequent deshelving of the $^2\mathrm{F}^o_{7/2}\,|F=3\rangle$ manifold followed by LIF will either reveal that we have not populated the $|1\rangle_m$ state properly (indicated by finding the ion in $^2\mathrm{S}_{1/2}$, and therefore scattering many photons), or that we have (indicated by a lack of scattered photons). While this heralding process does cause us to take a hit on the number of experiments we need to perform to attain a certain statistical certainty (i.e. if heralding is only 15% efficient, and we perform 1000 experiments, we will only get 150 useful experiments on average where we heralded preparation of the $|1\rangle_m$ state), the ability to perform high fidelity state preparation is very useful for future small scale metastable qubit experiments at UCLA.

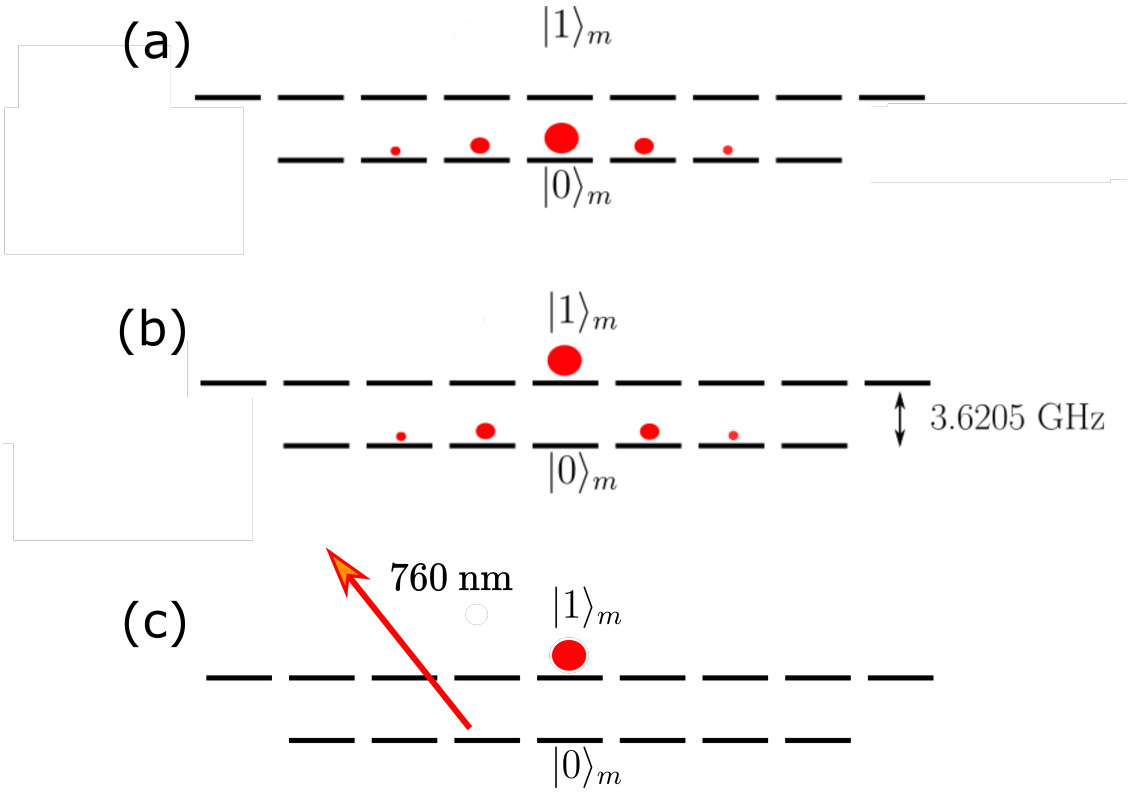

Figure 9.9: Diagramatic layout of the heralding procedure. In (a), we incoherently prepare population in the ${}^2\mathrm{F}^o_{7/2}\,|F=3\rangle$ manifold, ideally populating the $|0\rangle_m$ state as much as possible. We follow manifold preparation with a microwave π-pulse on the m-qubit to transfer population in $|0\rangle_m$ to $|1\rangle_m$, shown in (b). Following the π-pulse, we incoherently deshelve population remaining in ${}^2\mathrm{F}^o_{7/2}\,|F=3\rangle$. Subsequent Doppler cooling reveals if the the ion projected into $|1\rangle_m$ by producing no LIF photons, or that the heralding has failed by producing many LIF photons.

To exhibit the effect of heralding, we Rabi flop the qubit both with and without heralded state preparation. The difference of y-axis on this plot is simply due to the fact that when we do not herald, the initial state is the $|0\rangle_m$ state (and many other magnetic sublevels in the ${}^2\mathrm{F}^o_{7/2}\,|F=3\rangle$), where as when we perform successful heralded state preparation we are actually heralding the preparation of the $|1\rangle_m$ state.

The amplitude of the heralded Rabi curve is fitted to be 0.99(1), demonstrating that we can both herald the initial state preparation well and perform single qubit gates with reasonable fidelity. In order to understand our system better, we can perform a state preparation and measurement experiment.

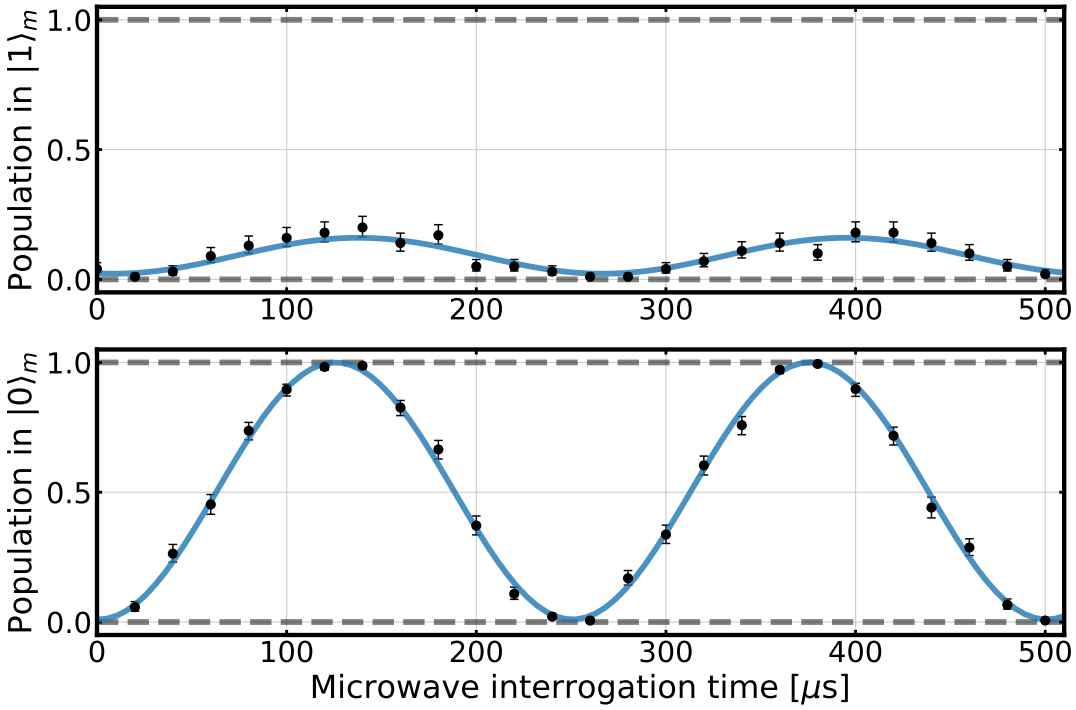

Figure 9.10: Resonant Rabi flopping of the metastable qubit, both without (top) and with (bottom) heralded state preparation of the m-qubit.

Note on heralding: in our system, we can only herald the preparation of a quantum state up to the fidelity with which we can perform that process. For instance, let's suppose we were trying to herald preparation of the $|1\rangle_m$ state by outcoupling the ${}^2\mathrm{F}^o_{7/2}\ |F=3\rangle$ manifold population, and we are not applying the 760 nm laser for a sufficient amount of time. If we only apply the 760 nm laser to return on average 80% of the population to the ground state, then there is a high probability that I do not register any photons in the laser induced fluorescence step but that I also left the ion in the $|F=3\rangle$ manifold, which would be a state preparation error. Likewise, if we do not perform LIF for a sufficient period of time to herald the state, then we will be subject to how well we can distinguish two nearby Poissonian distributions.

9.3.3 State preparation and measurement of m-qubit

Throughout our work with the m-type qubit thus far we have performed two difference SPAM measurements of the qubit with slightly different approaches to state preparation. In the first experiment, we herald state preparation of the $|1\rangle_m$ state as described in the previous section, followed by an optional microwave π-pulse to prepare $|0\rangle_m$ if that is the target state. Measurement is performed after state preparation by applying 760 nm laser light to deshelve population in the ${}^2\mathrm{F}^o_{7/2}$ $|F=3\rangle$ manifold for a period of time $t_{deshelve}$, followed by a period of LIF by applying the Doppler cooling laser light and the 935 nm repump laser light for a time t_{detect}. In this way, the $|0\rangle_m$ state can be labeled the "bright" state and the $|1\rangle_m$ state is the "dark" state.

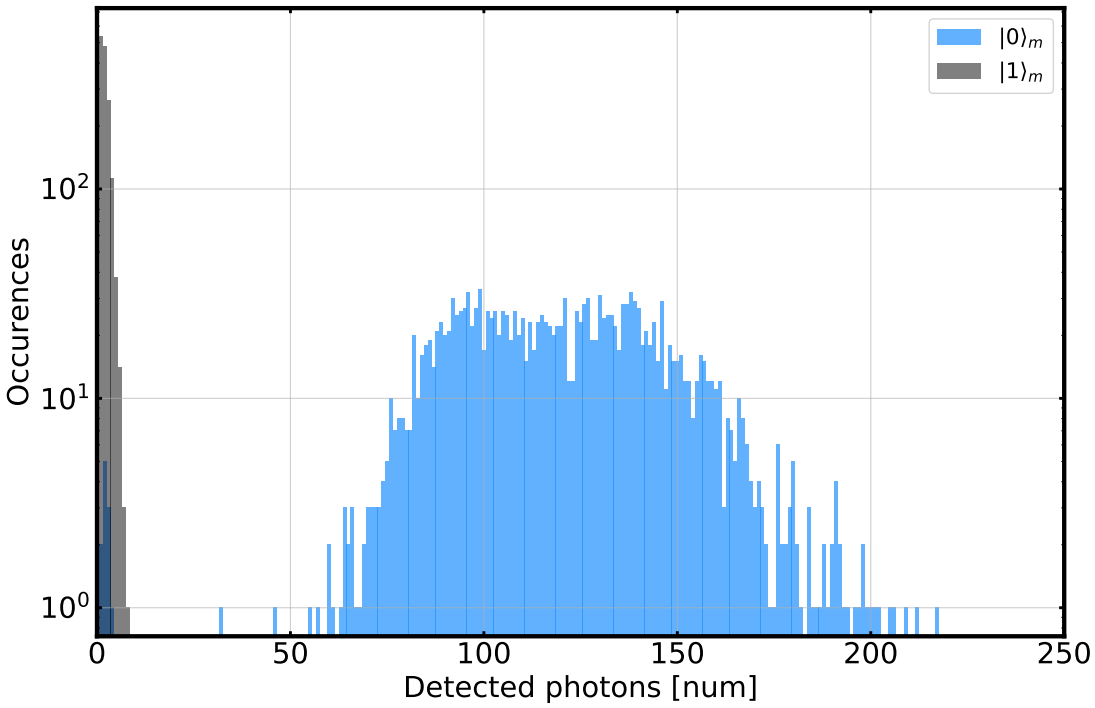

Figure 9.11: State preparation and measurment histograms of the m-type qubit where only $|1\rangle_m$ state preparation is heralded.

In this first version of the SPAM measurement, we find that our $|1\rangle_m$ state preparation

and measurement fidelity is $\mathcal{F}_{|1\rangle_m} = 1.0^{+0.0}_{-6e-4}$ in 1798 experiments, and that our $|0\rangle_m$ state preparation and measurement fidelity is $\mathcal{F}_{|0\rangle_m} = 0.994^{+1.5e-3}_{-2.0e-3}$ in 1894 experiments. The total SPAM fidelity is measured to be $\mathcal{F}_m = 0.9970^{+8e-4}_{-1e-3}$, with the histograms shown in Figure 9.11. The drift in the bright state histogram is due to our optical cavity drifting without correction over the course of the experiment. The relatively poor fidelity of the $|0\rangle_m$ state is likely due to poor characterization of the qubit transition as performing high quality Ramsey experiments to determine the transition frequency and high quality Rabi flopping to determine the proper interrogation time takes a long period of time with our heralding scheme.

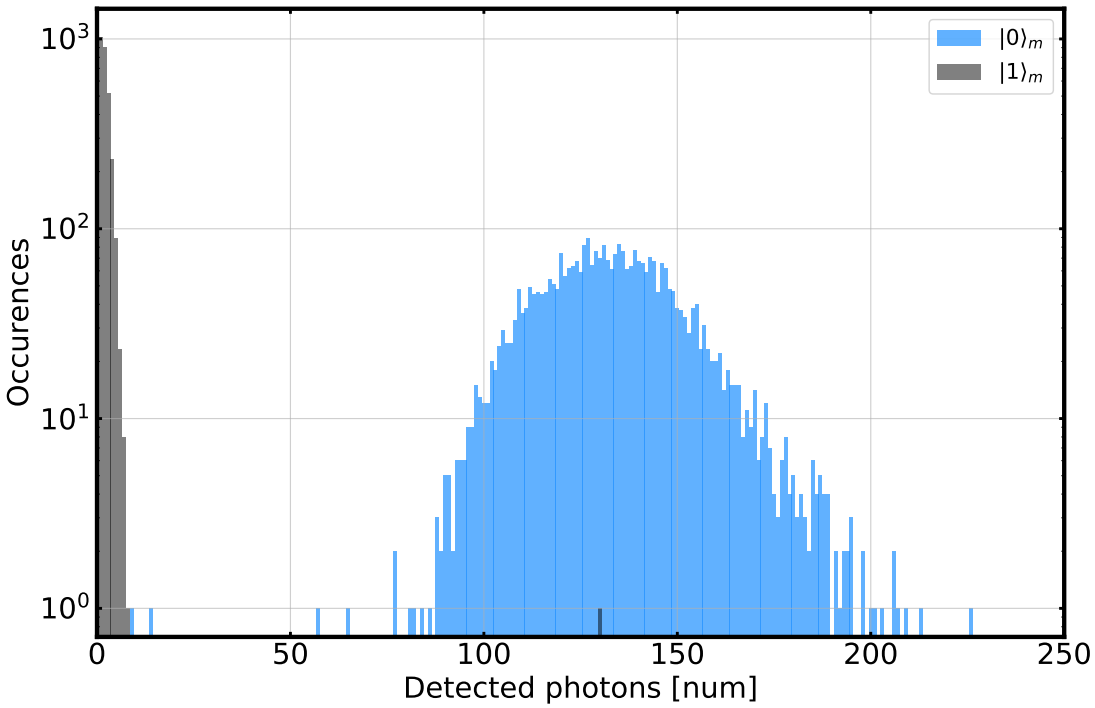

Figure 9.12: State preparation and measurment histograms of the m-type qubit where both $|1\rangle_m$ and $|0\rangle_m$ preparation is heralded.

The second SPAM measurement, with histograms shown in Figure 9.12, is very similar to the first with the exception that we herald preparation of *both* $|1\rangle_m$ and $|0\rangle_m$. This is done by inserting a heralding step after the microwave π-pulse that will state selectively deshelve

population left in the $^2\mathrm{F}^o_{7/2}\ |F=4\rangle$ to the ground state. What this effectively does is either project our ion into the $^2\mathrm{S}_{1/2}$ or into the $|0\rangle_m$ state, and we can check when the former even occurs by looking for population in the ground state. This scheme is advantageous, since so long as we can perform a reasonable π-pulse, it will not cause much experimental overhead for state preparation, and it will catch any errors we made in the microwave rotation.

In this second version of the SPAM measurement, we find that our $|1\rangle_m$ state preparation and measurement fidelity is $\mathcal{F}_{|1\rangle_m} = 0.99970^{+1.8e-4}_{-4.5e-4}$ in 3456 experiments, and that our $|0\rangle_m$ state preparation and measurement fidelity is $\mathcal{F}_{|0\rangle_m} = 1.0^{+0.0}_{-3.0e-4}$ in 3392 experiments. The total SPAM fidelity is measured to be $\mathcal{F}_m = 0.99985^{+9e-5}_{-2.3e-4}$. These fidelities are based on a procedure where we optimize the state discriminator to optimize the measured fidelity, though, and if we were running this system as an experimenter we would likely draw the histogram discriminator somewhere closer to d = 25, in the middle of the "valley of nothingness" between the histograms. With this value for the discriminator only the $|0\rangle_m$ state fidelity is changed, coming out to be $\mathcal{F}'_{|0\rangle_m} = 0.9994^{+3.0e-4}_{-6.0e-4}$ and a total SPAM fidelity $\mathcal{F}'_m = 0.99956^{+1.9e-4}_{-3.3e-4}$.

9.3.4 Limits of m-type SPAM

We unfortunately up to this point have not had a lot of time to work on the metastable qubit, an therefore have not had a lot of time to address sources of state preparation and measurement infidelity. Despite that, we can address in theory what issues there may be. We will limit out analysis strictly to the situation where we are heralding both qubit states, since this is likely the route to the lowest possible state preparation infidelity.

A first potential source of error is in the first heralding step. The main sources of error are:

- Incomplete depopulation of the $^2\mathrm{F}^o_{7/2}\ |F=3\rangle$ manifold. This should not be a problem in principle, since deshelving can readily be achieved with 1/e times of 0.5-1 ms with 760 nm and 976 nm laser light. Therefore achieving population transfer infidelities less

than 1×10^{-6} should be possible in less than 15 ms.

- Off resonant population of other magnetic sublevels in the $^2\mathrm{F}^o_{7/2}$ $|F = 4\rangle$ during first π pulse. This issue can be minimized by reducing the microwave intensity at the sacrifice of increased t_π, and should be easy to keep errors of this type below 1×10^{-6}.

- Off resonant deshelving of population of the $|1\rangle_m$ state, followed by a decay to $^2\mathrm{D}_{5/2}$, followed by a decay to $^2\mathrm{F}^o_{7/2}$. Without the 976 nm laser to clear out $^2\mathrm{D}_{5/2}$ population to the $^2\mathrm{S}_{1/2}$, this can cause an error $(2.2\%)(83\%) = 1.8\%$ of every off resonant scattering event. With the 976 nm laser present this should not be an issue.

Following the heralding of the $|1\rangle_m$ state, a microwave π-pulse is applied followed by a second heralding step. The sources of error in the second step are very similar to that of the first step, with the additional potential for improper heralding caused by insufficient suppression of the $^2\mathrm{D}_{5/2} \rightarrow ^2\mathrm{F}^o_{7/2}$ decay channel by the 976 nm laser.

9.3.5 Effects of g-type lasers on m-type qubit

One of the essential paradigms of the OMG platform is that g-type operations can be performed without necessitating physical separation of the g-type and m-type qubits. This type of operation is akin to dual-special operation in ion trap quantum information processors that is becoming more common as computational demands get higher and cooler ions are necessary for high fidelity operations [PDF20, BMS19]. We do not currently have the ability to test the effects of g-type qubit lasers on the m-type qubit, but what we can test is the effect of the 369 nm and 935 nm lasers on the m-type qubit properties.

The first thing we can check is a simple sanity test: do the 369 nm laser and 935 nm laser couple m-type qubit population out of the metastable manifold. One easy way to answer this is that if they did in such a way that population returned to the $^2\mathrm{S}_{1/2}$, there wouldn't be much need for repump lasers to depopulate the $^2\mathrm{F}^o_{7/2}$ when population gets trapped there. To check this a bit more systematically, we load two ions into the trap and pulse the 411 nm laser until one ion is in the ground state and one is in the metastable state.

We only performed this experiment a small number of times, with varying results that all point to the lasers having no observable effect on the ion. Of the times we performed this experiment we either: deshelved the dark ion manually after 10 minutes to confirm it was still there, the ion left the trap and we were left with the original bright ion, or a collision occurred (deduced by a complete drop out of fluorescence, and subsequent revival of fluorescence 10 seconds later) and the originally dark ion returned to the $^2S_{1/2}$.

To perform more systematic short timescale experiments investigating the effects of these lasers on the qubit, we perform Ramsey spectroscopy to deduce whether they cause a differential AC stark shift or a loss of qubit coherence.

Coherence measurement: to measure the coherence time of the qubit, we first herald preparation of the $|1\rangle_m$ state, followed by an immediate resonant $\pi/2$ - pulse. After a variable wait time t_{wait}, we apply a final $\pi/2$ pulse with relative phase $\phi = 0, \pi/2$ with respect to the first pulse. By performing the measurement for a given wait time twice with these two analysis phases, we can minimize the number of points we need to take on the Ramsey fringe and extract the contrast of the fringe using maximum likelihood analysis techniques.

We then perform the exact same experiment, but with the application of 369 nm and 935 nm laser light in the wait time with all the available intensity on our experiment. For us, this amounts to about 80 kW/m^2 of 935 nm laser intensity and 14 kW/m^2 of 369 nm laser intensity. The fringe contrast as a function of delay time is fit to a decaying Gaussian $\propto e^{-t^2/(2\tau)^2}$, a decay in contrast that occurs when the coherence time of the noise source causing decoherence is long compared to the wait time. The data implies that the decoherence rate due to the presence of the cooling lasers is

$$\gamma_{lasers} = (0.17 \pm 0.93) \text{ Hz} \tag{9.13}$$

which is consistent with the lasers having nearly no effect on the metastable qubit coherence in this particular experiment. Higher precision experiments will need to be carried out to determine the effect of g-type cooling lasers more precisely.

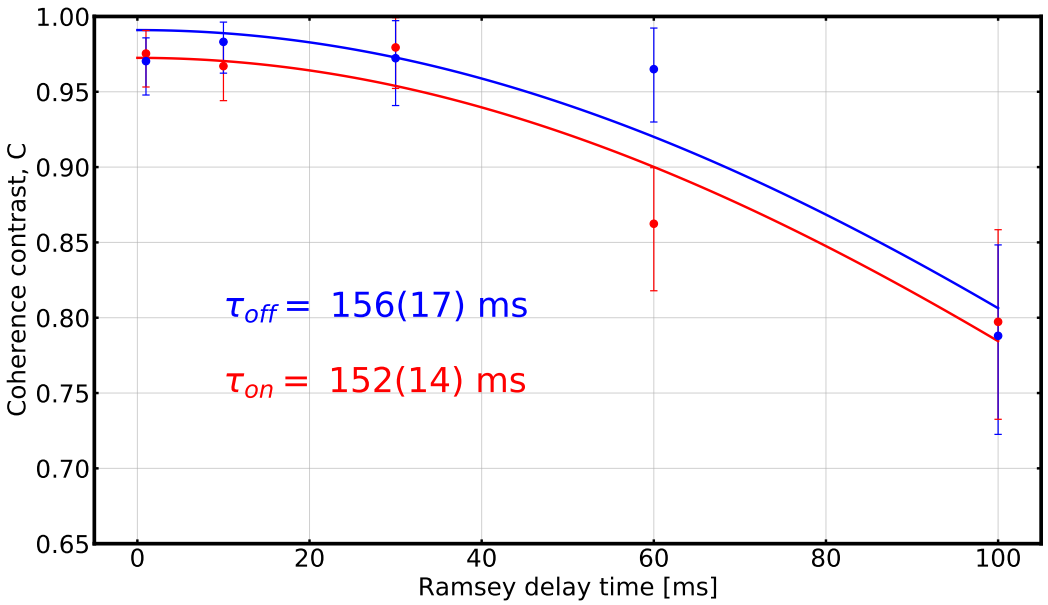

Figure 9.13: Coherence time measurement of the metastable qubit with and without g-type Doppler cooling lasers present during the Ramsey delay zone. We find no observable effect of these lasers on the metastable qubit coherence, which we believe may be limited by other factors such as the phase stability of our local oscillator.

Differential AC Stark shift measurement: To observe the effect of the lasers on the qubit energy splitting, we make a precision frequency measurement of the energy splitting via Ramsey spectroscopy again. By detuning the applied microwave from the qubit transition by $\Delta = 2\pi \times 1$ kHz and varying the delay time, we should trace out a Ramsey fringe of the form

$$P(\Delta) = \frac{1}{2}(1 + \cos(\Delta T_{delay})) \tag{9.14}$$

The measured detunings from the qubit transition for the two fringes are $\Delta_{off}/2\pi = 1.023 \pm 0.013$ kHz and $\Delta_{on}/2\pi = 1.021 \pm 0.010$, corresponding to a measured differential AC Stark shift due to the 369 nm and 935 nm lasers of

$$\Delta = 2\pi \times (2 \pm 16) \text{ Hz} \tag{9.15}$$

which is again consistent with the Doppler cooling lasers having no measurable effect on the

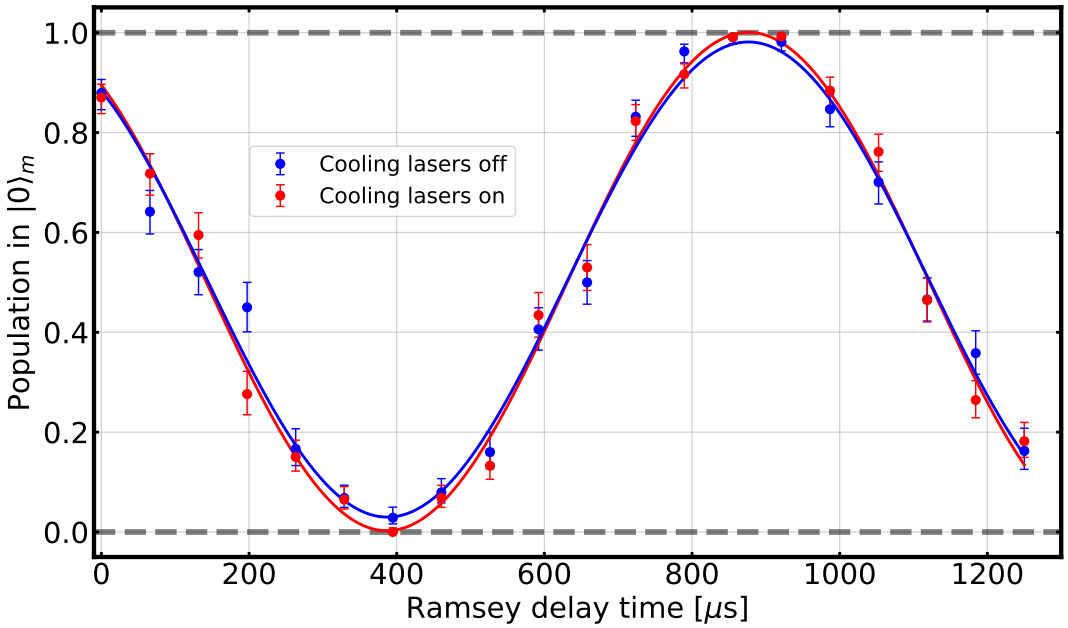

Figure 9.14: Qubit frequency measurement via Ramsey spectroscopy both with and without the g-type Doppler cooling lasers present during the variable delay time.

metastable qubit. Both of these results bode well for sympathetic cooling to the Dopppler limit of registers of m-type qubits by standard g-type refrigerant ions in the $^{171}Yb^{+}$ OMG system.

Another important test that we have not performed is to investigate sideband resolved sympathetic cooling to the motional ground state in a mixed g-type / m-type ion chain. If stimulated Raman transitions in the g-type qubit are to be used for resolved sideband cooling, the transitions in Table 9.1 will need to be taken carefully into account, as they all have the potential to be a strong channel for m-type qubit decoherence due to off resonant coupling. Of particular concern would be the popular choice of mode locked 355 nm lasers to perform this task in the g-type qubit, which is known to be a substitute for standard repump lasers for trapped population in the $^{2}F^{o}_{7/2}$.

9.4 Dissipation as a driver of quantum gates

One of the unique properties of the metastable qubit in $^{171}Yb^{+}$ is the ability to apply 760 nm laser light, and check for population in the ground state without affecting the dynamics of the metastable qubit. This led use to the idea of using measurement as a tool in the metastable qubit, potentially as a way to flag certain types of gate errors [Cam20] or to physically drive the gate. Our focus in this section will be on experiments implementing the latter type of gate, where measurement either once or many times during the gate will influence the result of the gate.

What these experiments will illuminate is how the act of measurement projects the wavefunction into the measurement basis, and how that can be taken advantage of to design schemes where full single qubit gates can be driven by projection.

9.4.1 Mid-gate projection

As a foyer into the effects of measurement during a gate, we perform some simple yet interesting experiments that can be understood with basic introductory quantum mechanics. The experiment goes as follows:

1. Herald state preparation of the $|1\rangle_m$ state
2. Perform a σ_x gate with $\theta_p = \pi$ or $\theta_p = \pi/2$.
3. Measure the qubit in the σ_z basis (when $\theta_p = \pi/2$) or the σ_x basis (when $\theta_p = \pi$).
4. Continue performing the gate from step 2.

The results of these experiments are shown below, where in each case the experiment was designed to project into one of the eigenstates of σ_z ($|\pm z\rangle$) or σ_x ($|\pm x\rangle$). In the case where the qubit was to be projected into one of the σ_x basis states at $\theta_p = \pi$, the measurement step was removed to illustrate the effect of measurement on the gate process.

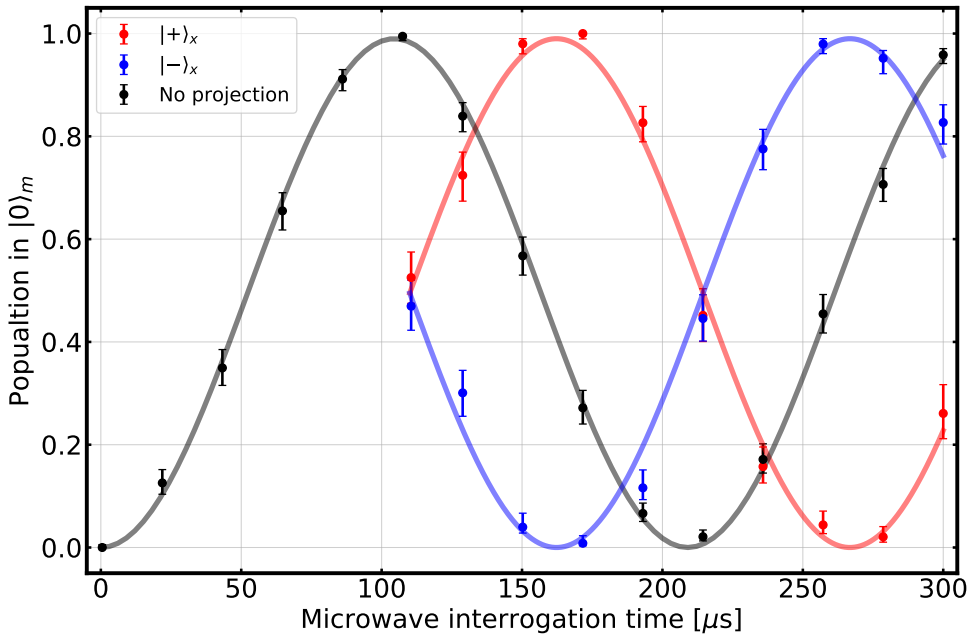

Figure 9.15: Projection onto $|\pm x\rangle$. When the qubit has reached the state $|0\rangle_m$ (an eigenstate of σ_z), we use an additional microwave pulse and a 760 nm laser to project the qubit into the σ_x basis. Blue shows an experiment designed to project onto the $|-\rangle_X$ basis state, and red shows an experiment designed to project onto the $|+\rangle_X$ eigenstate. In both cases, Rabi flopping and measurement in the σ_z basis is continued after projection. The black curve illustrates the same procedure as the blue curve, but with the projective measurement removed.

9.4.2 Gate driven by measurement

In order to drive a gate with measurement, we need to be able to measure in along an arbitrary axis on the Bloch sphere. To perform a full single qubit rotation by making N measurements, we will need to be able to measure in N different bases. For a π-pulse performed by N measurements, the protocol is as follows:

1. Herald preparation of the $|1\rangle_m$ state

2. Measure the qubit in the basis that makes an angle $\theta = \pi/N$ with the $|-z\rangle = |0\rangle_m$ axis, corresponding to a measurement in the $|\psi\rangle = \sin^2(\frac{\pi}{2N})\,|0\rangle_m + \cos^2(\frac{\pi}{2N})\,|1\rangle_m$ basis.

3. Follow step 1 by a measurements in the $|\psi\rangle = \sin^2(n\frac{\pi}{2N})\,|0\rangle_m + \cos^2(n\frac{\pi}{2N})\,|1\rangle_m$ for

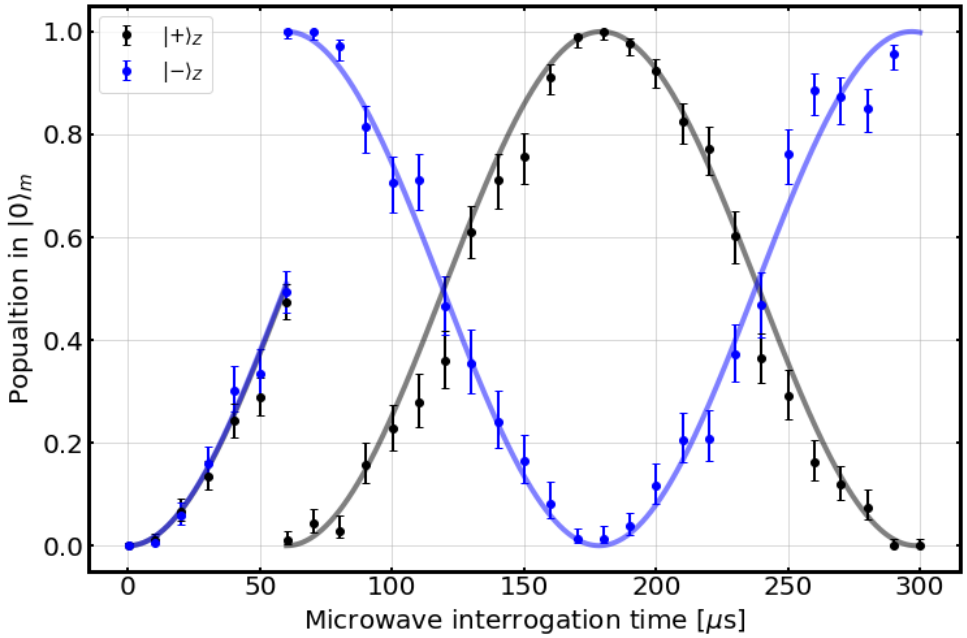

Figure 9.16: Projection onto $|\pm z\rangle$.

$n \in [2, N]$ bases.

4. At the end of the gate attempt, check for population in the $^2S_{1/2}$ which would indicate the gate failed.

5. End the protocol by checking directly for population in $|0\rangle_m$, which would indicate the gate has succeeded.

Each measurement step has a probability of success given by $\cos^2(\frac{\pi}{2N})$, which is the probability that the qubit projected onto the desired basis state. Therefore at the end of the protocol, assuming each measurement step is independent, the probability of a successful gate is $\cos^{2N}(\frac{\pi}{2N})$, and the probability of failing is $1-\cos^{2N}(\frac{\pi}{2N})$. The results of this protocol up to N = 25 are shown in Figure 9.17

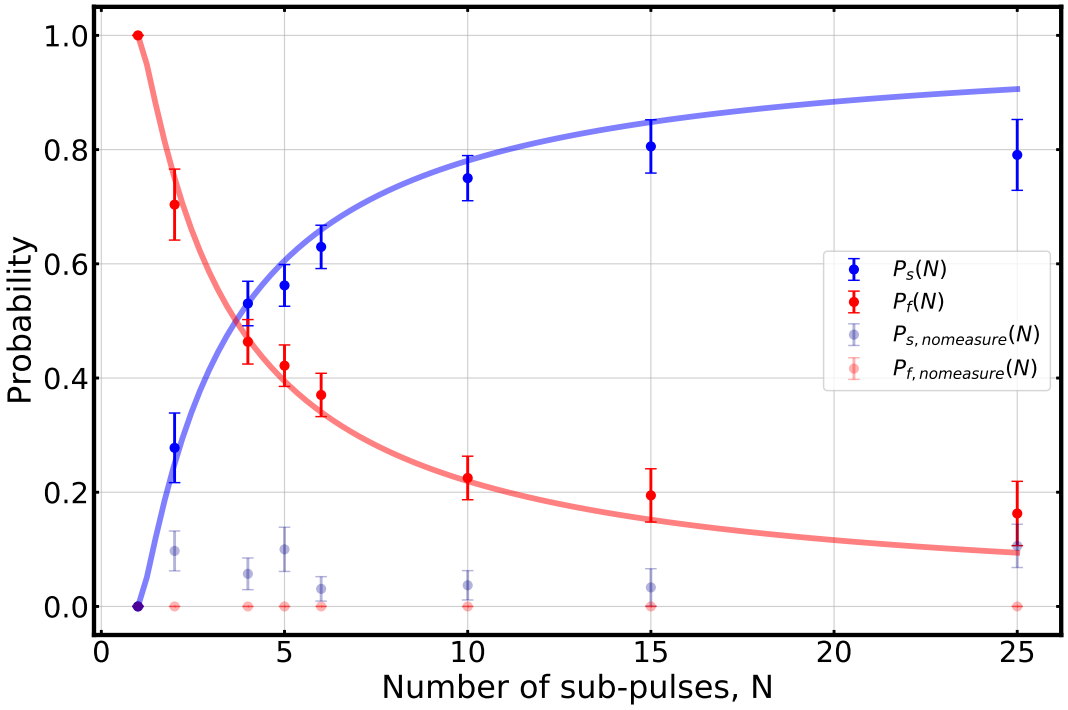

Figure 9.17: Measurement driven gate success and failure probability as a function of N.

9.5 Future work

To demonstrate the full capability of the OMG protocol in $^{171}Yb^{+}$, a few more primitives are necessary. Although $^{171}Yb^{+}$ has the arguable huge advantage of an extremely long T1 for the metastable qubit, this comes at the cost of likely much more difficult o-type operations. The original proposal was to perform o-type operations akin to how they would be performed in the other OMG-ions: via direct coupling with a laser. For other ion species considered ($^{43}Ca^{+}$, $^{88}Sr^{+}$, and $^{133}Ba^{+}$), this is an electric quadrupole transition where resonant Rabi frequencies $\sim$ MHz/mW are achievable. Comparatively, electric octupole transitions are much more challenging to drive and Rabi frequencies closer to (10 - 100) Hz/mW are achievable [FYK20]. An alternative option is to leverage stronger couplings to drive E2-E1 mediated stimulated Raman transitions via the $^{2}D_{5/2}$, where the E2 path is at 411 nm and the E1 path is at 3.43 μm.

A side note about the use of 3.43 μm light. There is a wonderful coincidence with 3.43 μm light that makes it readily integrable into most ion trap experiments utilizing Yb^+. UV grade fused silica transmission drops off pretty dramatically after $\lambda = 2.3\mu$m, and actually nearly zeroes out. But, the transmission revives and reaches a peak of about 82% at $\sim 3.3\mu$m and is approximately 77% at 3.43μm, which is a fairly minimal power hit as compared to the amount of laser intensity that will be necessary.

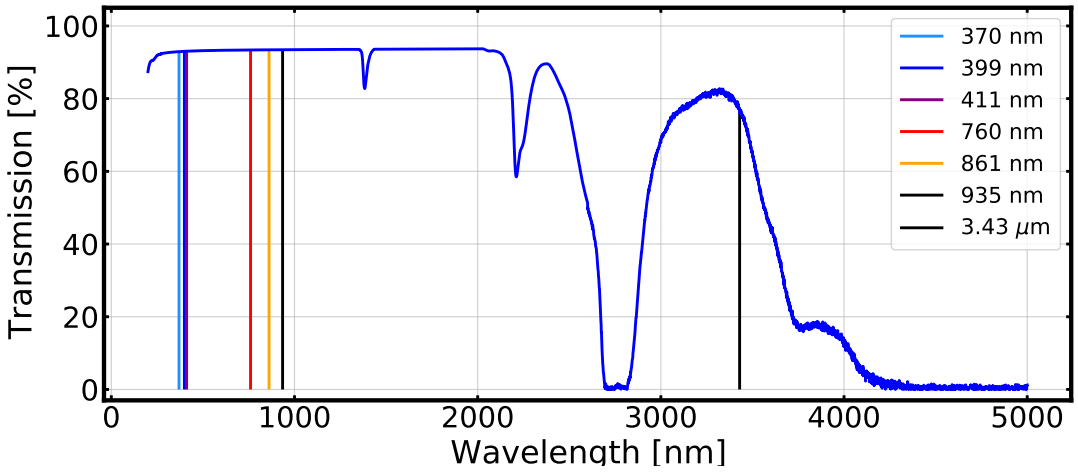

Figure 9.18: Transmission as a function of wavelength measured for uncoated UV grade fused silica. Data downloaded from ThorLabs.

Additionally, sympathetic resolved sideband cooling of an m-type qubit by a g-type qubit will be an essential component to the platform. The first thing will be to ensure that sideband cooling can be performed without deleterious effects for the stored m-type qubit. Second, if direct coupling to motion is to be investigated in the m-type qubit, enhancement of single and multi qubit gate fidelities in the metastable manifold via sympathetic ground state cooling by ground state ions will be particularly interesting.

CHAPTER 10

Ytterbium 173

The m = 173 isotope of ytterbium is the only other stable isotope that exhibits non-zero nuclear spin, with $\mathcal{I} = 5/2$. This higher order nuclear spin, and the availability of its convenient $\mathcal{I} = 1/2$ sibling, has caused $^{173}Yb^+$ to be overlooked as a resource in trapped ion quantum information experiments.

10.1 Motivation

The higher order nuclear spin allows for higher order interaction moments between the nuclear spin and the electron angular momentum, leading to higher order terms in the hyperfine interaction. Recent experiments have attempted to measure the magnitude of the higher order nuclear moments via precision spectroscopy of hyperfine structure, leading to results that differ significantly from theoretical treatments of the structure [GKK20, XLC20]. These precision measurements can give insight into various properties of the nucleus, such as its charge deformation.

Additionally, it has been suggested in theoretical treatments of the $^{173}Yb^+$ structure that the abnormally large electric quadrupole moment of the nucleus leads to perturbations of the normally hydrogen-like $^2S_{1/2}$ and $^2F^o_{7/2}$ wavefunctions such that they have a non-vanishing electric dipole moment. For certain transition lines on the typically electric octupole mediated interaction, this leads to predicted lifetimes that are potentially up to 3 orders of magnitude shorter than those coupled by the electric octupole moment alone [DF16].

To perform any experiment related to these interests, we first need to learn to trap and efficiently laser cool $^{173}Yb^+$ ions in our system.

10.2 Doppler cooling

The requirements for efficient Doppler cooling of higher nuclear spin isotopes of Yb^+ are no different than other isotopes: we need to be able to efficiently scatter photons on a strong cycling transition without population trapping in dark states. This will be achieved with the 369 nm and 935 nm lasers. The main hurdle to overcome at first is, as in $^{171}Yb^+$, we need to apply multiple microwave sidebands to each of these lasers so that population doesn't get pumping into unaddressed hyperfine levels.

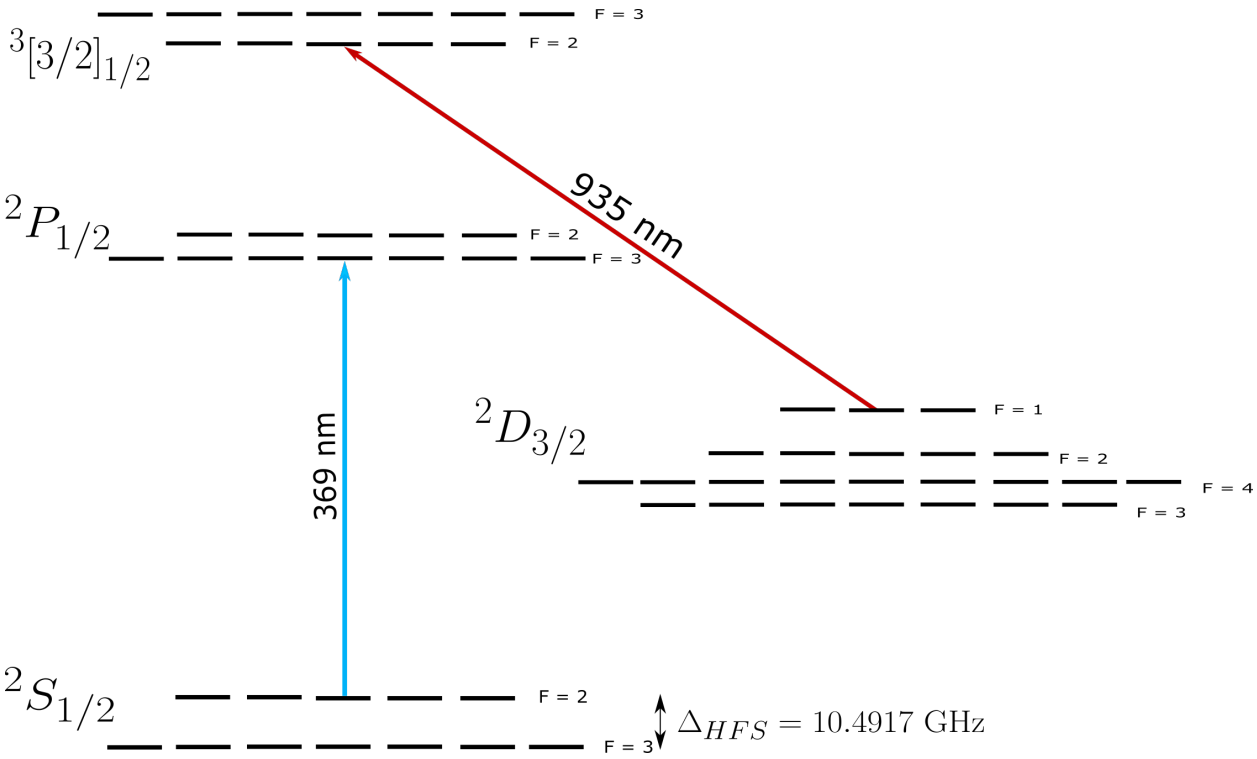

Figure 10.1: Diagram of energy levels needed for laser cooling of $^{173}Yb^+$.

The hyperfine splitting of the $^2S_{1/2}$ in $^{173}Yb^+$ was precisely measured to be $\omega_{HFS} = 2\pi \times 10.491$ GHz, corresponding to a hyperfine magnetic dipole coefficient $A = 3497$ MHz [MBG87]. It is be possible to run a full optical Bloch equation model of this system to determine an optimal laser cooling scheme given the hyperfine structure, but we have not done this. Detailed treatment of sophisticated cooling schemes for ions with complex hyperfine strucutre has been covered in [Jan15]. Instead, we choose a simple scheme where we pass

all AOM double passed 369 nm light through a resonant bulk EOM with resonant frequency 5.245 GHz. Both positive and negative frequency first order sidebands are used to address the $^2S_{1/2}\ |F=2,3\rangle \rightarrow {}^2P^o_{1/2}\ |F\rangle$ transition, where F = 2 or 3. We find that this is sufficient to achieve scattering rates comparable to what we achieve in $^{171}Yb^+$, with likely room for optimization in the future.

10.3 Theoretical hyperfine structure

Some of the more important states for laser cooling and of interest in our experiments have had some theoretical treatment to determine their hyperfine coefficients up to the electric quadrupole term. This will at the very least give us enough information to determine how to properly laser cool and formulate a plan for initial spectrsocopy of these states.

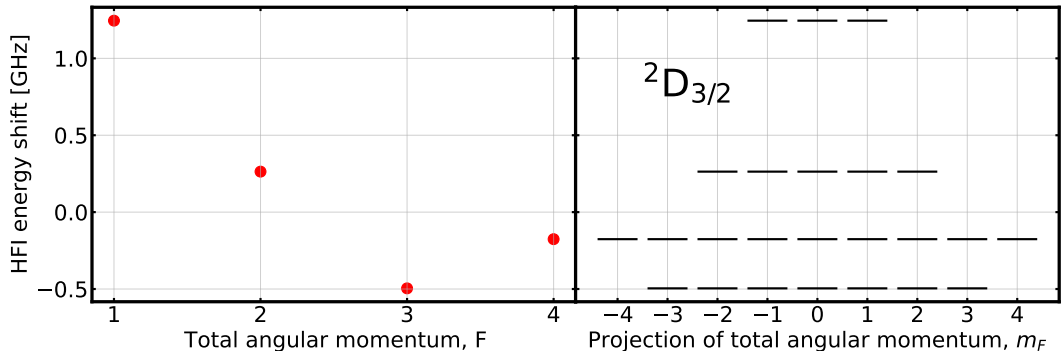

Figure 10.2: Theoretical hyperfine structure of the $^2D_{3/2}$ in $^{173}Yb^+$. The hyperfine coefficients are given in [Ita06].

Here the $^2D_{3/2}$ is shown, which exhibits a large hyperfine spitting between the F=1 and F=2 manifolds. Initial experiments to determine how to optimally laser cool $^{173}Yb^+$ began with the two 369 nm laser tones addressing the $^2S_{1/2}\ |F=2,3\rangle \rightarrow {}^2P^o_{1/2}\ |F=3\rangle$ level. Branching into the $^2D_{3/2}$ should therefore only populate the F = 2, 3 and 4 levels, which are closer energetically than the F = 1 level, although off resonant scatter to the $^2P^o_{1/2}\ |F=2\rangle$ will still occasionally populate $^2D_{3/2}\ |F=1\rangle$.

The scan shown in Figure 10.3 was taken by Doppler cooling the ion on the aforemen-

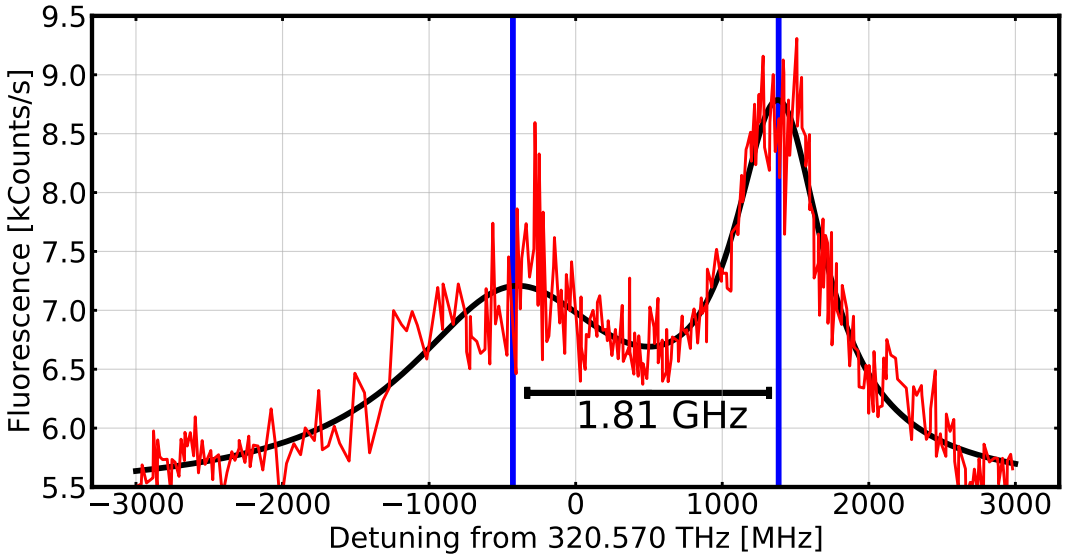

Figure 10.3: Linescans of the $^2D_{3/2} \rightarrow {}^3[3/2]^o_{1/2}$ transition taken by scanning the 935 nm laser frequency while laser cooling a single $^{173}Yb^+$ ion. The spectrum is fit to the sum of two lorentzians since the hyperfine intervals between the F = 2, 3, 4 manifolds are not resolved in these scans.

tioned transitions. The splitting of about 1.8 GHz is believed to be the hyperfine energy splitting between the $^3[3/2]_{1/2}$ F = 2 and F = 3 levels. Since this state will only have magnetic dipole hyperfine interaction, we can deduce what we would believe the hyperfine A_{M1} coefficient to be by comparison to known magnetic dipole hyperfine constants in other states in both $^{171}Yb^+$ and $^{173}Yb^+$.

$$A_{M1}^{173,B} = \frac{A_{M1}^{173,S} A_{M1}^{171,B}}{A_{M1}^{171,S}} \approx -608 MHz \tag{10.1}$$

which would give a hyperfine splitting of approximately 1.82 GHz, consistent with our measurement.

10.3.1 Future spectroscopy

To begin the high precision spectroscopy in the $^2F^o_{7/2}$, we first need to learn more about our pathway into the $^2F^o_{7/2}$, the $^2D_{5/2}$. Luckily, it appears based on theoretical values for

the hyperfine coefficients that the F = 0 hyperfine level is well separated from the remaining hyperfine levels in the $^2D_{5/2}$, as shown in Figure 10.4. This will help us build a strategy to

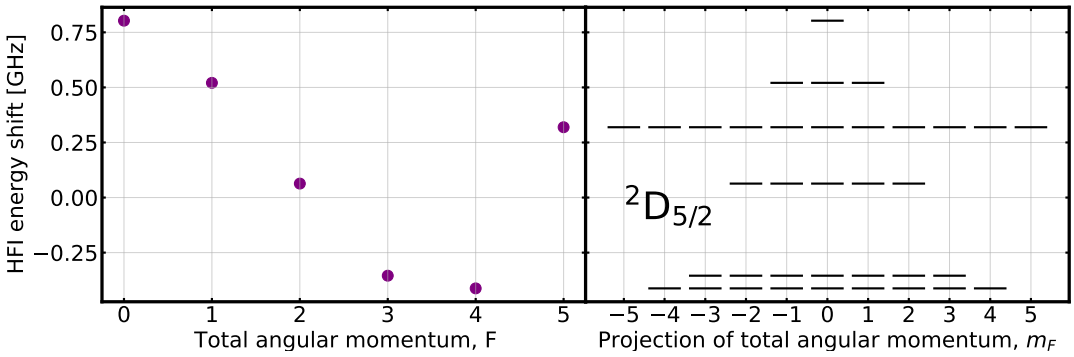

Figure 10.4: Theoretical hyperfine structure of the $^2D_{5/2}$ in $^{173}Yb^+$. The hyperfine coefficients are given in [Ita06].

do intial spectroscopy of these states. By driving only the $^2S_{1/2}\ |F=2\rangle \rightarrow {}^2D_{5/2}\ |F=0\rangle$ transition, we will selectively populate just the $^2F^o_{7/2}\ |F=1\rangle$ hyperfine manifold. We only currently have two 760 nm lasers available to us, so limiting our exposure to all the hyperfine levels in the $^2F^o_{7/2}$ will make finding the 760 nm transitions a bit easier. This form of state preparation will also make heralded state preparation of pure states in the $^2F^o_{7/2}$ of $^{173}Yb^+$ straightforward, and even might provide a way to optically pump into a pure state with the addition of microwave times to clean out neighboring states.

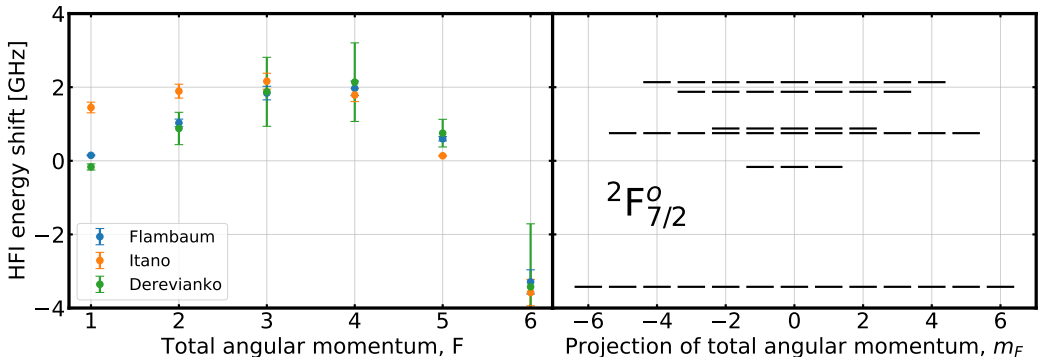

Figure 10.5: Theoretical hyperfine structure of the $^2F^o_{7/2}$ in $^{173}Yb^+$. The hyperfine coefficients are given in [Ita06, XLC20, PSW12]

[ABH06] M. Acton, K-A Brickman, P.C Haljan, L. Lee, L. Deslauriers, and C. Monroe. "Near-perfect simultaneous measurement of a qubit register." *Quantum. Inf. Comp.*, **6**:465, 2006.

[Arm71] L. Armstrong. *Theory of the hyperfine structure of free atoms.* Wiley Interscience, 1971.

[BBF21] C. H. Baldwin, B. J. Bjork, M. Foss-Feig, J. P. Gaebler, D. Hayes, M. G. Kokish, C. Langer, J. A. Sedlacek, D. Stack, and G. Vittorini. "High-fidelity light-shift gate for clock-state qubits." *Physical Review A*, **103**(1), Jan 2021.

[BCM19] Colin D. Bruzewicz, John Chiaverini, Robert McConnell, and Jeremy M. Sage. "Trapped-ion quantum computing: Progress and challenges." *Applied Physics Reviews*, **6**(2), 2019.

[BKD05] Dmitry Budker, Derek Kimball, David Demille, and Steve Lamoreaux. "Atomic Physics: An Exploration Through Problems and Solutions." *Physics Today*, **58**:62–64, 02 2005.

[BM92] R. W. Berends and L. Maleki. "Hyperfine structure and isotope shifts of transitions in neutral and singly ionized ytterbium." *J. Opt. Soc. Am. B*, **9**(3):332–338, Mar 1992.

[BMB98] D. J. Berkeland, J. D. Miller, J. C. Bergquist, W. M. Itano, and D. J. Wineland. "Minimization of ion micromotion in a Paul trap." *Journal of Applied Physics*, **83**(5025), 1998.

[BMC16] C. Bruzewicz, R. McConnell, J. Chiaverini, and J. Sage. "Scalable loading of a two-dimensional trapped-ion array." *Nature Communications*, 2016.

[BMS19] C.D. Bruzewicz, R. McConnell, J. Stuart, J.M. Sage, and J. Chiaverini. "Dual-species, multi-qubit logic primitives for Ca^+/Sr^+ trapped-ion crystals." *npj Quantum Information*, 2019.

[BN97] E. Burt and W. Nagourney. "Signal-to-noise enhancement in optical spectroscopy of single indium ions using amplitude modulation and synchronous detection." *Review of Scientific Instruments*, 1997.

[Cam20] Wesley C. Campbell. "Certified quantum gates." *Phys. Rev. A*, **102**:022426, Aug 2020.

[Cas36] H. B. G. Casimir. *One the Interaction Between Atomic Nuclei and Electrons.* Springer Netherlands, 1936.

[CGB94] J. I. Cirac, L. J. Garay, R. Blatt, A. S. Parkins, and P. Zoller. "Laser cooling of trapped ions: The influence of micromotion." *Phys. Rev. A*, **49**:421–432, Jan 1994.

[CHC19] Justin E. Christensen, David Hucul, Wesley C. Campbell, and Eric R. Hudson. "High fidelity manipulation of a qubit built from a synthetic nucleus." *arXiv*, **na**:1907.13331, 2019.

[Chr20] Justin Christensen. *High fidelity operation of a radioactive ion qubit*. PhD thesis, University of California, Los Angeles, Los Angeles, California, United States, 2020.

[DAB06] L. Deslauriers, M. Acton, B. B. Blinov, K.-A. Brickman, P. C. Haljan, W. K. Hensinger, D. Hucul, S. Katnik, R. N. Kohn, P. J. Lee, M. J. Madsen, P. Maunz, S. Olmschenk, D. L. Moehring, D. Stick, J. Sterk, M. Yeo, K. C. Younge, and C. Monroe. "Efficient photoionization loading of trapped ions with ultrafast pulses." *Phys. Rev. A*, **74**:063421, Dec 2006.

[DF16] V. A. Dzuba and V. V. Flambaum. "Hyperfine-induced electric dipole contributions to the electric octupole and magnetic quadrupole atomic clock transitions." *Phys. Rev. A*, **93**:052517, 2016.

[DiV00] David P. DiVincenzo. "The Physical Implementation of Quantum Computation." *Fortschritte der Physik*, **48**(9-11):771–783, 2000.

[EHH20] C. L. Edmunds, C. Hempel, R. J. Harris, V. Frey, T. M. Stace, and M. J. Biercuk. "Dynamically corrected gates suppressing spatiotemporal error correlations as measured by randomized benchmarking." *Phys. Rev. Research*, **2**:013156, Feb 2020.

[ET96] D Engelke and Chr Tamm. "Dark times in the resonance fluorescence of trapped 171 Yb ions caused by spontaneous quantum jumps to the 2D3/2(F= 2) state." *Europhysics Letters (EPL)*, **33**(5):347–352, feb 1996.

[ETH10] S. Ejtemaee, R. Thomas, and P. C. Haljan. "Optimization of Yb^+ fluorescence and hyperfine-qubit detection." *Phys. Rev. A*, **82**:063419, Dec 2010.

[FBA03] D. Felinto, C. A. C. Bosco, L. H. Acioli, and S. S. Vianna. "Coherent accumulation in two-level atoms excited by a train of ultrashort pulses." *Optics Communications*, **215**:69, 2003.

[Fey82] Richard P Feynman. "Simulating physics with computers." *International Journal of Theoretical Physics*, **21**(6):467–488, 1982.

[FFE18] T. Feldker, H. Fürst, N. V. Ewald, J. Joger, and R. Gerritsma. "Spectroscopy of the $^2S_{1/2} \rightarrow^2 P_{3/2}$ transition in Yb ii: Isotope shifts, hyperfine splitting, and branching ratios." *Phys. Rev. A*, **97**:032511, Mar 2018.

[FSL97] P. T. H. Fisk, M. J. Sellars, M. A. Lawn, and G. Coles. "Accurate measurement of the 12.6 GHz "clock" transition in trapped /sup 171/Yb/sup +/ ions." *IEEE Transactions on Ultrasonics, Ferroelectrics, and Frequency Control*, **44**(2):344–354, 1997.

[FYK20] H. A. Fürst, C.-H. Yeh, D. Kalincev, A. P. Kulosa, L. S. Dreissen, R. Lange, E. Benkler, N. Huntemann, E. Peik, and T. E. Mehlstäubler. "Coherent Excitation of the Highly Forbidden Electric Octupole Transition in $^{172}Yb^{+}$." *Phys. Rev. Lett.*, **125**:163001, Oct 2020.

[Gho95] Pradip K. Ghosh. *Ion Traps.* Oxford University Press, Oxford, 1995.

[GKK20] R. P. de Groote, S. Kujanpää, Á. Koszorús, J. G. Li, and I. D. Moore. "Study of the magnetic octupole moment of ^{173}Yb using collinear laser spectroscopy." *arXiv*, 2020.

[HAB14] T. P. Harty, D. T.C. Allcock, C. J. Ballance, L. Guidoni, H. A. Janacek, N. M. Linke, D. N. Stacey, and D. M. Lucas. "High-fidelity preparation, gates, memory, and readout of a trapped-ion quantum bit." *Physical Review Letters*, **113**(22):2–6, 2014.

[Har13] Thomas Harty. *Abstract High-Fidelity Microwave-Driven Quantum Logic in Intermediate-Field 43 Ca +.* PhD thesis, University of Oxford, Oxford, England, 2013.

[HS75] T. W. Hänsch and A. L. Schawlow. "Cooling of gases by laser radiation." *Optics Communications*, **13**:68, 1975.

[HSC08] Richard J. Hendricks, Jens L. Sørensen, Caroline Champenois, Martina Knoop, and Michael Drewsen. "Doppler cooling of calcium ions using a dipole-forbidden transition." *Phys. Rev. A*, **77**:021401, Feb 2008.

[HSL16] N. Huntemann, C. Sanner, B. Lipphardt, Chr Tamm, and E. Peik. "Single-Ion Atomic Clock with 3×10^{-18} Systematic Uncertainty." *Physical Review Letters*, **116**(6):1–5, 2016.

[Huc15] David Hucul. *A Modular Quantum System of Trapped Atomic Ions.* PhD thesis, University of Maryland, College Park, Maryland, United States, 2015.

[IRJ18] Michael Ip, Anthony Ransford, Andrew M Jayich, Xueping Long, Conrad Roman, and Wesley C Campbell. "Phonon lasing from optical frequency comb illumination of trapped ions." *Physical review letters*, **121**(4):043201, 2018.

[Ita06] Wayne M. Itano. "Quadrupole moments and hyperfine constants of metastable states of Ca^{+}, Sr^{+}, Ba^{+}, Yb^{+}, Hg^{+}, and Au." *Phys. Rev. A*, **73**:022510, Feb 2006.

[Jam98] D James. "Quantum dynamics of cold trapped ions with application to quantum computation." *Applied Physics B*, 1998.

[Jan15] Hugo Alexander Janacek. *Optical Bloch equations for simulating trapped-ion qubits*. PhD thesis, University of Oxford, Oxford, England, 2015.

[JG02] Berkeland D. J. and Boshier M. G. "Destabilization of dark states and optical spectroscopy in Zeeman-degenerate atomic systems." *Phys. Rev. A*, **65**:033413, Feb 2002.

[KLR08] E. Knill, D. Leibfried, R. Reichle, J. Britton, R. B. Blakestad, J. D. Jost, C. Langer, R. Ozeri, S. Seidelin, and D. J. Wineland. "Randomized benchmarking of quantum gates." *Phys. Rev. A*, **77**:012307, Jan 2008.

[LAS12] N.M Linke, D.T.C Allcock, D.J. Szwer, C.J. Ballance, T.P. Harty, H.A. Janacek, D.N. Stacey, A.M. Steane, and D.M. Lucas. "Background-free detection of trapped ions." *Applied Physics B*, 2012.

[LBM03] D. Leibfried, R. Blatt, C. Monroe, and D. Wineland. "Quantum dynamics of single trapped ions." *Rev. Mod. Phys.*, **75**:281, 2003.

[LRR21] Edmunds C. L., Tan T. R., Milne A. R., Singh A., and Biercuk M. J. "Scalable hyperfine qubit state detection via electron shelving in the $^2D_{5/2}$ and $^2F_{7/2}$ manifolds in $^{171}Yb^+$." *arXiV*, 2021.

[MBG87] A. Münch, M. Berkler, Ch. Gerz, D. Wilsdorf, and G. Werth. "Precise ground-state hyperfine splitting in ^{173}ii." *Phys. Rev. A*, **35**:4147–4150, May 1987.

[Mei13] Adam M. Meier. *Randomized Benchmarking of Clifford Operators*. PhD thesis, University of Colorado, 2013.

[MGH94] Ann-Marie Mårtensson-Pendrill, David S. Gough, and Peter Hannaford. "Isotope shifts and hyperfine structure in the 369.4-nm 6s-6$p_{1/2}$ resonance line of singly ionized ytterbium." *Phys. Rev. A*, **49**:3351–3365, May 1994.

[MS99] Harold J. Metcalf and Peter van der Straten. *Laser Cooling and Trapping*. Springer-Verlag, New York, 1999.

[NHT78] W. Neuhauser, M. Hohenstatt, P. Toschek, and H. Dehmelt. "Optical-Sideband Cooling of Visible Atom Cloud Confined in Parabolic Well." *Phys. Rev. Lett.*, **41**:233, 1978.

[NSD86] Warren Nagourney, Jon Sandberg, and Hans Dehmelt. "Shelved optical electron amplifier: Observation of quantum jumps." *Phys. Rev. Lett.*, **56**:2797–2799, Jun 1986.

[NVG13] Rachel Noek, Geert Vrijsen, Daniel Gaultney, Emily Mount, Taehyun Kim, Peter Maunz, and Jungsang Kim. "High speed, high fidelity detection of an atomic hyperfine qubit." *Opt. Lett.*, **38**(22):4735–4738, Nov 2013.

[OHM09] S. Olmschenk, D. Hayes, D. N. Matsukevich, P. Maunz, D. L. Moehring, K. C. Younge, and C. Monroe. "Measurement of the lifetime of the $6p\ ^2P^o_{1/2}$ level of Yb^+." *Phys. Rev. A*, **80**:022502, Aug 2009.

[OYM07] S. Olmschenk, K. C. Younge, D. L. Moehring, D. N. Matsukevich, P. Maunz, and C. Monroe. "Manipulation and detection of a trapped Yb^+ hyperfine qubit." *Phys. Rev. A*, **76**:052314, Nov 2007.

[PDF20] J. M. Pino, J. M. Dreiling, C. Figgatt, J. P. Gaebler, S. A. Moses, M. S. Allman, C. H. Baldwin, M. Foss-Feig, D. Hayes, K. Mayer, C. Ryan-Anderson, and B. Neyenhuis. "Demonstration of the QCCD trapped-ion quantum computer architecture." *arXiv*, 2020.

[PK15] Thaned Pruttivarasin and Hidetoshi Katori. "Compact field programmable gate array-based pulse-sequencer and radio-frequency generator for experiments with trapped atoms." *Rev. Sci. Instrum.*, **86**:115106, 2015.

[Pre18] John Preskill. "Quantum Computing in the NISQ era and beyond." *Quantum*, **2**:79, August 2018.

[PRK97] E. H. Pinnington, G. Rieger, and J. A. Kernahan. "Beam-laser measurements of the lifetimes of the $6p$ levels in Yb II." *Phys. Rev. A*, **56**:2421–2423, Sep 1997.

[PSW12] M.J. Petrasiunas, E.W. Streed, T.J. Weinhold, B.G. Norton, and D. Kielpinski. "Optogalvanic Spectroscopy of Metastable States in Yb+." *Applied Physics B*, 2012.

[Ran20] Anthony Ransford. *Old Dog, New Trick: High Fidelity, Background-free State Detection of an Ytterbium Ion Qubit*. PhD thesis, University of California, Los Angeles, Los Angeles, California, United States, 2020.

[Roo00] Christian Roos. *Controlling the quantums state of trapped ions*. PhD thesis, University of Innbruk, Innsbruk, Austria, 2000.

[SDN09] M. M. Schauer, J. R. Danielson, A.T. Nguyen, L.B. Wang, X. Zhao, and J. R. Torgerson. "Collisional population transfer in trapped Yb^+ ions." *Phys. Rev. A*, **79**:062705, Jun 2009.

[Sho96] P. W. Shor. "Fault-tolerant quantum computation." In *Proceedings of 37th Conference on Foundations of Computer Science*, pp. 56–65, 1996.

[SNM01] U. I. Safronova, C. Namba, I. Murakami, W. R. Johnson, and M. S. Safronova. "Electric-dipole, electric-quadrupole, magnetic-dipole, and magnetic-quadrupole transitions in the neon isoelectronic sequence." *Phys. Rev. A*, **64**:012507, Jun 2001.

[Ste20] D. Steck. *Quantum and Atom Optics*. Open Publication License, 2020.

[Sug99] Kazuhiko Sugiyama. "Laser cooling of single 174Yb+ ions stored in a RF trap." *Japanese Journal of Applied Physics, Part 2: Letters*, **38**(4 A):2137–2140, 1999.

[TEM21] T. R. Tan, C. L. Edmunds, A. R. Milne, M. J. Biercuk, and C. Hempel. "Precision Characterization of the $^2\mathrm{D}_{5/2}$ State and Quadratic Zeeman Coefficient in $^{171}\mathrm{Yb}^+$." *arXiv*, 2021.

[TRG97] P. Taylor, M. Roberts, S. V. Gateva-Kostova, R. B. M. Clarke, G. P. Barwood, W. R. C. Rowley, and P. Gill. "Investigation of the $^2S_{1/2}-^2D_{5/2}$ clock transition in a single ytterbium ion." *Phys. Rev. A*, **56**:2699–2704, Oct 1997.

[TVM21] S. L. Todaro, V. B. Verma, K. C. McCormick, D. T. C. Allcock, R. P. Mirin, D. J. Wineland, S. W. Nam, A. C. Wilson, D. Leibfried, and D. H. Slichter. "State Readout of a Trapped Ion Qubit Using a Trap-Integrated Superconducting Photon Detector." *Phys. Rev. Lett.*, **126**:010501, Jan 2021.

[VAS19] Geert Vrijsen, Yuhi Aikyo, Robert F. Spivey, I. Volkan Inlek, and Jungsang Kim. "Efficient isotope-selective pulsed laser ablation loading of 174Yb+ ions in a surface electrode trap." *Opt. Express*, **27**(23):33907–33914, Nov 2019.

[Wal13] Sean Wallis. "Binomial Confidence Intervals and Contingency Tests: Mathematical Fundamentals and the Evaluation of Alternative Methods." *Journal of Quantitative Linguistics*, **20**(3):178–208, 2013.

[WD75] D. J. Wineland and H. Dehmelt. "Proposed $10^{14}\Delta\nu < \nu$ laser fluorescence spectroscopy on Tl^+ mono-ion oscillator." *Bull. Am. Phys. Soc.*, **20**:637, 1975.

[WDW78] D. J. Wineland, R. E. Drullinger, and F. L. Walls. "Radiation-Pressure Cooling of Bound Resonant Absorbers." *Phys. Rev. Lett.*, **40**:1639, 1978.

[WI79] D. J. Wineland and Wayne M. Itano. "Laser cooling of atoms." *Phys. Rev. A*, **20**:1521–1540, Oct 1979.

[WLQ21] Pengfei Wang, Chun-Yang Luan, Mu Qiao, Mark Um, Junhua Zhang, Ye Wang, Xiao Yuan, Mile Gu, Jingning Zhang, and Kihwan Kim. "Single ion qubit with estimated coherence time exceeding one hour." *Nature Communications*, **12**(1):233, 2021.

[Woo80] Gordon Kemble Woodgate. *Elementary Atomic Structure*. Clarendon Press, 1980.

[XLC20] Di Xiao, Jiguang Li, Wesley C. Campbell, Thomas Dellaert, Patrick McMillin, Anthony Ransford, Conrad Roman, and Andrei Derevianko. "Hyperfine structure of $^{173}\mathrm{Yb}^+$: Toward resolving the ^{173}Yb nuclear-octupole-moment puzzle." *Phys. Rev. A*, **102**:022810, Aug 2020.

[YM00] N Yu and L Maleki. "Lifetime measurements of the 4 f 14 5 d metastable states in single ytterbium ions." *Physical Review A*, **61**(2):022507, 2000.

[YSD15] Bryce Yoshimura, Marybeth Stork, Danilo Dadic, Wesley C Campbell, and James K Freericks. "Creation of two-dimensional Coulomb crystals of ions in oblate Paul traps for quantum simulations." *EPJ Quantum Technology*, **2**:2, 2015.